Topological light-matter interactions at the nanoscale

Controlling THz frequency light with topological insulator nanostructures

Marie Rider

Department of Physics
Imperial College London

A thesis presented for the degree of
Doctor of Philosophy (PhD)

Abstract

Topological nanophotonics combines the high sensitivity of nanophotonic systems with the robustness of topological states, presenting an exciting new platform for both nanotechnological applications and fundamental research in topological light-matter interactions [1]. The work I present in this thesis focuses on **topological insulator (TI) nanostructures** and their interactions with light, with particular focus on the terahertz (THz) regime.

TIs are insulating in their bulk and host symmetry-protected, conducting surface states which are robust against disorder [2]. These surface states manifest as a Dirac cone traversing the bulk band gap. TI nanostructures (all dimensions $\leq$ 100 nm) exhibit a discretised Dirac cone due to quantum confinement of the topological surface states, with energy levels separated by THz frequencies. Due to their analogy with semiconductor quantum dots and 2D topological insulator quantum dots, I refer to this system as a **topological quantum dot (TQD)**.

The results of this thesis are organised thematically into three areas:

(i) I expand the current knowledge of **TI nanostructure electronic structures**, describing the surface states and energy levels for geometries ranging from the infinite nanowire to a flat nanodisk within a single mathematical framework [3].

(ii) I investigate the coupling of TQD states with THz frequency light, including selection rules and the suppression of transitions away from the Dirac point when the TQD is placed in a high quality cavity, allowing for a closed system of energy levels. Using Monte Carlo simulations I demonstrate that **a single TQD in a cavity will lase in the THz**, with an ultra-low threshold. The creation of robust, low threshold lasers in the THz regime is a crucial frontier in modern applied physics, due to the notorious absence of practical technologies for generating and sensing radiation in the THz gap ($0.1 - 10$ THz). I show that thermal photons are abundant enough to pump the system, and present a road map to room-temperature THz lasing with no additional external pumping source [4].

(iii) I describe how the quantised TI surface states modify the bulk properties of the nanostructure via a new **polariton mode (the SToP mode)** [5], and present the first experimental evidence of the SToP mode [6]. I demonstrate how the SToP mode can be used to manipulate the THz behaviour of light in the environment surrounding a TI nanostructure, by increasing the **photonic local density of states** by many orders of magnitude [7]. This phenomenon has potential applications in nanotechnology and also presents a new way of probing topological properties of matter using light.

I hope that this thesis serves as a guide to students new to the wonderful and interdisciplinary topic of topological nanophotonics, and that my work contributes to a slightly better understanding of topological light-matter interactions at the nanoscale, and the manipulation of THz frequency light.

Acknowledgements

This thesis is a culmination of an education that began long before my start at Imperial, and so the thanks contained here can't do justice to the innumerable people who have helped me along the way.

To all the students I've ever taught. Teaching you made me a better scientist, and seeing you discover new physics concepts that I had long considered 'mundane' has made me realise how privileged I am to work on such amazing topics every day. Thank you for challenging me to think and explain topics from different vantage points, and for your enthusiasm and energy.

To Vincenzo, Derek and Peter. I'm so lucky to have had such fantastic supervisors. Thank you to Derek and Peter for the ever-helpful discussions and support. Vincenzo, thank you for your unbridled love of science, your encouragement and your kindness. If the trope that students become their PhD supervisor is true, I'll be very happy with that outcome!

To Sam. I don't think either of us could have imagined the roller coaster the PhD would be, but you were there for the successes and the failures. I couldn't have asked for a better office mate (virtual or otherwise!) and I'm so glad we had each other. Thank you for your friendship!

To all the friends scattered around the world that I've had the pleasure to know through my physics journey. To the endless hours of discussing physics, of arguing over politics and philosophy and life. My time at Sussex, Perimeter, Innsbruck, Washington DC and London has shaped me as a physicist and a person and I'm so glad that I've had so many places to call home. In particular, thank you so much to Eva and James. You've been my biggest cheerleaders, and my second family. I can't imagine what this experience would have been like without you.

To Simon Penton. It may have been over 10 years since I sat in your physics classroom, as the only girl and too nervous to speak up, but I still think about the conversations we had about philosophy, faith and science. Thank you for helping me find my voice and my path.

To Francesco. It's hard to put into words just how thankful I am for your steadfastness, your patience and your unwavering support. *Grazie mille.*

Finally, to my family. Thank you. It was a really long journey to get here and you supported me, unquestioningly, every step of the way. I couldn't have done this without you.

Contents

Abstract i

Acknowledgements iii

Table of Contents v

List of Tables ix

List of Figures xi

Nomenclature xix

Preface xxiii

1 Introduction 1

Part I: Theoretical Background

2 Theory of Topological Insulators 7

2.1 Symmetry and topology 8

2.1.1 Symmetry and conventional order 8

2.1.2 Topological invariants 10

2.1.3 Topological band structures and surface states 12

2.2 Time-reversal symmetry and topological insulators 16

2.3 3D topological insulator (TI) materials 17

2.3.1 Crystal structure and symmetry 19

2.3.2 Four-band bulk Hamiltonian for TIs 21

2.3.3 Effective surface state Hamiltonian 22

2.3.4 Bulk phonons in topological insulator materials 25

2.4 Landscape of topological quantum systems 25

3 Theory of light 31

3.1 Maxwell's equations 32

3.1.1 Macroscopic Maxwell's equations 32

3.1.2 Auxiliary fields, polarization and magnetization 33

3.1.3 Microscopic Maxwell's equations 35

3.2 The shape of light 35

3.2.1 Vector and scalar potentials 35

3.2.2 The wave equation 36

3.2.3 Light polarisation 37

3.3 Quantisation of light 38

3.4 Light-matter interactions 40

3.4.1 The interaction Hamiltonian 40

3.4.2 Transitions 42

3.4.3 Calculating transition rates 43

3.5 Lasing 44

3.6 Green's functions 49

3.6.1 The mathematics of Green's functions 50

3.6.2 Deriving the Green's function for the electric field 51

3.6.3 Dipole radiation 53

3.7 The photonic density of states (DOS) 56

Part II: Research Topics

4 Topological Insulator Nanostructures 63

4.1 Prolate spheroidal TI nanoparticles 65

4.1.1 Bulk Hamiltonian 65

4.1.2 Surface state ansatz 67

4.1.3 Surface Hamiltonian 70

4.2 General and limiting cases 72

4.2.1 The nanosphere 72

4.2.2 The nanowire 76

4.2.3 General prolate spheroid 78

4.3 From prolate to oblate spheroidal TI nanoparticles 81

4.4 General and limiting cases 87

4.4.1 The nanosphere . . . 87

4.4.2 The nanodisk . . . 88

4.4.3 General oblate spheroid . . . 91

5 TQDs as a THz Lasing Source . . . 97

5.1 TQDs interacting with light 99

5.1.1 Photon-mediated transitions in free space . . . 99

5.1.2 Cavity QED: Transitions in a 1D Fabry-Pérot cavity . . . 103

5.1.3 Selection rules . . . 107

5.1.4 Higher order corrections . . . 111

5.2 Lasing TQD at zero temperature 114

5.2.1 Setup . . . 114

5.2.2 System dynamics . . . 116

5.3 Finite temperature lasing 119

5.3.1 Thermal photons . . . 120

5.3.2 Cavity QED: Transitions in a 3D Fabry-Pérot cavity . . . 120

5.3.3 Setup and outlook . . . 124

6 Modifying Light with Topology . . . 127

6.1 The SToP mode 128

6.1.1 Dielectric function . . . 129

6.1.2 Absorption cross-section for a topological insulator nanoparticle . 130

6.1.3 Understanding the absorption cross-section . . . 133

6.1.4 Modifying theory parameters . . . 134

6.1.5 Ensembles of TINPs . . . 139

6.1.6 Comparison to experimental results . . . 140

6.2 TINP modifying the photonic local density of states (LDOS) 141

6.2.1 Setup . . . 142

6.2.2 Calculating photonic LDOS . . . 144

7 Conclusions . . . 149
7.1 Summary 149
7.2 Outlook and future work 149
Appendices . . . 151
A Useful maths, formalisms and conventions 153
A.1 Pauli matrices . . . 153
A.2 Unusual algebraic operations . . . 153
A.3 Scalars, vectors and dyads . . . 154
A.4 Coordinate systems . . . 154
A.5 Jacobi polynomials . . . 156
A.6 2nd order ODEs from coupled 1st order ODES . . . 157
A.7 Useful integrals . . . 157
A.8 Time-dependent perturbation theory . . . 158
B Supplementary derivations and information 159
B.1 Berry phase . . . 159
B.2 Spectroscopy . . . 160
B.3 Choosing Gauges in electromagnetism . . . 161
B.4 Beyond the electric dipole approximation . . . 162
B.5 Fermi's golden rule . . . 164
B.6 Cross-section, spectral density and transition rates . . . 164
B.7 Deriving the effective surface Hamiltonian . . . 165
B.8 The Q factor . . . 166
B.9 Spontaneous emission and Purcell effect in 1D free space . . . 167
B.10 Particle statistics . . . 169
B.11 Fano resonances . . . 169
B.12 Experimental method for producing bismuth telluride nanoparticles 169
C Numerical methods 171
C.1 Finite difference method for solving ODEs . . . 171
C.2 Fermionic rate equations from Monte Carlo simulations . . . 172
C.3 Lorentzian decomposition . . . 174
Bibliography 175

List of Tables

2.1 **Four-band Hamiltonian parameters:** The parameters (taken from (49), originally extracted from DFT calculations) for the Hamiltonian describing the four bands nearest the Γ point of Bi_2Se_3 and Bi_2Te_3. 22

5.1 **Transition frequencies for TQDs:** To first order, $\nu^{(0)} = A/hR$ Hz, where R nm is the nanoparticle radius and A is 2.0 eVÅ for Bi_2Te_3 and 3.0 eVÅ for Bi_2Se_3. Including the second order term, the first transition frequency in each band is $\nu_{\mathrm{c,v}} = A/hR \pm A_1/hR^2$ Hz, where A_1 is 41.4 eVÅ^2 for Bi_2Te_3 and 23.7 eVÅ^2 for Bi_2Se_3. 113

6.1 **Parameters of $\epsilon_{\parallel}(\nu)$ for Bi_2Te_3:** Calculated from experimental data in (213). $\nu_{\mathrm{p,j}}$, $\nu_{0,\mathrm{j}}$ and γ_{j} denote the amplitude, resonance frequency and harmonic broadening parameters for each mode. 130

6.2 **Parameters of Lorentzian fit**: Parameters of the four peak Lorentzian fit with a fit error of 0.24%. 141

List of Figures

1.1 **Thesis schematic:** A graphical abstract of the content and main results covered in this thesis. 4

2.1 **Conventional phase transitions: (a)** Solid-liquid phase transition. **(b)** Displacement field $\mathbf{u}(\mathbf{r})$ gives the displacement needed to bring the ideal lattice into line with the atoms in the local neighbourhood of $\mathbf{r}$. There is an ambiguity in this definition due to freedom to choose the reference atom, such that $\mathbf{u}(\mathbf{r}) \equiv \mathbf{u}(\mathbf{r}) + (2ma_x, 2na_y)$, where m and n are integers. 9

2.2 **Topological invariants: (a)** A local geometry can have positive or negative curvature with respect to a reference point. When integrated over a closed surface, M, the Gauss-Bonnet theorem links the curvature of the surface to its genus, g, via the relation $\int_M K \, dS = 4\pi(1-g)$. The genus of **(b)** a sphere is $g = 0$, and **(c)** a torus is $g = 1$. 11

2.3 **The road to 3D topological insulators: (a)** Quantum Hall system, supporting protected edge states. First discovered in 1980 (61) with the explanation of the quantised Hall conductance following shortly after in 1982 (62). **(b)** The first proposals of the Quantum spin Hall system (2D topological insulator) came in 2005 (43) and 2006 (63). The generalisation to **(c)** the 3D topological insulator followed in 2007 (47) 12

2.4 **Topological band structures: (a)** Visualisation of the transformation $\mathbf{H} \rightarrow \mathbf{H}'$ in which **(i)** the band gap remains open during the transformation, meaning that both Hamiltonians exist in the same topological phase and **(ii)** the gap closes during the transformation, signalling a potential topological phase transition. **(b)** Typical band structure of a TI in which symmetry-protected conducting edge states traverse the gap. **(c)** In materials containing heavy elements, the spin-orbit coupling can be so strong that at the Γ point, higher bands are pushed below lower bands, resulting in band inversion. 14

2.5 **Crystal structure and band structure of topological insulator materials: (a)** Spatial view and (0001) projection of a Bi_2Te_3 unit cell with repetition of a Te II layer. The unit cell consists of three quintuple layers (QLs), which are bonded by weak van der Waals forces. A QL consists of five strongly bound alternating hexagonal Bi (purple) and Te (teal) atomic sheets, shifted relative to each other. The height of the unit cell is 3.051 nm, and so each QL is ~ 1 nm in depth. Energy and momentum dependence of the local density of states (LDOS) for **(b i)** Bi_2Se_3, and **(b ii)** Bi_2Te_3 on the (111) surface. Warmer colours represent higher LDOS. The surface states can be clearly seen around the Γ point as red lines traversing the bulk gap. Figure **(a)** created by S. Palmer. Figures **(b i)** and **(b ii)** taken from (48), reprinted with permission from Springer Nature, Nature Physics. 18

2.6 **The origin of the Bi_2Te_3 band structure:** Starting from the atomic orbitals of Bi and Te, the following four steps are required to understand the band structure: (I) The hybridization of Bi orbitals and Te orbitals, (II) the formation of the bonding and anti-bonding states due to the inversion symmetry, (III) the crystal field splitting, and (IV) the influence of the SOC. Figure reproduced from (49) with permission from the American Physical Society. This scheme also describes the band structure for other materials in the Bi_2Se_3 family. 20

2.7 **Optical phonons in Bi_2Te_3: (a)** Chain of five atoms in a quintuple layer used to demonstrate vibration dynamics highlighted with black outline and black lines indicating their covalent bonds. **(b)** The **(i)** Raman active and **(ii)** IR active modes of Bi_2Te_3, with subscripts g and u referring to Raman and IR active modes respectively. The superscripts $1, 2$ denote the low and high frequency modes respectively, while E and A refer to whether the modes are in-plane or out-of-plane. The $\pm$ signs denote in-plane and out-of-plane movement. Figure modified from (78) with permission from John Wiley and Sons, Physica status solidi (b). 24

2.8 **The landscape of topological quantum systems:** Schematic showing the different areas of topological quantum matter. 29

3.1 **Maxwell's equations: (a) Gauss' law**. Flux through a closed surface is equal to the charge, q_f enclosed by the surface. This is equivalent to saying that electric fields lines must always start and end at charges. **(b) Gauss' law for magnetism**. Magnetic flux through a closed surface is always equal to zero. This is equivalent to saying that magnetic field lines always join up, such that field lines entering and leaving a closed surface always sum to zero. Said another way, magnetic monopoles do not occur. **(c) Faraday's law of induction.** A time-varying magnetic field, $\mathbf{B}$, will always accompany a spatially-varying, non-conservative electric field, $\mathbf{E}$, and vice versa. **(d) Ampere's law**. A flowing electric current, $\mathbf{I}_\mathrm{f}$, gives rise to a magnetic field, $\mathbf{H}$, which circles the current. A time-changing displacement field, $\mathbf{D}$, gives rise to a magnetic field, $\mathbf{H}$, which circles $\mathbf{D}$. 33

3.2 **Maxwell's equations at an interface:** Boundary conditions for Maxwell's equations. The tangential component of $\mathbf{E}$ is continuous across the surface, as is the tangential component of $\mathbf{H}$ unless there is a surface current present. The normal component of $\mathbf{D}$ is continuous unless there is a surface charge, and the normal component of $\mathbf{B}$ is always continuous across the interface. 34

3.3 **The shape of light: (a)** A schematic of an electromagnetic wave and its components. $\mathbf{E}$ and $\mathbf{B}$ are perpendicular to each other, and lie in the plane perpendicular to $\mathbf{k}$. This plane is described by two basis vectors, $\mathbf{e}_1$ and $\mathbf{e}_2$. Wavelength λ is measured between two adjacent wave maxima. **(b)** The polarisation of the light wave is described in terms of $\mathbf{e}_1$ and $\mathbf{e}_2$, which need not be orthogonal, but should be linearly independent. Common polarisation bases are **(i)** linear and **(ii)** circular polarisation. 38

3.4 **Absorption and emission events: (a) Stimulated absorption**, in which a photon is absorbed, causing the electronic system to be excited to a higher energy corresponding to the energy of the absorbed photon. **(b i) Stimulated emission**, in which an incoming photon interacts with the electron system, triggering the emission of a photon with the same momentum and polarisation of the original photon. **(ii) Spontaneous emission**, in which a photon is emitted with random direction and polarisation. 43

3.5 **Lasing: (a)** A two level system such as **(i)** cannot reach population inversion, but at most can reach equal occupancy of its two levels as demonstrated in **(ii)** the time evolution of the system, where at steady-state $N_2 = N_1$. **b** For a three level system as shown in **(i)**, if $\Gamma^{\mathrm{stim}}_{3\to2} \gg \Gamma^{\mathrm{stim}}_{3\to1}, \Gamma^{\mathrm{stim}}_{2\to1}$ it is possible to reach population inversion such that $N_2 > N_1$. Spontaneous emission is considered negligible for both systems. 46

3.6 **The free space density of states: (a)** Dispersion relation of light in free space, $\omega = c|\mathbf{k}|$, and **(b)** the photonic density of states in 3D free space, $g(\omega) = \omega^2/c^3\pi^2$. 58

4.1 **Finding surface states for TI nanostructures:** Method for finding surface states and energies of TI nanostructures, taken from Imura *et al.* (34, 35) (purple) and extended to spheroidal coordinate systems, for the study of prolate and oblate spheroidal nanoparticles (green). 64

4.2 **Prolate spheroidal nanoparticles:** We describe our nanoparticles as prolate spheroids. **(a)** Prolate spheroidal nanoparticle with surface given by $\sigma = \sigma_0$ with semi-major axis $R_1 = a\sigma_0$ (parallel to the z-axis) and semi-minor axis $R_2 = a\sqrt{\sigma_0^2 - 1}$, where $R_1 \geq R_2$. **(b)** The spherical limit with $R_1 \approx R_2$, and **(c)** the limit of a nanowire, for which $R_1 \gg R_2$. 66

4.3 **The TI nanosphere:** A TI nanosphere of radius R has surface states described by three quantum numbers (s, n, m) where $s = \pm 1$, $n = 0, 1, 2, 3...$, $m = \pm 1/2, \pm 3/2, \pm 5/2, ...$, with their respective energy levels given by $E_{s,n,m} = s\frac{A}{R}(n + |m| + 1/2)$. 74

4.4 **The TI nanowire:** A TI nanowire of radius R and length L where $R \ll L$ has surface states described by the quantum numbers $s = \pm 1$ and $m = \pm 1/2, 3/2, 5/2, ...$ and k, the momentum along the length of the wire, which is continuous. The dispersion relation is given by $E_{s,k,m} = s\frac{A}{R}\sqrt{(kR)^2 + m^2}$. 77

4.5 **Eigenvalues of the general prolate spheroidal nanoparticle:** First three energy levels of the nanospheroid for varying R_1/R_2 for each of the the $|m|$ values $[7/2, 9/2, 11/2, 13/2]$ and normalised by A/R, where R is the minor-axis of the nanoparticle. In the nanosphere limit $R_1 \approx R_2$ ($\sigma_0 \gg 1$), we see that we recover the energy levels $E = \frac{A}{R}\left(n + |m| + \frac{1}{2}\right)$, and in the limit of the nanowire ($R_1 \gg R_2$) $\sigma_0 \to 1$, $E \approx A|m|/R$. 80

4.6 **Intermediate prolate spheroidal nanoparticle:** Energy levels for a prolate nanospheroid (nanocigar) with $\sigma_0 = 2$, such that $R_1 \approx 1.15R_2$. The degeneracy of the energy levels is seen to have lifted as the spherical symmetry is broken. . . 81

4.7 **Deforming the TI prolate nanospheroid:** First three energy levels for $m \in [7/2, 9/2, 11/2]$, under various constraints. **(a)** Energy levels of nanospheroid under deformation (by varying R_1/R_2) but with constant volume, equal to that of a nanosphere of $R = 50$ nm. **(b)** Energy levels of nanospheroid of constant surface area, with surface area of that of a nanosphere of R=50 nm. **(c)** Deforming energy levels of a nanospheroid with constant cross-section (retaining cross-section of a 50nm sphere) and changing length **(d)** Energy levels keeping constant a = 1. 82

4.8 **Oblate spheroidal nanoparticles:** We describe our nanoparticles as oblate spheroids. **(a)** Oblate spheroidal nanoparticle with surface given by $\zeta = \zeta_0$ with semi-minor axis $R_1 = a\zeta_0$ (parallel to the z-axis) and semi-major axis $R_2 = a\sqrt{1 + \zeta_0^2}$, where $R_1 \leq R_2$. **(b)** The spherical limit with $R_1 \approx R_2$, and **(c)** the limit of a disk, for which $R_1 \ll R_2$. 83

4.9 **The ideal TI nanodisk:** The energy levels of an ideal TI nanodisk of radius R and depth h, with aspect ratio $\ll 1$. This limit breaks the physically required conditions of confinement in the radial direction and a finite bulk, but is given here for completion. These energy levels are doubly degenerate, corresponding to $\mathrm{sign}(\tau) = \pm 1$, which relate to the decoupled upper and lower surfaces of the disk. 89

4.10 **Eigenvalues of the general oblate nanospheroid:** First four energy levels of the nanospheroid for varying R_1/R_2, for the $|m|$ values $[7/2, 9/2, 11/2, 13/2]$ and normalised by $A/R_1 = 2A/h$, where R_1 is the minor-axis of the spheroid or equivalently $h = 2R_1$, where h is the height of the spheroid. In the limit $R_1 \approx R_2$ ($\zeta_0 \gg 1$) we recover the limit of the sphere such that $E = s\frac{A}{R}(n + |m| + \frac{1}{2})$ and in the limit of the ideal, flat nanodisk $R_1 \ll R_2$ ($\zeta_0 \ll 1$), we observe the onset of degeneracy relating to the two sets of degenerate energy levels corresponding to the decoupled upper and lower surfaces off the disk. The physical limit of a nanodisk with complete quantum confinement ($R \leq 100$ nm)and a true bulk ($h = 2R_1 \geq 10$ nm) is denoted with the dotted line at $R_1 = 0.05R_2$ (which corresponds to $\zeta_0 = 0.05$). 93

4.11 **Finite nanodisk:** Energy levels for the finite nanodisk, in which the disk is assumed to be as flat as possible without losing the 3D bulk of the material ($h = 10$ nm) and the disk is as wide as possible before axial quantum confinement is relinquished ($R = 100$ nm). These combined conditions give a minimum value of $\zeta_0 = 0.05$. 94

4.12 **TI spheroidal nanoparticles:** Energy levels, normalised by A/R_2, for all cases from the nanodisk to the nanowire as a function of their aspect ratio, R_1/R_2, where $R_1/R_2 \leq 1$ for the oblate spheroid, and $R_1/R_2 \geq 1$ for the prolate spheroid. The prolate and oblate spheroids meet at the shared limit of the nanosphere, $R_1 = R_2$. At the limit $R_1 = R_2$ we recover the nanosphere energy levels $E_{+,n,m} = A(n + |m| + 1/2)/R_2$. For the limit $R_1 \gg R_2$ we recover the analytical nanowire energy levels for small $|\mathbf{k}|$, $E_{+,m} \approx A|m|/R_2$, and for $R_1 \ll R_2$ we recover the limit of the ideal nanodisk 95

5.1 **TQD in a cavity: (a)** TQD in an open, 1D Fabry-Pérot cavity, in which photons interact with the cavity along the cavity axis, or with free space in all other directions. An external pump can be implemented from outside the cavity. **(b)** The dispersion relation of the topological surface states is usually well approximated as a linear Dirac cone, however in a high Q cavity tuned to one of the TQD transitions near the Dirac cone, small quadratic deviations will result in the suppression of transitions away from the Dirac cone. 98

5.2 **Light in a cavity: (a)** Schematic for 1D Fabry-Pérot cavity in free space. The mirrors of the cavity have reflectivities R_1 and R_2 respectively. The spatial electric field pattern is given for the first four modes of the cavity. At the centre of the cavity, only odd modes are non-zero. **(b)** Discrete dispersion relation $\omega = m\pi c/L$, for light in a cavity of length $L = 0.94$ mm. **(c)** LDOS at position $z = 0$, normalised by the LDOS at frequency $\omega = \omega_{\text{cav}} = 1$ THz, for cavities with Q factor given by **(i)** 10, **(ii)** 10^2 and **(iii)** 10^4. Only modes with odd m (solid line) contribute to the LDOS at $z = 0$, due to the structure of the electric field. Contributions from even modes (dotted line) do not contribute to the LDOS at $z = 0$, and thus transitions at these frequencies will be suppressed in the cavity axis. However, shifting by a fraction of a wavelength along the cavity axis will give a different set of transition rates. 103

5.3 **TQD state labels and energies:** The states, $|\Psi_{s,n,m}\rangle = |s, n, m\rangle$ and corresponding energy levels are labelled for the first three energies above and below the Dirac point. 107

5.4 **TQD E1 selection rules:** Allowed transitions from the state $|-, 1, 1/2\rangle$. For light propagating from all directions, **(a)** intraband (purple) transitions couple energy levels within the same section of the Dirac cone and **(b)** interband (green) transitions couple levels above and below the Dirac point. 108

5.5 **Angular dependence of E1 matrix element: (a)** Schematic of incoming light with momentum $\mathbf{k}$, polar angle ϑ_0, with the c-axis of the material aligned with the z-axis. **(b)** Example of an interband transition $|\text{-}, 0, -\frac{1}{2}\rangle \rightarrow |\text{+}, 0, \frac{1}{2}\rangle$. **(c)** The matrix element $V_{\text{i,f}}$ for the transition in **(b)** varies as the polar angle ϑ_0 of incoming light varies. For light travelling parallel to the z-axis, only ϵ_{LH} **or** ϵ_{RH} light will mediate a transition. At intermediate angles, **both** polarisations may facilitate a transition. 110

5.6 **TQD E1 selection rules:** Allowed transitions from the state $|-,1,1/2\rangle$. For light propagating parallel to the c-axis of the material, **(a)** intraband and **(b)** interband transitions. 111

5.7 **k.p breakdown**: **(a)** Continuum band structure for Bi_2Te_3 with Dirac cone seen in the band gap (=165 meV (45)). Band structure up to and including $|\mathbf{k}|^2$ terms (solid black line) deviates from the linear $\mathbf{k}\cdot\mathbf{p}$ approximation (dotted black line) substantially away from the Γ-point. **(b)** For a $R = 30$ nm nanoparticle, discretised energy levels are expected. To first order (i.e. in the linear approximation), the transition frequency $\nu^{(0)} = 1.61$ THz. To second order (i.e. taking into account the $|\mathbf{k}|^2$ term) sequential transitions in the conduction band rapidly supersede the first transition, which when including the $|\mathbf{k}|^2$ correction has a frequency of $\nu_{\rm c} = 1.95$ THz. The first valence band transition is $\nu_{\rm v} = 1.28$ THz. Transitions in the valence band rapidly decrease in frequency away from the Γ-point. Interband transitions are unaffected by the second order correction due to cancellation of the $|\mathbf{k}|^2$ terms. 112

5.8 **Toy model lasing**: **(a)** Schematic of a TQD in a 1D open Fabry-Pérot cavity and allowed transitions. **(b)** Transitions involved in the lasing scheme. 115

5.9 **Evolution of toy model lasing system**: For a TQD of $R = 30$ nm in a cavity of length $50\lambda_{\rm v}$ and $\tau = 10^{-3}s$, pumped with incident photons $\bar{n}_{\rm pump} = 1$. **(a)** Schematic of transitions involved in the lasing scheme. **(b)** Average state occupation of energy levels in lasing scheme. Population inversion can be seen for lasing transition $E^1_- \rightarrow E^2_-$. **(c)** Average gain, normalised to the threshold value. The threshold value is exceeded nearly immediately. **(d)** Photon dynamics, with number of coherent photons in the cavity building up to a constant density and steady emission of coherent photons out of the cavity. Lasing rate, Γ, given by the gradient of photon number leaving the cavity. 117

5.10 **Threshold for toy model lasing**: **(a)** Steady-state lasing rate (coherent photons emitted from cavity per second) for a TQD with $E_{\rm F} = 0$ and $R = 30$ nm, and a cavity of length $50\lambda_{\rm v}$ and $\tau = 10^{-3}$ s., and varying $\bar{n}_{\rm pump}$. Inset showing ultra-low pumping regime $0 \leq \bar{n}_{\rm pump} \leq 0.15$, with a lasing threshold of $\sim$0.08. **(b)** Coherent photon number inside (green) and outside (purple) the cavity plotted for **(i)** $\bar{n}_{\rm pump} = 0.05$ which is below the lasing threshold and **(ii)**, $\bar{n}_{\rm pump} = 1$ which is above lasing threshold. 118

5.11 **Thermal radiation: (a)** Energy spectrum of photons at finite temperature **(b)** Average mode occupation of photonic states at finite temperature. 119

5.12 **Light in a 3D cavity: (a)** Schematic for 3D Fabry-Pérot cavity with sides of length L_x, L_y, L_z, where $L_x < L_y < L_z$. **(b)** Allowed cavity frequencies for $l + m + n = 2, 3$. **(c)** Normalised electric field spatial patterns for the mode (0,1,2) and **(d)** the mode (0,3,2) showing periodic minima and maxima. 122

6.1 **Bi_2Te_3 bulk dielectric function:** The real (purple) and imaginary (green) components of Bi_2Te_3 bulk dielectric function $\epsilon_{\|}(\nu)$, for incident light parallel to the **c**-axis using parameters fitted to data in reference (213), presented in Table 6.1. The positions of the α and β phonon frequencies are annotated for both $\mathbf{k}\|\mathbf{c}$ and $\mathbf{k}\perp\mathbf{c}$ incoming light (denoted $\alpha_{\|}$, $\beta\|$, $\alpha_{\perp}$, and $\beta\perp$ respectively). 129

6.2 **TINP absorption cross-section:(a)** Absorption cross-section of a TINP with $E_{\mathrm{F}} = A/R$, R=(15, 20, 25) nm and a TINP of radius 15 nm for which $\delta_R = 0$. The LSPP and β mode are visible and labelled, whilst the α mode is over-damped and thus not seen in the theoretically calculated absorption cross-section. Increased TINP radius results in a lower frequency SToP mode peak (also labelled). For $R = 15$ nm, the SToP mode and β modes overlap and a split peak is seen. For each SToP mode there is a point of zero absorption which occurs to the right of the peak. **(b)** Changing the Fermi level from $E_F = A/R$ to $E_F = 0$ (for $R = 40$ nm) results in the SToP mode occurring in the absorption cross-section at twice the frequency of incoming light, shown for $R = 40$ nm. **(c)** Absorption cross-section varying with R and ν. The bulk LSPP and β phonon positions remain constant for varying radius size, and the line of zero-absorption is annotated ($A = h\nu R$). Figures modified from (6), published by The Royal Society of Chemistry. 135

6.3 **Modifying the dielectric function: (a)** Absorption cross-section with no modifications. **(b)** Absorption cross-section with LSPP mode (highlighted with white dotted line)) removed from the dielectric function ($\nu_{\mathrm{p,f}} = 0$). **(c)** Absorption cross-section with both LSPP and α phonon contributions removed ($\nu_{\mathrm{p,f}} = \nu_{\mathrm{p},\alpha} = 0$). The trough of zero-absorption is still seen, but the SToP mode is no longer present. **(d)** Absorption cross-section with both LSPP and β phonon contributions (highlighted with a white dotted line) removed ($\nu_{\mathrm{p,f}} = \nu_{\mathrm{p},\beta} = 0$). Figures modified from (6), published by The Royal Society of Chemistry. 136

6.4 **Modifying theory parameters: (a)** For $R = 20$ nm, varying A by 10%, which shifts the position of the SToP mode peak and modifies the height of the peak. **(b)** Varying the magnitude of $\delta_R(\nu)$ by 10 %, which has no effect on the position of the SToP mode peak and very little effect on the height of the peak. **(c)** Introducing a small complex component to the denominator of $\delta_R(\nu)$, $i\Gamma A$, equivalent to introducing a finite life time to the excited surface states. Introduction of this finite lifetime reduces the height of the SToP mode peak. **(d)** Comparison of absorption cross-section for nanoparticles of varying geometry and size. Absorption cross-section of sphere (dotted blue) with $R = 20$ nm, projection $S = \pi R^2$. Absorption cross-section for a cube with diagonal length $2R = 40$ nm (green), such that $L = 28.2$ nm, and projection $S = L^2$. Absorption cross-section of cube of length $L = 32.2$ nm (purple) and $S = L^2$, with volume $V = L^3 = 4\pi R_{\mathrm{eff}}^3/3$ such that effective radius $R_{\mathrm{eff}} = 20$ nm. Figures modified from (6), published by The Royal Society of Chemistry. 137

6.5 **Ensembles of TINPs:** For an ensemble of particles with a Gaussian distribution of radii ($\bar{R} = 17.5$ nm and standard deviation 1.8 nm) and in which only (10,15,20) % of TINPs show a SToP mode, the peak height is greatly reduced and no longer displays a point of zero absorption. Figure modified from (6), published by The Royal Society of Chemistry. 139

6.6 **Experimental results: (a)** TEM images of **(i)** Bi nanoparticles, which are nearly spherical and of average radius 14.4 nm. **(ii)** Successfully synthesized Bi_2Te_3 nanoparticles with a slightly rhombohedral shape and average radius of 17.5 nm. **(b)** Experimental absorption cross-section data with impurity absorption band subtracted, superimposed with a Lorentzian decomposition of the same data, fitted with four peaks, P_1-P_4. Figure modified from (6), published by The Royal Society of Chemistry. 140

6.7 **Probing the photonic LDOS near a TINP:** Dipole at a distance h from the surface of a of a spherical TINP of radius R. 142

6.8 **Modifying the photonic LDOS near a TINP: (a)** Plot of the normalised partial LDOS, $g_z(h,\omega)/g_{3\mathrm{D}}(\omega)$, near a $R = 30$ nm particle with $E_\mathrm{F} = 0$ as a function of h and $\omega/2\pi$. **(b)** The normalised partial LDOS at a distance of 5 nm from the surface of a TINP with $E_\mathrm{F} = 0$ and $R = (30, 40, 50)$nm. **(c)** The normalised partial LDOS near a 15 nm particle with $E_\mathrm{F} = A/R$ as a function of h and $\omega/2\pi$. **(d)** The normalised partial LDOS at a distance of 5 nm from the surface of a TINP with $E_\mathrm{F} = A/R$ and $R = (15, 20, 25)$nm. **(e)** Maximum enhancement for a TINP of $R = 30$ nm, $E_\mathrm{F} = 0$ as a function of h, compared to a NP with the same $\epsilon(\nu)$ but no topological surface states. **(b)** A comparison of the normalised partial LDOS for varying E_F for TINPs of radius $R = 30$ nm. 148

B.1 **Thermal occupation: (a)** Probability of finding a boson in an excited state above the ground state $(E = 0)$ as a function of temperature. At $T = 0$ all bosonic particles reside in the ground state. **(b)** For fermionic particles, at $T = 0$ electronic states are occupied to the Fermi-level $E_\mathrm{F} = 0$. As the system increases in temperature particles have a non-zero probability of being found in an excited state. Occupancy of energy levels above the Fermi-level $\sim k_\mathrm{B}T$. 160

B.2 **Selection rules beyond E1:** Selection rules for left- and right-hand polarised light for M1 and E2 transitions, which coincide. 164

B.3 **Bi_2Te_3 nanoparticle synthesis: (a)** TEM images of Bi nanoparticles, which are nearly spherical and of average radius 14.4 nm. **(b)** Successfully synthesized Bi_2Te_3 nanoparticles with a slightly rhombohedral shape and average radius of 17.5 nm. **(c)** X-ray diffraction patterns illustrating the successful tellurisation of the Bi nanoparticles to form Bi_2Te_3 nanoparticles. Figure modified from (6), published by The Royal Society of Chemistry. 170

Nomenclature

Here I include the nomenclature used in this thesis. This list is non-exhaustive, and variables with superscripts and subscripts are not distinguished. Some symbols have multiple meanings across chapters, in order to not stray too far from standard symbol use, and their meaning is hopefully clear from context.

Acronyms and abbreviations

Acronym/abbreviation	Word/phrase
1D/2D/3D	1/2/3 dimensional
A.U.	Arbitrary units
Bi_2Se_3	Bismuth selenide, chemical compound
Bi_2Te_3	Bismuth telluride, chemical compound
Bi	Bismuth, chemical element
DFT	Density functional theory
DOS	Density of states
E1	Electric dipole
E2	Electric quadrupole
EM	Electromagnetic
FQH	Fractional quantum Hall
FT	Fourier transform
IQH	Integer quantum Hall
IR	Infrared
Laser	Light amplification by stimulated emission of radiation
LDOS	Local density of states
LRE	Long range entanglement
LSPP	Localised surface plasmon-polariton mode
M1	Magnetic dipole
MC	Monte Carlo
QH	Quantum Hall
QL	Quintuple layer
QSH	Quantum spin Hall
QSHO	Quantum simple harmonic oscillator
Sb	Antimony, chemical element
Sb_2Te_3	Antimony telluride, chemical compound
Se	Selenium, chemical element
SOC	Spin-orbit coupling
SRE	Short range entanglement
SToP mode	Surface Topological Particle mode
Te	Tellurium, chemical element
TEM	Tunneling electron microscope
TI	Topological insulator
TINP	Topological insulator nanoparticle (usually equiaxial)
TIQD	Topological insulator quantum dot (made with 2D TI)
TQD	Topological quantum dot (made with 3D TI)
TR	Time reversal
$\mathbb{Z}$	Set of all integers
$\mathbb{Z}_p$	Set of all integers modulo p
$\mathbb{Z}^{\geq}$	Set of all non-negative integers

Constants

All constants are given in S.I. units unless otherwise stated.

Symbol	Definition	Value
A_0, B_0	DFT-determined constants parameterising SOC strength, given in Table 2.1	
$A = (2A_0 + B_0)/3$	Assumption of SOC isotropy	2.0 (3.0) eV Å for Bi_2Te_3 (Bi_2Se_3)
α	Fine structure constant	$7.30 \cdot 10^{-3}$
Å	Angstrom (not an SI unit)	10^{-10} m
c	Speed of light	$3.0 \cdot 10^{8}$ ms^{-1}
C_0, C_1, C_2	DFT-determined constants parameterising particle-hole disparity, given in Table 2.1.	
e	Electron charge	$1.6 \cdot 10^{-19}$ C
eV	Electron volt	$1.6 \cdot 10^{-19}$ V
ϵ_0	Permittivity of free space	$8.85 \cdot 10^{-12}$A^{2}s^{2}N^{-1}m^{-2}
GHz	Gigahertz	10^9 Hz
h	Planck constant	$6.6 \cdot 10^{-34}$ m^{2}kg s^{-1}
$\hbar$	Reduced Planck constant	6.63×10^{-34}Js
k_B	Boltzmann constant	$1.38 \cdot 10^{-23}$ m^{2}kg s^{-2} K^{-1}
m_e	Electron mass	$9.1 \cdot 10^{-31}$ kg
m_0, m_1, m_2	DFT-determined constants parameterising the effective mass term, given in Table 2.1.	
μ_0	Permeability of free space	$1.3 \cdot 10^{-6}$m kg s^{-2}A^{-2}
nm	Nanometre	10^{-9} m
THz	Terahertz	10^{12} Hz

Variables, operators etc

Symbol	Definition
a	Lattice parameter, constant of dimension $[L]$ (Chapter 4)
$\mathbf{A}(\mathbf{r}, t)$	Magnetic vector potential
$\mathcal{A}(\mathbf{r})$	Vector field
$a^*_{\beta,\mathbf{k}}(t)$ ($a_{\beta,\mathbf{k}}(t)$)	Time-dependent Fourier coefficients
$a^\dagger_{\beta,\mathbf{k}}(a_{\beta,\mathbf{k}})$	Bosonic creation (annihilation) operators for mode $(\beta, \mathbf{k})$
α	Intrinsic loss factor
$\alpha(\omega)$	Polarizability
$\mathbf{B}(\mathbf{r}, t)$	Magnetic flux density
$\mathcal{B}(\mathbf{r})$	Source function
β	Photon polarisation index
$\mathbf{D}(\mathbf{r}, t)$	Electric displacement field
$d(\mathbf{e}_1, \mathbf{e}_2)$	Metric on a surface parameterized by $\mathbf{e}_1, \mathbf{e}_2$.
$\delta_R(\nu)$	Contribution of topological surface states to time-dependent charge density shift
$\mathbf{e}$	Unit vector
$\epsilon_0(\mathbf{k})$	Particle-hole disparity, characterised by DFT-determined constants, C_0, C_1, C_2.
E	Energy
E_g, A_{1g}, E_u, A_{1u}	Phonon modes. $E(A)$ denotes in-plane (out-of-plane), g (u) denotes Raman (IR) active modes.
$\epsilon(\nu)$	Dielectric function
$\mathbf{E}(\mathbf{r}, t)$	Electric field strength

Symbol	Definition
$\tilde{\mathbf{E}}(\mathbf{r},\omega)$	FT of electric field strength
$\mathcal{E}(\mathbf{r})$	Electric field spatial variation
(ζ,τ,φ)	Oblate spheroidal coordinates
$f(\omega)$	Probability distribution
F	Purcell factor
$F(\tau),G(\tau),H(\tau)$	Coefficients of general 2nd order ODE
g	Genus
$g(\omega)$	Density of states
$g(\mathbf{r},\omega)$	Local density of states
$g_z(\omega)$	Partial density of states
$g(\mathbf{k})$	Density of states in k-space
G	Gain
$\mathbf{G}_0(\mathbf{r},\mathbf{r}')$	Scalar Green's function
$\underline{\mathbf{G}}(\mathbf{r},\mathbf{r}')$	Dyadic Green's function
γ	Harmonic broadening parameter
Γ	Rate
h	Height
$h_\sigma,h_\tau,h_\varphi$	Prolate spheroidal scale factors
h_ζ,h_τ,h_φ	Oblate spheroidal scale factors
$\mathbf{H}$	Hamiltonian
$\tilde{\mathbf{H}}(\mathbf{r},\omega)$	FT of Hamiltonian
$\mathbf{H}(\mathbf{r},t)$	Magnetizing field
Θ	Anti-unitary matrix
$\mathbf{I}(t)$	Current
$\mathbf{J}(\mathbf{r},t)$	Current density
$J_n^{\mu,\nu}(x)$	Jacobi polynomials
$\mathbf{k}$	Wave vector
$k=\lvert\mathbf{k}\rvert$	Modulus of wave vector
K	Curvature
κ	Decay constant
L	Length
$\mathcal{L}$	Linear operator
λ	Wavelength
λ_i	Dimensionless eigenvalues such that $E_\mathrm{i}\propto\lambda_\mathrm{i}$
$m(\mathbf{k})$	Effective mass term, characterised by DFT-determined constants, m_0,m_1,m_2
M	Manifold
$\mathbf{M}(\mathbf{r},t)$	Magnetization field
μ	Relative permeability
$\boldsymbol{\mu}(t)$	Dipole moment
n	Chern number
$\hat{\mathbf{n}}$	Unit normal vector
$n_{\alpha,\mathbf{k}}$	Photon number in mode $(\alpha,\mathbf{k})$
N	Occupation number
N^0	Steady-state occupation number
N_+,N_-	Number of up-tending and down-tending edge states
ν	Frequency
$p_{\mathrm{i}\to\mathrm{f}}$	Probability
$P1_\alpha^\pm,P2_\alpha^\pm$	Bonding, anti-bonding states
$\mathbf{P}(\mathbf{r},t)$	Polarisation field
$\mathbf{p}$	Momentum
P_0	Average radiated power

Symbol	Definition
P	Power
$q(t)$	Charge
Q	Quality factor
R	Radius
$\mathbf{R}(t)$	Temporal component of the electric field strength
$\mathbf{r}$	Position vector
(r, ϑ, φ)	Spherical coordinates
$\rho(\mathbf{r}, t)$	Charge density
$u(\mathbf{r})$	Periodic function
(s, n, m)	Quantum numbers of TI nanostructure surface states
S	Surface area
$\mathbf{S}$	Poynting vector
$S(\omega)$	Spectral density
σ_{xy}	Hall conductivity
$\sigma_{\mathrm{i}\to\mathrm{j}}$	Interaction cross-section for transition $\mathrm{i} \to \mathrm{j}$
$\sigma_{\mathrm{abs}}(\nu)$	Absorption cross-section
(σ, τ, φ)	Prolate spheroidal coordinates
$\boldsymbol{\sigma_1}, \boldsymbol{\sigma_2}, \boldsymbol{\sigma_3}$	Pauli matrices
t	Time
T	Time period, temperature (Chapter 5)
$\mathcal{T}_{\mathrm{f}}$	Time-reversal operator
τ	Time scale
$\mathbf{u}(\mathbf{r})$	Displacement vector
$u(\omega)$	Energy spectrum
v	Band index
V	Volume
$V_{\mathrm{i,f}}$	Matrix element for transition $\mathrm{i} \to \mathrm{f}$
W	Work done
$\omega = 2\pi\nu$	Angular frequency
(x, y, z)	Cartesian coordinates
χ	Angular part of wavefunction such that $\Psi \propto \chi$
Ψ	Wave function
$\lvert\Psi\rangle$	Quantum state
$\Phi(\mathbf{r}, t)$	Scalar potential
Ω	General symmetry operator

Preface

When deciding on a topic for my PhD, I knew I wanted to work on something fundamental with the opportunity to use elegant maths, whilst not needing to rely too heavily on numerics. I also wanted a topic that could be directly evidenced by experimental work, and that could have potential impact in technology. The intersection of all these demands offers up very few topics, but I was lucky enough to discuss with Vincenzo on how topological electronic structures can be probed with light, and he immediately understood the types of problems I wanted to work on. I've greatly enjoyed my PhD in topological nanophotonics and can happily report that it fitted the brief. This thesis aims to give the background and context needed to understand the relatively new field of topological nanophotonics. It has a substantial amount of background theory - reflecting the interdisciplinary nature of the topic - followed by the research work of my PhD. I hope this thesis can be useful to students new to the field.

This thesis and the work described within have been completed solely by myself under the supervision of Dr Vincenzo Giannini, Dr Derek Lee and Prof Peter Haynes. Where others have contributed or other sources are quoted, full references are given.

Various sections of this thesis take content from the paper:

- **A perspective on topological nanophotonics: Current status and future challenges**, MS Rider, SJ Palmer, SR Pocock, X Xiao, P Arroyo Huidobro, V Giannini, **Journal of Applied Physics** (2019) [1].

Chapter 4 takes content from the manuscript (in preparation for submission):

- **Spheroidal topological insulator nanoparticles**, Marie Rider, Vincenzo Giannini, **In preparation** (2021) [3].

Chapter 5 is based on the manuscript (under review):

- **Proposal for THz lasing from a 3D topological quantum dot**, Marie Rider, Vincenzo Giannini, **arXiv:2105.04316** (2021) [4].

and Chapter 6 takes content from the manuscript (in preparation for submission):

- **Manipulating photonic local density of states with topological insulator nanostructures**, Marie Rider, Vincenzo Giannini, **In preparation** (2021) [7].

and the paper:

- **Experimental signature of a topological quantum dot**, Marie Rider, Maria Sokolikova, Stephen Hanham, Stefano Lupi, Peter Haynes, Derek Lee, Maddalena Daniele, Mariangela Cestelli Guidi, Cecilia Mattevi, Vincenzo Giannini, **Nanoscale** (2020) [6].

Contributions to my knowledge on light-matter interactions and quantum Hall states which informed some of the work of this thesis but before my PhD commenced comes from the paper:

- **Observation of chiral edge states with neutral fermions in synthetic Hall ribbons**, M. Mancini, G. Pagano, G. Capellini, L. Livi, M. Rider, J. Catani, C. Sias, P. Zoller, M. Inguscio, M. Dalmonte, L. Fallani, **Science** (2015) [8].

1. Introduction

"A physicist is just an atom's way of looking at itself."
- Niels Bohr[1]

One of the ultimate aims of modern science is the precise control of photons at the nanoscale. This is paramount for both nanotechnological applications and fundamental research in light-matter problems. **Topological nanophotonics** offers a promising path towards this goal [1, 10]. A key feature of **topological condensed matter systems** is the presence of topologically protected **surface states** immune to disorder and impurities. These unusual properties can be transferred to **nanophotonic systems**, allowing us to combine the high sensitivity of nanoscale systems with the robustness of topological states. This neoteric[2] field is already rewarding us with a plethora of potential new applications and increased physical insight into the nanoscale world.

Topological photonics is an umbrella term for systems involving light and some sort of non-trivial topology. When discussing topological photonics at any scale, the most commonly invoked idea is that of **purely photonic systems with non-trivial topology** [1, 11–14]. In these systems, electromagnetic fields take the place of electronic wave functions to mimic the band structure and topological properties of known topological electronic systems. Topological photonic systems with no electronic counterpart can also be produced, leading to topological behaviours uninhibited by the constraints of solid state systems. Excellent and extensive reviews already exist on these photonic topological systems [12, 13], and I will not cover the topic in any detail here. Topological photonics also covers the topic of **topological electronic systems interacting with light** [6, 15–20] and this is the area of focus in this thesis. The interaction between light and matter is arguably one of the most fascinating topics in modern physics, and also one that has brought us a myriad of technological advances. The burgeoning field of topological condensed matter adds yet another route to new physics and new applications.

Nanostructures are material structures with dimensions on the order of 1-100 nm (where nm = 10^{-9} m) and may be comprised of as little as a few hundred atoms, making them an ideal platform for studying quantum mechanical effects. In particular, surface effects are

[1] Bohr was a foundational contributor to quantum theory and atomic physics, receiving a Nobel prize in 1922. Heisenberg said of Bohr that he was primarily a philosopher, not a physicist. He also helped refugees escape the Nazis in the 1930s and he was eventually part of the Manhattan Project after escaping Nazi-occupied Denmark via Sweden. Worried about how the atomic bomb created by the project would be used, he was a fierce advocate of international arms control, and had a vision of countries abandoning isolationism in favour of true cultural exchange. On his return to Europe after the war he helped to establish CERN and also created the Atoms for Peace conference [9].

[2] Neoteric: New or modern; recent.

amplified in nanostructures due to their increased surface-to-volume ratio, making them especially useful in the study of topological surface states. The advances in our theoretical knowledge of electronic structures, as well as experimental capabilities at the nanoscale allow us to probe matter at this unique length-scale with unprecedented control.

In the work of this thesis I focus specifically on **topological insulator nanostructures interacting with light**. 3D topological insulators present an exciting class of materials which have challenged our understanding of condensed matter physics and demanded the development of new paradigms to describe their unusual properties. These materials support symmetry-protected, conducting surface states despite an insulating bulk. The surface states behave as relativistic, massless fermions described by a Dirac cone in the material dispersion relation. In very small (i.e. all dimensions $\lesssim$ 100 nm) topological insulator nanostructures, quantum confinement of the surface states leads to a **discretized Dirac cone**, with constant spacing between the discrete energy levels tunable with material type, nanostructure size and shape. The energy levels of the structure can be coupled with THz frequency light, and in analogy with semiconductor quantum dots and topological insulator quantum dots[3] (TIQDs) I refer to this system as a **topological quantum dot**[4] (TQD) at various points throughout this thesis. The detection and production of THz light is a crucial frontier in modern applied physics, due to the notorious absence of practical technologies for generating and sensing radiation in the THz gap (0.1-10 THz), with applications in areas such as agriculture [21, 22], manufacturing [23], bio-medicine [24, 25], wireless communications [26, 27] and security technologies [28]. THz waves penetrate materials opaque to other wavelengths, while posing only minimal risks due to their non-ionizing behaviour (unlike for example, x-rays). Academic applications range from molecular spectroscopy [29–31] to sub-millimetre astronomy [32, 33], influencing physics on vast length scales. The study of topological insulator nanostructures interacting with THz light thus presents **an exciting new platform for both fundamental research in topological light-matter interactions and for nanotechnological applications**.

This thesis sits at the interface of **topological condensed matter** and **photonics**. Conscious that the reader may only be expert in one of these areas (or neither), I cover the fundamental concepts needed to understand the work from both of these perspectives in **Part I: Theoretical Background**, split into two chapters - **2: Theory of topological insulators** and **3: Theory of light**. I do not assume any knowledge outside of that given in a standard undergraduate programme. I should note that a body of work already exists on the optical properties of bulk 3D topological insulators [15–19], but as the results of this thesis deal with nanoscale topological insulators I will not cover those works in any

[3] Topological insulator quantum dots usually refer to 2D systems, although the literature is not entirely consistent.

[4] There are various qualitative differences between semiconductor quantum dots and TQDs, an important one being that semiconductor quantum dots operate in the visible range, whereas TQDs operate in the THz. I use the acronym TQD to distinguish from 2D TIQDs.

detail here. Instead, I direct the reader to the literature and in particular section III D of [18], which gives an excellent summary of the topic.

In **Part II: Research topics**, the work is split thematically into three chapters. In **4: Topological insulator nanostructures**, I extend the results for the electronic structure of spherical TI nanoparticles (TINPs) and TI nanowires [34, 35] to include **TI nanostructures of wide-ranging dimensions**, allowing for the study of any nanostructure from an infinite nanowire to a flat nanodisk within a **single mathematical framework** [3]. **5: THz lasing with topological quantum dots** covers my work on using the discrete surface state energy levels of a TINP as a lasing system. I use a combination of analytical and numerical techniques to demonstrate that a single TINP in a cavity irradiated with a low-intensity external source will lase from its topological surface states with an ultra-low lasing threshold. This robust, low-threshold laser emits in the much coveted THz regime. At room temperature, thermal THz photons are abundant enough to provide the pumping source of the system, presenting an exciting path towards **room-temperature THz lasing with no additional external pumping source** [4]. The light-mediated transitions between TINP surface states drastically modifies its optical properties, resulting in an extraordinarily strong resonance (the SToP mode) in its absorption cross-section [5]. In **6: Modifying light with topology** I model this effect in Bi_2Te_3, and give the results of an experimental collaboration with the groups of Dr Cecilia Mattevi (Imperial College London) and Dr Stefano Lupi (Sapienza University of Rome), in which **the first experimental observation of the SToP mode was made in Bi_2Te_3** - remarkably at room-temperature [6]. Additionally, in this chapter I demonstrate that the SToP mode can be used to radically **modify the behaviour of light surrounding a TINP**, increasing the photonic local density of states by many orders of magnitude [7]. This phenomenon has potential applications in nanotechnologies and also presents a new way of probing topological properties of matter using light.

I then conclude and summarise, and speculate on some future research avenues. I also attach extensive appendices, split into **A: Useful maths, formalisms and conventions**, **B: Supplementary derivations and information** and **C: Numerical methods**. Many of the appendices simply provide extra information for interested readers, but slightly selfishly I have also included extended versions of derivations and definitions that did not make the final cut of the thesis but that I wanted to keep somewhere safe for my own reference. A diagrammatic summary of the topics and main results of this thesis can be found in Figure 1.1.

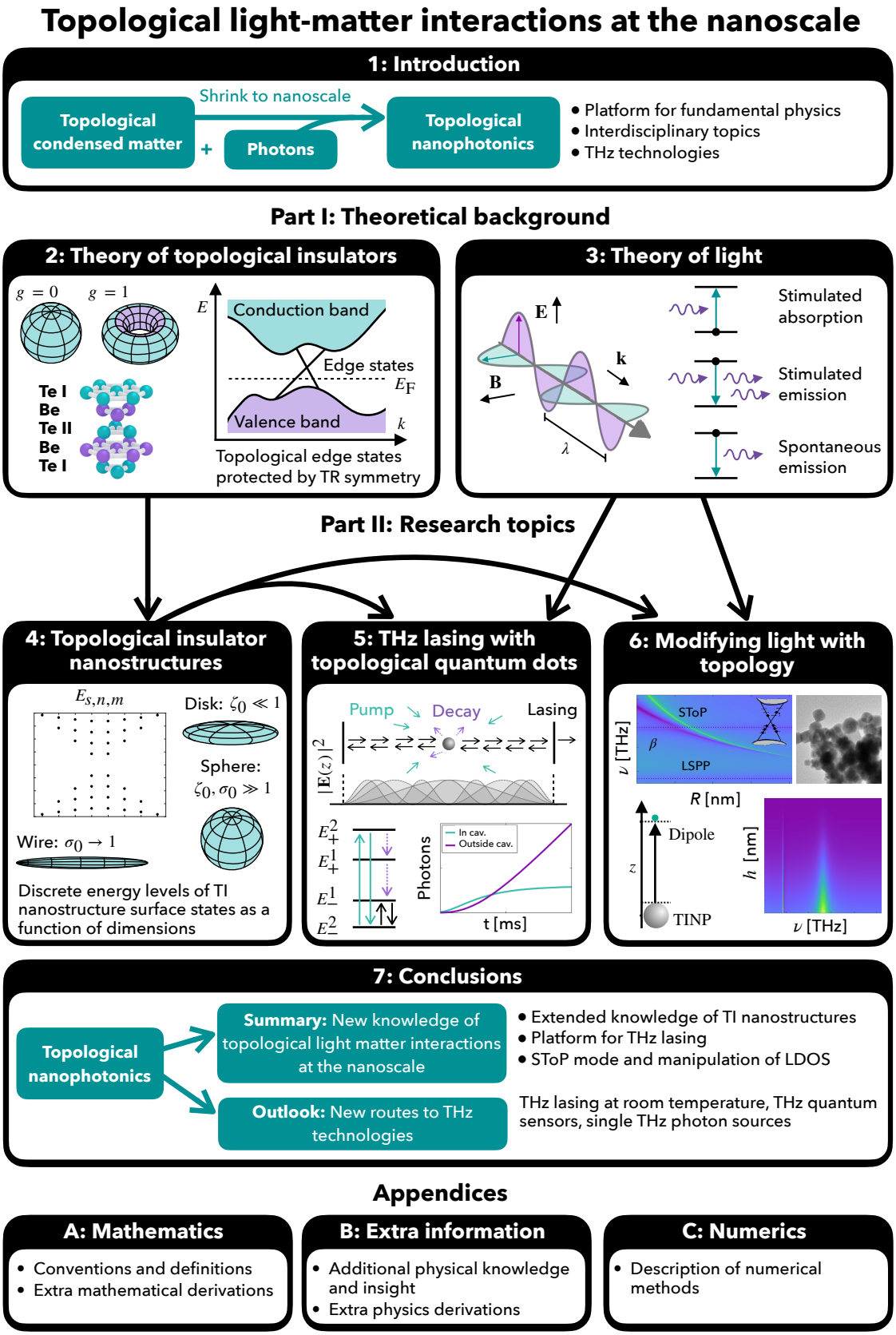

Figure 1.1: **Thesis schematic:** A graphical abstract of the content and main results covered in this thesis.

Part I: Theoretical Background

2. Theory of Topological Insulators

Much of modern physics is built on the concept of symmetries and the resulting conserved quantities elegantly described by **Noether's theorem**[1]. In condensed matter physics, we are most familiar with the symmetries and phases of matter characterised by local order parameters within the Landau theory of phase transitions [38, 39]. However, in the last few decades the exploration of **topological phases of matter** has led to many new developments in our understanding of condensed matter physics, culminating in a Nobel prize for Thouless, Haldane and Kosterlitz in 2016 [40] and a Breakthrough prize in fundamental physics for Kane and Mele in 2019 [41].

In particular, this thesis deals with **3D topological insulators** (TIs). Topological insulators are materials with a gapped Hamiltonian, whose topological surface states are protected by time-reversal symmetry [42–46]. In order to fully understand the physics of these systems, I will first explain how **symmetry** and **order** can be used to characterise material phases. The concepts of symmetry and order are key to the description of topological insulators, but the standard paradigm of **local order** is no longer sufficient to explain them and we must instead invoke the concept of **topological invariants**.

I will describe how topology manifests in the **band structure** of a material, and why edge states often arise in these systems. I demonstrate this specifically for **time-reversal (TR) symmetric** systems [44] and thus topological insulators.

The materials of interest in this thesis are in the Bi_2Se_3 family, which are some of the most theoretically well-studied [47–49] (and experimentally realised [46, 50, 51]) 3D TI materials. Knowledge of the **four-band bulk TI Hamiltonian** [48, 49] specific to these materials is crucial for the derivation of topological insulator nanostructure surface states given in Chapter 4, which then leads on to the applications of topological insulator nanostructures interacting with light, described in Chapters 5 and 6. The results of Chapter 6 concern hybrid modes involving the **bulk phonons** of topological insulators, and so I give an overview of the bulk phonons expected in these materials and their origin.

[1] Emmy Noether was a groundbreaking German mathematician who made seminal contributions to both mathematics and physics. As a student, she was only allowed to audit classes at the University of Erlangen as she was prohibited from fully participating due to her gender. When she began teaching, her classes were advertised under the name of her male colleague, David Hilbert, and she was only credited with assisting in teaching. Even when she published the theorem now known as 'Noether's theorem', it was Felix Klein who presented it to the Royal Society. In 1933 when Jewish professors were banned from working at universities by the Nazis, she moved to America where she taught until her death in 1935 (at the tragically young age of 53) [36]. Upon hearing of her death, Einstein wrote to the New York Times describing her as *"the most significant creative mathematical genius thus far produced since the higher education of women began."* [37] and some of her work became the basis of General Relativity.

A growing number of reviews and books on topological insulators exist [2, 18, 52–55], so I direct the reader to these for a more comprehensive overview of the field. Topological insulators are only one type of topological quantum matter - topology also crops up in various areas of condensed matter, as well as other areas of physics. In the last section of this chapter I will attempt to contextualise topological insulators in the larger landscape of **topological quantum systems**.

2.1 Symmetry and topology

"It is only slightly overstating the case to say that physics is the study of symmetry."
- P.W. Anderson[2]

Symmetry has a well-established role in physics and the search for symmetry has been a driving force behind many theoretical developments [57, 58]. In this section I will cover how the elementary concepts of symmetry and conventional (local) order are used to classify systems in condensed matter physics, and how these ideas can be extended to global order and topological phases of matter.

2.1.1 Symmetry and conventional order

Some **symmetries** are so intuitive that one might not even think to describe them in the formal language of symmetries. As an illustrative example, if we were to measure the time-averaged density of a liquid (such as the one illustrated in Figure 2.1a) at two points separated by an arbitrary translation, we would expect the results to be the same. Similarly, if we were to rotate the liquid by some arbitrary angle, we would expect the density and other physical properties of the liquid to be invariant. In physics, the idea of symmetry is synonymous with invariance. A symmetry entails a system being **invariant** under a transformation, either infinitesimal (leading to a continuous symmetry) or finite (resulting in a discrete symmetry).

If the liquid were to be cooled, we might expect it to undergo a **phase transition** to a solid, crystal phase as illustrated in Figure 2.1a. This periodic crystal of atoms no longer obeys continuous translational or rotational symmetries. It is now only invariant under discrete translations and rotations. The symmetries of the crystal give us a way to classify it.[3] It is also very important to note that symmetry is not only limited to spatial

[2]Taken from "More is different" [56]. This article is a good read for any budding condensed matter physicist, as it gives a nice summary of the shortcomings of reductionist science. Anderson made many seminal contributions to condensed matter on the topics of localization, antiferromagnetism and symmetry breaking. His work on symmetry-breaking also led to advancements in particle physics and the eventual development of the Standard Model.

[3]This is usually done with the elegant method of group theory, which is not strictly needed for the work of this thesis so I omit it here, but this method is demonstrated in Reference [49].

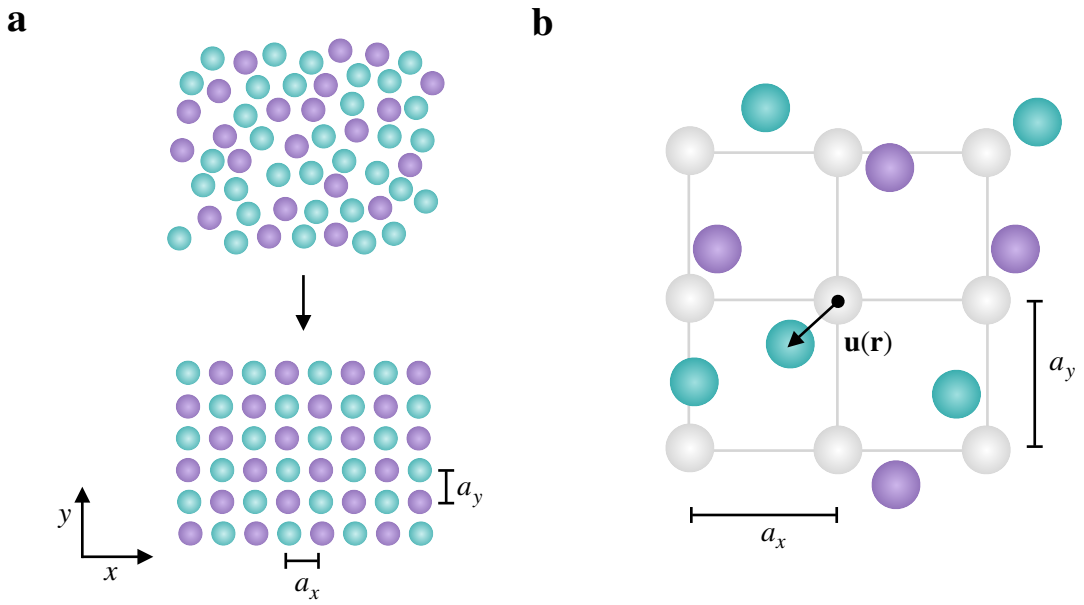

Figure 2.1: **Conventional phase transitions: (a)** Solid-liquid phase transition. **(b)** Displacement field $\mathbf{u}(\mathbf{r})$ gives the displacement needed to bring the ideal lattice into line with the atoms in the local neighbourhood of $\mathbf{r}$. There is an ambiguity in this definition due to freedom to choose the reference atom, such that $\mathbf{u}(\mathbf{r}) \equiv \mathbf{u}(\mathbf{r}) + (2ma_x, 2na_y)$, where m and n are integers.

transformations (such as translation, rotation, inversion, reflection etc), but a system can also display symmetries with respect to time, or internal symmetries relating to its internal degrees of freedom such as spin or charge.

We can say that the liquid phase has a higher level of symmetry than the solid phase, as the symmetries of the solid phase are a subset of those describing the liquid phase. In order to change between these phases (i.e. for a phase transition to occur), symmetries may be introduced or broken.[4] Every symmetry is linked to a conserved quantity. For example, temporal invariance leads to energy conservation in a system. Translational invariance results in the conservation of momentum. This important concept is described by **Noether's theorem** [59], and conservation laws for discrete symmetries also exist and reduce to Noether's theorem for infinitesimal transformations.

Complementary to the idea of symmetry, the notion of **order** can also be used in condensed matter to characterise the varying internal structures of different states of matter. When a crystal is deformed, defective or heated to high temperatures, the atoms will be displaced from their lattice positions to form the liquid phase. The vectors describing the displacements, $\mathbf{u}(\mathbf{r})$, are equivalently the vectors needed to bring the atoms back to an ideal lattice in their **local neighbourhood**, described by $\mathbf{r} - \mathbf{r}'$ (depicted in Figure 2.1b). As it is ambiguous which ideal atomic position should be associated with each atom, really the displacement vector is defined up to the addition of an integer sum of the lattice vectors,

[4] Phase transitions can also occur without symmetry breaking, but I will not comment on those here.

such that in 2D, $\mathbf{u}(\mathbf{r}) \equiv \mathbf{u}(\mathbf{r}) + (ma_x, na_y)$. A perfect crystal will be denoted by $|\mathbf{u}(\mathbf{r})| = 0$ (such that there is no displacement from the ideal atomic positions), and $|\mathbf{u}(\mathbf{r})| \neq 0$ denotes a disordered system. A small deformation of the system Hamiltonian may trigger $|\mathbf{u}(\mathbf{r})|$ to grow from zero, signalling a phase transition.[5] Phases can usually be determined via **local order parameters**, in which the order parameter field at a point is defined in the local neighbourhood of that point. e.g. the displacement field for the solid-liquid transition that we have just discussed. It should probably be noted that $\mathbf{u}(\mathbf{r})$ is a slightly messy order parameter as it would be rather difficult to measure. An alternative order parameter would be shear modulus (as liquids deform under shear stress, while solids do not).

2.1.2 Topological invariants

"Topology is precisely the mathematical discipline that allows the passage from local to global."
- René Thom[6]

So far we have spoken about how **symmetry** and **local order** can be used to characterize condensed matter systems. Local order parameters can be measured with local probes of the system (equivalent to our previous description that a local order parameter at $\mathbf{r}$ can be constructed only with the knowledge of the region $\mathcal{O}(\mathbf{r} - \mathbf{r}')$ where $\mathbf{r} - \mathbf{r}'$ is small). However, local order parameters are only one way to classify systems. As well as local order parameters, systems may also be described by their topological properties. **Topological invariants** give us another way to classify systems, where systems are categorised by parameters which require a global measurement of the entire system rather than local probing.

Mathematically, these invariants are usually constructed as integrals of a local property over a closed parameter space. The classic example used to demonstrate the difference between local and global measurements is that of the sphere versus the torus.[7] Local **curvature** of a surface can be measured via

$$K = \frac{\langle (\nabla_2 \nabla_1 - \nabla_1 \nabla_2)\, \mathbf{e}_1 | \mathbf{e}_2 \rangle}{\det(d(\mathbf{e}_1, \mathbf{e}_2)}, \tag{2.1}$$

where $\mathbf{e}_1$ and $\mathbf{e}_2$ are unit vectors on the surface and $d(\mathbf{e}_1, \mathbf{e}_2)$ is the metric of the surface.

[5] We will not worry about the distinction between first- and second-order transitions in this thesis, but for completeness, this is a first-order phase transition and there is a discontinuity in the entropy over the phase transition, due to the existence of latent heat. More details on the distinction can be found in [38, 39].

[6] Thom was a mathematician most well known for his work in topology and catastrophe theory, a subset of singularity theory. He was awarded a Fields medal in 1958 for the development of Cobordism theory, the study of the difference between all closed manifolds and those that are boundaries.

[7] This would hardly be a thesis on topological condensed matter without the obligatory reference to tori (plural of torus) morphing into coffee cups or a similar description.

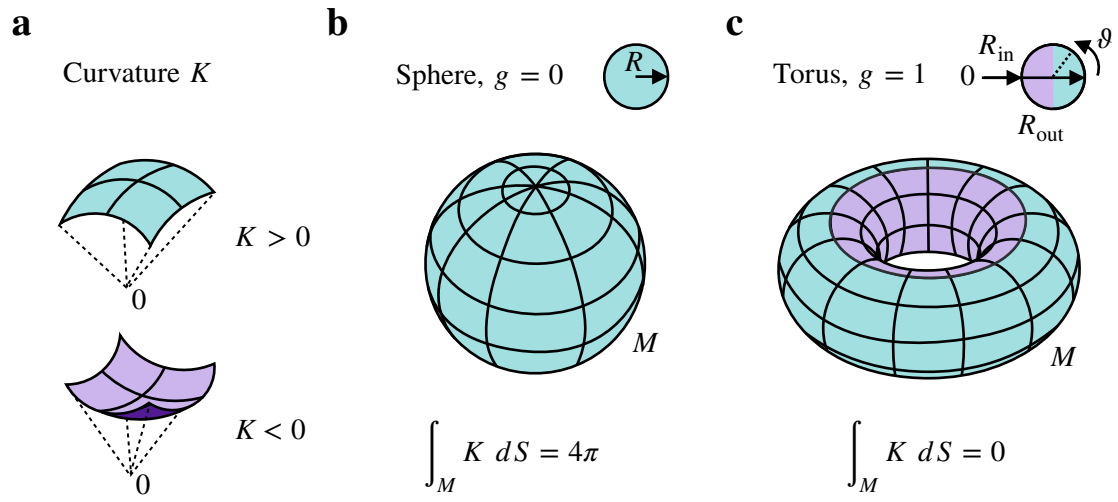

Figure 2.2: **Topological invariants: (a)** A local geometry can have positive or negative curvature with respect to a reference point. When integrated over a closed surface, M, the Gauss-Bonnet theorem links the curvature of the surface to its genus, g, via the relation $\int_M K\ dS = 4\pi(1-g)$. The genus of **(b)** a sphere is $g = 0$, and **(c)** a torus is $g = 1$.

For the sphere and torus,

$$\textbf{Sphere} \qquad K = 1/R^2, \tag{2.2}$$

$$\textbf{Torus} \qquad K = \frac{4\cos(\vartheta)}{(R_{\text{out}} + R_{\text{in}})((R_{\text{out}} + R_{\text{in}}) + (R_{\text{out}} - R_{\text{in}})\cos(\vartheta))}, \tag{2.3}$$

where R is the radius of the sphere, and for the torus, $\vartheta \in [0, 2\pi]$ and R_{in} and R_{out} are the inner and outer radii respectively. A good general reference on differential geometry is [60], for the interested reader. Curvature of a surface is positive or negative depending on if it is convex or concave with respect to a fixed point (as depicted in Figure 2.2a). For the sphere (given in Figure 2.2b), curvature is always positive, whereas for a torus (depicted in Figure 2.2c) the curvature is positive, zero or negative at different points on the surface. The curvature of the surface at a point may change under continuous deformation. However, integrating the curvature over the entire closed surface always gives the same value, as per the **Gauss-Bonnet theorem**, such that

$$\int_M K\ dS = 4\pi(1-g), \tag{2.4}$$

where g is a non-negative integer such that $g \in \mathbb{Z}^{\geq}$. For the sphere, this integral gives 4π, and for the torus we obtain 0. The **genus**, g, can be identified with the number of 'holes' in the surface, i.e. $g = 0$ for the sphere and $g = 1$ for the torus. The genus of a closed surface is identified as a **topological invariant** of the surface, and cannot be measured by a local probe, but can only be ascertained by integrating over the entire surface. Surfaces with the same value of genus (such as a coffee cup and a torus, or a sphere and a disk) can

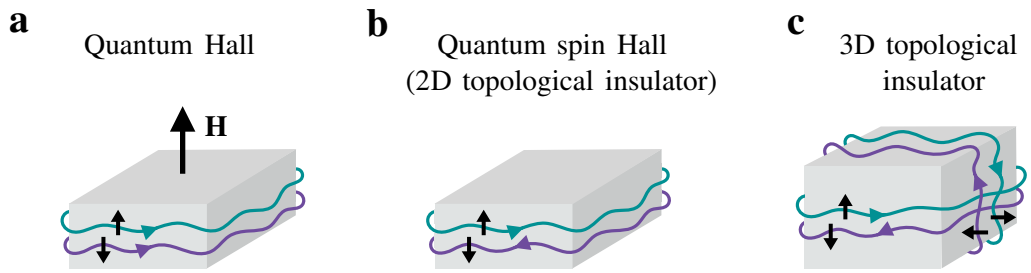

Figure 2.3: **The road to 3D topological insulators: (a)** Quantum Hall system, supporting protected edge states. First discovered in 1980 [61] with the explanation of the quantised Hall conductance following shortly after in 1982 [62]. **(b)** The first proposals of the Quantum spin Hall system (2D topological insulator) came in 2005 [43] and 2006 [63]. The generalisation to **(c)** the 3D topological insulator followed in 2007 [47] .

be smoothly deformed[8] into each other, and no smooth transformation will deform a sphere to a torus or vice versa.[9]

This brings us to the idea that topology is really about whether or not you can continuously deform things into each other. We will see in the next section how this applies to condensed matter systems, in which the space of eigenstates of a system takes the place of the closed surface, M.

2.1.3 Topological band structures and surface states

The notion of topology in condensed matter physics was introduced by Klitzing and his discovery of the **2D quantum Hall** (QH) state [61], with Thouless *et al.* explaining the quantization of the Hall conductance in 1982 [62]. A quantum Hall system is created by passing a strong magnetic field through a 2D system of electrons at low temperature (illustrated in Figure 2.3a). Physically this could be something like a sheet of graphene or a thin, semiconductor film. The band structure of a conducting material would normally have overlapping valence and conduction bands, with electrons able to move through the material on the application of a voltage. The magnetic field causes a gap to open between the energy bands, and the strong cyclotron orbits of the electrons in the bulk material cause them to become localized, such that they cannot move freely. Charge builds up on the edge of the 2D system and a transverse conductance called the **Hall conductance**, σ_{xy}, can be measured. A stair-like series of quantised plateaux is seen in the Hall conductance, and we can only change between plateaux by a large deformation of the Hamiltonian.

The space of eigenstates of a Hamiltonian holds the information on the effect of the crystal

[8] By smooth deformation I mean a continuous transformation in which we are not allowed to cut or puncture the surface.

[9] This is reflected in g being an integer, as a sphere cannot slowly be deformed to a torus with g taking an intermediate value between zero and one - the number of holes in the surface can intuitively only be an integer.

on electrons in a material [64, 65]. Their corresponding eigenvalues give the band structure. Analogous to the Gaussian curvature described in Section 2.1.2, the **Berry curvature** of the space of eigenstates can tell us a lot about the physical behaviour of a condensed matter system. In a crystalline structure, we can exploit the periodic nature of the crystal potential to employ **Bloch's theorem** [64, 65], such that the wavefunctions can be written in the form

$$\Psi_{v,\mathbf{k}}(\mathbf{r}) = e^{i\mathbf{k}\cdot\mathbf{r}} u_{v,\mathbf{k}}(\mathbf{r}), \tag{2.5}$$

where v is a band index, $\mathbf{k}$ is a wave-vector in **reciprocal space** (conventionally chosen to be in the **Brillouin zone**[10]) and $u_{v,\mathbf{k}}(\mathbf{r})$ is a periodic function. We can then calculate the Berry curvature in reciprocal space. Bloch's theorem also implies that the Brillouin zone itself is closed, and so we are able to integrate curvature and other quantities over a closed surface, as we did with Gaussian curvature of the previous section. Integrating the Berry curvature over all occupied eigenstates (i.e. filled bands), the resulting topological invariant tells us something about the system (much like genus in the case of the sphere and the torus[11]).

The Berry curvature can be calculated by measuring the phase picked up when moving through the space of eigenstates. The phase measured can be split into two parts - a dynamical phase and a geometric phase, known as the **Berry phase**. The Berry phase is an incredibly important quantity in topological condensed matter, but the results conveyed in this thesis can actually be discussed without too much knowledge of the Berry phase or resulting Berry curvature, once the idea of topological invariants is accepted. For that reason, I give a short discussion of the Berry phase in Appendix B.1 but otherwise leave in-depth discussion to many excellent references [54, 55, 66–69].

The topological invariant resulting from the integration of the Berry curvature over the occupied eigenstates of the system is a $\mathbb{Z}$ invariant known as the **first Chern number** of the system, n. As we already know, systems with differing values of a particular topological invariant cannot be smoothly deformed into each other, and a topological phase transition must occur to pass from one phase to another. For the quantum Hall system, the first Chern number directly relates to the the Hall conductivity, $\sigma_{xy} = ne^2/h$, explaining the experimentally observed plateaux.

The topological invariants of a system are encoded in the eigenstates of the system, but the band structure can also exhibit signatures of topology. While topological phases can occur for a plethora of different condensed matter types (explained more in Section 2.4), for the purpose of the topics covered in this thesis we limit ourselves to **single-electron models of insulators**. We assume a gapped band structure with **Fermi level** residing in the gap

[10] The 1st Brillouin zone is the **Wigner-Seitz cell**, a primitive cell in **reciprocal space**.

[11] In fact, the equivalency of Berry curvature and Gaussian curvature can be directly calculated by considering a parameter space using the instantaneous eigenstates of the system as a basis [66].

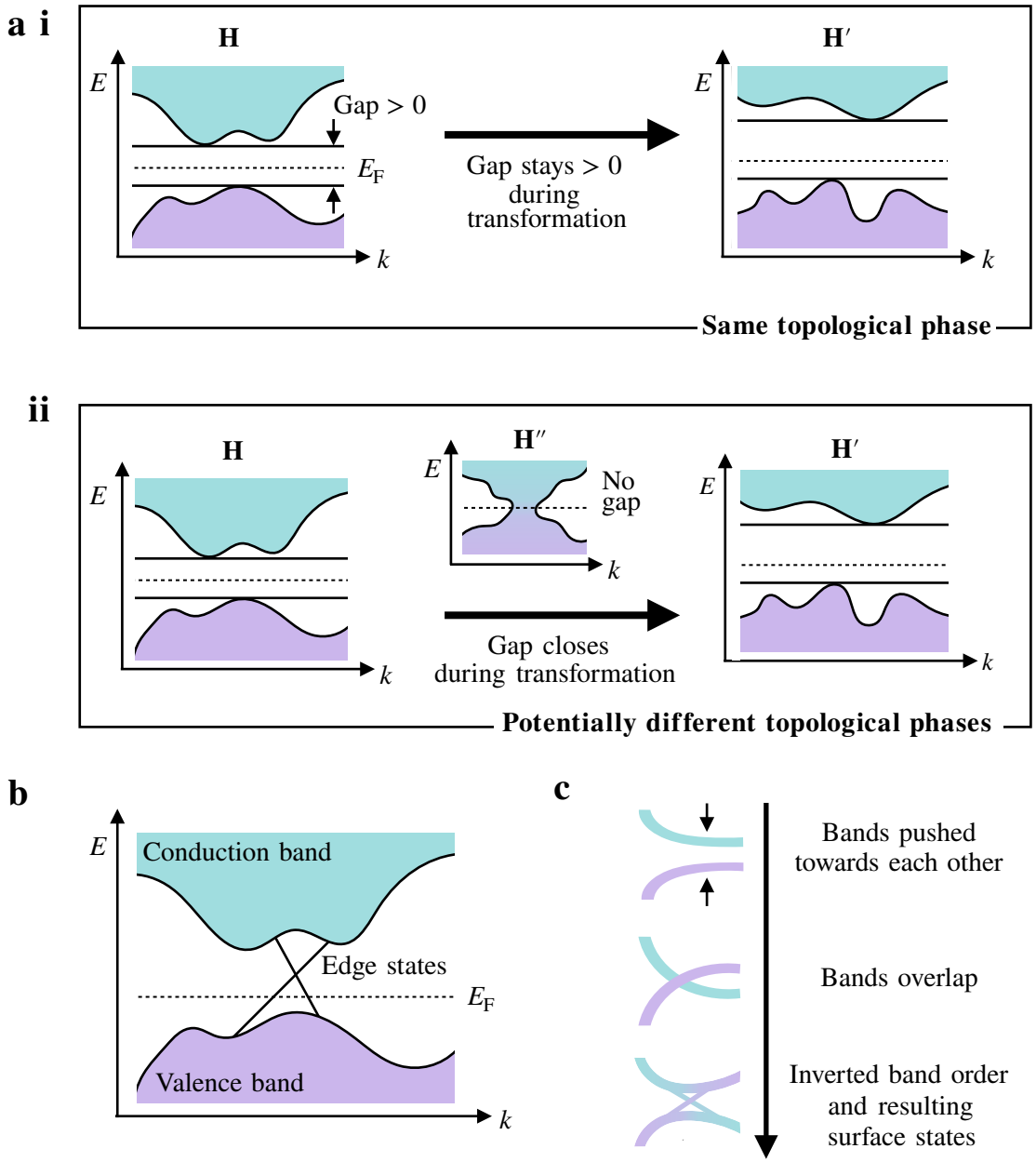

Figure 2.4: **Topological band structures:** **(a)** Visualisation of the transformation $\mathbf{H} \rightarrow \mathbf{H}'$ in which **(i)** the band gap remains open during the transformation, meaning that both Hamiltonians exist in the same topological phase and **(ii)** the gap closes during the transformation, signalling a potential topological phase transition. **(b)** Typical band structure of a TI in which symmetry-protected conducting edge states traverse the gap. **(c)** In materials containing heavy elements, the spin-orbit coupling can be so strong that at the Γ point, higher bands are pushed below lower bands, resulting in band inversion.

(i.e. bands are filled up to the gap, and so the occupied eigenstates of the system are simply the valence band). We now discuss how topology manifests in the band structure of these systems.

For a general, insulating system described by the Hamiltonian $\mathbf{H}$, we may smoothly deform our system to one described by a new Hamiltonian $\mathbf{H}'$ by slowly varying the parameters of the Hamiltonian, as illustrated in Figure 2.4a. If the band gap remains open during the transformation (as shown in Figure 2.4a(i)), the number of states residing in the valence band is necessarily conserved, as although these states can mix amongst themselves during the transformation the only way for the number of states to change is to close the gap and allow states to enter from or leave to the conduction band. Topological invariants of the system are calculated by integrating curvature or an analogous property over the occupied bands of the material, and so will only change value if the band gap closes during a transformation (shown in Figure 2.4a(ii)). The band gap closing signals that a **topological phase transition** may occur, as it is at this point that the topological invariant can change value. If a topological phase transition does occur, then $\mathbf{H}$ and $\mathbf{H}'$ exist in different topological phases. If the gap remains open during the transformation then $\mathbf{H}$ and $\mathbf{H}'$ remain in the same topological phase. The gap remaining open is often enforced by a system symmetry, and so in order for a topological phase transition to occur a symmetry breaking must occur. If the symmetry is preserved then no topological phase transition will take place.

The Hamiltonian $\mathbf{H}$ describes all electrons in the material and is thus a bulk Hamiltonian - the topological invariant described above is a bulk quantity. For an insulating material with a non-zero topological invariant surrounded or adjoined by an insulating material of a different topological invariant (for example vacuum, which is a trivial insulator with a topological invariant of zero), we have a boundary on the interface of these two insulators with differing topological invariants. The change in topological invariant at the boundary requires the band gap to close, whilst remaining gapped in the bulks of both media. This results in **localized boundary states**, which necessarily traverse the band gap. Physically, the picture we then have is of an insulating bulk, with conducting states localized on the boundary of the material as illustrated in Figure 2.4b. For the case of a quantum Hall system, the **bulk-boundary correspondence** [70–72] tells us that the first Chern number, n, also tells us the net number of edge states,

$$n = N_+ - N_-, \tag{2.6}$$

where N_+ is the number of edge states going from the valence band to the conduction band (with increasing $k = |\mathbf{k}|$) and N_- counts the number of edge states travelling from the conduction band to the valence band.

It is important to emphasise that looking at the energy spectrum is not enough to characterise the topological state of a system. Information on topology is encoded in the eigenstates.

However, band structure and the existence of states traversing the band structure of an otherwise gapped system does give a signature of topology.

2.2 Time-reversal symmetry and topological insulators

Whereas quantum Hall states explicitly break **time-reversal (TR) symmetry**, new topologically non-trivial materials obeying TR symmetry have been discovered. The first proposals of the 2D **topological insulator** (TI) - otherwise know as the quantum spin Hall state (depicted in Figure 2.3b) - were remarkably recent (Kane and Mele, 2005 [43], Bernevig and Zhang, 2006 [63]), and the 3D generalisation came soon after in 2007 [47] (depicted in Figure 2.3c). Experiments have shown that these new phases of matter are both realisable and accessible [46, 50, 51].

Topological insulators owe their non-trivial topology to **strong spin-orbit coupling**,[12] which causes the bottom of the conduction band and top of the valence band to be pushed towards each other and overlap, with a gap at the band crossing. This process and resulting band inversion is depicted in Figure 2.4c. The band gap is protected by time-reversal symmetry, and will only close if a TR-breaking perturbation such as an external magnetic field is introduced. As explained in the previous section, we expect surface states to traverse the gap. The surface states of topological insulators manifest as a **Dirac cone**, that is to say a linear dispersion relation. The surface states thus describe relativistic[13], massless fermions. These surface states are protected by time-reversal symmetry and so are robust against both disorder and non-TR breaking perturbations. These states experience spin-momentum locking, such that the surface state is spin non-degenerate and the direction of the spin is perpendicular to the momentum vector and is primarily confined in the surface plane. This results in a dissipationless spin current existing on the surface in equilibrium, as there is no net charge flow but the spin angular momentum flows in the direction perpendicular to the spin direction.

As the band gap is protected by time-reversal symmetry, the conducting edge states are only present when TR symmetry is preserved, such that the fermionic time-reversal operator $\mathcal{T}_\mathrm{f}$ commutes with the system Hamiltonian $[\mathbf{H}, \mathcal{T}_\mathrm{f}] = 0$, and the fermion condition, $\mathcal{T}_\mathrm{f}^2 = -1$, is obeyed. The TR symmetry enforces **Kramers degeneracy**, that is to say that for every eigenstate $|\Psi_\mathrm{i}\rangle$, its time-reversed partner $\mathcal{T}_\mathrm{f}|\Psi_\mathrm{i}\rangle$ is also an eigenstate and has the same energy, but is orthogonal. These are known as **Kramers pairs**. This can be demonstrated

[12] This is the interaction of an electron's spin with its motion inside the potential of the nuclei, and can be thought of as an effective magnetic field seen by the spin of the electron in the rest frame.

[13] Relativistic in the sense that they are described by the relativistic Dirac equation, with the **Fermi velocity** taking the role of the effective speed of light.

using the anti-unitary nature of $\mathcal{T}_\mathrm{f}$ and the fermion condition, such that[14]

$$\langle \Psi_\mathrm{i}, \mathcal{T}_\mathrm{f}\Psi_\mathrm{i}\rangle = \langle \mathcal{T}_\mathrm{f}\Psi_\mathrm{i}, \mathcal{T}_\mathrm{f}^2\Psi_\mathrm{i}\rangle^* = -\langle \mathcal{T}_\mathrm{f}\Psi_\mathrm{i}, \Psi_\mathrm{i}\rangle^* = -\langle \Psi_\mathrm{i}, \mathcal{T}_\mathrm{f}\Psi_\mathrm{i}\rangle, \tag{2.7}$$

and so $\langle \Psi_\mathrm{i}, \mathcal{T}_\mathrm{f}\Psi_\mathrm{i}\rangle = 0$. **Consequently, in the presence of time-reversal symmetry these counter-propagating states cannot backscatter into one another**. If a TR breaking perturbation is applied (such as a magnetic impurity in a topological insulator), a gap will open within the dispersion relation of the edge states and they will no longer conduct, reducing the TI to a trivial insulator. However if a non-TR breaking perturbation is applied the states will remain gapless and will be robust against the perturbation.

The Chern number from Section 2.1.3, n, does not survive in a time-reversal invariant system. The new system has a new topological invariant which is not an integer, but rather a **Chern parity** - it can be either odd or even. It is called a **$\mathbb{Z}_2$ invariant**[15]. Essentially, this $\mathbb{Z}_2$ invariant counts the number of Kramers pairs of edge modes, integrating over half of the Brillouin zone. If the overall $\mathbb{Z}_2$ sum of occupied bands is even, the system is a regular insulator; if the sum is odd, it is a topological insulator. For example, the 2D system graphene possesses two Kramers pairs, has an even $\mathbb{Z}_2$ and is thus a 'trivial' system, whereas a material with one or three Kramers pairs would be a topological system. A nontrivial value for this quantity implies the existence of an odd number of gapless Dirac fermion boundary states as well as a non-zero magnetoelectric polarization in three dimensions [18].

2.3 3D topological insulator (TI) materials

The first **3D TI material** to be experimentally identified was $Bi_{1-x}Sb_x$ [42], predicted by Fu and Kane [47]. It turned out to be poorly suited to detailed topological surface state studies due to a complicated surface state structure - Rashba-split[16] surface states are present alongside the topological surface states and predicted surface state structure has not agreed well with experimental results. Instead, we focus on the Bi_2Se_3 family of materials (in particular **Bi_2Te_3**), predicted by Zhang in 2009 [48], whose model Hamiltonian for this family of materials is used ubiquitously in theoretical studies alongside modifications by Liu et al [49]. Much work was done on these materials before their identification as potential topological insulators, in part because of their excellent thermoelectric properties [73, 74]. We describe the crystal structure and symmetries of this material family, and follow the derivation in [49] to write down the **four-band Hamiltonian** and the following **effective surface state Hamiltonian** for topological insulators.

[14] Using the definition of an anti-unitary matrix Θ, such that $\langle a, b\rangle = \langle \Theta a, \Theta b\rangle^*$ and the fermion condition $\mathcal{T}_\mathrm{f}^2 = -1$.

[15] This simply means the integers, $\mathbb{Z}$, modulo 2.

[16] A momentum-dependent splitting of spin bands in bulk crystals, a combined effect of spin–orbit interaction and asymmetry of the crystal potential.

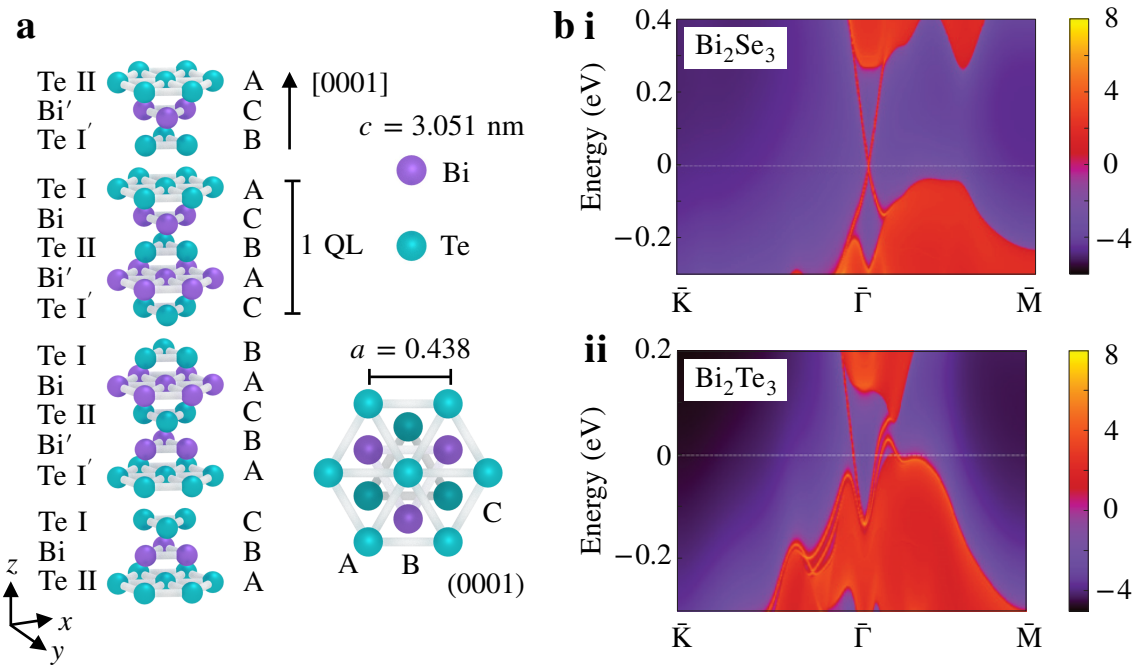

Figure 2.5: **Crystal structure and band structure of topological insulator materials: (a)** Spatial view and (0001) projection of a Bi_2Te_3 unit cell with repetition of a Te II layer. The unit cell consists of three quintuple layers (QLs), which are bonded by weak van der Waals forces. A QL consists of five strongly bound alternating hexagonal Bi (purple) and Te (teal) atomic sheets, shifted relative to each other. The height of the unit cell is 3.051 nm, and so each QL is ~ 1 nm in depth. Energy and momentum dependence of the local density of states (LDOS) for **(b i)** Bi_2Se_3, and **(b ii)** Bi_2Te_3 on the [111] surface. Warmer colours represent higher LDOS. The surface states can be clearly seen around the Γ point as red lines traversing the bulk gap. Figure **(a)** created by S. Palmer. Figures **(b i)** and **(b ii)** taken from [48], reprinted with permission from Springer Nature, Nature Physics.

2.3.1 Crystal structure and symmetry

Bi_2Te_3 (and other materials in the same family, such as Bi_2Se_3) consists of five-atom layers stacked along the z direction (shown in Figure 2.5a), and bonded by **mixed ionic-covalent bonding**. The coupling between two atomic layers within a **quintuple layer** (QL) is strong, whilst that between QLs is predominantly due to **van der Waals** forces and is thus much weaker. A unit cell consists of three QLs, and has a height of 3.051 nm, with each QL thus approximately 1 nm thick. Lattice symmetries of the material are comprised of a three-fold **rotation symmetry** along the z-direction, an additional two-fold **rotation symmetry** along the x-direction and an **inversion symmetry** with Te II (Se II) as the centre of inversion. The material also obeys **time-reversal symmetry**, as we would expect for topological insulators (as per Section 2.2).

To understand the band structure of these materials, we use Bi_2Te_3 as our example, and starting with the isolated atomic orbitals we study all of the relevant interactions until we get to the final band structure, following the scheme in [49] and given diagrammatically in Figure 2.6. Starting with the atomic orbitals of Bi and Te, we note that the electronic configurations of these elements are $\mathbf{6s^2 6p^3}$ for Bi and $\mathbf{5s^2 5p^4}$ for Te.[17]

As the outermost shells for both elements are **p-orbitals**, it is sensible to neglect all other orbitals and only consider the p-orbitals. Within one QL, there are five atoms in each unit cell, each of which have 3 p-orbitals, p_x, p_y and p_z, so overall there are 15 orbitals. We label these orbitals $|\Lambda, \alpha\rangle$ where $\Lambda =$ Bi, Bi′, Te I, Te I′, Te II, and $\alpha = x, y, z$, as illustrated in Figure 2.5a. As the Bi and Te atoms occur in alternate layers of the QL (with weak Van der Waals forces inbetween QLs), the strongest interaction is the coupling between Bi and Te layers.

This type of coupling causes **level repulsion**, such that the Bi levels are pushed up and form the new, hybridised states $|B_\alpha\rangle$ and $|B'_\alpha\rangle$, and the Te levels are pushed down and form the new, hybridised states $|T_\alpha\rangle$, $|T'_\alpha\rangle$ and $|T0_\alpha\rangle$ demonstrated in Figure 2.6 (I).

As our system has **inversion symmetry**, it is convenient to rewrite these orbitals as **bonding** and **anti-bonding states** with definite parity,[18] such that

$$|P1^{\pm}, \alpha\rangle = \frac{1}{\sqrt{2}} \left(|B_\alpha\rangle \mp |B'_\alpha\rangle \right), \tag{2.8}$$

$$|P2^{\pm}, \alpha\rangle = \frac{1}{\sqrt{2}} \left(|T_\alpha\rangle \mp |T'_\alpha\rangle \right). \tag{2.9}$$

The upper index gives the parity of each state. When the energies of each level are calculated, we find that $P1^+_\alpha$ and $P2^-_\alpha$ are closest to the Fermi level, as shown in Figure 2.6 (II). We focus on these levels and neglect the others. We now note that due to the **anisotropy**

[17] The same approach can be taken for Bi_2Se_3, noting that the electronic configuration of Se is $4s^2 4p^4$.

[18] States can be reduced to linear combinations of states which are definitively even or odd under a parity (inversion) transformation.

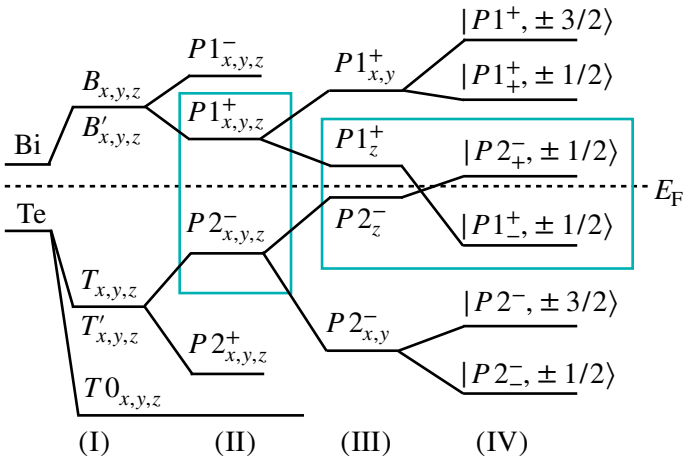

Figure 2.6: **The origin of the Bi_2Te_3 band structure:** Starting from the atomic orbitals of Bi and Te, the following four steps are required to understand the band structure: (I) The hybridization of Bi orbitals and Te orbitals, (II) the formation of the bonding and anti-bonding states due to the inversion symmetry, (III) the crystal field splitting, and (IV) the influence of the SOC. Figure reproduced from [49] with permission from the American Physical Society. This scheme also describes the band structure for other materials in the Bi_2Se_3 family.

of the crystal (i.e. that the x and y directions are different to the z direction due to the layered structure of the material), there is an energy splitting between the $p_{x,y}$ orbitals and the p_z orbitals for both states. The $P1^+_{x,y}$ states have a higher energy than $P1^+_z$, and the $P2^-_{x,y}$ states have a lower energy than $P2^-_z$. This means that the conduction band is primarily dominated by $P1^+_z$, and the valence band is predominantly $P2^-_z$, as demonstrated in Figure 2.6 (III).

So far we have neglected **spin**, which we now include. The states $|P1^+, \alpha, \sigma\rangle$ and $|P2^-, \alpha, \sigma\rangle$ are doubly degenerate, where we have added the extra index $\sigma = \pm 1/2$ to denote spin. It is convenient to transform the states such that

$$|\Lambda, p_\pm, \sigma\rangle = \mp \frac{1}{\sqrt{2}} \left(|\Lambda, p_x, \sigma\rangle \pm i |\Lambda, p_y, \sigma\rangle \right), \tag{2.10}$$

where $\Lambda = P1^+, P2^-$. The **spin-orbit interaction** couples $|\Lambda, p_z, \uparrow\rangle$ to $|\Lambda, p_+, \downarrow\rangle$ and $|\Lambda, p_z, \downarrow\rangle$ to $|\Lambda, p_-, \uparrow\rangle$, inducing level repulsion. Consequently $|P1^+_-, \pm 1/2\rangle$ is pushed down and $|P2^-_+, \pm 1/2\rangle$ is pushed up and the levels cross, as shown in Figure 2.6 (IV). As these two pairs of states have opposite parity, their swapping leads to **band inversion**, and gives the topological signature of these materials. As these four bands are the closest to the Fermi level, when considering the bulk Hamiltonian, it is sufficient to neglect the other bands and use a **four-band Hamiltonian**, with the other bands giving corrective perturbations [49].

2.3.2 Four-band bulk Hamiltonian for TIs

The Hamiltonian can be derived by symmetry principles and considering the symmetries of the crystal structure given in Section 2.3.1, or by using **k · p theory**. I briefly cover the $\mathbf{k}\cdot\mathbf{p}$ method here and refer interested readers to [49] for the symmetry derivation. $\mathbf{k}\cdot\mathbf{p}$ theory is an approximated, semi-empirical approach used for calculating band structures. The important topological physics in this material occurs near the Γ point[19], and so the wave function at the Γ point is used as the zeroth order wave function, and

$$\mathbf{H}^{\mathbf{k}\cdot\mathbf{p}} = \frac{\hbar}{m_0}\mathbf{k}\cdot\mathbf{p}, \tag{2.11}$$

is treated as a perturbation, where $\mathbf{p} = -i\hbar\partial_{\mathbf{r}}$ is the momentum operator acting on the zeroth-order wave function and the crystal momentum is regarded as a small parameter for the perturbation procedure. Then, the Hamiltonian can be expanded in powers of $\mathbf{k}$ allowing us to write down a **low-energy, effective Hamiltonian** [49]. As described in the previous section, we only consider the four bands nearest the Fermi level and so we project the Hamiltonian onto the four bands $|P1^+_-, \pm 1/2\rangle$ and $|P2^-_+, \pm 1/2\rangle$. The obtained model Hamiltonian will depend on a series of matrix elements of momentum $\langle \Lambda_1, \alpha|\mathbf{p}|\Lambda_2, \beta\rangle$, which can be simplified by considering the symmetries of the crystal. The wave function at the Γ point can be obtained through ***ab initio*** calculations, and consequently all of these matrix elements can be calculated. The in-depth calculation can be found in [49]. Following this scheme, the final four band Hamiltonian is given by

$$\mathbf{H}(\mathbf{k}) = \epsilon_0(\mathbf{k})\mathbb{I}_4 + \begin{pmatrix} m(\mathbf{k}) & B_0k_z & 0 & A_0k_- \\ B_0k_z & -m(\mathbf{k}) & A_0k_- & 0 \\ 0 & A_0k_+ & m(\mathbf{k}) & -B_0k_z \\ A_0k_+ & 0 & -B_0k_z & -m(\mathbf{k}) \end{pmatrix}, \tag{2.12}$$

where $k_\pm = k_x \pm ik_y$, $m(\mathbf{k}) = m_0 + m_1k_z^2 + m_2(k_x^2 + k_y^2)$ and $\epsilon_0(\mathbf{k}) = C_0 + C_1k_z^2 + C_2(k_x^2 + k_y^2)$. All constants have numerical values $\mathcal{O}(1)$ in A.U., extracted from **density functional theory** (DFT) calculations (given in Table 2.1). For all following calculations, we set $m_1 = m_2$, (which gives a **symmetric parabolic dispersion** in all three dimensions without sacrificing accuracy, as we will later find that terms involving m_1 are negligible anyway), $A_0 = B_0$ (i.e. assuming **isotropy** in spin-orbit coupling strength in all three directions to make the problem more tractable - we will take an average $A = (2A_0 + B_0))/3$ to find an effective value), $\epsilon(\mathbf{k}) = 0$ (restoring **particle-hole symmetry** without sacrificing

[19] The Γ point is simply the formal name for the high-symmetry point of a dispersion relation for which $\mathbf{k} = 0$. After we have demonstrated that the surface state dispersion relation takes the form of a Dirac cone, the Γ point from then on will be referred to as the Dirac point.

	A_0 (eV Å)	B_0 (eV Å)	A (eV Å)	C_0 (eV)	C_1 (eV Å^2)	C_2 (eV Å^2)	m_0 (eV)	m_1 (eV Å^2)	m_2 (eV Å^2)
Bi_2Se_3	3.33	2.26	3.0	-0.0083	5.74	30.4	-0.28	6.86	44.5
Bi_2Te_3	2.87	0.30	2.0	-0.18	6.55	49.68	-0.3	57.38	45.02

Table 2.1: **Four-band Hamiltonian parameters:** The parameters (taken from [49], originally extracted from DFT calculations) for the Hamiltonian describing the four bands nearest the Γ point of Bi_2Se_3 and Bi_2Te_3.

too much accuracy, particularly when close to the Γ point), giving the simplified Hamiltonian

$$\mathbf{H}(\mathbf{k}) = \begin{pmatrix} m(\mathbf{k}) & Ak_z & 0 & Ak_- \\ Ak_z & -m(\mathbf{k}) & Ak_- & 0 \\ 0 & Ak_+ & m(\mathbf{k}) & -Ak_z \\ Ak_+ & 0 & -Ak_z & -m(\mathbf{k}) \end{pmatrix}. \tag{2.13}$$

This Hamiltonian can be rewritten[20] in terms of the **Pauli matrices** (given in Appendix A.1),

$$\mathbf{H}(\mathbf{k}) = m(\mathbf{k})\mathbb{1}_2 \otimes \boldsymbol{\sigma_3} + Ak_z\boldsymbol{\sigma_3} \otimes \boldsymbol{\sigma_1} + Ak_x\boldsymbol{\sigma_1} \otimes \boldsymbol{\sigma_1} + Ak_y\boldsymbol{\sigma_2} \otimes \boldsymbol{\sigma_1}. \tag{2.14}$$

This form will be particularly useful in Chapter 4 when dealing with other coordinate systems in which the Hamiltonian is more cumbersome.

2.3.3 Effective surface state Hamiltonian

We can now consider the physics at the **surface of a TI material**, still following the method in Reference [49]. For mathematical ease, let us consider that the surface is the plane $z = 0$, such that surface states are localised near the surface in the z direction. Close to the Γ point, linear terms will dominate and so all quadratic terms can be neglected[21]. We can split the bulk Hamiltonian in Equation 2.14 into parts parallel and perpendicular to the surface, such that $\mathbf{H} = \mathbf{H}_\parallel + \mathbf{H}_\perp$ (and including constant terms in $\mathbf{H}_\perp$). Perpendicular to the surface, we have that

$$\mathbf{H}_\perp = m_0\mathbb{1}_2 \otimes \boldsymbol{\sigma_3} + Ak_z\boldsymbol{\sigma_3} \otimes \boldsymbol{\sigma_1}. \tag{2.15}$$

We can replace $k_z \to -i\partial_z$ and obtain the eigenvalue problem

$$\left[m_0\mathbb{1}_2 \otimes \boldsymbol{\sigma_3} - iA\boldsymbol{\sigma_3} \otimes \boldsymbol{\sigma_1}\partial_z\right]\Psi = E\Psi. \tag{2.16}$$

[20] The tensor product, ⊗, is defined in Appendix A.2.
[21] We will see in Chapter 5 that this is not always the case.

Due to the block diagonal form of the Hamiltonian, the eigenstates will have the form

$$\Psi_{\uparrow}(z) = \begin{pmatrix} \Psi_0 \\ \mathbf{0} \end{pmatrix}, \quad \Psi_{\downarrow}(z) = \begin{pmatrix} \mathbf{0} \\ \Psi_0 \end{pmatrix}, \tag{2.17}$$

where $\mathbf{0}$ is the two-component zero vector. $\Psi_{\downarrow}(z)$ and $\Psi_{\uparrow}(z)$ are related by the time-reversal operator. Ψ must then satisfy the eigenvalue equation given by $\mathbf{H}_{\parallel}$, where

$$\mathbf{H}_{\parallel} = Ak_x\boldsymbol{\sigma_1} \otimes \boldsymbol{\sigma_1} + Ak_y\boldsymbol{\sigma_2} \otimes \boldsymbol{\sigma_1}. \tag{2.18}$$

Equivalently, this means that Ψ_0 obeys the **effective surface Hamiltonian**

$$\mathbf{H}_{\text{surf}}(k_x, k_y) = A\left(\boldsymbol{\sigma_1}k_x + \boldsymbol{\sigma_2}k_y\right) + \text{const.} \tag{2.19}$$

This is a **Dirac Hamiltonian** giving a linear, relativistic dispersion relation and tells us that the surface states are described by massless Dirac fermions. By diagonalising, we find the **dispersion relation**

$$E = \pm A|\mathbf{k}|, \tag{2.20}$$

where $|\mathbf{k}| = \sqrt{k_x^2 + k_y^2}$. The surface states can also be directly extracted from *ab initio* calculations by constructing maximally localized Wannier functions and calculating the local density of states (LDOS) on an open boundary. The band structures of Bi_2Se_3 and Bi_2Te_3 are given in Figures 2.5b i and 2.5b ii respectively, showing a bulk band gap and surface states traversing the gap in the form of a single Dirac cone[22]. With a relatively large band gap (0.3 eV [76]) and simple surface spectrum, Bi_2Se_3 is a good material with which to study topological surface phenomena and was the focus of the original work on topological insulator nanoparticles [5], but due to preexisting experimental abilities to produce Bi_2Te_3 nanoparticles, my work in Chapters 5 and 6 utilise Bi_2Te_3 (which has a band gap of 0.17 eV [77]). It should be noted that the placement of the Dirac cone relative to the conduction and valence bands will depend on the **surface termination**[23] of the system. For Bi_2Te_3 this subtlety is particularly important, as if the conventional termination of a complete quintuple layer is used (such that the surface is made entirely of Te atoms) then the Dirac point will touch the valence band. It is necessary to use a non-conventional termination of part of a quintuple layer in order to achieve a Dirac cone in the middle of the band gap [77]. Experimental confirmation of a single Dirac-cone surface state for Bi_2Te_3 was reported in 2009 [45].

[22] Note that true 2D systems with TR symmetry will have an even number of Dirac cones (e.g. Graphene, which has six Dirac cones [75]). 2D surface systems allow for a single Dirac cone, with the system described as a 'holographic metal'. This links back nicely to our discussion of Kramers pairs in Section 2.2.

[23] Surface termination refers to the configuration of atoms at the surface of a finite sample of material. In the case of a flat sample of Bi_2Te_3, with a surface perpendicular to the z-axis, there are five possible terminations - one conventional termination resulting from a surface at the van-der-Waals gap of the material, and four non-conventional, fractional quintuple layer terminations.

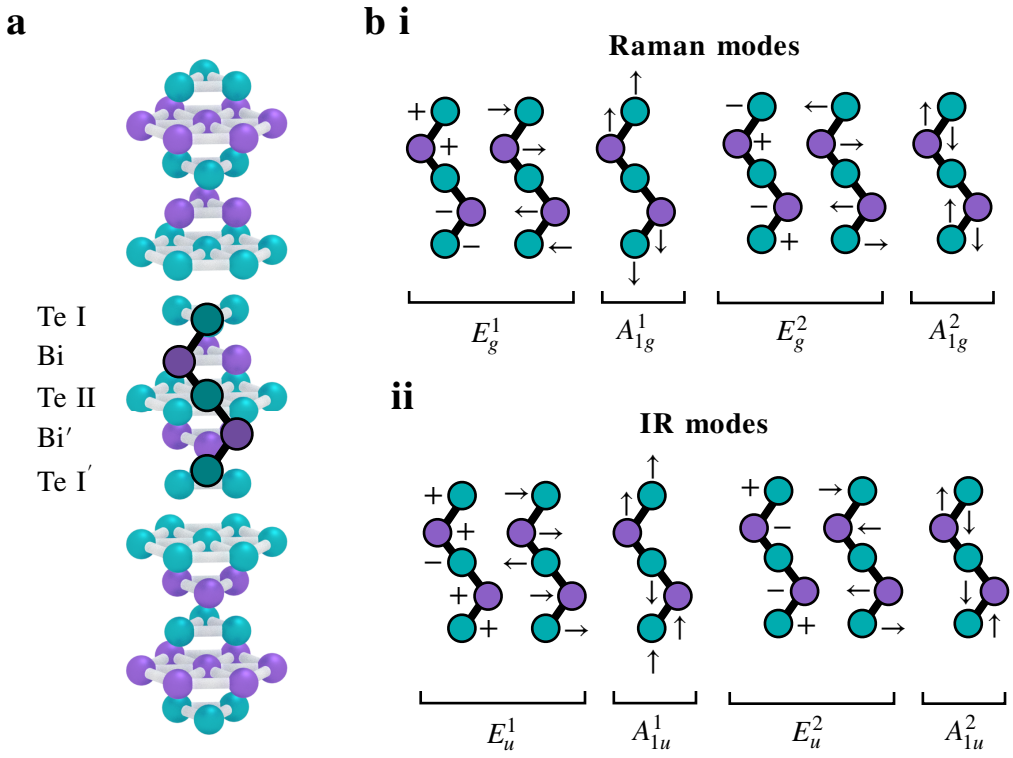

Figure 2.7: **Optical phonons in Bi_2Te_3: (a)** Chain of five atoms in a quintuple layer used to demonstrate vibration dynamics highlighted with black outline and black lines indicating their covalent bonds. **(b)** The **(i)** Raman active and **(ii)** IR active modes of Bi_2Te_3, with subscripts g and u referring to Raman and IR active modes respectively. The superscripts $1, 2$ denote the low and high frequency modes respectively, while E and A refer to whether the modes are in-plane or out-of-plane. The $\pm$ signs denote in-plane and out-of-plane movement. Figure modified from [78] with permission from John Wiley and Sons, Physica status solidi (b).

2.3.4 Bulk phonons in topological insulator materials

So far we have discussed the ground state properties of the topological insulator Hamiltonian. For the work of this thesis (in particular Chapter 6), we will also need to understand a little about the excitations of these materials. The idea of **phonons** - i.e. the collective excitations which propagate through crystal lattices when they are perturbed - should be a familiar concept from any undergraduate course in solid state physics. In keeping with the discussion of symmetry in this chapter, Reference [79] provides an interesting discussion on how vibrational modes in lattices can be predicted by spontaneous breaking of the lattice symmetry. Both **acoustic** and **optical**[24] phonons can be described in this way.

By inspecting the lattice structure of our system, the type of bulk phonons can be predicted. We use Bi_2Te_3 as our example, but these results will be the same for Bi_2Se_3 and Sb_2Te_3. The ***c*-axis**[25] [0001], is aligned with the z-axis, and labelled in Figure 2.5a. The normal modes of vibration propagating along the c-axis of the material involve motion of the entire planes of atoms, either parallel or perpendicular to the c-axis and so directly depend on the inter-planar forces. There are 15 lattice vibration modes - 12 optical and three acoustic, of which we focus on the optical modes. The 12 optical branches have $2A_{1g}$, $2E_g$, $2A_{1u}$ and $2E_u$ symmetry [78], where E and A indicate the in-plane and out-of-plane lattice vibrations. The g and u subscripts denote **Raman active** (see Figure 2.7bi) and **IR active**[26] modes (Figure 2.7bii) respectively. The optical modes belonging to A_{1u} and E_u can also be Raman active. I give more information on Raman and IR spectroscopy in Appendix B.2, and more details of the spectroscopic probing of Bi_2Te_3 in particular can be found in references [78, 80–82].

2.4 Landscape of topological quantum systems

This section is not necessary to understand the work of this thesis, however I include it to place topological insulators into the context of the much larger landscape of **topological quantum systems**, depicted in the (non-exhaustive) diagram presented in Figure 2.8. The concept of topology has made a profound impact on modern condensed matter physics, and as many topics fall under its general framework, the myriad of definitions, quantities and systems demonstrating topological features can be overwhelming.

We start with the idea of **quantum phases of matter**, which are generally understood

[24] Acoustic phonons are coherent movements of the material atoms away from their equilibrium positions, comparable to the compression and expansion of air due to a sound wave, hence their name. Optical phonons are out of phase excitations in which atoms within the lattice basis move in different directions. Fluctuations like this typically create an electric polarisation in the material allowing coupling to the electromagnetic field, hence the name of optical phonons.

[25] The c-axis (optical axis) of a material is a direction in which a ray of incoming light suffers no double refraction. A material such as Bi_2Te_3 has a single c-axis, and so is known as **uniaxial**.

[26] Raman spectroscopy probes matter using the weak, inelastic Raman scattering process whereas IR spectroscopy relies on the absorption of light by the material.

to be phases of matter at zero temperature. Quantum phases correspond to the ground states of the quantum Hamiltonians which govern these systems. The topological insulator Hamiltonians we have been discussing are exactly of this Hamiltonian type. As I have mentioned in earlier sections, it was once assumed that all possible quantum phases of matter and all possible (continuous) quantum phase transitions could be described by Landau's theory of symmetry breaking. However, the discovery of **chiral spin states** [83–85] cast doubt on this idea, as many demonstrably different chiral spin states were found, all obeying the same symmetries. Symmetry alone was thus not enough to characterize and distinguish different chiral spin states, and it was surmised that these systems must contain a new kind of order that is beyond the usual symmetry description.

The new type of order proposed was **topological order** [86][27]. The non-Abelian geometric phase of degenerate ground states [86, 88], was introduced to both define and characterize the different topological orders in chiral spin states. It was observed that the similarity [89] between chiral spin states and **fractional quantum Hall** (FQH) states [90, 91] also allowed one to use the theory of topological order to describe different FQH states. Just like chiral spin states, differing FQH states may have the same symmetry and cannot be distinguished by symmetry breaking, despite having distinguishable physical properties. It was concluded that FQH states must have a new type of order, and it was found that the new order in quantum Hall states can be described by topological order [92]. This discovery confirmed that topological order can be experimentally realised. However, FQH states were not the first experimentally discovered states with topological order - **superconductors** with topological order had previously been discovered, but their topological order unappreciated until much later [93].

We have already discussed in some detail how topological systems can be defined by their topological invariants, which can be measured by following the dynamical phase of a closed path in reciprocal space. States with non-local order parameters can be called topologically ordered - more generally, however, the definition of a topological phase is a phase of matter whose low-energy field theory is a **topological field theory**. More details on this type of classification are given in [55, 94–96]. Microscopically, the notion of topological order is a measure of entanglement patterns. Systems with **short range entanglement** (SRE) can all be transformed into each other via local unitary transformations, and so they all belong to the same trivial phase. Systems with **long range entanglement** (LRE), however, cannot be transformed into each other (or into systems with SRE) via local unitary transformations, and so LRE states can belong to many different phases. These phases can be defined as different topological orders.

Topological ordered systems have new characteristic properties with important ramifications. Topologically ordered systems exhibit new collective excitations which can be experimen-

[27] Naming motivated by the low-energy effective field theory of the chiral spin states, a topological quantum field theory [83, 87].

tally measured, for example in neutron scattering experiments. The **quasiparticles**[28] of topologically ordered systems can carry fractional statistics [97, 98] (including non-Abelian statistics [99]) and fractional charges if there is a symmetry [91]. This property could allow for the systems to be used for **topological quantum memory and topological quantum computation** [100] (for example in surface codes [101] - it was proposed that the topologically protected degeneracy of the $\mathbb{Z}_2$ spin liquid could be used to perform fault-tolerant quantum computation as a Toric code.). Some topological orders have topologically protected gapless boundary excitations [102, 103], which lead to perfectly conducting boundary channels - this has the potential for revolutionary device applications.

Although the concept of topologically ordered phases has been around for some time now, most examples have involved complicated states of matter, such as the FQH [90, 91], quantum double models [100], doubled Chern-Simons [104] theories, amongst others. The topologically ordered states that have been experimentally realized and theoretically investigated until now have all involved strong electron-electron interactions.

Free fermion states of matter have been assumed to be topologically trivial in the past, in part due to the exactly solvable nature of their Hamiltonian spectra. However, a subset of these systems do have properties indicating topological behaviour, such as gapless edge states - even though they are formed from non-interacting fermions. The epitomic system is that of the **integer quantum Hall** (IQH) effect, as described in Section 2.1.3. IQH is an example of topological order, and specifically **invertible topological order**[29]. This system cannot be smoothly deformed into a **product state**[30] without a phase transition occurring [105]. By another definition, this system is not necessarily classified as topological - Kitaev says that only states with non-trivial topological excitations can be called long range entangled [106], and so IQH is SRE under this definition.

Our discussion so far has glaringly omitted discussion of topological insulators, the systems of focus in this thesis. As we already know, topological insulators are formed from non-interacting fermions, much like the IQH state. We also know this system exhibits properties indicative of topology, such as gapless edge states. However, topological insulators exhibit short range entanglement, and thus do not exhibit topological order. It has been found that if a system must preserve a symmetry, Ω, then not all SRE states can be deformed to a product state while respecting Ω. This means that SRE states can have non-trivial topological phases which are protected by the symmetry Ω. These are **symmetry protected topological**

[28] Although the exact definition is not universally agreed upon, a quasiparticle is an elementary excitation of a collection of particles. Some physicists reserve the term *quasiparticles* for fermionic excitations, while bosonic excitations such as phonons are described as *collective excitations*. I am in the camp of physicists content to describe both fermionic and bosonic excitations as quasiparticles, but the point is not of any importance for this thesis.

[29] Invertible topological order means that another system with topological order exists such that stacking the two states will result in a gapped state with no topological order. Systems with invertible topological order do not host fractional excitations.

[30] A product state is a state which can be decomposed into the form $|\Psi\rangle = \otimes|\psi\rangle$, where $\otimes$ is the tensor product described in Appendix A.2.

states (SPT) [107, 108]. Topological insulators are a small subset of SPT states. Unlike systems with LRE and thus intrinsic topological order, SPT states are only protected as long as the symmetry is not broken. These systems typically have interesting boundary physics, such as gapless modes or gapped topological order on the boundary. Characterizing them usually requires global quantities too and cannot be done by local order parameters. This is exactly what we have seen for topological insulators in Section 2.2, in which topological insulator systems obey time-reversal symmetry, and the state is characterised by a $\mathbb{Z}_2$ topological invariant.

A **periodic table** classifying topological insulators and superconductors has been created [109]. The table organizes the possible topological states according to their space-time dimension and the symmetries that must remain protected: TR, charge-conjugation, and/or chiral symmetries. The relevant entries in this table within the context of this thesis are the 2D and 3D TR-invariant topological insulators. In this definition, **quantum Hall** states and the **SSH model** [110–112] are classified as topological insulators, as the definition relies on whether **bulk-boundary correspondence** is obeyed or not. The current classification of topological insulators covers only TR, charge-conjugation, or chiral symmetries and does not exhaust the number of all possible topological insulators. In principle, for every discrete symmetry, there must exist topological insulating phases with distinct physical properties and a topological number that classifies these phases and distinguishes them from the trivial ones.

The explosion of interest in topological insulators (whilst far from being over) has also led to the rapid acceleration in the search for other topological phases, leading to **topological crystalline insulators** (in which crystal symmetries lead to SPT phases) [113, 114], **topological semi-metals** [115, 116], **topological superconductors** [18, 54, 114, 117, 118] and many more. The study of topological insulators themselves as a more mature topic now lends itself to a great many potential applications, such as topological quantum computing, quantum information, spintronics, topological lasing and plasmonics [46, 119–125]. Composite systems involving topological insulators, such as topological insulators interacting with superconductors [125–127], topological insulator materials interfaced with magnetic systems to produce **magnetic TIs** [128, 129] and so on are also exciting avenues of study.

Another area that has benefited from development is that of bosonic analogues of topological phases. For example, **topological magnon insulators** [130, 131] and **photonic topological insulators** [1, 12, 13, 132] in which bosons (magnons and photons respectively) experience an enforced pseudo time-reversal symmetry, and replicate many of the benefits of electronic topological insulators, such as dissipationless surface currents and robustness against backscattering. Many platforms used for analogues of topological electronic systems showcasing unique strengths and limitations are currently being studied in the drive towards

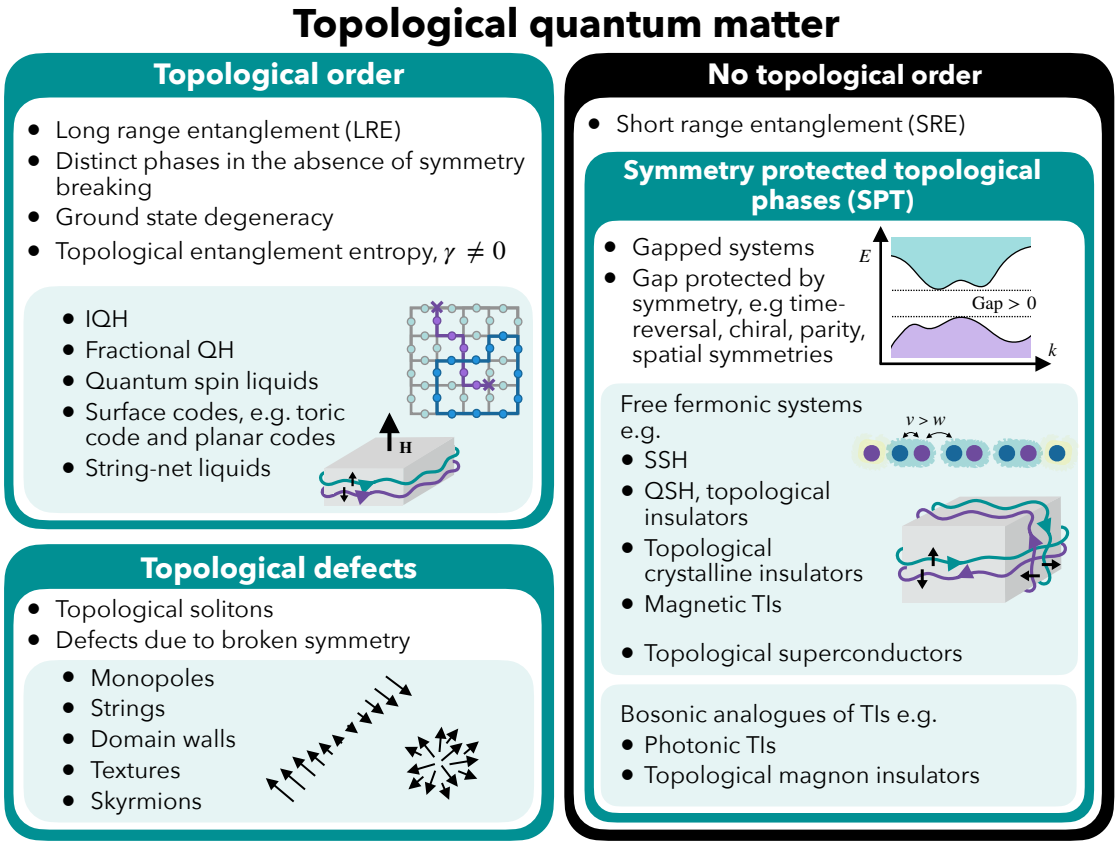

Figure 2.8: **The landscape of topological quantum systems:** Schematic showing the different areas of topological quantum matter.

new applications in topological photonics, such as cold atoms [133], liquid helium [134], polaritons [135], acoustic [136] and mechanical systems [137].

The final area that I briefly mention to complete the discussion of topological quantum matter is that of **topological defects** - a topic well known in cosmology [138–140], but also with its place in condensed matter [134, 141–143]. Topological defects are defects in a material or field due to symmetry breakdown, and are fundamental in the explanation of many interesting phenomena in condensed matter, such as the unusual hydrodynamic properties of **superfluid Helium-3** [144, 145]. Topology has found itself integral to many topics in condensed matter and other disciplines beyond - it is a booming area intersecting multiple fields of work with common mathematical techniques and phenomena.

3. Theory of light

This chapter deals with the optics and photonics theory needed to understand the work of this thesis. Much of what will be covered at the start of the chapter should be familiar from undergraduate electromagnetism, but I include it for completeness and to introduce notation that I will use throughout the rest of the thesis.

I start with the classical, macroscopic formulation of **Maxwell's equations**. These equations allow us to understand the effects of light on bulk materials, such as induced polarisation and bound charge density. This theory is needed to understand the work on topological polaritons and the modification of the photonic local density of states using TI nanostructures covered in Chapter 6. I discuss how Maxwell's equations can be reformulated as the **wave equation for electromagnetic fields** and the importance of **polarisation** of these fields. A good understanding of polarisation is needed to calculate the selection rules of TI nanoparticles coupled with light, which are derived and used in Chapter 5 and also needed for Chapter 6.

In order to study the interactions of single photons interacting with TI nanostructures, as covered in Chapter 5, it is important to understand the **quantised formulation of light**. Readers will probably be familiar with second quantisation and modes of the quantum simple harmonic oscillator (QSHO), but the link to electromagnetism is not always explicitly made in undergraduate quantum mechanics courses and so I cover this in some detail. My favourite classical electromagnetism references are [146–148] and the treatment of quantised fields is covered nicely in [149, 150] so I point the reader to these resources for additional reading.

We also need to cover the fundamentals of **light-matter interactions**, so I introduce the light-matter interaction Hamiltonian and the electric dipole approximation. I introduce the concept of **spectral densities** to calculate **light-mediated transition rates** between electronic states. This is a less common but very powerful approach to calculating transition rates. This method will then be employed in Chapter 5 to describe how light-mediated transitions of TQDs are modified by the presence of a cavity. The method of spectral densities can be found in more detail in [151, 152].

I cover the concept of **lasing**, which is needed to motivate and understand the results on TQD lasing in Chapter 5.

I introduce the idea of **Green's functions**, a powerful formalism for understanding how electromagnetic fields behave with non-trivial boundary conditions. I also introduce the concept of the **photonic density of states (DOS)**. I use Green's functions and the

photonic density of states in Chapter 6 to demonstrate how TI nanostructures can alter the electromagnetic properties of their environment.

3.1 Maxwell's equations

"I have also a paper afloat, with an electromagnetic theory of light, which, until I am convinced to the contrary, I hold to be great guns."
- James Clerk Maxwell[1]

Maxwell's equations are some of the most well-known equations in science. These four differential equations form the theoretical basis for describing classical electromagnetism. We start with **macroscopic Maxwell's equations**, which reduce to microscopic (vacuum) Maxwell's equations when material bulk effects can be neglected.

3.1.1 Macroscopic Maxwell's equations

In SI units (which I attempt to use consistently throughout this thesis), the inhomogeneous, macroscopic equations are given by

$$\textbf{Gauss}' \textbf{ law} \qquad \nabla \cdot \mathbf{D}(\mathbf{r},t) = \rho_{\mathrm{f}}(\mathbf{r},t), \tag{3.1}$$

$$\textbf{Gauss}' \textbf{ law for magnetism} \qquad \nabla \cdot \mathbf{B}(\mathbf{r},t) = 0, \tag{3.2}$$

$$\textbf{Faraday}'\textbf{s law of induction} \qquad \nabla \times \mathbf{E}(\mathbf{r},t) = -\frac{\partial \mathbf{B}(\mathbf{r},t)}{\partial t}, \tag{3.3}$$

$$\textbf{Ampere}'\textbf{s law} \qquad \nabla \times \mathbf{H}(\mathbf{r},t) = \mathbf{J}_{\mathrm{f}}(\mathbf{r},t) + \frac{\partial \mathbf{D}(\mathbf{r},t)}{\partial t}, \tag{3.4}$$

where $\mathbf{E}(\mathbf{r},t)$ and $\mathbf{B}(\mathbf{r},t)$ are the electric field strengths and magnetic flux density respectively, $\mathbf{D}(\mathbf{r},t)$ and $\mathbf{H}(\mathbf{r},t)$ are the displacement field and magnetizing field, and $\rho_{\mathrm{f}}(\mathbf{r},t)$ and $\mathbf{J}_{\mathrm{f}}(\mathbf{r},t)$ denote the free charge and current densities. These equations are demonstrated diagrammatically in Figure 3.1. Maxwell's equations imply that all classical electromagnetic radiation is ultimately generated by accelerating charges[2]. These quantities satisfy boundary

[1] Quote taken from a letter to C. H. Cay, 5th January 1865. James Clerk Maxwell was a 19th century physicist, who discovered that electric and magnetic fields could be described in the single, unified theory of electromagnetism. His work arguably laid the foundations for much of modern physics, and Einstein is said to have been quoted *"I stand on the shoulders of Maxwell"*. For all the radical vision he demonstrated in science, he held incredibly conservative views on gender. He barred women from studying physics at Cambridge when he established the Cavendish Laboratory, going as far as to pen several regrettable verses of poetry on why women were unsuited to study the physical sciences. This decision was only reversed during the tenure of Lord Rayleigh, some years later.

[2] We will not explicitly cover this, but the concept can be quickly understood by recalling that a stationary charge generates a radial electric field, and then considering what happens to the radial and transverse components of the field(s) when the charge undergoes a small acceleration.

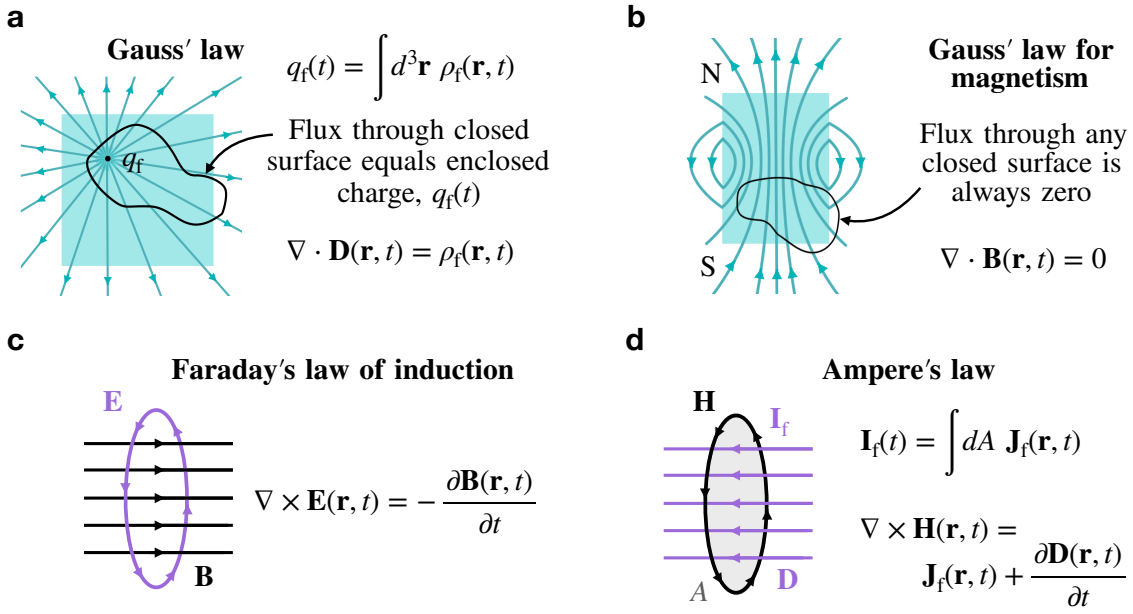

Figure 3.1: **Maxwell's equations: (a) Gauss' law**. Flux through a closed surface is equal to the charge, q_f enclosed by the surface. This is equivalent to saying that electric fields lines must always start and end at charges. **(b) Gauss' law for magnetism**. Magnetic flux through a closed surface is always equal to zero. This is equivalent to saying that magnetic field lines always join up, such that field lines entering and leaving a closed surface always sum to zero. Said another way, magnetic monopoles do not occur. **(c) Faraday's law of induction.** A time-varying magnetic field, $\mathbf{B}$, will always accompany a spatially-varying, non-conservative electric field, $\mathbf{E}$, and vice versa. **(d) Ampere's law**. A flowing electric current, $\mathbf{I}_f$, gives rise to a magnetic field, $\mathbf{H}$, which circles the current. A time-changing displacement field, $\mathbf{D}$, gives rise to a magnetic field, $\mathbf{H}$, which circles $\mathbf{D}$.

conditions (see Figure 3.2), such that

$$[\mathbf{D}_2(\mathbf{r}, t) - \mathbf{D}_1(\mathbf{r}, t)] \cdot \hat{\mathbf{n}} = \rho_f(\mathbf{r}, t), \tag{3.5}$$

$$[\mathbf{B}_2(\mathbf{r}, t) - \mathbf{B}_1(\mathbf{r}, t)] \cdot \hat{\mathbf{n}} = 0, \tag{3.6}$$

$$\hat{\mathbf{n}} \times [\mathbf{E}_2(\mathbf{r}, t) - \mathbf{E}_1(\mathbf{r}, t)] = 0, \tag{3.7}$$

$$\hat{\mathbf{n}} \times [\mathbf{H}_2(\mathbf{r}, t) - \mathbf{H}_1(\mathbf{r}, t)] = \hat{\mathbf{n}} \times \mathbf{J}_f(\mathbf{r}, t). \tag{3.8}$$

3.1.2 Auxiliary fields, polarization and magnetization

The definitions of the **auxiliary fields** (the displacement and magnetizing fields, $\mathbf{D}(\mathbf{r}, t)$ and $\mathbf{H}(\mathbf{r}, t)$) are given by

$$\mathbf{D}(\mathbf{r}, t) = \epsilon_0 \mathbf{E}(\mathbf{r}, t) + \mathbf{P}(\mathbf{r}, t), \tag{3.9}$$

$$\mathbf{H}(\mathbf{r}, t) = \frac{1}{\mu_0} \mathbf{B}(\mathbf{r}, t) - \mathbf{M}(\mathbf{r}, t), \tag{3.10}$$

where $\mathbf{P}(\mathbf{r}, t)$ is the polarisation field and $\mathbf{M}(\mathbf{r}, t)$ is the magnetization field. These quantities can in turn be described by the bound charge density $\rho_b(\mathbf{r}, t)$ and bound current density

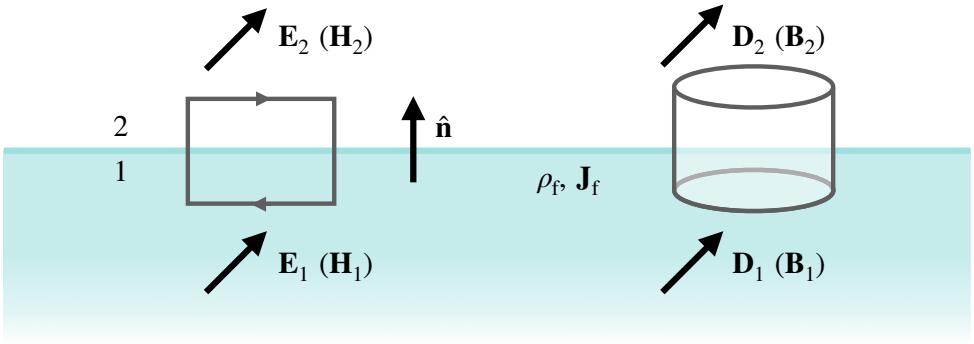

$$\hat{\mathbf{n}} \times [\mathbf{E}_2(\mathbf{r},t) - \mathbf{E}_1(\mathbf{r},t)] = 0 \qquad [\mathbf{D}_2(\mathbf{r},t) - \mathbf{D}_1(\mathbf{r},t)] \cdot \hat{\mathbf{n}} = \rho_f(\mathbf{r},t)$$
$$\hat{\mathbf{n}} \times [\mathbf{H}_2(\mathbf{r},t) - \mathbf{H}_1(\mathbf{r},t)] = \hat{\mathbf{n}} \times \mathbf{J}_f(\mathbf{r},t) \qquad [\mathbf{B}_2(\mathbf{r},t) - \mathbf{B}_1(\mathbf{r},t)] \cdot \hat{\mathbf{n}} = 0$$

Figure 3.2: **Maxwell's equations at an interface:** Boundary conditions for Maxwell's equations. The tangential component of $\mathbf{E}$ is continuous across the surface, as is the tangential component of $\mathbf{H}$ unless there is a surface current present. The normal component of $\mathbf{D}$ is continuous unless there is a surface charge, and the normal component of $\mathbf{B}$ is always continuous across the interface.

$\mathbf{J}_b(\mathbf{r},t)$, which are defined as

$$\rho_b(\mathbf{r},t) = -\nabla \cdot \mathbf{P}(\mathbf{r},t), \tag{3.11}$$
$$\mathbf{J}_b(\mathbf{r},t) = \nabla \times \mathbf{M}(\mathbf{r},t) + \frac{\partial \mathbf{P}(\mathbf{r},t)}{\partial t}. \tag{3.12}$$

The total charge and current density are then described by

$$\rho(\mathbf{r},t) = \rho_b(\mathbf{r},t) + \rho_f(\mathbf{r},t), \tag{3.13}$$
$$\mathbf{J}(\mathbf{r},t) = \mathbf{J}_b(\mathbf{r},t) + \mathbf{J}_f(\mathbf{r},t). \tag{3.14}$$

If the above relations are used to eliminate $\mathbf{D}(\mathbf{r},t)$ and $\mathbf{H}(\mathbf{r},t)$ from Maxwell's equations, the microscopic form of the equations is then recovered. For linear materials, **the constitutive relations** (i.e. the specific relation between polarisation, magnetization and the auxiliary fields) are particularly simple, in that $\mathbf{P}(\mathbf{r},t)$ and $\mathbf{M}(\mathbf{r},t)$ are approximately proportional to $\mathbf{E}(\mathbf{r},t)$ and $\mathbf{B}(\mathbf{r},t)$ respectively, such that

$$\mathbf{D}(\mathbf{r},t) = \epsilon \mathbf{E}(\mathbf{r},t), \tag{3.15}$$
$$\mathbf{H}(\mathbf{r},t) = \frac{1}{\mu}\mathbf{B}(\mathbf{r},t). \tag{3.16}$$

Interesting complications arise often arise, such as (i) inhomogeneous materials (such that that ϵ and μ have spatial dependence), (ii) anisotropic materials (such that ϵ and μ are tensors rather than scalars) and (iii) dispersive materials (ϵ and μ depend on the frequency of the incoming light, ν). Anisotropy and dispersion are both relevant for the proper

treatment of topological insulators at THz scales, and so will be revisited later in this thesis (specifically in Chapter 6).

3.1.3 Microscopic Maxwell's equations

Macroscopic Maxwell's equations are incredibly important for studying the optical properties of bulk materials and so we will continue to use them later in this chapter and in Chapter 6. However, TI surface states occur (somewhat unsurprisingly) at the surface of the material and optical transitions between surface states can be considered separate from bulk effects. When we do not need to include contributions from the bulk, we can employ **microscopic Maxwell's equations**[3]. For the case that we are in vacuum, such that there is no polarization or magnetization, the constitutive relations are given by

$$\mathbf{D}(\mathbf{r},t) = \epsilon_0 \mathbf{E}(\mathbf{r},t), \tag{3.17}$$

$$\mathbf{H}(\mathbf{r},t) = \frac{1}{\mu_0}\mathbf{B}(\mathbf{r},t), \tag{3.18}$$

and Maxwell's equations reduce to

$$\nabla \cdot \mathbf{E}(\mathbf{r},t) = \frac{\rho_{\mathrm{f}}(\mathbf{r},t)}{\epsilon_0}, \tag{3.19}$$

$$\nabla \cdot \mathbf{B}(\mathbf{r},t) = 0, \tag{3.20}$$

$$\nabla \times \mathbf{E}(\mathbf{r},t) = -\frac{\partial \mathbf{B}(\mathbf{r},t)}{\partial t}, \tag{3.21}$$

$$\nabla \times \mathbf{B}(\mathbf{r},t) = \mu_0 \left(\mathbf{J}_{\mathrm{f}}(\mathbf{r},t) + \epsilon_0 \frac{\partial \mathbf{E}(\mathbf{r},t)}{\partial t} \right). \tag{3.22}$$

3.2 The shape of light

I now introduce the **vector potential**, and demonstrate that Maxwell's equations can be reformulated into the form of the **wave equation**. This allows us to write an ansatz for the fields and gain an intuition for how electromagnetic waves look. We also discuss choices of polarisation basis. For now we continue to work in vacuum for simplicity (i.e. employing microscopic Maxwell's equations), but the ideas can easily be extended to the macroscopic case.

3.2.1 Vector and scalar potentials

The form of Gauss' law (Equation 3.19) suggests that $\mathbf{E}(\mathbf{r},t)$ can be rewritten in terms of a **scalar potential** such that $\mathbf{E}(\mathbf{r},t) = -\nabla\Phi(\mathbf{r},t)$ where

$$\Phi(\mathbf{r},t) = \frac{1}{4\pi\epsilon_0} \int d^3\mathbf{r}' \, \frac{\rho_{\mathrm{f}}(\mathbf{r}',t)}{|\mathbf{r}-\mathbf{r}'|}. \tag{3.23}$$

[3] Also known as vacuum Maxwell's equations.

However, in the presence of a time-varying magnetic field (which in reality is always the case if there is a time-varying electric field), the electric field is no longer conservative (such that $\nabla \times \mathbf{E}(\mathbf{r},t) \neq 0$ as per Faraday's law of induction given in Equation 3.21) and so can no longer be written simply in terms of a scalar potential. This can be remedied by introducing the **magnetic vector potential**, $\mathbf{A}(\mathbf{r},t)$, such that

$$\mathbf{B}(\mathbf{r},t) = \nabla \times \mathbf{A}(\mathbf{r},t). \tag{3.24}$$

Then, $\mathbf{E}(\mathbf{r},t)$ is of the form

$$\mathbf{E}(\mathbf{r},t) = -\nabla\Phi(\mathbf{r},t) - \frac{\partial \mathbf{A}(\mathbf{r},t)}{\partial t}. \tag{3.25}$$

Maxwell's equations and any resulting calculations can then be written in terms of either $\mathbf{E}(\mathbf{r},t)$ and $\mathbf{B}(\mathbf{r},t)$ or $\mathbf{A}(\mathbf{r},t)$ and $\Phi(\mathbf{r},t)$.

3.2.2 The wave equation

For now we will not be considering systems with free charge densities or charge currents, meaning that $\rho_\mathrm{f}(\mathbf{r},t) = \mathbf{J}_\mathrm{f}(\mathbf{r},t) = 0$, and consequently $\Phi(\mathbf{r},t) = 0$. By working in the **Coulomb gauge**[4], such that $\nabla \cdot \mathbf{A}(\mathbf{r},t) = 0$, we see that Ampere's law (Equation 3.22) becomes (making use of $\epsilon_0\mu_0 = 1/c^2$) the homogeneous wave equation,

$$\nabla^2\mathbf{A}(\mathbf{r},t) - \frac{1}{c^2}\frac{\partial^2\mathbf{A}(\mathbf{r},t)}{\partial t^2} = 0. \tag{3.26}$$

The Fourier expansion of $\mathbf{A}(\mathbf{r},t)$ can be written as

$$\mathbf{A}(\mathbf{r},t) = \sum_{\beta=1,2}\sum_{\mathbf{k}} \mathbf{A}_{\beta,\mathbf{k}}(\mathbf{r},t) = \sum_{\beta,\mathbf{k}} \left[a_{\beta,\mathbf{k}}(t)u_{\beta,\mathbf{k}}(\mathbf{r}) + a^*_{\beta,\mathbf{k}}(t)u^*_{\beta,\mathbf{k}}(\mathbf{r})\right], \tag{3.27}$$

and for periodic boundary conditions, $u_{\beta,\mathbf{k}}(\mathbf{r})$ can be written in the form $u_{\beta,\mathbf{k}}(\mathbf{r}) = e^{i\mathbf{k}\cdot\mathbf{r}}\mathbf{e}_\beta$ or $u_{\beta,\mathbf{k}}(\mathbf{r}) = \sin(\mathbf{k}\cdot\mathbf{r})\mathbf{e}_\beta$. The vector $\mathbf{k}$ is the momentum of the wave and $\mathbf{e}_\beta$ are unit vectors in the plane perpendicular to $\mathbf{k}$. $a_{\beta,\mathbf{k}}(t), a^*_{\beta,\mathbf{k}}(t)$ are the time-dependent Fourier coefficients. In later chapters we will see that the sinusoidal solution is often convenient, but for now we will take the exponential form, such that

$$\mathbf{A}(\mathbf{r},t) = \sum_{\beta=1,2}\sum_{\mathbf{k}} \mathbf{A}_{\beta,\mathbf{k}}(\mathbf{r},t) = \sum_{\beta,\mathbf{k}} \left[e^{i\mathbf{k}\cdot\mathbf{r}}a_{\beta,\mathbf{k}}(t)\mathbf{e}_\beta + e^{-i\mathbf{k}\cdot\mathbf{r}}a^*_{\beta,\mathbf{k}}(t)\mathbf{e}^*_\beta\right]. \tag{3.28}$$

When plugged into Equation 3.26, we find the time-dependence of the Fourier coefficients such that $a_{\beta,\mathbf{k}}(t) \propto e^{-i\omega_\mathbf{k}t}$, with $\omega_\mathbf{k} = c|\mathbf{k}|$. The fields can now easily be found from $\mathbf{A}(\mathbf{r},t)$,

[4] I briefly discuss gauge choices in Appendix B.3.

such that

$$\mathbf{E}(\mathbf{r},t) = \sum_{\beta,\mathbf{k}} \mathbf{E}_{\beta,\mathbf{k}}(\mathbf{r},t) = i\sum_{\beta,\mathbf{k}} \omega_{\mathbf{k}} \left[e^{i\mathbf{k}\cdot\mathbf{r}} a_{\beta,\mathbf{k}}(t)\mathbf{e}_\beta - e^{-i\mathbf{k}\cdot\mathbf{r}} a^*_{\beta,\mathbf{k}}(t)\mathbf{e}^*_\beta \right], \tag{3.29}$$

$$\mathbf{B}(\mathbf{r},t) = \sum_{\beta,\mathbf{k}} \mathbf{B}_{\beta,\mathbf{k}}(\mathbf{r},t) = i\sum_{\beta,\mathbf{k}} \left[e^{i\mathbf{k}\cdot\mathbf{r}} a_{\beta,\mathbf{k}}(t)\left(\mathbf{k}\times\mathbf{e}_\beta\right) - e^{-i\mathbf{k}\cdot\mathbf{r}} a^*_{\beta,\mathbf{k}}(t)\left(\mathbf{k}\times\mathbf{e}^*_\beta\right) \right]. \tag{3.30}$$

We thus have the picture (denoted in Figure 3.3a) of a light wave propagating in the direction of $\mathbf{k}$, with $\mathbf{E}(\mathbf{r},t)$ perpendicular to $\mathbf{k}$ and described by basis vectors $\mathbf{e}_1$ and $\mathbf{e}_2$, and $\mathbf{B}(\mathbf{r},t)$ is perpendicular to both $\mathbf{k}$ and $\mathbf{E}(\mathbf{r},\mathbf{t})$. The Hamiltonian of the field has the form

$$\begin{aligned} \mathbf{H}^{\text{rad}} &= \frac{\epsilon_0}{2}\int_V \left(\left|\mathbf{E}(\mathbf{r},t)\right|^2 + \left|\mathbf{B}(\mathbf{r},t)\right|^2 \right) d^3\mathbf{r} \\ &= V\epsilon_0 \sum_{\beta,\mathbf{k}} \omega^2_{\mathbf{k}} \left[a_{\beta\mathbf{k}}(t) a^*_{\beta,\mathbf{k}}(t) + a^*_{\beta,\mathbf{k}}(t) a_{\beta\mathbf{k}}(t) \right]. \end{aligned} \tag{3.31}$$

Currently this Hamiltonian (and thus the total energy of the system) appears to grow with volume, V, and so the fields will need to be normalised - which can be done via the specific form of $a_{\beta,\mathbf{k}}(t)$ and $a^*_{\beta,\mathbf{k}}(t)$ - if we wish to maintain a sensible expression for very large system sizes.

3.2.3 Light polarisation

For light propagating in the direction $\hat{\mathbf{k}} = (\sin\vartheta_0\cos\varphi_0, \sin\vartheta_0\sin\varphi_0, \cos\vartheta_0)$, the **polarisation vectors** $\mathbf{e}_1$ and $\mathbf{e}_2$ reside in the plane perpendicular to $\hat{\mathbf{k}}$ (depicted in the inset of Figure 3.3a), described by the two orthonormal vectors

$$\mathbf{r}_1 = (\cos\vartheta_0\cos\varphi_0, \cos\vartheta_0\sin\varphi_0, -\sin\vartheta_0) \tag{3.32}$$

$$\mathbf{r}_2 = (-\sin\varphi_0, \cos\varphi_0, 0), \tag{3.33}$$

and so general polarisation vectors are given by

$$\mathbf{e} = ae^{i\alpha_1}\mathbf{r}_1 + \sqrt{1-a^2}e^{i\alpha_2}\mathbf{r}_2. \tag{3.34}$$

For light travelling parallel to the z-axis, $\hat{\mathbf{k}} = (0,0,1)$, i.e. $\vartheta_0 = 0$,

$$\mathbf{e} = ae^{i\alpha_1}(\cos\varphi_0, \sin\varphi_0, 0) + \sqrt{1-a^2}e^{i\alpha_2}(-\sin\varphi_0, \cos\varphi_0, 0). \tag{3.35}$$

We can recover common basis choices such as linear polarisation, such that $\varphi_0 = 0$, $\alpha_1 = \alpha_2 = 0$ and $a = 0$ or 1 (illustrated in Figure 3.3b i),

$$\mathbf{e}_\text{x} = (1,0,0) \quad \text{and} \quad \mathbf{e}_\text{y} = (0,1,0), \tag{3.36}$$

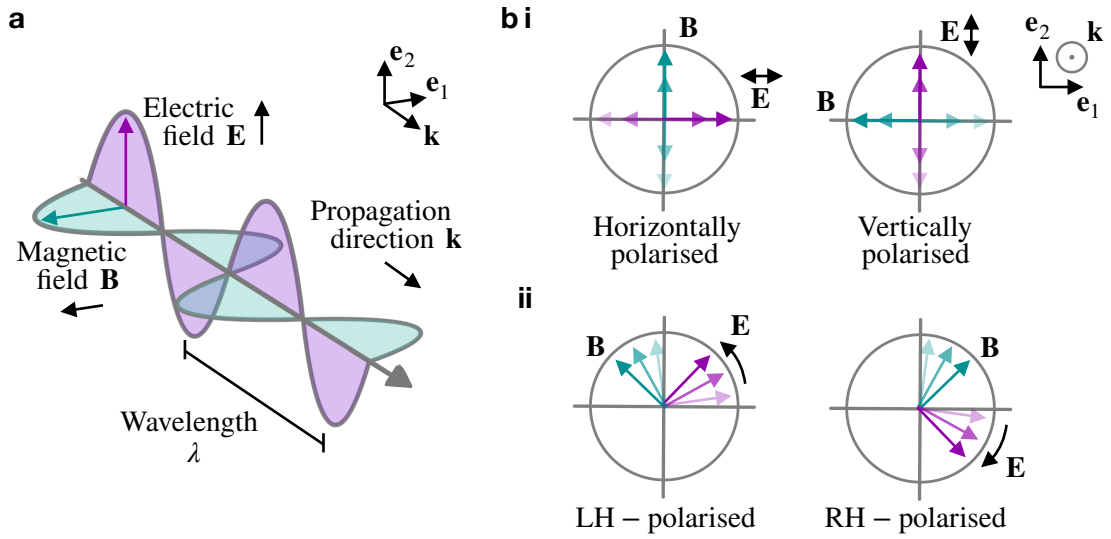

Figure 3.3: **The shape of light: (a)** A schematic of an electromagnetic wave and its components. **E** and **B** are perpendicular to each other, and lie in the plane perpendicular to **k**. This plane is described by two basis vectors, $\mathbf{e}_1$ and $\mathbf{e}_2$. Wavelength λ is measured between two adjacent wave maxima. **(b)** The polarisation of the light wave is described in terms of $\mathbf{e}_1$ and $\mathbf{e}_2$, which need not be orthogonal, but should be linearly independent. Common polarisation bases are **(i)** linear and **(ii)** circular polarisation.

or circular polarisation such that $a = 1/\sqrt{2}$, $\varphi_0 = 0$, $\alpha_1 = 0$ and $\alpha_2 = \pm\pi/2$ (illustrated in Figure 3.3b ii), and so

$$\mathbf{e}_{\mathrm{LH}} = \frac{1}{\sqrt{2}}(1, i, 0) \quad \text{and} \quad \mathbf{e}_{\mathrm{RH}} = \frac{1}{\sqrt{2}}(1, -i, 0). \tag{3.37}$$

There are many (in fact, infinite) polarisation basis vectors, but so long as two linearly independent vectors in the plane perpendicular to $\hat{\mathbf{k}}$ are chosen, the polarisation of the light can be fully described. We will come back to polarisation in Chapter 5, and will demonstrate that it is important when calculating the selection rules of TQDs interacting with light.

3.3 Quantisation of light

When dealing with electronic systems quantum-mechanically, it is often sufficient to use a semi-classical approach to describe their interactions with the electromagnetic field, such that the field is treated classically. However it will sometimes be necessary to describe a system in a purely quantum way, such that the electromagnetic field is also quantised. We will use this in Chapter 5. We will now cover the method of **second quantisation**[5] to describe the electromagnetic field in terms of photons.

[5] First quantisation describes the semi-classical treatment of quantum systems, in which the position and momentum of particles are quantised, but the surrounding environment (such as the electromagnetic field) is treated classically. In second quantisation, the fields are also quantised.

We have already done most of the groundwork needed to describe photons by writing the Fourier expanded form of $\mathbf{E}(\mathbf{r},t)$ and $\mathbf{B}(\mathbf{r},t)$ (given in Equations 3.29 and 3.30 in Section 3.2.2). Now we simply promote the Fourier coefficients $a_{\beta,\mathbf{k}}, a^*_{\beta,\mathbf{k}}$ to operators, and explicitly write the time-dependence (on the understanding that we choose to view the system in the **Heisenberg picture**[6] such that time-dependence is attached to the operators). We thus have that

$$a_{\beta,\mathbf{k}}(t) \to \sqrt{\frac{\hbar}{2\omega_{\mathbf{k}} V \epsilon_0}} a_{\beta,\mathbf{k}} e^{-i\omega_{\mathbf{k}} t}, \tag{3.38}$$

$$a^*_{\beta,\mathbf{k}}(t) \to \sqrt{\frac{\hbar}{2\omega_{\mathbf{k}} V \epsilon_0}} a^\dagger_{\beta,\mathbf{k}} e^{i\omega_{\mathbf{k}} t}. \tag{3.39}$$

The prefactor is chosen so that the Hamiltonian (and thus photon energy) has a simple form, which we will shortly illustrate. Also, although hats are often used to denote operators (e.g. $\hat{a}_{\beta,\mathbf{k}}$), the context should be clear from here onwards so I preemptively drop the hats to save on extra notation.

The operators obey the bosonic commutation relations given by

$$\left[a_{\beta,\mathbf{k}}, a^\dagger_{\beta',\mathbf{k}'}\right] = \delta_{\mathbf{k},\mathbf{k}'}\delta_{\beta,\beta'} \quad \text{and} \quad \left[a_{\beta,\mathbf{k}}, a_{\beta',\mathbf{k}'}\right] = \left[a^\dagger_{\beta,\mathbf{k}}, a^\dagger_{\beta',\mathbf{k}'}\right] = 0, \tag{3.40}$$

and act on photon states

$$|n_{\beta,\mathbf{k}}\rangle = \frac{1}{\sqrt{n_{\beta,\mathbf{k}}!}} \left(a^\dagger_{\beta,\mathbf{k}}\right)^{n_{\beta,\mathbf{k}}} |0\rangle, \tag{3.41}$$

(where $|0\rangle$ is the vacuum state) in the following way,

$$a_{\beta,\mathbf{k}}|n_{\beta,\mathbf{k}}\rangle = \sqrt{n_{\beta,\mathbf{k}}}|n_{\beta,\mathbf{k}}-1\rangle \quad \text{and} \quad a^\dagger_{\beta,\mathbf{k}}|n_{\beta,\mathbf{k}}\rangle = \sqrt{n_{\beta,\mathbf{k}}+1}|n_{\beta,\mathbf{k}}+1\rangle, \tag{3.42}$$

leading us to describe $a^\dagger_{\beta,\mathbf{k}}, a_{\beta,\mathbf{k}}$, as creation and annihilation operators respectively. Promoting the Hamiltonian (first given in Equation 3.31) of the system to its operator form, we see that

$$\mathbf{H}^{\text{rad}} = \sum_{\beta,\mathbf{k}} \hbar\omega_{\mathbf{k}} \left(a^\dagger_{\beta,\mathbf{k}} a_{\beta,\mathbf{k}} + \frac{1}{2}\right). \tag{3.43}$$

This is nothing but the Hamiltonian of a set of independent **quantum Harmonic oscil-**

[6] As opposed to the Schrödinger picture in which the state vectors evolve with time, or the interaction picture in which operators (and thus observables) as well as state vectors evolve with time.

lators. The quantised operator fields now become

$$\mathbf{A}(\mathbf{r},t) = \sum_{\beta,\mathbf{k}} \mathbf{A}_{\beta,\mathbf{k}}(\mathbf{r},t) = \sum_{\beta,\mathbf{k}} \sqrt{\frac{\hbar}{2\omega_{\mathbf{k}} V \epsilon_0}} \left[e^{i(\mathbf{k}\cdot\mathbf{r}-\omega_{\mathbf{k}}t)} a_{\beta,\mathbf{k}} \mathbf{e}_\beta + e^{-i(\mathbf{k}\cdot\mathbf{r}-\omega_{\mathbf{k}}t)} a^\dagger_{\beta,\mathbf{k}} \mathbf{e}^*_\beta \right], \tag{3.44}$$

$$\mathbf{E}(\mathbf{r},t) = \sum_{\beta,\mathbf{k}} \mathbf{E}_{\beta,\mathbf{k}}(\mathbf{r},t) = i \sum_{\beta,\mathbf{k}} \sqrt{\frac{\hbar\omega_{\mathbf{k}}}{2V\epsilon_0}} \left[e^{i(\mathbf{k}\cdot\mathbf{r}-\omega_{\mathbf{k}}t)} a_{\beta,\mathbf{k}} \mathbf{e}_\beta - e^{-i(\mathbf{k}\cdot\mathbf{r}-\omega_{\mathbf{k}}t)} a^\dagger_{\beta,\mathbf{k}} \mathbf{e}^*_\beta \right], \tag{3.45}$$

$$\begin{aligned} \mathbf{B}(\mathbf{r},t) &= \sum_{\beta,\mathbf{k}} \mathbf{B}_{\beta,\mathbf{k}}(\mathbf{r},t) \\ &= i \sum_{\beta,\mathbf{k}} \sqrt{\frac{\hbar\omega_{\mathbf{k}}}{2V\epsilon_0}} \left[e^{i(\mathbf{k}\cdot\mathbf{r}-\omega_{\mathbf{k}}t)} a_{\beta,\mathbf{k}} \left(\mathbf{k}\times\mathbf{e}_\beta\right) - e^{-i(\mathbf{k}\cdot\mathbf{r}-\omega_{\mathbf{k}}t)} a^\dagger_{\beta,\mathbf{k}} \left(\mathbf{k}\times\mathbf{e}^*_\beta\right) \right]. \end{aligned} \tag{3.46}$$

3.4 Light-matter interactions

Now that we have successfully quantised the electromagnetic field, we study **photon-mediated electronic transitions**. This topic is discussed in generality here (i.e. generic, discrete electronic states) and no boundary conditions specified on the electric field. This will then be used to address topological electronic systems in Chapters 5 and 6, both in free space and within a cavity.

3.4.1 The interaction Hamiltonian

For a single-electron system in a time-dependent electromagnetic field (with no free charges or currents), the Hamiltonian of the system (minus $\mathbf{H}^{\text{rad}}$ given in the previous subsection) is given by

$$\mathbf{H} = \frac{1}{2m_{\text{e}}} \left(\mathbf{p} + e\mathbf{A}(\mathbf{r},t)\right)^2 + V(\mathbf{r}), \tag{3.47}$$

where $\mathbf{p}$ is the momentum operator of the electron, $\mathbf{A}(\mathbf{r},t)$ is the electromagnetic vector potential described in Section 3.1 and $V(\mathbf{r})$ describes other potentials felt by the electron. Expanding this Hamiltonian, we find

$$\mathbf{H} = \mathbf{H}^{\text{elec}} + \mathbf{H}^{\text{int}} + \mathbf{H}^{\text{dia}}, \tag{3.48}$$

where

$$\mathbf{H}^{\text{elec}} = \frac{\mathbf{p}^2}{2m_{\text{e}}} + V(\mathbf{r}) \tag{3.49}$$

is the unperturbed Hamiltonian of the electron,

$$\mathbf{H}^{\text{int}} = \frac{e}{m_{\text{e}}} \mathbf{A}(\mathbf{r},t) \cdot \mathbf{p} \tag{3.50}$$

is the paramagnetic term describing the coupling of the atom to the electromagnetic field and

$$\mathbf{H}^{\text{dia}} = \frac{(e\mathbf{A}(\mathbf{r},t))^2}{2m_{\text{e}}} \tag{3.51}$$

is the diamagnetic term, which, as we are primarily interested in the absorption and emission of single photons, is taken to be negligible. $\mathbf{H}^{\text{int}}$ tells us about the strength and nature of the photon-mediated electronic transitions, where

$$\mathbf{H}^{\text{int}}_{\beta,\mathbf{k}}(\mathbf{r},t) = \frac{e}{m_{\text{e}}}\mathbf{A}_{\beta,\mathbf{k}}(\mathbf{r},t)\cdot\mathbf{p} \tag{3.52}$$

is specifically the Hamiltonian describing the atom interacting with radiation of polarisation β and momentum $\mathbf{k}$. Writing it out explicitly using Equation 3.44,

$$\mathbf{H}^{\text{int}}_{\beta,\mathbf{k}}(\mathbf{r},t) = \frac{e}{m_{\text{e}}}\sqrt{\frac{\hbar}{2\omega_{\mathbf{k}}V\epsilon_0}}\left[e^{i(\mathbf{k}\cdot\mathbf{r}-\omega_{\mathbf{k}}t)}\ a_{\beta,\mathbf{k}}\mathbf{e}_\beta\cdot\mathbf{p} + e^{-i(\mathbf{k}\cdot\mathbf{r}-\omega_{\mathbf{k}}t)}\ a^\dagger_{\beta,\mathbf{k}}\mathbf{e}^*_\beta\cdot\mathbf{p}\right]. \tag{3.53}$$

This Hamiltonian will act on the combined[7] state of the initial electronic and photonic states, $|\Psi_{\text{i}}\rangle\otimes|n_{\beta,\mathbf{k}}\rangle$ and bring it to a new state $|\Psi_{\text{f}}\rangle\otimes|n'_{\beta,\mathbf{k}}\rangle$, where there are initially $n_{\beta,\mathbf{k}}$ photons in mode $(\beta,\mathbf{k})$ and $n'_{\beta,\mathbf{k}}$ after the transition. The interaction is described by the expression $\langle\Psi_{\text{f}}|\otimes\langle n'_{\beta,\mathbf{k}}|\mathbf{H}^{\text{int}}_{\beta,\mathbf{k}}(\mathbf{r},t)|\Psi_{\text{i}}\rangle\otimes|n_{\beta,\mathbf{k}}\rangle$, and writing this out in full and separating into the electronic and photonic contributions, we have

$$\begin{aligned}&\frac{e}{m_{\text{e}}}\sqrt{\frac{\hbar}{2\omega_{\mathbf{k}}V\epsilon_0}}\langle\Psi_{\text{f}}|e^{i(\mathbf{k}\cdot\mathbf{r}-\omega_{\mathbf{k}}t)}\mathbf{e}_\beta\cdot\mathbf{p}|\Psi_{\text{i}}\rangle\langle n'_{\beta,\mathbf{k}}|a_{\beta,\mathbf{k}}|n_{\beta,\mathbf{k}}\rangle\\ &\quad+\frac{e}{m_{\text{e}}}\sqrt{\frac{\hbar}{2\omega_{\mathbf{k}}V\epsilon_0}}\langle\Psi_{\text{f}}|e^{-i(\mathbf{k}\cdot\mathbf{r}-\omega_{\mathbf{k}}t)}\mathbf{e}^*_\beta\cdot\mathbf{p}|\Psi_{\text{i}}\rangle\langle n'_{\beta,\mathbf{k}}|a^\dagger_{\beta,\mathbf{k}}|n_{\beta,\mathbf{k}}\rangle.\end{aligned} \tag{3.54}$$

For an electronic structure with centre of mass at $\mathbf{r}_0$ we can rewrite the spatial component of the exponential as

$$e^{i\mathbf{k}\cdot\mathbf{r}} = e^{i\mathbf{k}\cdot\mathbf{r}_0}e^{i\mathbf{k}\cdot(\mathbf{r}-\mathbf{r}_0)}. \tag{3.55}$$

For electronic structures whose spatial expanse is much smaller than the wavelength of irradiating light, $e^{i\mathbf{k}\cdot(\mathbf{r}-\mathbf{r}_0)} = 1 + i\mathbf{k}\cdot(\mathbf{r}-\mathbf{r}_0) + ... \approx 1$, and so $e^{i\mathbf{k}\cdot\mathbf{r}} \approx e^{i\mathbf{k}\cdot\mathbf{r}_0}$. This is the **electric dipole approximation** (E1). This simplification lets us move the exponential outside of the expectation value and rewrite the expectation value as[8]

$$\langle\Psi_{\text{f}}|\mathbf{e}_\beta\cdot\mathbf{p}|\Psi_{\text{i}}\rangle = im_{\text{e}}\omega_{\text{i,f}}\langle\Psi_{\text{f}}|\mathbf{e}_\beta\cdot\mathbf{r}|\Psi_{\text{i}}\rangle, \tag{3.56}$$

[7] The combined state is described using the tensor product, $\otimes$, outlined in Appendix A.2.
[8] Using that $[\mathbf{r},\mathbf{H}^{\text{elec}}] = i\hbar\mathbf{p}/m_{\text{e}}$

where $\omega_{\mathrm{i,f}} = (E_{\mathrm{f}} - E_{\mathrm{i}})/\hbar$. We find it convenient to define the **matrix element**

$$V_{\mathrm{i,f},\beta} = \langle \Psi_{\mathrm{f}} | \mathbf{e}_\beta \cdot \mathbf{r} | \Psi_{\mathrm{i}} \rangle. \tag{3.57}$$

By noting the relationship between $\mathbf{A}_{\beta,\mathbf{k}}(\mathbf{r},t)$ and $\mathbf{E}_{\beta,\mathbf{k}}(\mathbf{r},t)$ (Equations 3.44 and 3.45 respectively), the interaction in the electric dipole approximation can then be described by

$$\begin{aligned} &\langle \Psi_{\mathrm{f}} | \otimes \langle n'_{\beta,\mathbf{k}} | \mathbf{H}^{\mathrm{int}}_{\beta,\mathbf{k}}(\mathbf{r},t) | \Psi_{\mathrm{i}} \rangle \otimes | n_{\beta,\mathbf{k}} \rangle \\ &\qquad = \frac{e}{m_{\mathrm{e}}} \langle \Psi_{\mathrm{f}} | \otimes \langle n'_{\beta,\mathbf{k}} | \mathbf{A}_{\beta,\mathbf{k}}(\mathbf{r},t) \cdot \mathbf{p} | \Psi_{\mathrm{i}} \rangle \otimes | n_{\beta,\mathbf{k}} \rangle \qquad (3.58) \\ &\qquad \approx -e \frac{\omega_{\mathrm{i,f}}}{\omega_{\mathbf{k}}} \langle \Psi_{\mathrm{f}} | \otimes \langle n'_{\beta,\mathbf{k}} | \mathbf{E}_{\beta,\mathbf{k}}(\mathbf{r}_0,t) \cdot \mathbf{r} | \Psi_{\mathrm{i}} \rangle \otimes | n_{\beta,\mathbf{k}} \rangle. \qquad (3.59) \end{aligned}$$

In the limit of perfect resonance such that $\omega_{\mathrm{i,f}} = \omega_{\beta,\mathbf{k}}$, this leads to the rather nice approximation that

$$\mathbf{H}^{\mathrm{int}}_{\beta,\mathbf{k}}(\mathbf{r},t) \approx -e\mathbf{E}_{\beta,\mathbf{k}}(\mathbf{r}_0,t) \cdot \mathbf{r}. \tag{3.60}$$

For certain situations (such as cavities, as will be covered in Chapter 5), we should be cautious as the resonance condition is not necessarily fulfilled. Generally, I work in the electric dipole approximation for the research areas of this thesis as this is the dominant regime for processes in which we are interested (as we will see in Chapter 5). For discussion of interactions beyond E1, see Appendix B.4.

3.4.2 Transitions

The parts of the expression in Equation 3.54 pertaining to the photonic states are the expectation values $\langle n'_{\beta,\mathbf{k}} | a_{\beta,\mathbf{k}} | n_{\beta,\mathbf{k}} \rangle$ and $\langle n'_{\beta,\mathbf{k}} | a^\dagger_{\beta,\mathbf{k}} | n_{\beta,\mathbf{k}} \rangle$, where $a^\dagger_{\beta,\mathbf{k}}(a_{\beta,\mathbf{k}})$ were defined in Section 3.3. For a given $n_{\beta,\mathbf{k}}$, the only non-zero expectation values will be for $n'_{\beta,\mathbf{k}} = n_{\beta,\mathbf{k}} \pm 1$.

For $|n_{\beta,\mathbf{k}}\rangle \to \sqrt{n_{\beta,\mathbf{k}}} |n_{\beta,\mathbf{k}} - 1\rangle$, a photon is removed from mode $(\beta,\mathbf{k})$ and its energy is absorbed by the electronic system, resulting in the excitation of the electronic system to a higher energy, as illustrated in Figure 3.4a. This process is **stimulated absorption**. If there are zero photons in mode $(\beta,\mathbf{k})$ such that $n_{\beta,\mathbf{k}} = 0$, this process cannot occur. For $|n_{\beta,\mathbf{k}}\rangle \to \sqrt{n_{\beta,\mathbf{k}}+1} |n_{\beta,\mathbf{k}}+1\rangle$, in the presence of a photon in mode $(\beta,\mathbf{k})$ a photon with the same momentum, polarization and phase[9] is created, increasing the number of photons in that mode by 1. The increase in energy of the photon field is transferred from the electronic system, which undergoes a loss of energy. This process is called **stimulated emission** and is illustrated in Figure 3.4b i. Unlike absorption processes, an emission process can occur even if $n_{\beta,\mathbf{k}} = 0$. This process is known as **spontaneous emission** (see Figure 3.4b ii) and

[9] As the creation and annihilation operators are non-hermitian, their eigenvalues are in general complex, such that $a|\varphi\rangle = \xi|\varphi\rangle$ where $\xi = |\xi|e^{i\vartheta}$. Stimulated processes necessarily involve photons with the same phase, and as the phase does not appear in observables of interest in this thesis, we acknowledge its existence and then conveniently ignore it.

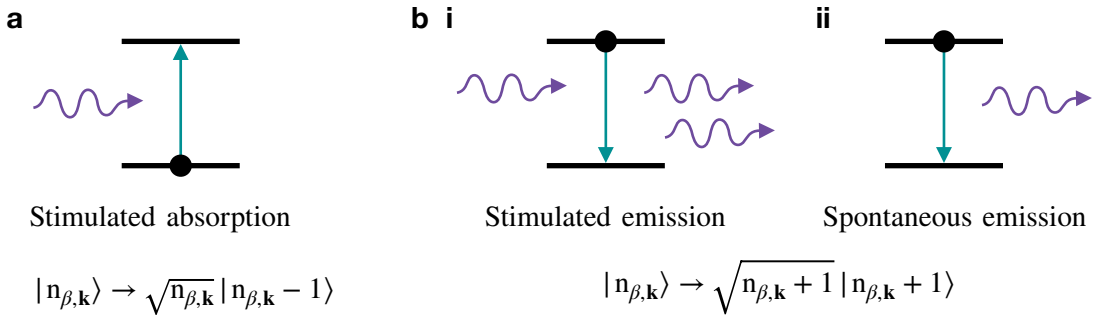

Figure 3.4: **Absorption and emission events: (a) Stimulated absorption**, in which a photon is absorbed, causing the electronic system to be excited to a higher energy corresponding to the energy of the absorbed photon. **(b i) Stimulated emission**, in which an incoming photon interacts with the electron system, triggering the emission of a photon with the same momentum and polarisation of the original photon. **(ii) Spontaneous emission**, in which a photon is emitted with random direction and polarisation.

it should be highlighted that unlike photons which are emitted via a stimulated process, spontaneously emitted photons are emitted with random direction and phase.

3.4.3 Calculating transition rates

We have so far described which types of transitions can occur, but we are also very much interested in how quickly these transitions occur. We thus now discuss how to calculate the transition rates for **photon-mediated electronic transitions**. The rate of transition, $\Gamma_{i\rightarrow f,\beta,\mathbf{k}}$, between two electronic states, $|\Psi_i\rangle \rightarrow |\Psi_f\rangle$, facilitated by radiation of polarisation β and momentum $\mathbf{k}$ is given by

$$\frac{d}{d\omega}\Gamma_{i\rightarrow f,\beta,\mathbf{k}} = \frac{2\pi}{\hbar^2} S_{i,f,\beta,\mathbf{k}}(\omega)\delta(\omega-\omega_{i,f}), \tag{3.61}$$

where $S_{i,j,\beta,\mathbf{k}}(\omega)$ is the **spectral density**. The spectral density is defined using either the power or energy spectral density, depending on the nature of the system being studied. The spectral density describes the frequency-dependent coupling of the electronic states with the electromagnetic field. This method has a similar spirit to work on quantum systems coupled to noise [151, 152], and gives a compelling interpretation of the continuum of electromagnetic states acting as a quantum noise source. I feel this gives a complementary insight on **quantum electrodynamics** [149, 153] which is rarely covered in standard courses. This method also allows us to calculate transition rates in both vacuum and cavities with the same method, while treating both the spatial and temporal components of the fields rigorously.[10]

[10]Fermi's golden rule offers an alternative path to calculating transition rates, tying in nicely with the concept of the DOS covered in Section 3.7. However, as discussed in Appendix B.5, transition rates with spatial dependence do not always simplify nicely into the form of Fermi's golden rule, giving additional motivation for employing the method of spectral densities instead.

Note that the δ-function in Equation 3.61 ensures conservation of energy, where $\hbar\omega_{\mathrm{i,f}} = E_{\mathrm{f}} - E_{\mathrm{i}}$ is the energy difference between the two electronic states. For multi-fermionic electronic states, this rate assumes that the initial state is occupied and final state is unoccupied, otherwise Fermi-blocking prevents the transition. The physical effect of this on rate equations and photon-mediated multi-electron dynamics is commented on in Section 3.5, and multi-level electron systems interacting via the electromagnetic field are discussed in much more detail in Chapter 5.

For **steady-state** electric fields (i.e. energy held by the electric field is not being lost from the system), we are interested in the **power spectral density**, such that

$$S_{\mathrm{i,f},\beta,\mathbf{k}}(\omega) = \lim_{T\to\infty} \frac{1}{T} \left| \langle \Psi_{\mathrm{f}}| \otimes \langle n'_{\beta,\mathbf{k}}| \tilde{\mathbf{H}}^{\mathrm{int}}_{\beta,\mathbf{k}}(\mathbf{r},\omega) |\Psi_{\mathrm{i}}\rangle \otimes |n_{\beta,\mathbf{k}}\rangle \right|^2, \tag{3.62}$$

where

$$\tilde{\mathbf{H}}^{\mathrm{int}}_{\beta,\mathbf{k}}(\mathbf{r},\omega) = \frac{1}{\sqrt{2\pi}} \int_{-\frac{T}{2}}^{\frac{T}{2}} \mathbf{H}^{\mathrm{int}}_{\beta,\mathbf{k}}(\mathbf{r},t) e^{i\omega t} dt \tag{3.63}$$

and there are initially $n_{\beta,\mathbf{k}}$ photons in mode $(\beta,\mathbf{k})$, and $n'_{\beta,\mathbf{k}}$ after the transition.

For **transient** electric fields, such as an electric field confined to an imperfect cavity with a cavity timescale τ_{cav}, we work with the **energy spectral density** of the field, given by

$$S_{\mathrm{i,f},\beta,\mathbf{k}}(\omega) = \frac{1}{\tau_{\mathrm{cav}}} \left| \langle \Psi_{\mathrm{f}}| \otimes \langle n'_{\beta,\mathbf{k}}| \tilde{\mathbf{H}}^{\mathrm{int}}_{\beta,\mathbf{k}}(\mathbf{r},\omega) |\Psi_{\mathrm{i}}\rangle \otimes |n_{\beta,\mathbf{k}}\rangle \right|^2. \tag{3.64}$$

The characteristic timescale of the system is τ_{cav}, rather than T (in the limit that $T \to \infty$) as in free-space. Equations 3.62 and 3.64 are very general expressions, and we will use them explicitly in Chapter 5 for TI nanostructure states interacting with light.

It is crucial to note that the spectral densities, and thus transition rates of stimulated processes will be proportional to the number of photons, $n_{\beta,\mathbf{k}}$, present at the required frequency, whereas spontaneous emission is unaffected by photon density. This will be demonstrated and used in Chapter 5.

3.5 Lasing

The aim of **lasing**[11] is the production of multiple photons of the same momentum, polarisation and phase (i.e. **coherent photons**). Invented in 1960[12], traditional lasers use an external pump to excite electrons within the atoms of a lasing material — usually a gas, crystal, or semiconductor. With strong enough pumping, more electrons are in the

[11] The word **laser** is an acronym, standing for **l**ight **a**mplification by **s**timulated **e**mission of **r**adiation.

[12] The first laser was built in 1960 by Theodore H. Maiman at Hughes Research Laboratories, based on theoretical work by Charles Hard Townes and Arthur Leonard Schawlow [154, 155].

excited state than the ground state, such that **population inversion** is achieved. When one of these excited electrons falls back to its original state it spontaneously emits a photon, which in turn stimulates another excited electron to emit a photon, and so on. An effect can be achieved in which stimulated emission outpaces spontaneous emission and almost all photons produced are coherent. Unlike the spreading beams of an incoherent source, the photons in a laser emerge in a tightly packed stream with a single frequency. **Spatial coherence** allows a laser to be focused to a tight spot, enabling applications such as laser cutting [156] and lithography [157]. Spatial coherence also allows a laser beam to stay narrow over great distances (collimation), enabling applications such as laser pointers and lidar [158]. Lasers can also have high **temporal coherence**, emitting light with a very narrow spectrum (so narrow that they can emit a single colour of light). Alternatively, temporal coherence can be used to produce broad-spectrum pulses of light with durations as short as a femtosecond[13] (known as ultrashort pulses).

Lasers are ubiquitous in modern technologies. Most lasers currently in commercial use operate in the **infrared** (300 GHz[14] - 430 THz) or **visible** range (400-790 THz), as these energy scales are naturally accessible in electronic systems. Their applications can be found in electronic equipment [159–161], communication technologies [162], bio-medical and dentistry applications [163–165], manufacturing [166, 167], military [168] and law enforcement devices [169–171].

In order to understand the dynamics leading to lasing, we will study the rate equations governing discrete electronic energy levels coupled by light. The transition rates by which electrons are excited between levels can be calculated as per Section 3.4.3, specific to the electronic system in question.

Let us say we have N two-level electronic systems, each with a single electron. The ground state has energy E_1 and occupation N_1, and the excited state has energy E_2 and occupation N_2, where $N = N_1 + N_2$. The system is illustrated in Figure 3.5a i. We pump the system via a resonant transition, where $\hbar\omega_{2,1} = E_2 - E_1$, via a constant bath of photons with frequency $\omega_{2,1}$. We wish to find the condition for **lasing** in this system, such that stimulated emission overcomes spontaneous emission.

The time-evolution of the occupation of the states can be found from

$$\frac{dN_2}{dt} = -N_2\Gamma^{\text{spon}}_{2\to1} - \Gamma^{\text{stim}}_{2\to1}(N_2 - N_1), \tag{3.65}$$

$$\frac{dN_1}{dt} = -\frac{dN_2}{dt}, \tag{3.66}$$

where we have used that $\Gamma^{\text{stim}}_{2\to1} = \Gamma^{\text{abs}}_{1\to2}$ and the constraint that $N = N_1 + N_2$, is constant. The second equation is simply the statement that N is constant. Focusing on the first of

[13] A femtosecond is 10^{-15}s.
[14] Giga = 10^9.

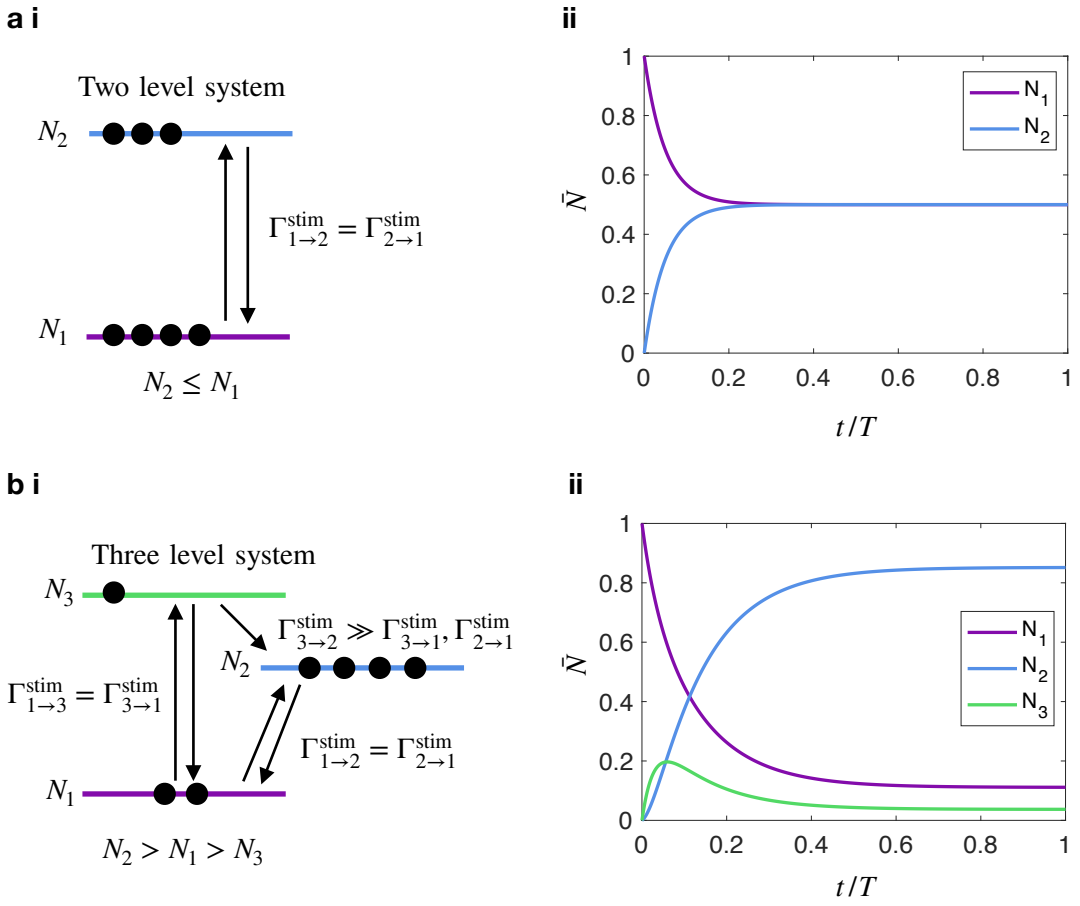

Figure 3.5: **Lasing:** **(a)** A two level system such as **(i)** cannot reach population inversion, but at most can reach equal occupancy of its two levels as demonstrated in **(ii)** the time evolution of the system, where at steady-state $N_2 = N_1$. **b** For a three level system as shown in **(i)**, if $\Gamma^{stim}_{3\to2} \gg \Gamma^{stim}_{3\to1}, \Gamma^{stim}_{2\to1}$ it is possible to reach population inversion such that $N_2 > N_1$. Spontaneous emission is considered negligible for both systems.

the two equations, for stimulated emission to dominate over spontaneous emission we need that

$$\Gamma_{2\to1}^{\text{stim}}(N_2 - N_1) > N_2\Gamma_{2\to1}^{\text{spon}}, \tag{3.67}$$

and so

$$\frac{N_2 - N_1}{N_2} > \frac{\Gamma_{2\to1}^{\text{spon}}}{\Gamma_{2\to1}^{\text{stim}}}. \tag{3.68}$$

Generally $\Gamma_{2\to1}^{\text{spon}} \ll \Gamma_{2\to1}^{\text{stim}}$, such that

$$\frac{N_2 - N_1}{N_2} \gtrapprox 0, \tag{3.69}$$

and so the condition for lasing is simply **population inversion**, such that $N_2 - N_1 > 0$. This is intuitive - the stimulated absorption and emission rates are equal, and so for stimulated photons to be emitted more than absorbed, the excited state needs a higher occupation than the ground state. Note that this is a necessary but not sufficient condition for lasing - a feedback mechanism such as a cavity is needed, so that coherent photons remain in the system at a time-scale which allows them to trigger subsequent stimulated processes. This idea is discussed heavily in Chapter 5. Population inversion does not occur naturally in thermal equilibrium (as will be revisited in Chapter 5) and so a mechanism for population inversion (such as pumping) is needed.

At steady-state, the occupation of the energy levels N_0^1 and N_0^2 is constant, such that

$$\frac{dN_2^0}{dt} = -N_2^0\Gamma_{2\to1}^{\text{spon}} - \Gamma_{2\to1}^{\text{stim}}(N_2^0 - N_1^0) = 0, \tag{3.70}$$

$$\frac{dN_1^0}{dt} = -\frac{dN_2^0}{dt} = 0. \tag{3.71}$$

Rearranged, the first equation gives us the steady-state relation

$$N_2^0 = N_1^0\frac{\Gamma_{2\to1}^{\text{stim}}}{\Gamma_{2\to1}^{\text{spon}} + \Gamma_{2\to1}^{\text{stim}}}, \tag{3.72}$$

and so it follows that $N_2^0 \leq N_1^0$.

This result means that **we cannot achieve steady-state population inversion in a two level system**. The upper-limit of the dynamics (for which $N_2^0 = N_1^0$) is given in Figure 3.5a ii.

We now repeat the same procedure for a three-level system, in which the third (and highest) energy level, E_3, is metastable, and so electrons undergo a fast, non-radiative decay to level E_2. We pump from energy level E_1 and aspire to lase between energy levels E_2 and E_1. This system is given diagrammatically in Figure 3.5b i. The rate equations for occupation

of the three levels are given by

$$\frac{dN_3}{dt} = -N_3\left(\Gamma_{3\to2}^{\text{non-rad}} + \Gamma_{3\to1}^{\text{spon}}\right) + \Gamma_{3\to1}^{\text{stim}}(N_1 - N_3), \tag{3.73}$$

$$\frac{dN_2}{dt} = -N_2\Gamma_{2\to1}^{\text{spon}} - (N_2 - N_1)\Gamma_{2\to1}^{\text{stim}} + N_3\Gamma_{3\to2}^{\text{non-rad}}, \tag{3.74}$$

$$\frac{dN_1}{dt} = N_3\Gamma_{3\to1}^{\text{spon}} + N_3\Gamma_{3\to1}^{\text{stim}} + N_2\Gamma_{2\to1}^{\text{spon}} - N_1\Gamma_{3\to1}^{\text{stim}} - N_1\Gamma_{2\to1}^{\text{stim}} + N_2\Gamma_{2\to1}^{\text{stim}}. \tag{3.75}$$

As before, we assume a bath of photons at the pumping frequency $\omega_{3,1}$, and feedback in the lasing frequency $\omega_{2,1}$ (i.e. we assume the electronic structure is in a cavity, tuned to resonance with the lasing frequency). At steady state,

$$0 = -N_3^0\left(\Gamma_{3\to2}^{\text{non-rad}} + \Gamma_{3\to1}^{\text{spon}}\right) + \Gamma_{3\to1}^{\text{stim}}(N_1^0 - N_3^0), \tag{3.76}$$

$$0 = -N_2^0\Gamma_{2\to1}^{\text{spon}} - (N_2^0 - N_1^0)\Gamma_{2\to1}^{\text{stim}} + N_3^0\Gamma_{3\to2}^{\text{non-rad}}, \tag{3.77}$$

$$0 = N_3^0\Gamma_{3\to1}^{\text{spon}} + N_3^0\Gamma_{3\to1}^{\text{stim}} + N_2^0\Gamma_{2\to1}^{\text{spon}} - N_1^0\Gamma_{3\to1}^{\text{stim}} - N_1^0\Gamma_{2\to1}^{\text{stim}} + N_2^0\Gamma_{2\to1}^{\text{stim}}. \tag{3.78}$$

We assume that at steady state, spontaneous processes are much slower than stimulated processes, such that

$$N_3^0\Gamma_{3\to2}^{\text{non-rad}} = \Gamma_{3\to1}^{\text{stim}}(N_1^0 - N_3^0), \tag{3.79}$$

$$(N_2^0 - N_1^0)\Gamma_{2\to1}^{\text{stim}} = N_3^0\Gamma_{3\to2}^{\text{non-rad}}, \tag{3.80}$$

$$(N_2^0 - N_1^0)\Gamma_{2\to1}^{\text{stim}} = (N_1^0 - N_3^0)\Gamma_{3\to1}^{\text{stim}}. \tag{3.81}$$

From the first equation, $N_1^0 \geq N_3^0$, and so it follows from the third equation that $N_2^0 \geq N_1^0$. We thus immediately find the hierarchy that $N_2^0 \geq N_1^0 \geq N_3^0$. For optimal population inversion in the lasing transition (such that $N_2^0 - N_1^0$ is maximal, with the constraint that $N = N_1^0 + N_2^0 + N_3^0$), we need that

$$\Gamma_{3\to2}^{\text{non-rad}} \gg \Gamma_{3\to1}^{\text{stim}}, \Gamma_{2\to1}^{\text{stim}}, \tag{3.82}$$

and thus N_3^0 is as low as possible, such that $N_2^0 > N_1^0 \gg N_3^0$. From the third equation, to obtain increasingly better population inversion, $\Gamma_{3\to1}$ must be increased, thus pumping the system with increased intensity. In Figure 3.5a ii I have plotted an exemplary 3-level system for which population inversion is achieved between E_2 and E_1.

As already emphasised, population inversion is **necessary but not sufficient** for lasing. Rates for stimulated processes rely on the number of coherent photons present at the lasing frequency, via the relation $\Gamma_{2\to1}^{\text{stim}} = cn_{1,2}\sigma_{2\to1}$, where $\sigma_{2\to1}$ is the **interaction cross-section**[15], and the number of coherent photons is time-varying. We must also assume the system is in a cavity, such that a feedback mechanism (such as mirrors) is present to allow the photons to re-interact with the electronic structure once emitted. The system will never

[15]This is simple to derive, and is given in Appendix B.6.

be completely perfect, and as such there will be losses - some losses are even necessary for lasing, otherwise coherent photons would never be emitted from the system to produce a functional laser. We measure the losses by the cavity life-time, τ_{cav}, and can also include intrinsic losses such as absorption by the cavity walls, quantified by α. The rate of change of coherent photon number can then be described by

$$\frac{dn_{1,2}}{dt} = \Gamma_{2\to1}^{\text{stim}}\left(N_2 - N_1\right) - \frac{n_{1,2}}{\tau_{\text{cav}}} - \alpha\, n_{1,2} \tag{3.83}$$

$$= n_{1,2}\left[c\,\sigma_{2\to1}\left(N_2 - N_1\right) - \frac{1}{\tau_{\text{cav}}} - \alpha\right], \tag{3.84}$$

For a constant or increasing number of coherent photons,

$$\sigma_{2\to1}(N_2 - N_1) \geq \frac{1}{c\tau_{\text{cav}}} + \frac{\alpha}{c}, \tag{3.85}$$

which for a perfect cavity (such that $\tau_{\text{cav}} \to \infty$) and no intrinsic losses, would reduce to the minimal condition of population inversion. We thus define a better metric to measure for lasing, called **gain**, defined as

$$G = \sigma_{2\to1}(N_2 - N_1). \tag{3.86}$$

For no population inversion, G is negative. The **threshold for lasing** is given by

$$G_{\text{th}} = \frac{1}{c\tau_{\text{cav}}} + \frac{\alpha}{c}. \tag{3.87}$$

The systems used to demonstrate the concepts of lasing in this section have comprised ensembles of N, non-interacting single-electron systems. Complications arise for multiple electrons within a single set of energy levels, and either fermionic density equations or a numerical method will need to used in order to include Pauli-blocking[16], however the general definitions and concepts remain the same. This will be covered more in Chapter 5.

3.6 Green's functions

Green's functions[17] are an incredibly important and useful concept. In electromagnetism problems, we solve differential equations with varying initial conditions, boundary conditions and geometries. The method of Green's functions allows us to solve certain types of differential equations that often crop up in electromagnetic systems, and we will rely on this method in Chapter 6. Resources I find indispensable for the topic of Green's functions

[16] Pauli blocking is the phenomenon by which fermionic particles such as electrons cannot transition to a state which is already occupied.

[17] Named for George Green, who was the first person to create a mathematical theory of electricity and magnetism, amongst other achievements in maths and physics.

include [147, 172–174], and other useful references are given by [175–178]. We start by covering the mathematical basis of Green's functions.

3.6.1 The mathematics of Green's functions

We can write a general, inhomogeneous linear differential equation as

$$\mathcal{L}\ \mathcal{A}(\mathbf{r}) = \mathcal{B}(\mathbf{r}), \tag{3.88}$$

where $\mathcal{A}(\mathbf{r})$ is a vector field, $\mathcal{B}(\mathbf{r})$ is a known **source** function, and $\mathcal{L}$ is a **linear differential operator** representing the unknown **response** of the system. The general solution of this differential equation is given by the sum of the homogeneous solution (found by solving the equation when $\mathcal{B}(\mathbf{r}) = 0$), and a particular inhomogeneous solution. By assuming that the homogeneous solution (which we denote $\mathcal{A}_0(\mathbf{r})$) is already known, our mission is to find an arbitrary, particular solution to Equation 3.88. To do so, we begin by studying the simple inhomogeneous case

$$\mathcal{L}\ \mathbf{G}_{\mathrm{i}}(\mathbf{r}, \mathbf{r}') = \mathbf{n}_{\mathrm{i}}\ \delta(\mathbf{r} - \mathbf{r}') \qquad (\mathrm{i} = x, y, z), \tag{3.89}$$

where $\mathbf{n}_{\mathrm{i}}$ is an arbitrary, constant unit vector. We can write these three equations compactly as a single equation, by introducing the concept of **dyads**. A **dyad** is a quantity that has magnitude and two associated directions.[18] We introduce the **dyadic Green's function**,[19] $\underline{\mathbf{G}}(\mathbf{r}, \mathbf{r}')$, and rewrite Equation 3.89 as

$$\mathcal{L}\ \underline{\mathbf{G}}(\mathbf{r}, \mathbf{r}') = \underline{\mathbb{I}}\ \delta(\mathbf{r} - \mathbf{r}'), \tag{3.90}$$

where $\mathcal{L}$ acts on each column of $\underline{\mathbf{G}}(\mathbf{r}, \mathbf{r}')$ separately, and $\underline{\mathbb{I}}$ is the **unit dyad**. We post-multiply both sides of Equation 3.90 by $\mathcal{B}(\mathbf{r}')$, and integrate both sides over a volume V, such that

$$\int_V dV'\ \mathcal{L}\ \underline{\mathbf{G}}(\mathbf{r}, \mathbf{r}')\mathcal{B}(\mathbf{r}') = \int_V dV' \delta(\mathbf{r} - \mathbf{r}')\mathcal{B}(\mathbf{r}'). \tag{3.91}$$

The right-hand side can be identified as $\mathcal{B}(\mathbf{r})$, and so recalling from Equation 3.88 that $\mathcal{B}(\mathbf{r}) = \mathcal{L}\ \mathcal{A}(\mathbf{r})$, we can write

$$\mathcal{L}\ \mathcal{A}(\mathbf{r}) = \int_V dV'\ \mathcal{L}\ \underline{\mathbf{G}}(\mathbf{r}, \mathbf{r}')\mathcal{B}(\mathbf{r}'). \tag{3.92}$$

By taking the operator $\mathcal{L}$ out of the integral on the right-hand side,[20] the solution of Equation 3.88 can be written as

[18] I give a little more information on dyads in Appendix A.3.

[19] A **dyadic** is the sum of dyads.

[20] If $\underline{\mathbf{G}}(\mathbf{r}, \mathbf{r}')$ is singular at the point $= \mathbf{r} - \mathbf{r}'$ we should be cautious of simply extracting $\mathcal{L}$ from the integral and this subtlety is discussed more in Reference [174]. This issue can largely be ignored by only considering field points $\mathbf{r}$ sensibly far away from the source point, $\mathbf{r}$', such that the volume of integration does not include $\mathbf{r}'$.

$$\mathcal{A}(\mathbf{r}) = \int_V dV' \, \underline{\mathbf{G}}(\mathbf{r}, \mathbf{r}')\mathcal{B}(\mathbf{r}'). \tag{3.93}$$

With Equation 3.93 giving the solution of the differential equation, $\mathcal{A}(\mathbf{r})$, in terms of $\underline{\mathbf{G}}(\mathbf{r}, \mathbf{r}')$ and $\mathcal{B}(\mathbf{r}')$, our task has now been diverted to that of finding the Green's function which solves Equation 3.90 for the particular linear differential operator, $\mathcal{L}$ of the problem at hand. The next sections are devoted to the discussion of how this can be applied to problems in electromagnetism.

3.6.2 Deriving the Green's function for the electric field

We now derive the Green's function for the electric field. It is convenient to work with the vector potential $\mathbf{A}(\mathbf{r}, t)$ and scalar potential $\Phi(\mathbf{r}, t)$. We recall from Section 3.2 that

$$\mathbf{B}(\mathbf{r}, t) = \nabla \times \mathbf{A}(\mathbf{r}, t), \tag{3.94}$$

$$\mathbf{E}(\mathbf{r}, t) = -\nabla\Phi(\mathbf{r}, t) - \frac{\partial \mathbf{A}(\mathbf{r}, t)}{\partial t}. \tag{3.95}$$

Using these expressions, the linear constitutive relations, and assuming the usual time-harmonic vector potential (such that $\mathbf{A}(\mathbf{r}, t) = \mathbf{A}(\mathbf{r})e^{i\omega_{\mathbf{k}}t} + \mathbf{A}^*(\mathbf{r})e^{-i\omega_{\mathbf{k}}t}$), Ampere's law (Equation 3.4) reduces to

$$\nabla \times (\nabla \times \mathbf{A}(\mathbf{r})) = \mu \, \mathbf{J}(\mathbf{r}) - i\omega_{\mathbf{k}}\mu\epsilon \left[i\omega_{\mathbf{k}}\mathbf{A}(\mathbf{r}) - \nabla\Phi(\mathbf{r})\right]. \tag{3.96}$$

We choose to work in the Lorenz gauge[21], such that $\nabla \cdot \mathbf{A}(\mathbf{r}) = i\omega_{\mathbf{k}}\mu\epsilon\Phi(\mathbf{r})$. Using this gauge condition and the mathematical identity $\nabla \times \nabla \times f(\mathbf{r}) = -\nabla^2 f(\mathbf{r}) + \nabla\left(\nabla \cdot f(\mathbf{r})\right)$, we can rewrite Equation 3.96 as

$$\left[\nabla^2 + k^2\right] \mathbf{A}(\mathbf{r}) = -\mu \, \mathbf{J}_{\mathrm{f}}(\mathbf{r}). \tag{3.97}$$

This is the inhomogeneous **Helmholtz equation**[22], where $k^2 = |\mathbf{k}|^2 = \omega_{\mathbf{k}}^2\mu\epsilon/c^2$, and $\nabla^2 + k^2$ is the Helmholtz operator. We can derive a similar equation for the scalar potential $\Phi(\mathbf{r})$, such that

$$\left[\nabla^2 + k^2\right] \Phi(\mathbf{r}) = -\frac{\rho(\mathbf{r})}{\epsilon}. \tag{3.98}$$

[21] See Appendix B.3 for a short discussion of gauge choices.

[22] Hermann von Helmholtz was a physicist with broad-ranging scientific interests. He made contributions in many fields, from physiology to physics, publishing on topics reaching from the philosophy of science to optics, including the mathematics of the eye and vision.

We now have four Helmholtz equations (as Equation 3.97 holds independently for all three components of $\mathbf{A}(\mathbf{r})$), of the form

$$\left[\nabla^2 + k^2\right] f(\mathbf{r}) = -g(\mathbf{r}). \tag{3.99}$$

To obtain the **scalar Green's function** $G_0(\mathbf{r}, \mathbf{r}')$, we replace the source term by a single point source and find

$$\left[\nabla^2 + k^2\right] G_0(\mathbf{r}, \mathbf{r}') = -\delta(\mathbf{r} - \mathbf{r}'). \tag{3.100}$$

In free space, the only physical solution is

$$G_0(\mathbf{r}, \mathbf{r}') = \frac{e^{\pm ik|\mathbf{r}-\mathbf{r}'|}}{4\pi|\mathbf{r} - \mathbf{r}'|}. \tag{3.101}$$

Physically, this is a spherical wave propagating away from or towards the origin. We can then directly find the vector potential from

$$\mathbf{A}(\mathbf{r}) = \mu \int_V dV' \ \mathbf{J}(\mathbf{r}')G_0(\mathbf{r}, \mathbf{r}'). \tag{3.102}$$

A similar expression holds for $\Phi(\mathbf{r})$, with both expressions requiring knowledge of $G_0(\mathbf{r}, \mathbf{r}')$. We can thus calculate the vector and scalar potential for any known current distribution and charge distribution. The particular form of $G_0(\mathbf{r}, \mathbf{r}')$ in Equation 3.101 is for 3D homogeneous space, and will take a different form in 2D space or a half-space.

From here, we can use $\mathbf{A}(\mathbf{r})$ and $\Phi(\mathbf{r})$ to find $\mathbf{E}(\mathbf{r})$ and $\mathbf{B}(\mathbf{r})$. Working with $\mathbf{A}(\mathbf{r})$ and $\Phi(\mathbf{r})$ was straightforward as we could use scalar quantities. If we wish to solve directly for the electric field, we must now use the dyadic Green's function. The wave equation for the electric field is given by

$$\nabla \times \nabla \times \mathbf{E}(\mathbf{r}) = -k^2 \mathbf{E}(\mathbf{r}) = i\omega_{\mathbf{k}}\mu \ \mathbf{J}(\mathbf{r}). \tag{3.103}$$

For each component of $\mathbf{J}(\mathbf{r})$ we can define a Green's function, such that for $i = (x, y, z)$,

$$\nabla \times \nabla \times \mathbf{G}_i(\mathbf{r}, \mathbf{r}') = -k^2 \ \mathbf{G}_i(\mathbf{r}, \mathbf{r}') = \mathbf{n}_i \delta(\mathbf{r} - \mathbf{r}'). \tag{3.104}$$

Combining all three components into a compact form using the dyadic Green's function, we have

$$\nabla \times \nabla \times \underline{\mathbf{G}}(\mathbf{r}, \mathbf{r}') = -k^2 \ \underline{\mathbf{G}}(\mathbf{r}, \mathbf{r}') = \underline{\mathbb{I}} \ \delta(\mathbf{r} - \mathbf{r}'). \tag{3.105}$$

From here, we see that a particular solution for $\mathbf{E}(\mathbf{r})$ is given by

$$\mathbf{E}(\mathbf{r}) = i\omega_{\mathbf{k}}\mu \int_V dV' \ \underline{\mathbf{G}}(\mathbf{r}, \mathbf{r}')\mathbf{J}(\mathbf{r}'). \tag{3.106}$$

The general solution is thus

$$\mathbf{E}(\mathbf{r}) = \mathbf{E}_0(\mathbf{r}) + i\omega_{\mathbf{k}}\mu \int_V dV' \, \underline{\mathbf{G}}(\mathbf{r}, \mathbf{r}')\mathbf{J}(\mathbf{r}'). \tag{3.107}$$

For completeness, the corresponding magnetic field is given by

$$\mathbf{H}(\mathbf{r}) = \mathbf{H}_0(\mathbf{r}) + i\omega_{\mathbf{k}}\mu \int_V dV' \, \left[\nabla \times \underline{\mathbf{G}}(\mathbf{r}, \mathbf{r}')\right] \mathbf{J}(\mathbf{r}'). \tag{3.108}$$

In order to solve for $\mathbf{E}(\mathbf{r})$ and $\mathbf{B}(\mathbf{r})$ for a specific distribution of currents, we need to determine $\underline{\mathbf{G}}(\mathbf{r}, \mathbf{r}')$. Applying the Lorenz gauge to Equation 3.95, we have that

$$\mathbf{E}(\mathbf{r}) = i\omega_{\mathbf{k}} \left[1 + \frac{1}{k^2}\nabla\nabla\cdot\right] \mathbf{A}(\mathbf{r}). \tag{3.109}$$

Each column of $\underline{\mathbf{G}}(\mathbf{r}, \mathbf{r}')$ is simply the response of the system to a single point source current, $\mathbf{J}(\mathbf{r}) = -i\delta(\mathbf{r} - \mathbf{r}')\mathbf{n}_i/\omega_{\mathbf{k}}\mu_0$, as described by Equation 3.104. From Equation 3.102, the vector current relating to each point source current is

$$\mathbf{A}(\mathbf{r}) = -\frac{i}{\omega_{\mathbf{k}}} G_0(\mathbf{r}, \mathbf{r}')\mathbf{n}_i, \tag{3.110}$$

and inserting this vector potential for each component into Equation 3.109 we find the three equations

$$\mathbf{G}_i(\mathbf{r}, \mathbf{r}') = \left[1 + \frac{1}{k^2}\nabla\nabla\cdot\right] G_0(\mathbf{r}, \mathbf{r}') \, \mathbf{n}_i \qquad (i \in x, y, z), \tag{3.111}$$

which, using the definition $\nabla G_0 = \nabla \cdot [G_0 \mathbb{I}]$, we can group into a single equation using the dyadic Green's function, such that

$$\underline{\mathbf{G}}(\mathbf{r}, \mathbf{r}') = \left[\underline{\mathbb{I}} + \frac{1}{k^2}\nabla\nabla\right] G_0(\mathbf{r}, \mathbf{r}'). \tag{3.112}$$

We can now use this result to find the electric and magnetic fields for any configuration of charges and currents.

3.6.3 Dipole radiation

As stated in Section 3.1, electromagnetic waves are generated by accelerating charges. To good approximation, many sources can be considered **dipoles**[23] and for this reason we now use the Green's function method to study the properties of dipole radiation. We can create such a source by having a point charge undergo simple harmonic motion, such that it is

[23] When the dimension of the source is small compared to the wavelength of the light, then electric dipole radiation gives the dominant contribution to the emitted radiation (compared to higher order multipoles). We will come across this again in later chapters.

oscillating with small displacement

$$\mathbf{a}(t) = \mathbf{a}_0 e^{-i\omega_{\mathbf{k}} t}, \tag{3.113}$$

thus creating a simple oscillating dipole. The corresponding dipole moment is given by

$$\boldsymbol{\mu}(t) = \boldsymbol{\mu}_0 e^{-i\omega_{\mathbf{k}} t}, \tag{3.114}$$

where $\boldsymbol{\mu}_0 = q\mathbf{a}_0$. For a dipole placed at $\mathbf{r}_0$, the current density will likewise be time-harmonic and take the form

$$\mathbf{J}(\mathbf{r}, t) = \frac{\partial \boldsymbol{\mu}(t)}{\partial t} \delta(\mathbf{r} - \mathbf{r}_0), \tag{3.115}$$

such that

$$\mathbf{J}(\mathbf{r}) = -i\omega_{\mathbf{k}} \boldsymbol{\mu}_0 \delta(\mathbf{r} - \mathbf{r}_0), . \tag{3.116}$$

From Equation 3.102, the vector potential will take the form

$$\mathbf{A}(\mathbf{r}) = -i\omega_{\mathbf{k}} \mu \frac{e^{ik|\mathbf{r}-\mathbf{r}_0|}}{4\pi|\mathbf{r} - \mathbf{r}_0|} \boldsymbol{\mu}_0, \tag{3.117}$$

and

$$\mathbf{E}(\mathbf{r}) = \omega_{\mathbf{k}}^2 \mu \underline{\mathbf{G}}(\mathbf{r}, \mathbf{r}_0) \boldsymbol{\mu}_0, \tag{3.118}$$

$$\mathbf{H}(\mathbf{r}) = -i\omega_{\mathbf{k}} \left[\nabla \times \underline{\mathbf{G}}(\mathbf{r}, \mathbf{r}_0)\right] \boldsymbol{\mu}_0. \tag{3.119}$$

In Cartesian coordinates, the dyadic Green's function can be written as

$$\underline{\mathbf{G}}(\mathbf{r}, \mathbf{r}_0) = \frac{e^{ikR}}{4\pi R} \left[\left(1 + \frac{ikR - 1}{k^2 R^2}\right) \mathbb{I} + \frac{3 - 3ikR - k^2R^2}{k^2 R^2} \frac{\mathbf{R} \otimes \mathbf{R}}{R^2} \right], \tag{3.120}$$

where $\mathbf{R} = \mathbf{r} - \mathbf{r}_0$, $R = |\mathbf{r} - \mathbf{r}_0|$ and $\mathbf{R} \otimes \mathbf{R}$ is the outer product of $\mathbf{R}$ with itself, as per the definition of the outer product given in Appendix A.2. Plugging this in, and going through rather laborious algebra we find that

$$\mathbf{H} = \frac{ck^2}{4\pi} \left(\hat{\mathbf{k}} \times \boldsymbol{\mu}\right) \frac{e^{ikR}}{R} \left(1 - \frac{1}{ikR}\right), \tag{3.121}$$

$$\mathbf{E} = \frac{1}{4\pi\epsilon_0} \left[k^2 \left(\hat{\mathbf{k}} \times \boldsymbol{\mu}\right) \times \hat{\mathbf{k}} \frac{e^{ikR}}{R} + \left[3\hat{\mathbf{k}}(\hat{\mathbf{k}} \cdot \boldsymbol{\mu}) - \boldsymbol{\mu}\right] \left(\frac{1}{R^3} - \frac{ik}{R^2}\right) e^{ikR} \right]. \tag{3.122}$$

3.6.3.1 Power dissipation in a homogeneous medium

We now calculate how much power is dissipated by a dipole in a homogeneous medium, so we can later see how the power dissipation is affected by the presence of inhomogeneities.

The fields have terms which vary as $(kR)^{-1}$, $(kR)^{-2}$ and $(kR)^{-3}$. In the **far-field**, for which $R \gg \lambda$, $(kR)^{-1}$ terms dominate. Only the far-fields contribute to the time-averaged power flow, and so we assume that we measure the effects of the dipole very far away from the dipole itself[24], where the fields reduce to

$$\mathbf{H} = \frac{\mu c k^2}{4\pi} \left(\hat{\mathbf{k}} \times \boldsymbol{\mu}\right) \frac{e^{ikR}}{R}, \tag{3.123}$$

$$\mathbf{E} = \frac{\mu c^2 k^2}{4\pi} \hat{\mathbf{k}} \times \left(\hat{\mathbf{k}} \times \boldsymbol{\mu}\right) \frac{e^{ikR}}{R}. \tag{3.124}$$

The **Poynting vector** represents the directional energy flux of the electromagnetic field, and is given by

$$\mathbf{S} = \frac{1}{2} \mathrm{Re}\left\{\mathbf{E} \times \mathbf{H}^*\right\}, \tag{3.125}$$

where the factor of $1/2$ comes from time-averaging. The power radiated by a dipole can be calculated by integrating $\mathbf{S}$ over a closed, spherical surface with normal $\mathbf{n}$ surrounding the dipole, such that

$$P_0 = \int d\Omega \; r^2 \frac{1}{2} \mathrm{Re}\left\{\mathbf{n} \cdot (\mathbf{E} \times \mathbf{H}^*)\right\}. \tag{3.126}$$

Using the far-field expressions for $\mathbf{H}$ and $\mathbf{E}$ given in Equations 3.123 and 3.124 respectively, this reduces to

$$P_0 = \frac{|\boldsymbol{\mu}_0|^2}{4\pi\epsilon} \frac{\omega^4}{3c^3}. \tag{3.127}$$

3.6.3.2 Power dissipation in an inhomogeneous medium

We should now calculate how the power dissipation of the dipole will be affected by the presence of an inhomogeneity (such as the presence of a surface, or an unusual boundary condition such as a cavity) - we will need this in Chapter 6. According to **Poynting's theorem** [147], the radiated power of a time-harmonic current distribution in a linear medium will be equal to the rate of energy dissipation, such that

$$P = \frac{\partial W}{\partial t} = -\frac{1}{2} \int_V dV \mathrm{Re}\left\{\mathbf{J}^*(\mathbf{r}) \cdot \mathbf{E}(\mathbf{r_0})\right\}, \tag{3.128}$$

where V is the source volume. This tells us that the energy radiated by the dipole is equal to the work done by the dipole's own field on the dipole itself. Recalling from Equation 3.116 that $\mathbf{J}(\mathbf{r}) = -i\omega_{\mathbf{k}} \boldsymbol{\mu}_0 \delta(\mathbf{r} - \mathbf{r}_0)$, we can write the power dissipated by a dipole as

$$P = \frac{\omega_{\mathbf{k}}}{2} \mathrm{Im}\left[\boldsymbol{\mu}_0^* \cdot \mathbf{E}(\mathbf{r}_0)\right]. \tag{3.129}$$

[24] Radiative fields dominate in the far field - in the near field, $\mathbf{E}$ and $\mathbf{B}$ store a lot of energy and so there is reactive power, which does not contribute to power flow.

Inserting Equation 3.118, we can rewrite the dissipated power in terms of the Green's function, such that

$$P = \frac{\omega_{\mathbf{k}}^3 |\boldsymbol{\mu}_0|^2}{2c^2\epsilon_0} \mathrm{Im}\left[\underline{\mathbf{G}}(\mathbf{r}_0, \mathbf{r}_0)\right]. \tag{3.130}$$

The electric field at the position of the dipole, $\mathbf{r}_0$, will be given as the sum of the electric field produced by the dipole, $\mathbf{E}_0(\mathbf{r}_0)$, and the electric field induced by the presence of inhomogeneities in the system, $\mathbf{E}_{\mathrm{scat}}$. We can thus write the electric field at $\mathbf{r}_0$ as

$$\mathbf{E}(\mathbf{r}_0) = \mathbf{E}_0(\mathbf{r}_0) + \mathbf{E}_{\mathrm{scat}}(\mathbf{r}_0). \tag{3.131}$$

We can rewrite the **normalised power dissipation** as

$$\frac{P}{P_0} = 1 + \frac{6\pi\epsilon_0}{|\boldsymbol{\mu}_0|^2} \frac{1}{k^3} \mathrm{Im}\left\{\boldsymbol{\mu}_0^* \cdot \mathbf{E}_{\mathrm{scat}}(\mathbf{r}_0)\right\}. \tag{3.132}$$

This allows us to calculate the effect of an inhomogeneity on the ability of the electromagnetic field to dissipate power. Depending on the sign (phase) of the scattered field returning to the dipole, it enhances or suppresses power dissipation.

3.7 The photonic density of states (DOS)

The **photonic density of states** (DOS)[25] describes the proportion of photonic states in a system available for occupation as a function of energy (or frequency). The photonic DOS can be modified by the surrounding environment, which is of paramount importance in multiple applications, and will be used in Chapter 6.

The number of states $dN(\omega)$ between ω and $\omega + d\omega$ is by definition

$$dN(\omega) = V g(\omega) d\omega, \tag{3.133}$$

where V is the volume occupied by the states and $g(\omega)$ is the density of states. This can be written equivalently in $\mathbf{k}$-space, where we consider states which lie in the infinitesimal 3D[26] $\mathbf{k}$-space volume, $d^3\mathbf{k}$, having a frequency $\omega_{\mathbf{k}}$, such that

$$g(\omega_{\mathbf{k}}) d\omega_{\mathbf{k}} = g(\mathbf{k}) d^3\mathbf{k}. \tag{3.134}$$

The density of states can then be found by summing over contributions from all states,

$$g(\omega) = \int g(\omega_{\mathbf{k}}) d\omega_{\mathbf{k}} \delta(\omega - \omega_{\mathbf{k}}) = \int d^3\mathbf{k} g(\mathbf{k}) \delta(\omega - \omega_{\mathbf{k}}). \tag{3.135}$$

[25] The density of states is often first encountered for electronic systems, but the concept for photonic systems is governed by very much the same principles.

[26] A similar procedure can be made in 1D and 2D.

The allowed states in **k**-space are given by a uniformly spaced grid of points given the correct boundary conditions, and so the density of states in **k**-space is constant and independent of **k** or ω, $g(\mathbf{k}) = 1/(2\pi)^3$, and so we can simplify Equation 3.135,

$$g(\omega) = \frac{1}{(2\pi)^3} \int d^3\mathbf{k} \delta(\omega - \omega_{\mathbf{k}}). \tag{3.136}$$

We assume free space such that the dispersion relation is $\omega_{\mathbf{k}} = c|\mathbf{k}|$ (plotted in Figure 3.6a), and the states with a given frequency, $\omega_{\mathbf{k}}$, will reside in a spherical shell of radius $|\mathbf{k}|$ and thickness $d|\mathbf{k}|$. The volume of this shell in **k**-space is given by $d^3\mathbf{k} = 4\pi d|\mathbf{k}||\mathbf{k}|^2$. The density of states can be calculated as

$$g(\omega) = \frac{4\pi}{(2\pi)^3} \int d|\mathbf{k}||\mathbf{k}|^2 \delta(\omega - \omega_{\mathbf{k}}) = \frac{4\pi}{(2\pi)^3 c^3} \int d\omega_{\mathbf{k}} \omega_{\mathbf{k}}^2 \delta(\omega - \omega_{\mathbf{k}}) = \frac{\omega^2}{2\pi^2 c^3}. \tag{3.137}$$

Each photonic state can have two independent polarisations (as described in Section 3.2.3), and so we must multiply this result by two to find the total density of states, thus given by[27]

$$g(\omega) = \frac{\omega^2}{\pi^2 c^3}, \tag{3.138}$$

which is plotted in Figure 3.6b. Generally, the photonic density of states is a continuous function, however in certain (usually very well isolated) systems, such as high-quality cavities and photonic crystals [1, 12], the density of states may be discrete. In this case, integrating the DOS over an interval simply amounts to counting the number of modes in the interval, and so we can equivalently write that

$$g(\omega) = 2 \sum_{\mathbf{k}} \delta(\omega - \omega_{\mathbf{k}}). \tag{3.139}$$

This is akin to a spectroscopy function, in which the function shows a peak whenever ω coincides with an eigenfrequency, $\omega_{\mathbf{k}}$. It reduces to the continuum version above by using that $\sum_{\mathbf{k}} \to \frac{1}{(2\pi)^3} \int d^3\mathbf{k}$. In systems in which there is spatial distortion, it can be useful to define the **local density of states** (LDOS) to describe the space-resolved density of states. The photonic LDOS becomes particularly important in confined devices where reflection and the resulting interference causes spatial variation in the density of states (such as in highly confining optical cavities). For the photonic LDOS, the contribution of each state is weighted by the normalised density of its electric field at a spatial point **r**, such that

$$g(\mathrm{r}, \omega) = 2 \sum_{\mathbf{k}} \mathcal{E}_{\mathbf{k}}(\mathbf{r})^2 \delta(\omega - \omega_{\mathbf{k}}), \tag{3.140}$$

where $\mathcal{E}_{\mathbf{k}}(\mathbf{r})$ gives the spatial variation of the electric field. When integrated over the spatial

[27] I will sometimes write this result as $g_{3\mathrm{D}}(\omega)$ if the context is not clear.

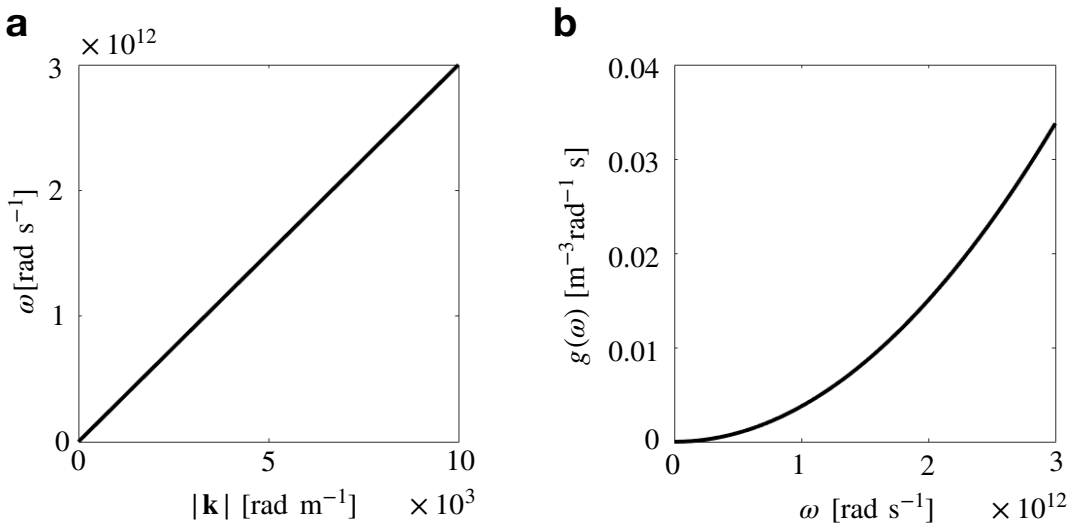

Figure 3.6: **The free space density of states: (a)** Dispersion relation of light in free space, $\omega = c|\mathbf{k}|$, and **(b)** the photonic density of states in 3D free space, $g(\omega) = \omega^2/c^3\pi^2$.

expanse of the system (or summed, for discrete systems), the usual expression for the DOS is recovered.

The final observation we will make is the link between the photonic LDOS, Green's functions and normalised power dissipation, a concept already raised in Section 3.6.3. We already discussed in Section 3.6.3 that the power dissipated by a dipole in a homogeneous medium is given by (repeating Equation 3.127 for clarity)

$$P_0 = \frac{|\boldsymbol{\mu}_0|^2}{4\pi\epsilon_0}\frac{\omega^4}{3c^3}, \tag{3.141}$$

which we can rewrite in terms of the free-space LDOS,

$$P_0 = \frac{\omega^2|\boldsymbol{\mu}_0|^2\pi}{12\epsilon_0}g(\omega). \tag{3.142}$$

The power dissipated in an inhomogeneous medium can be written in terms of the Green's function, such that (repeating Equation 3.130),

$$P = \frac{\omega^3|\boldsymbol{\mu}_0|^2}{2c^2\epsilon_0}\mathrm{Im}\left[\underline{\mathbf{G}}(\mathbf{r},\mathbf{r})\right], \tag{3.143}$$

which can be written in terms of the LDOS by identifying that[28]

$$g(\mathbf{r},\omega) = \frac{6\omega}{\pi c^2}\mathrm{Im}\left[\underline{\mathbf{G}}(\mathbf{r},\mathbf{r})\right], \tag{3.144}$$

[28]While the connection between Green's functions and the LDOS is an important concept, it is not directly needed to recover or understand the results of this thesis once the link between the LDOS and power is made, so I refer the dedicated reader to additional references [179, 180].

and so

$$P = \frac{\omega^2 |\boldsymbol{\mu}_0|^2 \pi}{12\epsilon_0} g(\mathbf{r}, \omega). \tag{3.145}$$

We can thus write the LDOS in an inhomogeneous medium as

$$g(\mathbf{r}, \omega) = \frac{\omega^2}{\pi^2 c^3} \frac{P}{P_0}, \tag{3.146}$$

and so the photonic LDOS in a non-homogeneous medium is the LDOS in free space multiplied by the normalised power dissipation, where the **amplification** or **suppression** of the LDOS can be surmised from whether normalised dissipated power is greater or less than 1. This formulation will be used in Chapter 6 to study the effect of TI nanostructures on their surroundings using a dipole as a probe.

Part II: Research Topics

4. Topological Insulator Nanostructures

"There's plenty of room at the bottom"
- Richard Feynman[1]

In Chapter 2 I introduced the symmetry-protected surface states of 3D topological insulators, which manifest in the band structure of the material as a **Dirac cone** in the bulk band gap.

We now look to **topological insulator nanostructures**, whose electronic structure and novel interactions with light form the basis of the research topics covered in this thesis. The nanoscale (1-100 nm, where nm = 10^{-9} m) is a length-scale at which a structure may be made up of only a few thousand or even hundred atoms. In this limit, the number of atoms participating in the surface state dynamics can be comparatively large in comparison to the total number of atoms, leading to an enhancement of surface state contributions to electronic and optical properties. This makes the nanoscale an ideal regime in which to study the properties of topological insulators, and an exciting playground for new applications and technologies [1, 10].

In particular, it has been found in various studies that in small TI nanostructures, **quantum confinement** of states on the surface results in the **discretization of the Dirac cone**, with discrete energy level spacing a function of nanostructure dimensions. This phenomenon has already been described for nanospheres [35], and nanowires [34, 182], with foundational experimental realisations and theoretical proposals for applications [5, 6, 120, 183–186]. Very recent work has studied the transport properties of a TI nanodisk, modelled as two circular surfaces coupled via a tunneling term [187]. In this chapter, I extend this theory to **general spheroidal TI nanoparticles**. I use this model to recover the surface states and energy levels for the nanosphere [35] and nanowire [34]. I also present a novel numerical study of the general nanospheroid, including results for the finite nanocigar[2], the finite nanodisk and the ideal, flat nanodisk.

This work gives a more complete view of topological insulator nanostructures, as the previous results are now described within a single framework. As will be discussed in Chapter 6, the growth of equiaxial nanoparticles (such as nanospheres) is experimentally

[1] *There's Plenty of Room at the Bottom: An Invitation to Enter a New Field of Physics* was a lecture given by Feynman in 1959, and later transcribed to be published in the Caltech magazine [181]. Although this lecture is said to have had little influence on the birth of the field of nanotechnology, it is often cited as evidence that the idea of miniaturisation and nanoscale technologies has long been dreamt about.

[2] I coin the term **nanocigar** to describe prolate nanospheroids, with geometry somewhere between the nanosphere and the nanowire. Reference [188] describes this geometry as 'needle-like', rather than 'cigar-like'.

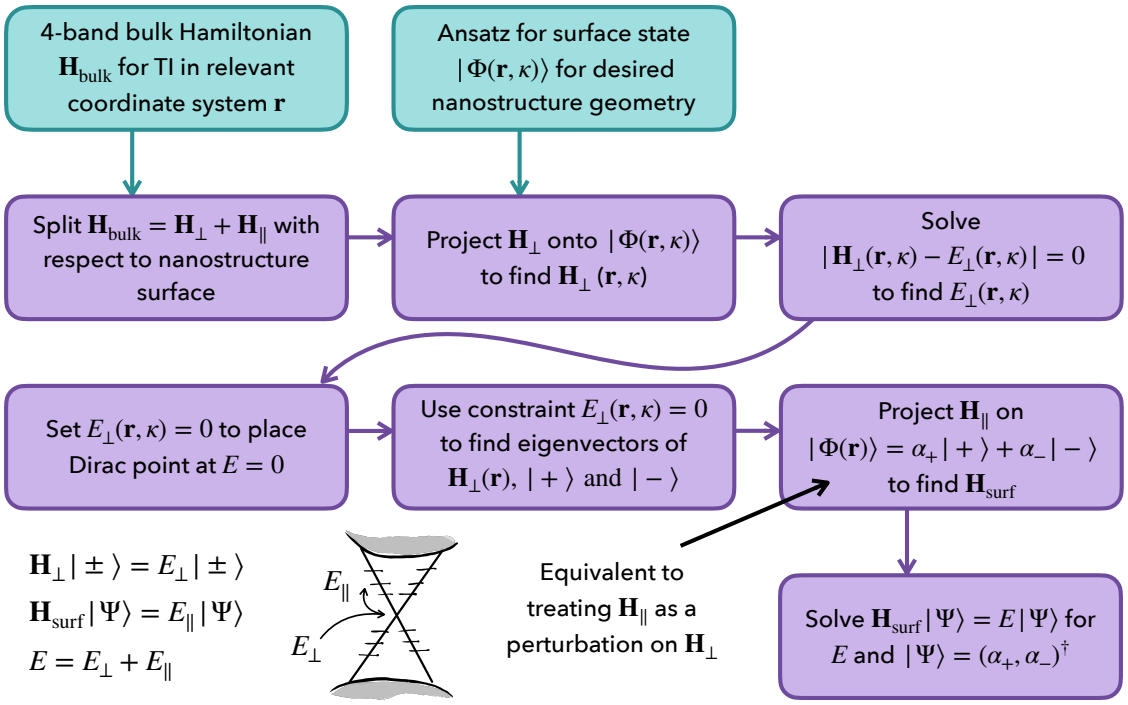

Figure 4.1: **Finding surface states for TI nanostructures:** Method for finding surface states and energies of TI nanostructures, taken from Imura *et al.* [34, 35] (purple) and extended to spheroidal coordinate systems, for the study of prolate and oblate spheroidal nanoparticles (green).

challenging, and while it can be done successfully [6] it is difficult to control the sample size. This poses a challenge when aiming to observe phenomena which are parameterized by the nanostructure dimensions. TI islands (or nanoflakes) are much easier to grow to high precision [189–192] and can be modelled as nanodisks. Finite-length TI nanowires or pillars have received little attention, but can be theoretically modelled as nanocigars (described in more detail in Section 4.2.3), and so the results of this work on non-spherical systems may well prove to be important in the study of TI nanostructures.

For TI nanostructures with confined dimensions on the scale of nanometers, transitions between surface states are of the order of terahertz (THz), the importance of which will be covered in Chapters 5 and 6.

In order to arrive at the surface states and energies for a **spheroidal TI nanoparticle**, we follow the same method as described by Imura *et al.*. [34, 35] (given schematically in Figure 4.1), extended to spheroids. We begin with the bulk Hamiltonian for TI materials discussed in Chapter 2, and by considering the confinement effects on the surface of small, spheroidal particles we find an effective Dirac surface Hamiltonian and the resulting surface states and energy levels. We start with **prolate spheroids**, and then show that by repeating the process with **oblate spheroids**, the full range of spheroidal dimensions can be covered.

The results of this chapter are taken from the manuscript (in preparation to be submitted):

- **Spheroidal topological insulator nanoparticles**, Marie Rider, Vincenzo Giannini, **In preparation** (2021) [3].

4.1 Prolate spheroidal TI nanoparticles

Prolate spheroids (see Figure 4.2) are the limiting case of an ellipsoid with symmetry about one axis, such that the three principal semi-axes, $R_1 \geq R_2 \geq R_3$, reduce to $R_1 \geq R_2 = R_3$. Modelling a nanoparticle as a prolate spheroid allows us to study particles between the two limiting cases of the **nanosphere** ($R_1 \approx R_2$) and the **nanowire** ($R_1 \gg R_2$).

4.1.1 Bulk Hamiltonian

We begin with the bulk Hamiltonian for TI materials in the Bi_2Se_3 family (Equation 2.12) which I repeat here for clarity.

$$\mathbf{H}_{\text{bulk}}(\mathbf{k}) = \; m(\mathbf{k})\mathbb{1}_2 \otimes \boldsymbol{\sigma_3} + Ak_x\boldsymbol{\sigma_1} \otimes \boldsymbol{\sigma_1} + Ak_y\boldsymbol{\sigma_2} \otimes \boldsymbol{\sigma_1} + Ak_z\boldsymbol{\sigma_3} \otimes \boldsymbol{\sigma_1}, \tag{4.1}$$

where $m(\mathbf{k}) = m_0 + m_1(k_x^2 + k_y^2 + k_z^2)$ and $\boldsymbol{\sigma_1}, \boldsymbol{\sigma_2}, \boldsymbol{\sigma_3}$ are the Pauli matrices (given in Appendix A.1). We will convert this system from Cartesian to **prolate spheroidal coordinates** (σ, τ, φ), where

$$\begin{aligned} x &= a\sqrt{(\sigma^2-1)(1-\tau^2)}\cos\varphi, \\ y &= a\sqrt{(\sigma^2-1)(1-\tau^2)}\sin\varphi, \\ z &= a\sigma\tau, \end{aligned} \tag{4.2}$$

where σ is real-valued ≥ 1 (and not to be confused with the Pauli matrices, $\boldsymbol{\sigma_1}, \boldsymbol{\sigma_2}, \boldsymbol{\sigma_3}$), $\tau \in [-1, 1]$, $\varphi \in [-\pi, \pi]$, and a is a constant of dimension $[L]$. The unit vectors $\hat{\tau}$ and $\hat{\varphi}$ are parallel to the surface of the particle, while $\hat{\sigma}$ is perpendicular to the surface. Constant σ gives a closed spheroidal surface and we define $\sigma = \sigma_0$ to demarcate the particle surface such that the particle is described by $\sigma \leq \sigma_0$. The surface is constrained by the equation

$$\frac{x^2 + y^2}{a^2(\sigma_0^2 - 1)} + \frac{z^2}{a^2\sigma_0^2} = 1, \tag{4.3}$$

where we can identify $R_1 = a\sigma_0$ and $R_2 = a\sqrt{\sigma_0^2 - 1}$ as the semi-major and semi-minor axes respectively (i.e. $R_1 \geq R_2$), illustrated in Figure 4.2a. In the limit $\sigma_0 \gg 1$ this reduces to the equation of the surface of a sphere with radius $R_2 \approx R_1 = a\sigma_0$ (demonstrated in Figure 4.2b), and the infinite nanowire (i.e. an infinitely long cigar) is given by $\sigma_0 \to 1$ with length $L = 2a$ and $R = a\sqrt{\sigma_0^2 - 1}$. (see Figure 4.2c). For $\sigma_0 \to 1$ we have that $R_2 \ll R_1$,

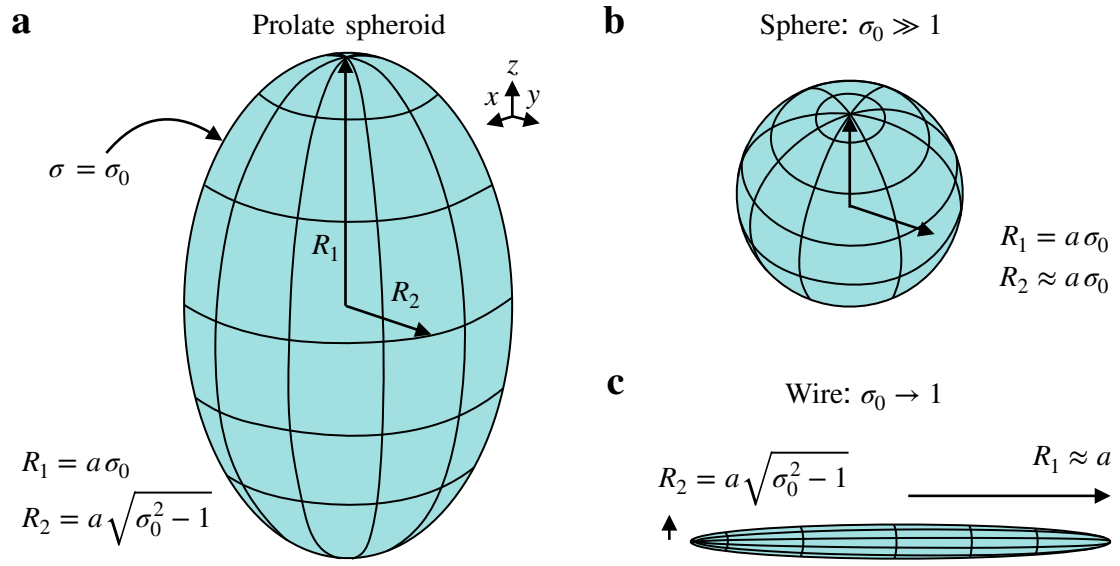

Figure 4.2: **Prolate spheroidal nanoparticles:** We describe our nanoparticles as prolate spheroids. **(a)** Prolate spheroidal nanoparticle with surface given by $\sigma = \sigma_0$ with semi-major axis $R_1 = a\sigma_0$ (parallel to the z-axis) and semi-minor axis $R_2 = a\sqrt{\sigma_0^2 - 1}$, where $R_1 \geq R_2$. **(b)** The spherical limit with $R_1 \approx R_2$, and **(c)** the limit of a nanowire, for which $R_1 \gg R_2$.

but we still use parameters which ensure that $R_2 \geq 5$ nm so that the TI bulk Hamiltonian is still valid.

The momentum operator $\mathbf{k} = k_x\hat{\mathbf{x}} + k_y\hat{\mathbf{y}} + k_z\hat{\mathbf{z}}$ can be projected onto the prolate spheroidal unit vectors, such that $\mathbf{k} = k_\sigma\hat{\sigma} + k_\tau\hat{\tau} + k_\varphi\hat{\varphi}$, where

$$k_\sigma = -\frac{i}{h_\sigma}\partial_\sigma, \quad k_\tau = -\frac{i}{h_\tau}\partial_\tau \quad \text{and} \quad k_\varphi = -\frac{i}{h_\varphi}\partial_\varphi, \tag{4.4}$$

where I have introduced the **scale factors**

$$h_\sigma = a\sqrt{\frac{\sigma^2 - \tau^2}{\sigma^2 - 1}}, \quad h_\tau = a\sqrt{\frac{\sigma^2 - \tau^2}{1 - \tau^2}}, \quad \text{and} \quad h_\varphi = a\sqrt{(\sigma^2 - 1)(1 - \tau^2)}. \tag{4.5}$$

I give more details on this infrequently-used coordinate system in Appendix A.4. Rewriting Equation 4.1 in prolate spheroidal coordinates (where some useful details on transforming

from Cartesian to spheroidal coordinates are also given in Appendix A.4), we have that

$$\begin{aligned}\mathbf{H}_{\text{bulk}}(\mathbf{k}) = \; & m_0 \; \mathbb{1}_2 \otimes \boldsymbol{\sigma_3} \\ & - m_1 \; \mathbb{1}_2 \otimes \boldsymbol{\sigma_3} \left[\frac{1}{h_\sigma^2}\partial_\sigma^2 + \frac{2\sigma}{a^2(\sigma^2-\tau^2)}\partial_\sigma \right] \\ & + m_1 \; \mathbb{1}_2 \otimes \boldsymbol{\sigma_3} \left[\frac{2\tau}{a^2(\sigma^2-\tau^2)}\partial_\tau - \frac{1}{h_\tau^2}\partial_\tau^2 - \frac{1}{h_\varphi^2}\partial_\varphi^2 \right] \\ & - iA \; \boldsymbol{\sigma_3} \otimes \boldsymbol{\sigma_1} \left[\frac{a\tau}{h_\sigma^2}\partial_\sigma + \frac{a\sigma}{h_\tau^2}\partial_\tau \right] \\ & - iA \; \boldsymbol{\sigma_1} \otimes \boldsymbol{\sigma_1} \left[\frac{a\sigma}{h_\sigma h_\tau}\cos\varphi \; \partial_\sigma - \frac{a\tau}{h_\sigma h_\tau}\cos\varphi \; \partial_\tau - \frac{\sin\varphi}{h_\varphi}\partial_\varphi \right] \\ & - iA \; \boldsymbol{\sigma_2} \otimes \boldsymbol{\sigma_1} \left[\frac{a\sigma}{h_\sigma h_\tau}\sin\varphi \; \partial_\sigma - \frac{a\tau}{h_\sigma h_\tau}\sin\varphi \; \partial_\tau + \frac{\cos\varphi}{h_\varphi}\partial_\varphi \right].\end{aligned} \tag{4.6}$$

We can now separate the Hamiltonian into components **perpendicular** (i.e. in the direction of $\hat{\sigma}$) and **parallel** ($\hat{\tau}$ and $\hat{\varphi}$) to the surface, such that $\mathbf{H} = \mathbf{H}_\perp + \mathbf{H}_\parallel$, where

$$\begin{aligned}\mathbf{H}_\perp(\mathbf{k}) = \; & m_0 \; \mathbb{1}_2 \otimes \boldsymbol{\sigma_3} - m_1 \; \mathbb{1}_2 \otimes \boldsymbol{\sigma_3} \left[\frac{1}{h_\sigma^2}\partial_\sigma^2 + \frac{2\sigma}{a^2(\sigma^2-\tau^2)}\partial_\sigma \right] \\ & - iA \; \boldsymbol{\sigma_3} \otimes \boldsymbol{\sigma_1} \left[\frac{a\tau}{h_\sigma^2}\partial_\sigma \right] - iA \; \boldsymbol{\sigma_1} \otimes \boldsymbol{\sigma_1} \left[\frac{a\sigma}{h_\sigma h_\tau}\cos\varphi \; \partial_\sigma \right] \\ & - iA\boldsymbol{\sigma_2} \otimes \boldsymbol{\sigma_1} \left[\frac{a\sigma}{h_\sigma h_\tau}\sin\varphi \; \partial_\sigma \right],\end{aligned} \tag{4.7}$$

and

$$\begin{aligned}\mathbf{H}_\parallel(\mathbf{k}) = \; & - m_1 \; \mathbb{1}_2 \otimes \boldsymbol{\sigma_3} \left[-\frac{2\tau}{a^2(\sigma^2-\tau^2)}\partial_\tau + \frac{1}{h_\tau^2}\partial_\tau^2 + \frac{1}{h_\varphi^2}\partial_\varphi^2 \right] \\ & - iA \; \boldsymbol{\sigma_3} \otimes \boldsymbol{\sigma_1} \left[\frac{a\sigma}{h_\tau^2}\partial_\tau \right] - iA \; \boldsymbol{\sigma_1} \otimes \boldsymbol{\sigma_1} \left[-\frac{a\tau}{h_\sigma h_\tau}\cos\varphi \; \partial_\tau - \frac{\sin\varphi}{h_\varphi}\partial_\varphi \right] \\ & - iA\boldsymbol{\sigma_2} \otimes \boldsymbol{\sigma_1} \left[-\frac{a\tau}{h_\sigma h_\tau}\sin\varphi \; \partial_\tau + \frac{\cos\varphi}{h_\varphi}\partial_\varphi \right].\end{aligned} \tag{4.8}$$

We have chosen the definition $\mathbf{H}_\perp = \mathbf{H}_{\text{bulk}}|_{k_\tau, k_\varphi = 0}$, such that $\mathbf{H}_\perp(\mathbf{k})$ contains all constant terms and ∂_σ terms, and $\mathbf{H}_\parallel(\mathbf{k})$ contains only ∂_τ and ∂_φ terms.

4.1.2 Surface state ansatz

Recalling that the surface of the nanospheroid is given by the condition $\sigma = \sigma_0$, we introduce an ansatz for the 4-component **surface state** of the form

$$|\Phi(\sigma, \tau, \varphi)\rangle = e^{\kappa a(\sigma - \sigma_0)}|u(\sigma_0, \tau, \varphi)\rangle, \tag{4.9}$$

where κ is the **decay constant** describing the evanescence of the surface wave function into the bulk. Generally we would not expect a separable solution for a spheroid (except

in the limiting cases), hence we would expect $u(\sigma,\tau,\varphi)$. However due to the rapid decay of the surface state into the bulk such that $\kappa^{-1} \ll R_1,\ R_2$, we assume $u(\sigma_0,\tau,\varphi)$. This is of course an approximation[3], but allows us to write down a separable function. When $|\Phi(\sigma,\tau,\varphi)\rangle$ is acted upon by $\mathbf{H}_\perp$, we find that

$$\begin{aligned}\mathbf{H}_\perp(\kappa) = \ & m_0\ \mathbb{1}_2 \otimes \boldsymbol{\sigma_3} - m_1\ \mathbb{1}_2 \otimes \boldsymbol{\sigma_3}\left[\frac{1}{h_\sigma^2}a^2\kappa^2 + \frac{2\sigma}{a(\sigma^2-\tau^2)}\kappa\right] \\ & - iA\ \boldsymbol{\sigma_3}\otimes\boldsymbol{\sigma_1}\left[\frac{a^2\tau}{h_\sigma^2}\kappa\right] - iA\ \boldsymbol{\sigma_1}\otimes\boldsymbol{\sigma_1}\left[\frac{a^2\sigma}{h_\sigma h_\tau}\cos\varphi\ \kappa\right] \\ & - iA\boldsymbol{\sigma_2}\otimes\boldsymbol{\sigma_1}\left[\frac{a^2\sigma}{h_\sigma h_\tau}\sin\varphi\ \kappa\right].\end{aligned} \tag{4.10}$$

The inverse of the decay constant, κ^{-1}, is physically of the order of a few Å [193], and so it is sensible to set $\sigma = \sigma_0$ throughout the following calculations. This is only valid for nanoparticles for which the limiting dimension $R_2 = a\sqrt{\sigma_0^2-1} \gg \kappa^{-1}$, but the same is true for the bulk Hamiltonian, which will not accurately describe a particle less than a few unit cells in size. In addition, in such a small particle the surface states would most likely experience an overlap of their exponentially decaying tails from opposite sides of the surface. For all of these reasons, we constrain ourselves to the study of nanostructures for which $a\sqrt{\sigma_0^2-1} \geq 5$ nm, and in general we stay much above this limit.

The component of the Hamiltonian perpendicular to the surface, $\mathbf{H}_\perp = \mathbf{H}_{\text{bulk}}|_{k_\tau=0,k_\varphi=0}$, sets the energy of the surface Γ-point, $E_\perp$. In Chapter 2 we already chose $\epsilon(\mathbf{k}) = 0$ in order to preserve particle-hole symmetry, which automatically gives the **zero-energy condition** $E_\perp = 0$, such that the dispersion relation is symmetric with respect to $E = 0$. This leaves us with the condition that

$$\mathbf{H}_\perp|\Phi(\sigma_0,\tau,\varphi)\rangle = E_\perp|\Phi(\sigma_0,\tau,\varphi)\rangle = 0. \tag{4.11}$$

Solving for the eigenvalues of $\mathbf{H}_\perp$ via $|\mathbf{H}_\perp - E_\perp\mathbb{1}_4| = 0$, we find the condition that

$$E_\perp = \pm\frac{1}{a\left(h_\sigma^0\right)^2 h_\tau^0\left(\sigma_0^2-\tau^2\right)}\sqrt{f(\kappa)}, \tag{4.12}$$

where

$$\begin{aligned}f(\kappa) = & -a^6\left(h_\tau^0\right)^2\kappa^2\left(\sigma_0^2-\tau^2\right)^2\left(A^2\tau^2-\kappa^2m_1^2\right) \\ & + \left(h_\sigma^0\right)^4\left(h_\tau^0\right)^2\left(2\kappa m_1\sigma_0 - am_0\left(\sigma_0^2-\tau^2\right)\right)^2 \\ & - a^3\left(h_\sigma^0\right)^2\kappa^2(\sigma_0^2-\tau^2)\Big[a^3A^2\sigma_0^2(\sigma_0^2-\tau^2) \\ & - 2\left(h_\tau^0\right)^2 m_1\left(2\kappa m_1\sigma_0 - am_0\left(\sigma_0^2-\tau^2\right)\right)\Big].\end{aligned} \tag{4.13}$$

[3]This approximation amounts to the assumption that $u(\sigma,\tau,\varphi)$ is a slow-varying function of σ, such that $\partial_\sigma u(\sigma,\tau,\varphi)|_{\sigma=\sigma_0}$ is negligible.

To enforce the zero-energy condition $E_\perp = 0$, we must satisfy the condition that $f(\kappa) = 0$, which results in four possible expressions for κ,

$$\kappa_{q,s} = -\frac{\sigma_0}{a(1-\sigma_0^2)} + q\sqrt{g_q(\sigma_0,\tau)} + \frac{sAh_\sigma^0}{2m_1 a}, \tag{4.14}$$

where

$$\begin{aligned} g_q(\sigma_0,\tau) = &\frac{\left(h_\sigma^0\right)^4\sigma_0^2}{a^6\left(\sigma_0^2-\tau^2\right)^2} + \frac{A^2}{4m_1^2}\left(\frac{\sigma_0^2\left(h_\sigma^0\right)^2}{\left(h_\tau^0\right)^2}+\tau^2\right) \\ &+ \frac{\left(h_\sigma^0\right)^2}{a^2 m_1}\left(m_0 - q\frac{A\sigma_0 h_\sigma^0}{a^2(\sigma_0^2-\tau^2)}\right), \end{aligned} \tag{4.15}$$

and $q, s = -1, 1$. Substituting these rather unwieldy expressions for κ into $\mathbf{H}_\perp$ and after some algebraic gymnastics, we find two degenerate eigenstates of $\mathbf{H}_\perp$,

$$|+\rangle = \frac{\sqrt{1-\tau}}{2}\left((1,i)\,\frac{h_\tau^0}{\sigma_0}\left(\frac{1}{a}+\frac{\tau}{h_\sigma^0}\right)e^{i\varphi/2}, (1,i)\,e^{-i\varphi/2}\right)^\dagger, \tag{4.16}$$

$$|-\rangle = \frac{\sqrt{1+\tau}}{2}\left((1,-i)\,\frac{h_\tau^0}{\sigma_0}\left(\frac{1}{a}-\frac{\tau}{h_\sigma^0}\right)e^{i\varphi/2}, (-1,i)\,e^{-i\varphi/2}\right)^\dagger. \tag{4.17}$$

Any surface state can then be written as a linear combination of $|+\rangle$ and $|-\rangle$ with amplitude specified by α_+ and α_- respectively, such that the 4-component surface state is given by

$$|\Phi\rangle = \alpha_+(\tau,\varphi,\sigma_0)|+\rangle + \alpha_-(\tau,\varphi,\sigma_0)|-\rangle. \tag{4.18}$$

Note that we are now using the **surface scale factors**[4],

$$h_\sigma^0 = a\sqrt{\frac{\sigma_0^2-\tau^2}{\sigma_0^2-1}}, \quad h_\tau^0 = a\sqrt{\frac{\sigma_0^2-\tau^2}{1-\tau^2}}, \quad \text{and} \quad h_\varphi^0 = a\sqrt{(\sigma_0^2-1)(1-\tau^2)}. \tag{4.19}$$

Result: Prolate spheroidal TI nanostructure surface state form

The 4-component **surface state** has the form

$$|\Phi\rangle = \alpha_+(\tau,\varphi,\sigma_0)|+\rangle + \alpha_-(\tau,\varphi,\sigma_0)|-\rangle \tag{4.20}$$

where

$$|+\rangle = \frac{\sqrt{1-\tau}}{2}\left((1,i)\,\frac{h_\tau^0}{\sigma_0}\left(\frac{1}{a}+\frac{\tau}{h_\sigma^0}\right)e^{i\varphi/2}, (1,i)\,e^{-i\varphi/2}\right)^\dagger, \tag{4.21}$$

$$|-\rangle = \frac{\sqrt{1+\tau}}{2}\left((1,-i)\,\frac{h_\tau^0}{\sigma_0}\left(\frac{1}{a}-\frac{\tau}{h_\sigma^0}\right)e^{i\varphi/2}, (-1,i)\,e^{-i\varphi/2}\right)^\dagger. \tag{4.22}$$

[4] i.e. we are using the scale factors with $\sigma \to \sigma_0$.

4.1.3 Surface Hamiltonian

We now focus our attention on $\mathbf{H}_{\parallel}$, given in Equation 4.94, but repeated here for clarity,

$$\begin{aligned}\mathbf{H}_{\parallel}(\mathbf{k}) = &- m_1\ \mathbb{1}_2 \otimes \boldsymbol{\sigma_3}\left[-\frac{2\tau}{a^2(\sigma_0^2-\tau^2)}\partial_\tau + \frac{1}{(h_\tau^0)^2}\partial_\tau^2 + \frac{1}{(h_\varphi^0)^2}\partial_\varphi^2\right] \\ &- iA\ \boldsymbol{\sigma_3}\otimes\boldsymbol{\sigma_1}\left[\frac{a\sigma_0}{(h_\tau^0)^2}\partial_\tau\right] - iA\ \boldsymbol{\sigma_1}\otimes\boldsymbol{\sigma_1}\left[-\frac{a\tau}{h_\sigma^0 h_\tau^0}\cos\varphi\ \partial_\tau - \frac{\sin\varphi}{h_\varphi^0}\partial_\varphi\right] \\ &- iA\ \boldsymbol{\sigma_2}\otimes\boldsymbol{\sigma_1}\left[-\frac{a\tau}{h_\sigma^0 h_\tau^0}\sin\varphi\ \partial_\tau + \frac{\cos\varphi}{h_\varphi^0}\partial_\varphi\right].\end{aligned} \tag{4.23}$$

We note that all terms scale either with $m_1/a^2\sigma_0^2$, $A/a\sigma_0$ or A/a, where $\sigma_0 \geq 1$, and as discussed in Chapter 2, m_1 ∼1-10 eV Å^2 and A ∼1-10 eV Å with exact values dependent on material choice. As such, all terms with coefficient m_1 can be considered negligible. This greatly simplifies the form of $\mathbf{H}_{\parallel}$, and in particular removes all second derivatives, such that

$$\begin{aligned}\mathbf{H}_{\parallel}(\mathbf{k}) = &- iA\ \boldsymbol{\sigma_3}\otimes\boldsymbol{\sigma_1}\left[\frac{a\sigma_0}{(h_\tau^0)^2}\partial_\tau\right] - iA\ \boldsymbol{\sigma_1}\otimes\boldsymbol{\sigma_1}\left[-\frac{a\tau}{h_\sigma^0 h_\tau^0}\cos\varphi\ \partial_\tau - \frac{\sin\varphi}{h_\varphi^0}\partial_\varphi\right] \\ &- iA\boldsymbol{\sigma_2}\otimes\boldsymbol{\sigma_1}\left[-\frac{a\tau}{h_\sigma^0 h_\tau^0}\sin\varphi\ \partial_\tau + \frac{\cos\varphi}{h_\varphi^0}\partial_\varphi\right].\end{aligned} \tag{4.24}$$

Projecting this Hamiltonian onto the general surface state $|\Phi\rangle$, we recover a 2×2 effective surface Hamiltonian, such that

$$\begin{pmatrix}\langle +|\mathbf{H}_{\parallel}|\Phi\rangle \\ \langle -|\mathbf{H}_{\parallel}|\Phi\rangle\end{pmatrix} = \begin{pmatrix}\mathbf{H}_{\text{surf}}^{++} & \mathbf{H}_{\text{surf}}^{+-} \\ \mathbf{H}_{\text{surf}}^{-+} & \mathbf{H}_{\text{surf}}^{--}\end{pmatrix}\begin{pmatrix}\alpha_+ \\ \alpha_-\end{pmatrix} = \mathbf{H}_{\text{surf}}|\Psi\rangle, \tag{4.25}$$

where $|\Psi\rangle$ is the 2-component state

$$|\Psi\rangle = \begin{pmatrix}\alpha_+ \\ \alpha_-\end{pmatrix}. \tag{4.26}$$

This process is equivalent to employing **degenerate perturbation theory**, where $\mathbf{H}_{\parallel}$ is considered a perturbation on $\mathbf{H}_{\perp}$, acting on the degenerate eigenstates of $\mathbf{H}_{\perp}$, $|\pm\rangle$. To find the final, degeneracy-lifted spectrum of the total perturbed Hamiltonian we calculate the matrix elements $\langle\pm|\mathbf{H}_{\parallel}|\pm\rangle$, $\langle\pm|\mathbf{H}_{\parallel}|\mp\rangle$ and then diagonalise. After some arduous algebra (with some helpful details given in Appendix B.7), we find that

$$\mathbf{H}_{\text{surf}}^{++} = \mathbf{H}_{\text{surf}}^{--} = 0, \tag{4.27}$$

$$\mathbf{H}_{\text{surf}}^{+-} = \frac{A}{a\sigma_0\sqrt{1-\tau^2}}\left[(1-\tau^2)\partial_\tau + i\frac{h_\sigma^0}{a}\partial_\varphi + \frac{1-\tau}{2} - \frac{a}{2h_\sigma^0} - \frac{\tau a^2}{2\,(h_\tau^0)^2}\right], \tag{4.28}$$

$$\mathbf{H}_{\text{surf}}^{-+} = \frac{A}{a\sigma_0\sqrt{1-\tau^2}}\left[-(1-\tau^2)\partial_\tau + i\frac{h_\sigma^0}{a}\partial_\varphi + \frac{1+\tau}{2} - \frac{a}{2h_\sigma^0} + \frac{\tau a^2}{2\,(h_\tau^0)^2}\right]. \tag{4.29}$$

The surface states satisfy the eigenvalue equation

$$\mathbf{H}_{\text{surf}}|\Psi\rangle = E|\Psi\rangle. \tag{4.30}$$

As the spheroid has azimuthal symmetry[5], we are able to separate variables, such that

$$|\Psi_m\rangle = e^{im\varphi}\begin{pmatrix}\alpha_{m,+}(\tau)\\ \alpha_{m,-}(\tau)\end{pmatrix}. \tag{4.31}$$

As $|\Psi\rangle$ should transform as a vector, but $|+\rangle$ and $|-\rangle$ transform as **spinors**[6], it can be demonstrated that m (not to be confused with the mass parameters) is restricted to half-integer values [35], such that $m = \pm 1/2, \pm 3/2, ...$ Physically, m is the projection of the angular momentum on the z-axis. When applying $\mathbf{H}_{\text{surf}}$ to this state, Equation 4.30 reduces to the coupled, first-order ordinary differential equations (ODEs)

$$\mathbf{H}^{+-}_{\text{surf}}\alpha_{m,+} = E_m\alpha_{m,-}, \tag{4.32}$$
$$\mathbf{H}^{-+}_{\text{surf}}\alpha_{m,-} = E_m\alpha_{m,+}, \tag{4.33}$$

such that

$$\frac{A}{a\sigma_0\sqrt{1-\tau^2}}\left[(1-\tau^2)\partial_\tau + i\frac{h^0_\sigma}{a}\partial_\varphi + \frac{1-\tau}{2} - \frac{\tau a^2}{2\left(h^0_\tau\right)^2} - \frac{a}{2h^0_\sigma}\right]\alpha_{m,+} = E_m\alpha_{m,-} \tag{4.34}$$

$$\frac{A}{a\sigma_0\sqrt{1-\tau^2}}\left[-(1-\tau^2)\partial_\tau + i\frac{h^0_\sigma}{a}\partial_\varphi + \frac{1+\tau}{2} - \frac{a}{2h^0_\sigma} + \frac{\tau a^2}{2\left(h^0_\tau\right)^2}\right]\alpha_{m,-} = E_m\alpha_{m,+}. \tag{4.35}$$

[5] Symmetry about the z-axis.

[6] A spinor, like a vector, is an element of a complex vector space. However, unlike a vector (which returns to its original form under a 2π rotation), a spinor transforms to its negative under a 2π rotation, and must be rotated 4π to return to its original form.

Result: Prolate spheroidal TI nanostructure surface state Hamiltonian

The 2-component **surface state** $|\Psi_m\rangle = e^{im\varphi}(\alpha_{m,+}, \alpha_{m,-})^T$, obeys the surface state eigenvalue equation

$$\mathbf{H}_{\text{surf}}|\Psi_m\rangle = \begin{pmatrix} 0 & \mathbf{H}_{\text{surf}}^{+-} \\ \mathbf{H}_{\text{surf}}^{-+} & 0 \end{pmatrix} |\Psi_m\rangle = E_m|\Psi_m\rangle, \tag{4.36}$$

where $m = \pm 1/2, \pm 3/2, \pm 5/2, ...$ and

$$\mathbf{H}_{\text{surf}}^{++} = \mathbf{H}_{\text{surf}}^{--} = 0 \tag{4.37}$$

$$\mathbf{H}_{\text{surf}}^{+-} = \frac{A}{a\sigma_0\sqrt{1-\tau^2}}\left[(1-\tau^2)\partial_\tau - \frac{mh_\sigma^0}{a} + \frac{1-\tau}{2} - \frac{a}{2h_\sigma^0} - \frac{\tau a^2}{2\left(h_\tau^0\right)^2}\right] \tag{4.38}$$

$$\mathbf{H}_{\text{surf}}^{-+} = \frac{A}{a\sigma_0\sqrt{1-\tau^2}}\left[-(1-\tau^2)\partial_\tau - \frac{mh_\sigma^0}{a} + \frac{1+\tau}{2} - \frac{a}{2h_\sigma^0} + \frac{\tau a^2}{2\left(h_\tau^0\right)^2}\right] \tag{4.39}$$

This eigenvalue problem can be written as two first-order coupled ODEs,

$$\mathbf{H}_{\text{surf}}^{+-}\alpha_{m,+} = E_m\alpha_{m,-} \tag{4.40}$$

$$\mathbf{H}_{\text{surf}}^{-+}\alpha_{m,-} = E_m\alpha_{m,+}. \tag{4.41}$$

In the next section we will study the limiting cases in which there are analytical solutions to these equations, and discuss the numerical solution for the general case.

4.2 General and limiting cases

We now examine the limiting cases of this result, in order to analytically solve for the final surface states and energy levels of nanostructures of specific geometries. The limits to consider for the prolate spheroid are (i) the **nanosphere** [35] and (ii) the **nanowire** [34]. We will also discuss the numerical solution of the general prolate spheroid.

4.2.1 The nanosphere

In order to recover the limit of the **nanosphere**, we set $\sigma_0 \gg 1$. The surface of the particle (from Equation 4.3) reduces to

$$x^2 + y^2 + z^2 = R^2, \tag{4.42}$$

where we have identified $R = a\sigma_0$ as the radius of the nanosphere, as illustrated in Figure 4.3a. The surface scale factors for the sphere reduce to

$$h_\sigma^0 = a, \quad h_\tau^0 = \frac{R}{\sqrt{1-\tau^2}} \quad \text{and} \quad h_\varphi^0 = R\sqrt{1-\tau^2}. \tag{4.43}$$

A sanity check comes at the point of simplifying the $\mathbf{H}_\perp$ eigenstates, which reduce to the eigenstates obtained by Imura *et al.* [35],

$$|+\rangle = \frac{1}{2}\left((1,i)\sqrt{1+\tau}e^{i\varphi/2}, (1,i)\sqrt{1-\tau}e^{-i\varphi/2}\right)^\dagger, \tag{4.44}$$

$$|-\rangle = \frac{1}{2}\left((1,-i)\sqrt{1-\tau}e^{i\varphi/2}, (-1,i)\sqrt{1+\tau}e^{-i\varphi/2}\right)^\dagger. \tag{4.45}$$

In this limit, the coupled first order equations describing the 2-component surface states and their energy levels reduce to

$$\frac{A}{R\sqrt{1-\tau^2}}\left[(1-\tau^2)\partial_\tau - m - \frac{\tau}{2}\right]\alpha_{m+} = E_m\alpha_{m,-}, \tag{4.46}$$

$$\frac{A}{R\sqrt{1-\tau^2}}\left[-(1-\tau^2)\partial_\tau - m + \frac{\tau}{2}\right]\alpha_{m-} = E_m\alpha_{m,+}. \tag{4.47}$$

We can combine these into a single, second-order equation

$$\left[(1-\tau^2)\partial_\tau^2 - 2\tau\partial_\tau - \frac{m^2 - mx\tau + 1/4}{1-\tau^2} + \frac{R^2}{A^2}E_m^2 - \frac{1}{4}\right]\alpha_{m,x} = 0, \tag{4.48}$$

where $x = \pm$ specifies the spin index in the subscript of $\alpha_{m,x}$. With the substitution

$$\alpha_{m,x} = (1-\tau)^{\frac{1}{2}|m-\frac{x}{2}|}(1+\tau)^{\frac{1}{2}|m+\frac{x}{2}|}\beta_{m,x}, \tag{4.49}$$

and

$$E_m = \frac{A}{R}\lambda_m, \tag{4.50}$$

Equation 4.48 becomes

$$\left[(1-\tau^2)\partial_\tau^2 + \left(x\frac{m}{|m|} - (2|m|+2)\,\tau\right)\partial_\tau - |m|\,(|m|+1) + \lambda_m^2 - \frac{1}{2}\right]\beta_{m,x} = 0. \tag{4.51}$$

We can compare this to the standard form of the Jacobi differential equation (discussed in Appendix A.5),

$$\left[(1-\tau^2)\partial_\tau^2 + (\nu-\mu-(\mu+\nu+2)\tau)\,\partial_\tau + n(n+\mu+\nu+1)\right]J_n^{\mu,\nu}(\tau), \tag{4.52}$$

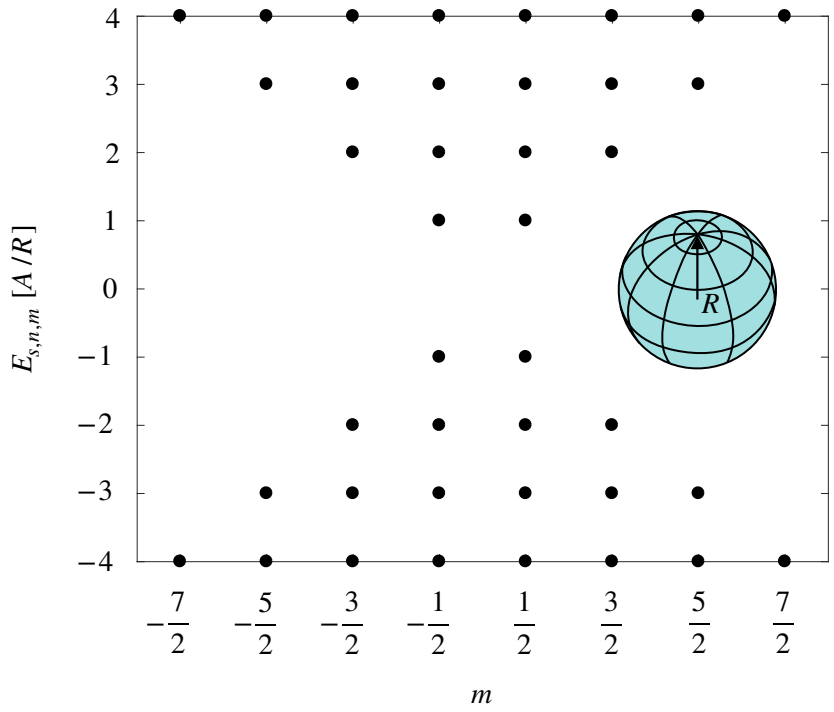

Figure 4.3: **The TI nanosphere:** A TI nanosphere of radius R has surface states described by three quantum numbers (s, n, m) where $s = \pm 1$, $n = 0, 1, 2, 3...$, $m = \pm 1/2, \pm 3/2, \pm 5/2, ...$, with their respective energy levels given by $E_{s,n,m} = s\frac{A}{R}(n+|m|+1/2)$.

where $J_n^{\mu,\nu}(\tau)$ are the Jacobi polynomials and $n = 0, 1, 2, 3, ...$[7]. We identify

$$\mu = |m| - \frac{x}{2}\frac{m}{|m|} = |m - \frac{x}{2}|, \tag{4.53}$$

$$\nu = |m| + \frac{x}{2}\frac{m}{|m|} = |m + \frac{x}{2}|. \tag{4.54}$$

and thus

$$\lambda_m^2 = n(n + \mu + \nu + 1) + |m|(|m| + 1) + \frac{1}{4} \tag{4.55}$$

$$= \left(n + |m| + \frac{1}{2}\right)^2. \tag{4.56}$$

Introducing the additional parameter $s = \pm 1$ for convenience to denote energy levels above and below the Dirac point, we can write the **surface state energies** as

$$E_{s,n,m} = \frac{sA}{R}\left(n + |m| + \frac{1}{2}\right). \tag{4.57}$$

[7]The values of n are necessarily positive integers to allow for the normalisation of the solutions, discussed more in [35].

We can then identify[8]

$$\beta_{m,+} = \beta_{n,m,+} = c_{n,m,+} J_n^{|m-\frac{1}{2}||m+\frac{1}{2}|}(\tau) = N_{n,m} J_n^{|m-\frac{1}{2}||m+\frac{1}{2}|}(\tau), \tag{4.58}$$

$$\beta_{m,-} = \beta_{n,m,-} = c_{n,m,-} J_n^{|m+\frac{1}{2}||m-\frac{1}{2}|}(\tau) = -s\frac{m}{|m|} N_{n,m} J_n^{|m+\frac{1}{2}||m-\frac{1}{2}|}(\tau), \tag{4.59}$$

where $N_{n,m}$ are normalisation constants described in Appendix A.5.

We can then finally recover the (normalised) **surface states**

$$|\Psi_{s,n,m}\rangle = \frac{e^{im\varphi}}{2\sqrt{\pi}R} N_{n,m} \begin{pmatrix} (1-\tau)^{\frac{1}{2}|m-\frac{1}{2}|}(1+\tau)^{\frac{1}{2}|m+\frac{1}{2}|} J_n^{|m-\frac{1}{2}||m+\frac{1}{2}|}(\tau) \\ -\frac{sm}{|m|}(1-\tau)^{\frac{1}{2}|m+\frac{1}{2}|}(1+\tau)^{\frac{1}{2}|m-\frac{1}{2}|} J_n^{|m+\frac{1}{2}||m-\frac{1}{2}|}(\tau) \end{pmatrix}. \tag{4.60}$$

The surface states may be more easily compared to the result of Imura *et al.* [35] by rewriting $\tau = \cos(\vartheta)$, thus demonstrating that we have arrived at the correct result for the limiting case of a TI nanosphere. The discrete energy levels of the TI nanosphere are plotted in Figure 4.3.

We can see that the energy levels have equal spacing (with no energy level at $E = 0$) and degeneracy that grows linearly away from the Dirac point (increasing as 2,4,6,8...). The energy levels inversely scale with R, and so for increasing R the energy level spacing decreases. In the limit of a large particle such that R is large, a continuous Dirac cone is recovered as expected.

Result: TI nanosphere surface states and energy levels

The **surface states** are given by

$$|\Psi_{s,n,m}\rangle = \frac{e^{im\varphi}}{2\sqrt{\pi}R} N_{n,m} \chi_{s,n,m}(\vartheta), \tag{4.61}$$

where

$$\chi_{s,n,m}(\vartheta) = \begin{pmatrix} (1-\cos\vartheta)^{\frac{1}{2}|m-\frac{1}{2}|}(1+\cos\vartheta)^{\frac{1}{2}|m+\frac{1}{2}|} J_n^{|m-\frac{1}{2}||m+\frac{1}{2}|}(\cos\vartheta) \\ -\frac{sm}{|m|}(1-\cos\vartheta)^{\frac{1}{2}|m+\frac{1}{2}|}(1+\cos\vartheta)^{\frac{1}{2}|m-\frac{1}{2}|} J_n^{|m+\frac{1}{2}||m-\frac{1}{2}|}(\cos\vartheta) \end{pmatrix}, \tag{4.62}$$

and the respective **surface state energies** are given by

$$E_{s,n,m} = \frac{sA}{R}\left(n + |m| + \frac{1}{2}\right), \tag{4.63}$$

where $s = \pm 1$, $n = 0, 1, 2, ...$, $m = \pm 1/2, 3/2, 5/2, ...$ [35]

[8] The additional factor of $sm/|m|$ in front of β_{nm-} can be deduced by the rather laborious task of substituting Equations 4.58 and 4.59 into Equations 4.46 and 4.46.

4.2.2 The nanowire

For the nanowire we go to the opposite limit, $\sigma_0 \to 1$ (recalling that σ_0 can take any value ≥ 1.) In this limit, the surface scale factors reduce to

$$h^0_\sigma \sim \frac{L^2}{R}\sqrt{1-\tau^2}, \quad h^0_\tau \sim L, \quad \text{and} \quad h^0_\varphi = R\sqrt{1-\tau^2}, \tag{4.64}$$

where $R = a\sqrt{\sigma_0^2 - 1}$ and $L \sim a$. The eigenstates of $\mathbf{H}_\perp$ reduce to the same expressions as found in [34], such that

$$|+\rangle = \frac{\sqrt{1-\tau}}{2} e^{i\varphi/2} \left((1,i), (1,i)\, e^{-i\varphi}\right)^\dagger, \tag{4.65}$$

$$|-\rangle = \frac{\sqrt{1+\tau}}{2} e^{i\varphi/2} \left((1,-i), (-1,i)\, e^{-i\varphi}\right)^\dagger. \tag{4.66}$$

The components of the surface Hamiltonian reduce to

$$\mathbf{H}^{++}_{\text{surf}} = \mathbf{H}^{--}_{\text{surf}} = 0, \tag{4.67}$$

$$\mathbf{H}^{+-}_{\text{surf}} = A\left[\frac{\sqrt{1-\tau^2}}{L}\partial_\tau - \frac{m}{R} + \frac{1}{L\sqrt{1-\tau^2}}\left(\frac{1}{2} - \tau\right)\right], \tag{4.68}$$

$$\mathbf{H}^{-+}_{\text{surf}} = A\left[-\frac{\sqrt{1-\tau^2}}{L}\partial_\tau - \frac{m}{R} + \frac{1}{L\sqrt{1-\tau^2}}\left(\frac{1}{2} + \tau\right)\right]. \tag{4.69}$$

For $L \gg R$, the particle approaches the dimensions of an infinite cylinder, where the surface states are still confined in the azimuthal direction, but there is no longer confinement along the z axis of the material, and it is sensible to transform to cylindrical coordinates where $\tau^2 \ll 1$ and momentum in the z direction[9] is given by

$$k = -i\partial_z = -i\frac{1}{L}\partial_\tau. \tag{4.70}$$

Appendix A.4 has more details on transforming between coordinate systems. The surface Hamiltonian then reduces to

$$\mathbf{H}_{\text{surf}} = A\begin{pmatrix} 0 & -ik - \frac{m}{R} \\ ik - \frac{m}{R} & 0 \end{pmatrix}. \tag{4.71}$$

Diagonalizing this Hamiltonian, we find the energy eigenvalues to be

$$E_{s,k,m} = \frac{sA}{R}\sqrt{(kR)^2 + m^2}, \tag{4.72}$$

where $s = \pm 1$, k is continuous and $m = \pm 1/2, 3/2, 5/2, ...$ in agreement with Reference [34]. The energy levels for the TI nanowire are plotted in Figure 4.4. We can see a continuum

[9] Recall from Equation 4.2 that $z = a\sigma\tau$, so in the limit of the nanowire, $z = L\tau$. The definition of k then follows.

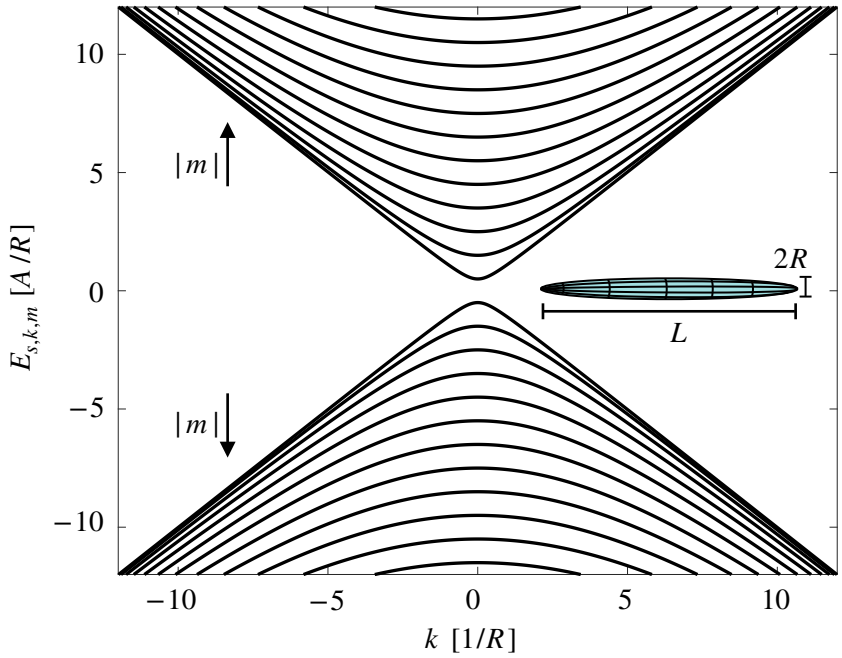

Figure 4.4: **The TI nanowire:** A TI nanowire of radius R and length L where $R \ll L$ has surface states described by the quantum numbers $s = \pm 1$ and $m = \pm 1/2, 3/2, 5/2, ...$ and k, the momentum along the length of the wire, which is continuous. The dispersion relation is given by $E_{s,k,m} = s\frac{A}{R}\sqrt{(kR)^2 + m^2}$.

of states as a function of k, but quantisation in the azimuthal direction is retained, and parameterized by quantum number m. The greatest energy level spacing for a given pair of m values is found at $k = 0$, and the levels get increasingly closer together for higher values of k. The corresponding eigenstates are found to be

$$|\Psi_{s,k,m}\rangle = \frac{e^{i(kz+m\varphi)}}{2\sqrt{\pi RL}} \begin{pmatrix} -s\ i\frac{\sqrt{(kR)^2+m^2}}{kR-im} \\ 1 \end{pmatrix}. \tag{4.73}$$

Result: TI nanowire surface states and energy levels

The **surface states** are given by

$$|\Psi_{s,k,m}\rangle = \frac{e^{i(kz+m\varphi)}}{2\sqrt{\pi RL}} \begin{pmatrix} -s\ i\frac{\sqrt{(kR)^2+m^2}}{kR-im} \\ 1 \end{pmatrix} \tag{4.74}$$

and the respective **surface state energies** are given by

$$E_{s,k,m} = \frac{sA}{R}\sqrt{(kR)^2 + m^2}, \tag{4.75}$$

where $s = \pm 1$, k is continuous and $m = \pm 1/2, 3/2, 5/2, ...$ [34].

4.2.3 General prolate spheroid

A full analytical solution to the general spheroid is unlikely, and so to study the full parameter space of the prolate spheroid we continue with numerics using a **finite-difference** method (given in more detail in Appendix C.1). We start with the two first order, coupled ODEs with σ_0 a real number ≥ 1,

$$\mathbf{H}^{+-}_{\text{surf}}\alpha_{m+} = E_m\alpha_{m-} \tag{4.76}$$

$$\mathbf{H}^{-+}_{\text{surf}}\alpha_{m-} = E_m\alpha_{m+}. \tag{4.77}$$

where (from Equations 4.34 and 4.35),

$$\mathbf{H}^{+-}_{\text{surf}} = \frac{A}{a\sigma_0\sqrt{1-\tau^2}}\left[(1-\tau^2)\partial_\tau - \frac{mh^0_\sigma}{a} + \frac{1-\tau}{2} - \frac{a}{2h^0_\sigma} - \frac{\tau a^2}{2\left(h^0_\tau\right)^2}\right], \tag{4.78}$$

$$\mathbf{H}^{-+}_{\text{surf}} = \frac{A}{a\sigma_0\sqrt{1-\tau^2}}\left[-(1-\tau^2)\partial_\tau - \frac{mh^0_\sigma}{a} + \frac{1+\tau}{2} - \frac{a}{2h^0_\sigma} + \frac{\tau a^2}{2\left(h^0_\tau\right)^2}\right]. \tag{4.79}$$

We combine this into a single, second order ODE, such that

$$\left[F(\tau)\partial^2_\tau + G(\tau)\partial_\tau + H(\tau) - E^2_m\right]\alpha_{m+} = 0, \tag{4.80}$$

where

$$F(\tau) = -\frac{A^2}{a^2\sigma_0^2}(1-\tau^2) \tag{4.81}$$

$$G(\tau) = \frac{A^2}{a^2\sigma_0^2}\frac{\tau\left(1+2\sigma_0^2-3\tau^2\right)}{\sigma_0^2-\tau^2} \tag{4.82}$$

$$\begin{aligned} H(\tau) = \frac{A^2}{4a^2\sigma_0^2}\Bigg(&\frac{\left(1-\frac{a}{h^0_\sigma}-2m\frac{h^0_\sigma}{a}\right)^2 - \tau^2\left(\frac{a^2}{(h^0_\tau)^2}-1\right)^2}{1-\tau^2} + \frac{2}{1+\tau} + \frac{2}{\sigma_0^2-\tau^2} \\ &+ \frac{4\tau^2(1-\sigma_0^2)}{(\sigma_0^2-\tau^2)^2} + \frac{2a^3\tau(1+(1+2m)\sigma_0^2) - 4a^3(m+1)\tau^3}{\left(h^0_\sigma\right)^3(\sigma_0^2-1)(1-\tau^2)}\Bigg). \end{aligned} \tag{4.83}$$

The general form for a second order ODE of this type is given in Appendix A.6. We then solve this second-order equation using the finite-difference method for E_m, and find the energy levels of the prolate nanospheroid. The first three energy levels for values of $|m| \in (7/2, 9/2, 11/2)$ are plotted for all prolate nanospheroids in Figure 4.5, as a function of R_1/R_2, the ratio of the particle axes.[10] For $R_1 \approx R_2$ (from $\sigma_0 \gg 1$) the degenerate levels of the nanosphere are recovered, and for $R_1 \gg R_2$ (equivalently $\sigma_0 \to 1$), we can see that $E \approx A|m|/R$, which are the energy levels of the nanowire for small $|\mathbf{k}|$, as expected. The energy level spectrum for a nanocigar of $R_1 = 1.15R_2$ ($\sigma_0 = 2$) is plotted in Figure 4.6, showing the lifting degeneracy of the energy levels as spherical symmetry is broken.

[10]The lowest values of $|m|$ (i.e. $|m| = 1/2, 3/2$) require slightly more intensive numerics to solve, due to the importance of contributions close to the poles of the particle (such that $|\tau|$ approaches 1), and so I demonstrate the behaviour of the energy levels using larger values of $|m|$ out of convenience.

In Figure 4.7 we demonstrate the changing energy levels for prolate TI nanospheroids deformed in different ways. We plot the first three energy levels for $|m| \in [7/2, 9/2, 11/2, 13/2]$, for varying R_1/R_2 (by varying σ_0). In Figure 4.7a, we take a nanosphere of volume $V = 4\pi R^3/3$ where $R = 50$ nm, and deform it into a long cigar while keeping the volume constant. The volume of the general nanospheroid is given by

$$V = \frac{4\pi}{3} a^3 \sigma_0 (\sigma_0^2 - 1) \tag{4.84}$$

and so to keep volume constant we vary a as a function of σ_0, such that

$$a = \left(\frac{3V}{4\pi\sigma_0(\sigma_0^2 - 1)} \right)^{\frac{1}{3}}. \tag{4.85}$$

In Figure 4.7b we take a nanosphere of surface area $S = 4\pi R^2$ for $R = 50$ nm and deform it into a cigar whilst keeping the surface area constant. The surface area of a prolate nanospheroid is given by

$$S = 2\pi a^2 \left(\sigma_0^2 - 1 + \frac{\eta\sigma_0\sqrt{\sigma_0^2 - 1}}{\sin\eta} \right), \tag{4.86}$$

where $\eta = \arccos(R_2/R_1) = \arccos(\sqrt{\sigma_0^2 - 1}/\sigma_0)$ and so we vary a, such that

$$a = \sqrt{\frac{S_{\text{const}}}{2\pi a^2 \left(\sigma_0^2 - 1 + \frac{\eta\sigma_0\sqrt{\sigma_0^2 - 1}}{\sin\eta} \right)}}. \tag{4.87}$$

In Figure 4.7c we keep the minor-radius, $R_2 = 50$ nm, and thus the cross-section (πR_2^2) of the spheroid constant, whilst elongating along the z-axis to an infinitely long cigar. Under these conditions a varies as

$$a = \frac{R_2}{\sqrt{\sigma_0^2 - 1}}. \tag{4.88}$$

Finally, in Figure 4.7d we keep a constant, which is not a physically motivated condition but which I include for completion. When a is constant, the variation of the energy levels depends inversely on σ_0, and so energies for the nanowire are very large, while those for the nanosphere are small. For all deformations, the solution at $R_1 \approx R_2$ recovers the expected energy levels of the nanosphere, and $R_1 \gg R_2$ gives the nanowire. A geometry of $R_1 \approx 1.1R_2$ ($\sigma_0 \approx 2.5$) already approximately recovers the eigenvalues of the nanosphere. In Figures 4.7a and 4.7b, in which the deformation is performed conserving volume and surface area respectively, for each value of $|m|$ we see lower minimum energies for the sphere than for the wire. This is due to the surface state energies scaling inversely with the semi-minor axis of the particle, which increases when deforming from the nanowire to the nanosphere.

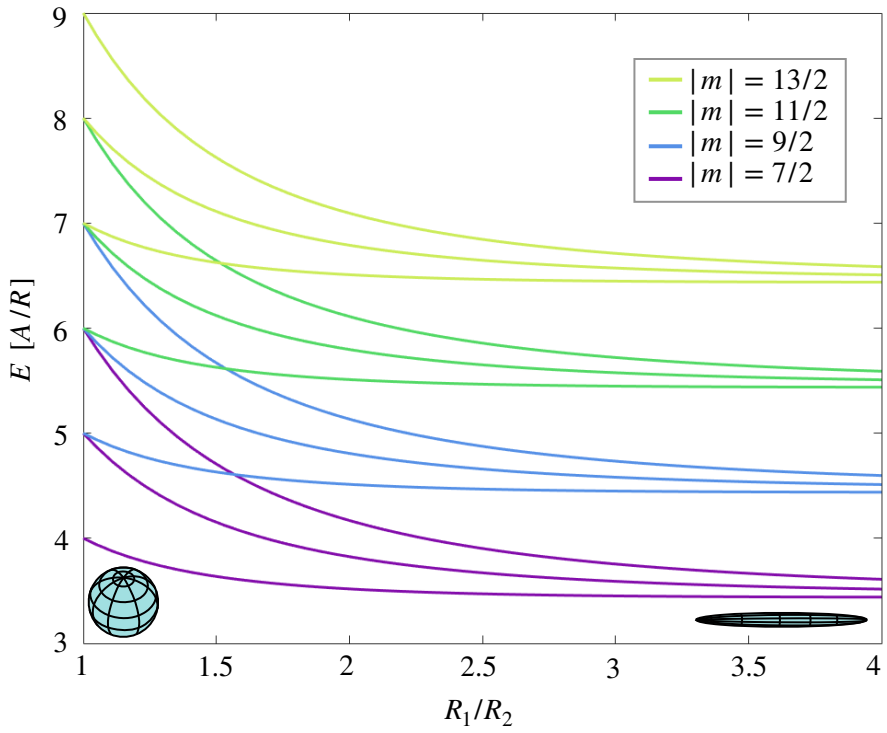

Figure 4.5: **Eigenvalues of the general prolate spheroidal nanoparticle:** First three energy levels of the nanospheroid for varying R_1/R_2 for each of the the $|m|$ values $[7/2, 9/2, 11/2, 13/2]$ and normalised by A/R, where R is the minor-axis of the nanoparticle. In the nanosphere limit $R_1 \approx R_2$ ($\sigma_0 \gg 1$), we see that we recover the energy levels $E = \frac{A}{R}\left(n + |m| + \frac{1}{2}\right)$, and in the limit of the nanowire ($R_1 \gg R_2$) $\sigma_0 \to 1$, $E \approx A|m|/R$.

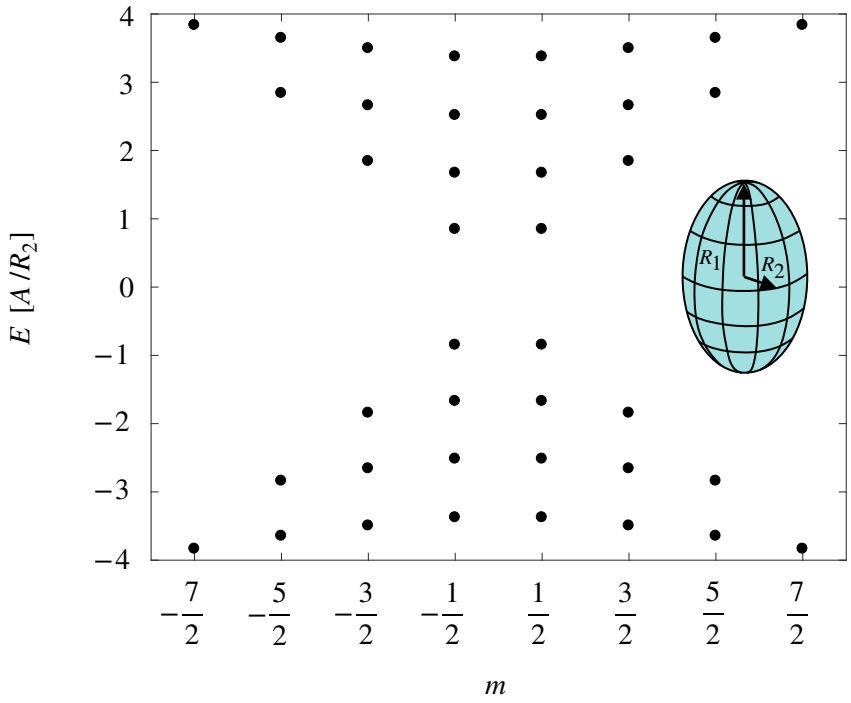

Figure 4.6: **Intermediate prolate spheroidal nanoparticle:** Energy levels for a prolate nanospheroid (nanocigar) with $\sigma_0 = 2$, such that $R_1 \approx 1.15R_2$. The degeneracy of the energy levels is seen to have lifted as the spherical symmetry is broken.

4.3 From prolate to oblate spheroidal TI nanoparticles

To study spheroids for which $R_1 \leq R_2$, we now repeat the same process for **oblate spheroids**. Oblate spheroids allow us to study nanoparticles between the two limiting cases of a **sphere** ($R_1 \approx R_2$) and a **disk** ($R_1 \ll R_2$). As this process is almost entirely repetition of the previous section, I aim to keep it brief and just give major results.

We use the non-standard[11] **oblate spheroidal coordinates** (ζ, τ, φ), where

$$\begin{aligned} x &= a\sqrt{(1+\zeta^2)(1-\tau^2)}\cos\varphi, \\ y &= a\sqrt{(1+\zeta^2)(1-\tau^2)}\sin\varphi, \\ z &= a\zeta\tau, \end{aligned} \tag{4.89}$$

where ζ is a non-negative real number, $\tau \in [-1, 1]$, $\varphi \in [-\pi, \pi]$, and a is a constant of dimension $[L]$. The unit vectors $\hat{\tau}$ and $\hat{\varphi}$ are parallel to the surface of the particle, while $\hat{\zeta}$ is perpendicular to the surface. Constant ζ gives a closed spheroidal surface and we define $\zeta = \zeta_0$ to demarcate the particle surface such that the particle is described by $\zeta \leq \zeta_0$. The

[11] Oblate spheroidal coordinates are usually denoted (ζ, ξ, φ), where $\zeta = \sinh\mu$ and $\xi = \sin\nu$. I instead use the equivalent system, (ζ, τ, φ) where $\tau = \cos(\nu)$ is the same variable defined for prolate coordinates. This does not change much, but allows us to more nicely reduce to the spherical case in the limit $\zeta \gg 1$.

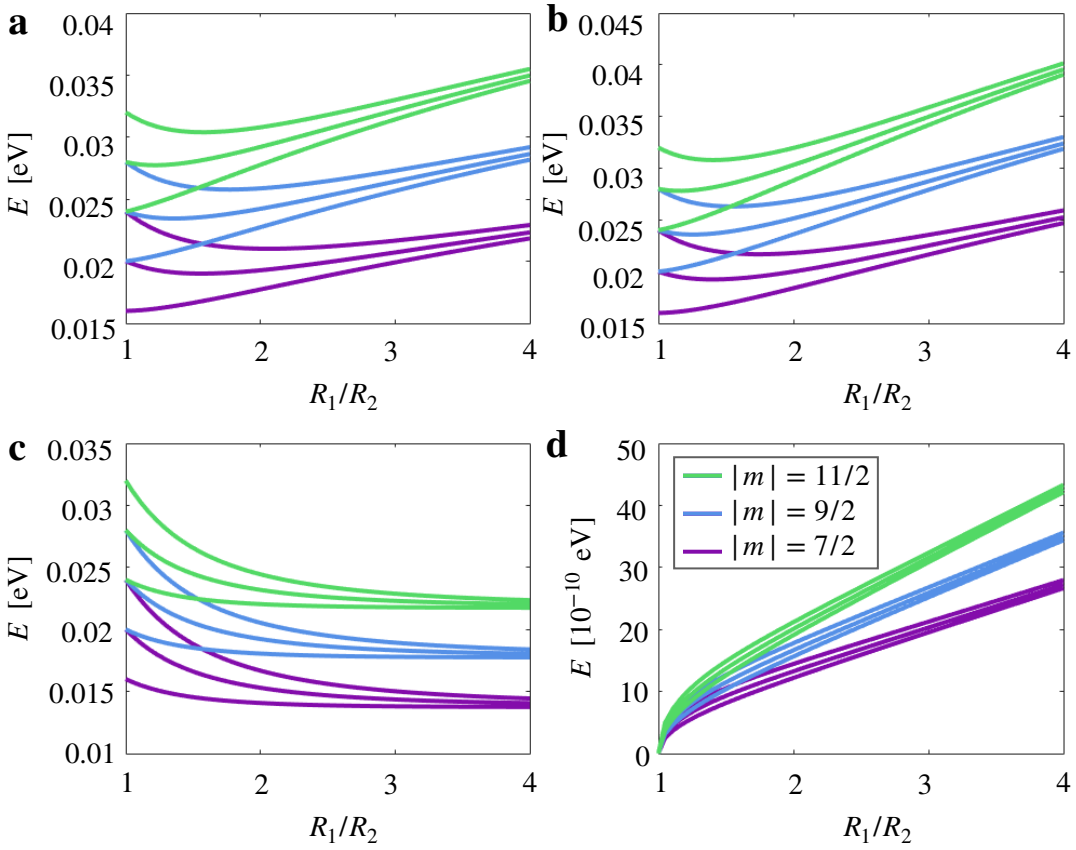

Figure 4.7: **Deforming the TI prolate nanospheroid:** First three energy levels for $m \in [7/2, 9/2, 11/2]$, under various constraints. **(a)** Energy levels of nanospheroid under deformation (by varying R_1/R_2) but with constant volume, equal to that of a nanosphere of $R = 50$ nm. **(b)** Energy levels of nanospheroid of constant surface area, with surface area of that of a nanosphere of R=50 nm. **(c)** Deforming energy levels of a nanospheroid with constant cross-section (retaining cross-section of a 50nm sphere) and changing length **(d)** Energy levels keeping constant a = 1.

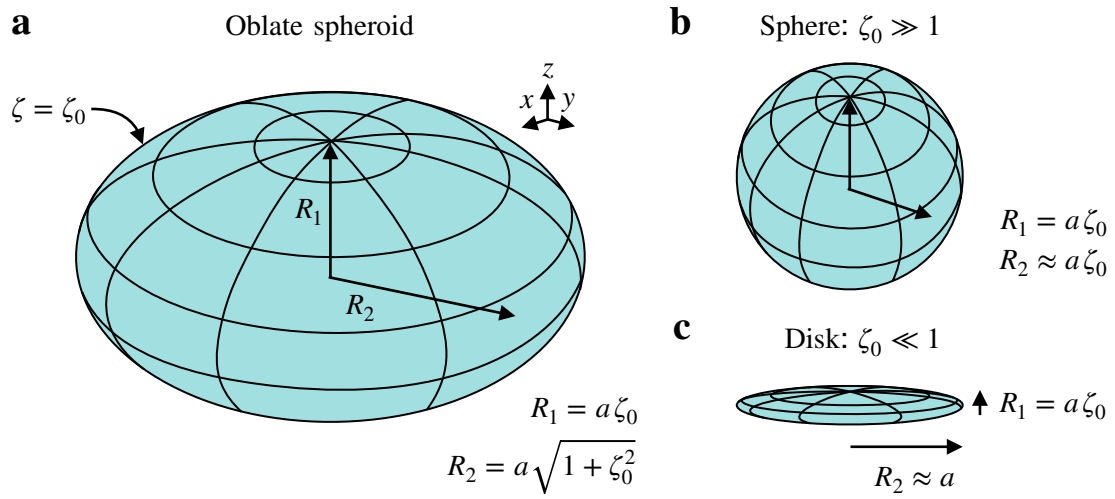

Figure 4.8: **Oblate spheroidal nanoparticles:** We describe our nanoparticles as oblate spheroids. **(a)** Oblate spheroidal nanoparticle with surface given by $\zeta = \zeta_0$ with semi-minor axis $R_1 = a\zeta_0$ (parallel to the z-axis) and semi-major axis $R_2 = a\sqrt{1+\zeta_0^2}$, where $R_1 \leq R_2$. **(b)** The spherical limit with $R_1 \approx R_2$, and **(c)** the limit of a disk, for which $R_1 \ll R_2$.

surface is constrained by the equation

$$\frac{x^2+y^2}{a^2(1+\zeta_0^2)} + \frac{z^2}{a^2\zeta_0^2} = 1, \tag{4.90}$$

where $R_1 = a\zeta_0$ and $R_2 = a\sqrt{1+\zeta_0^2}$ are the semi-minor and semi-major axes respectively (i.e. $R_1 \leq R_2$), illustrated in Figure 4.8a. In the limit $\zeta_0^2 \gg 1$ this reduces to the equation of the surface of a sphere with radius $R_2 \approx R_1 = a\zeta_0$ (demonstrated in Figure 4.8b), and for $\zeta_0 \ll 1$, this reduces to the limit of a disk with radius $R_2 \approx a$ and half-depth $R_1 = a\zeta_0$ (see Figure 4.8c). As for the prolate case, we constrain ourselves to $R_1, R_2 \geq 5$ nm in order that the TI bulk Hamiltonian is still valid. The momentum operator $\mathbf{k} = k_x\hat{\mathbf{x}} + k_y\hat{\mathbf{y}} + k_z\hat{\mathbf{z}}$ can be projected onto the oblate spheroidal unit vectors, such that $\mathbf{k} = k_\zeta\hat{\zeta} + k_\tau\hat{\tau} + k_\varphi\hat{\varphi}$, where

$$k_\zeta = -\frac{i}{h_\zeta}\partial_\zeta, \quad k_\tau = -\frac{i}{h_\tau}\partial_\tau \quad \text{and} \quad k_\varphi = -\frac{i}{h_\varphi}\partial_\varphi, \tag{4.91}$$

where I have introduced the **scale factors**

$$h_\zeta = a\sqrt{\frac{\zeta^2+\tau^2}{1+\zeta^2}}, \quad h_\tau = a\sqrt{\frac{\zeta^2+\tau^2}{1-\tau^2}}, \quad \text{and} \quad h_\varphi = a\sqrt{(1+\zeta^2)(1-\tau^2)}, \tag{4.92}$$

respectively. More details on the oblate coordinate system can be found in Appendix A.4.

The bulk Hamiltonian in oblate coordinates, $\mathbf{H}_{\text{bulk}} = \mathbf{H}_\perp + \mathbf{H}_\parallel$ is given by

$$\begin{aligned}\mathbf{H}_\perp(\mathbf{k}) = \; & m_0 \; \mathbb{1}_2 \otimes \boldsymbol{\sigma_3} - m_1 \; \mathbb{1}_2 \otimes \boldsymbol{\sigma_3} \left[\frac{1}{h_\zeta^2} \partial_\zeta^2 + \frac{2\zeta}{a^2(\zeta^2+\tau^2)} \partial_\zeta \right] \\ & - iA \; \boldsymbol{\sigma_3} \otimes \boldsymbol{\sigma_1} \; \frac{a\tau}{h_\zeta^2} \partial_\zeta - iA \; \boldsymbol{\sigma_1} \otimes \boldsymbol{\sigma_1} \; \frac{a\zeta}{h_\zeta h_\tau} \cos\varphi \; \partial_\zeta \\ & - iA \; \boldsymbol{\sigma_2} \otimes \boldsymbol{\sigma_1} \frac{a\zeta}{h_\zeta h_\tau} \sin\varphi \; \partial_\zeta,\end{aligned} \tag{4.93}$$

and

$$\begin{aligned}\mathbf{H}_\parallel(\mathbf{k}) = \; & - m_1 \; \mathbb{1}_2 \otimes \boldsymbol{\sigma_3} \left[-\frac{2\tau}{a^2(\zeta^2+\tau^2)} \partial_\tau + \frac{1}{h_\tau^2} \frac{\partial^2}{\partial \tau^2} + \frac{1}{h_\varphi^2} \partial_\varphi^2 \right] \\ & - iA \; \boldsymbol{\sigma_3} \otimes \boldsymbol{\sigma_1} \frac{a\zeta}{h_\tau^2} \partial_\tau + iA \; \boldsymbol{\sigma_1} \otimes \boldsymbol{\sigma_1} \left[\frac{a\tau}{h_\zeta h_\tau} \cos\varphi \; \partial_\tau + \frac{\sin\varphi}{h_\varphi} \partial_\varphi \right] \\ & + iA \; \boldsymbol{\sigma_2} \otimes \boldsymbol{\sigma_1} \left[\frac{a\tau}{h_\zeta h_\tau} \sin\varphi \; \partial_\tau - \frac{\cos\varphi}{h_\varphi} \partial_\varphi \right].\end{aligned} \tag{4.94}$$

I choose an ansatz for the 4-component **surface state** of the form

$$|\Phi(\zeta,\tau,\varphi)\rangle = e^{\kappa a(\zeta-\zeta_0)} |u(\zeta_0,\tau,\varphi)\rangle, \tag{4.95}$$

which when acted upon by $\mathbf{H}_\perp$ results in

$$\begin{aligned}\mathbf{H}_\perp(\kappa) = \; & m_0 \; \mathbb{1}_2 \otimes \boldsymbol{\sigma_3} - m_1 \left[\frac{1}{h_\zeta^2} \kappa^2 a^2 + \frac{2\kappa\zeta}{a(\zeta^2+\tau^2)} \right] \mathbb{1}_2 \otimes \boldsymbol{\sigma_3} \\ & - iA \; \frac{\kappa a^2 \tau}{h_\zeta^2} \; \boldsymbol{\sigma_3} \otimes \boldsymbol{\sigma_1} - iA \; \frac{\kappa a^2 \zeta}{h_\zeta h_\tau} \cos\varphi \; \boldsymbol{\sigma_1} \otimes \boldsymbol{\sigma_1} - iA \frac{\kappa a^2 \zeta}{h_\zeta h_\tau} \sin\varphi \; \boldsymbol{\sigma_2} \otimes \boldsymbol{\sigma_1},\end{aligned} \tag{4.96}$$

where κ is the **decay constant** describing the evanescence of the surface wave function into the bulk. κ^{-1} is of the order of a few Å, and so we set $\zeta = \zeta_0$ for the rest of these calculations.

By enforcing that the Γ-point be at $E = 0$, we have the condition that

$$\mathbf{H}_\perp |\Phi(\zeta_0,\tau,\varphi)\rangle = E_\perp |\Phi(\zeta_0,\tau,\varphi)\rangle = 0, \tag{4.97}$$

and we find two degenerate eigenstates of $\mathbf{H}_\perp$,

$$|+\rangle = \frac{\sqrt{1-\tau}}{2} \left((1,i) \, h_\tau^0 \left(\frac{1}{a\zeta_0} + \frac{\tau}{h_\zeta^0 \zeta} \right) e^{i\varphi/2}, (1,i) \, e^{-i\varphi/2} \right)^\dagger, \tag{4.98}$$

$$|-\rangle = \frac{\sqrt{1+\tau}}{2} \left((1,-i) \, h_\tau^0 \left(\frac{1}{a\zeta_0} - \frac{\tau}{h_\zeta^0 \zeta_0} \right) e^{i\varphi/2}, (-1,i) \, e^{-i\varphi/2} \right)^\dagger, \tag{4.99}$$

where any surface state can then be written as a linear combination of $|+\rangle$ and $|-\rangle$ with

amplitude specified by α_+ and α_- respectively, such that the 4-component surface state is given by

$$|\Phi\rangle = \alpha_+(\tau,\varphi,\zeta_0)|+\rangle + \alpha_-(\tau,\varphi,\zeta_0)|-\rangle. \tag{4.100}$$

Result: Oblate spheroidal TI nanostructure surface state form

The 4-component **surface state** has the form

$$|\Phi\rangle = \alpha_+(\tau,\varphi,\zeta_0)|+\rangle + \alpha_-(\tau,\varphi,\zeta_0)|-\rangle \tag{4.101}$$

where

$$|+\rangle = \frac{\sqrt{1-\tau}}{2}\left((1,i)\,e^{i\varphi/2}\left(\frac{h_\tau^0}{a\zeta_0}+\frac{\tau h_\tau^0}{h_\zeta^0\zeta_0}\right),\ (1,i)\,e^{-i\varphi/2}\right)^\dagger, \tag{4.102}$$

$$|-\rangle = \frac{\sqrt{1+\tau}}{2}\left((1,-i)\,e^{i\varphi/2}\left(\frac{h_\tau^0}{a\zeta_0}-\frac{\tau h_\tau^0}{h_\zeta^0\zeta_0}\right),\ (-1,i)\,e^{-i\varphi/2}\right)^\dagger. \tag{4.103}$$

We now focus our attention on $\mathbf{H}_\parallel$, given in Equation 4.94, but repeated here for clarity,

$$\begin{aligned}\mathbf{H}_\parallel(\mathbf{k}) = &-m_1\ \mathbb{1}_2\otimes\boldsymbol{\sigma_3}\left[-\frac{2\tau}{a^2(\zeta_0^2+\tau^2)}\partial_\tau+\frac{1}{(h_\tau^0)^2}\frac{\partial^2}{\partial\tau^2}+\frac{1}{(h_\varphi^0)^2}\partial_\varphi^2\right]\\ &-iA\ \boldsymbol{\sigma_3}\otimes\boldsymbol{\sigma_1}\frac{a\zeta_0}{(h_\tau^0)^2}\partial_\tau+iA\ \boldsymbol{\sigma_1}\otimes\boldsymbol{\sigma_1}\left[\frac{a\tau}{h_\zeta^0 h_\tau^0}\cos\varphi\ \partial_\tau+\frac{\sin\varphi}{h_\varphi^0}\partial_\varphi\right]\\ &+iA\ \boldsymbol{\sigma_2}\otimes\boldsymbol{\sigma_1}\left[\frac{a\tau}{h_\zeta^0 h_\tau}\sin\varphi\ \partial_\tau-\frac{\cos\varphi}{h_\varphi^0}\partial_\varphi\right].\end{aligned} \tag{4.104}$$

We note that all terms scale either with $m_1/(a\zeta_0)^2$ or $A/(a\zeta_0)$, where, as discussed in Chapter 2, m_1 ∼1-10 eV Å^2 and A ∼1-10 eV Å with exact values dependent on material choice. Recalling the condition on system size in order for the bulk Hamiltonian and surface state ansatz to hold, we work in the limit $a\zeta_0 \gg$Å, and so all terms with coefficient $m_1/(a\zeta_0)^2$ can be considered negligible. This greatly simplifies the form of $\mathbf{H}_\parallel$, and in particular removes all second derivatives, such that

$$\begin{aligned}\mathbf{H}_\parallel(\mathbf{k}) = &\ iA\ \boldsymbol{\sigma_3}\otimes\boldsymbol{\sigma_1}\frac{a\zeta_0}{(h_\tau^0)^2}\partial_\tau+iA\ \boldsymbol{\sigma_1}\otimes\boldsymbol{\sigma_1}\left[\frac{a\tau}{h_\zeta^0 h_\tau^0}\cos\varphi\ \partial_\tau+\frac{\sin\varphi}{h_\varphi^0}\partial_\varphi\right]\\ &+iA\ \boldsymbol{\sigma_2}\otimes\boldsymbol{\sigma_1}\left[\frac{a\tau}{h_\zeta^0 h_\tau}\sin\varphi\ \partial_\tau-\frac{\cos\varphi}{h_\varphi^0}\partial_\varphi\right].\end{aligned} \tag{4.105}$$

Projecting this Hamiltonian onto the general surface state $|\Phi\rangle$, we recover a 2×2 effective

surface Hamiltonian, such that

$$\begin{pmatrix} \langle + | \mathbf{H}_{\parallel} | \Phi \rangle \\ \langle - | \mathbf{H}_{\parallel} | \Phi \rangle \end{pmatrix} = \begin{pmatrix} \mathbf{H}_{\text{surf}}^{++} & \mathbf{H}_{\text{surf}}^{+-} \\ \mathbf{H}_{\text{surf}}^{-+} & \mathbf{H}_{\text{surf}}^{--} \end{pmatrix} \begin{pmatrix} \alpha_+ \\ \alpha_- \end{pmatrix} = \mathbf{H}_{\text{surf}} |\Psi\rangle, \tag{4.106}$$

where $|\Psi\rangle$ is the 2-component state

$$|\Psi\rangle = \begin{pmatrix} \alpha_+ \\ \alpha_- \end{pmatrix}. \tag{4.107}$$

We find that

$$\mathbf{H}_{\text{surf}}^{++} = \mathbf{H}_{\text{surf}}^{--} = 0, \tag{4.108}$$

$$\mathbf{H}_{\text{surf}}^{+-} = \frac{A}{a\zeta_0\sqrt{1-\tau^2}} \left[(1-\tau^2)\partial_\tau + i\frac{h_\zeta^0}{a}\partial_\varphi - \frac{a}{2h_\zeta^0} + \frac{(1-\tau)}{2} + \frac{a^2\tau}{2\left(h_\tau^0\right)^2} \right] \tag{4.109}$$

$$\mathbf{H}_{\text{surf}}^{-+} = \frac{A}{a\zeta_0\sqrt{1-\tau^2}} \left[-(1-\tau^2)\partial_\tau + i\frac{h_\zeta^0}{a}\partial_\varphi - \frac{a}{2h_\zeta^0} + \frac{(1+\tau)}{2} - \frac{a^2\tau}{2\left(h_\tau^0\right)^2} \right] \tag{4.110}$$

This 2×2 effective surface Hamiltonian is in the form of a Dirac Hamiltonian, that is the Hamiltonian describing the dynamics of massless fermions and the surface states satisfy the eigenvalue equation

$$\mathbf{H}_{\text{surf}} |\Psi\rangle = E |\Psi\rangle. \tag{4.111}$$

As the spheroid has azimuthal symmetry[12], we are able to separate variables, such that

$$|\Psi_m\rangle = e^{im\varphi} \begin{pmatrix} \alpha_{m,+}(\tau) \\ \alpha_{m,-}(\tau) \end{pmatrix}, \tag{4.112}$$

where m is restricted to half-integer values [35], such that $m = \pm 1/2, \pm 3/2, ...$ When applying $\mathbf{H}_{\text{surf}}$ to this state, Equation 4.111 reduces to the coupled, first-order ordinary differential equations (ODEs)

$$\frac{A}{a\zeta_0\sqrt{1-\tau^2}} \left[(1-\tau^2)\partial_\tau - \frac{mh_\zeta^0}{a} - \frac{a}{2h_\zeta^0} + \frac{(1-\tau)}{2} + \frac{a^2\tau}{2\left(h_\tau^0\right)^2} \right] \alpha_{m,-} = E_m \alpha_{m,+}, \tag{4.113}$$

$$\frac{A}{a\zeta_0\sqrt{1-\tau^2}} \left[-(1-\tau^2)\partial_\tau - \frac{mh_\zeta^0}{a} - \frac{a}{2h_\zeta^0} + \frac{(1+\tau)}{2} - \frac{a^2\tau}{2\left(h_\tau^0\right)^2} \right] \alpha_{m,+} = E_m \alpha_{m,-}.. \tag{4.114}$$

In the next section we will study the limiting cases and discuss the solution for the general case.

[12] Symmetry about the z-axis.

Result: Oblate spheroidal TI nanostructure surface state Hamiltonian

The 2-component **surface state** $|\Psi_m\rangle = e^{im\varphi}(\alpha_{m+}, \alpha_{m-})^T$, obeys the **Dirac** surface state eigenvalue equation

$$\mathbf{H}_{\text{surf}}|\Psi_m\rangle = \begin{pmatrix} 0 & \mathbf{H}_{\text{surf}}^{+-} \\ \mathbf{H}_{\text{surf}}^{-+} & 0 \end{pmatrix} |\Psi_m\rangle = \lambda \frac{A}{a\zeta_0}|\Psi_m\rangle, \tag{4.115}$$

where $m = \pm 1/2, \pm 3/2, \pm 5/2, ...$ and

$$\mathbf{H}_{\text{surf}}^{+-} = \frac{A}{a\zeta_0\sqrt{1-\tau^2}}\left[(1-\tau^2)\partial_\tau - \frac{mh_\zeta^0}{a} - \frac{a}{2h_\zeta^0} + \frac{(1-\tau)}{2} + \frac{a^2\tau}{2\left(h_\tau^0\right)^2}\right], \tag{4.116}$$

$$\mathbf{H}_{\text{surf}}^{-+} = \frac{A}{a\zeta_0\sqrt{1-\tau^2}}\left[-(1-\tau^2)\partial_\tau - \frac{mh_\zeta^0}{a} - \frac{a}{2h_\zeta^0} + \frac{(1+\tau)}{2} - \frac{a^2\tau}{2\left(h_\tau^0\right)^2}\right]. \tag{4.117}$$

This can be written as two first-order coupled ODEs,

$$\mathbf{H}_{\text{surf}}^{+-}\alpha_{m,-} = E_m\alpha_{m,+} \tag{4.118}$$

$$\mathbf{H}_{\text{surf}}^{-+}\alpha_{m,+} = E_m\alpha_{m,-}. \tag{4.119}$$

4.4 General and limiting cases

The limits to consider for the oblate spheroid are (i) the nanosphere, which was already covered in some detail in Section 4.2.1 and (ii) the nanodisk. We will also discuss the solution of the general oblate spheroid.

4.4.1 The nanosphere

In order to recover the limit of the **nanosphere**, we set $\zeta_0 \gg 1$. We identify $R = a\zeta_0$. The surface of the particle (from Equation 4.90) reduces to

$$x^2 + y^2 + z^2 = R^2, \tag{4.120}$$

where we have identified $R = a\zeta_0$ as the radius of the nanosphere, as illustrated in Figure 4.3a. The reduced surface scale factors are given by

$$h_\zeta^0 = a, \quad h_\tau^0 = \frac{R}{\sqrt{1-\tau^2}}, \quad \text{and} \quad h_\varphi^0 = R\sqrt{1-\tau^2}. \tag{4.121}$$

The first-order coupled equations then reduce to (neglecting $1/R^3$ terms)

$$\frac{A}{R\sqrt{1-\tau^2}}\left[(1-\tau^2)\partial_\tau - m - \frac{\tau}{2}\right]\alpha_{m,+} = E_m\alpha_{m,-} \tag{4.122}$$

$$\frac{A}{R\sqrt{1-\tau^2}}\left[-(1-\tau^2)\partial_\tau - m + \frac{\tau}{2}\right]\alpha_{m,-} = E_m\alpha_{m,+}, \tag{4.123}$$

which is exactly the same form as recovered in Section 4.2.1, and so the calculation follows identically from here. We thus arrive at the usual result for the nanosphere, where the **surface states** are given by

$$|\Psi_{s,n,m}\rangle = \frac{e^{im\varphi}}{2\sqrt{\pi}R}N_{n,m}\begin{pmatrix}(1-\tau)^{\frac{1}{2}|m-\frac{1}{2}|}(1+\tau)^{\frac{1}{2}|m+\frac{1}{2}|}J_n^{|m-\frac{1}{2}||m+\frac{1}{2}|}(\tau)\\ -\frac{sm}{|m|}(1-\tau)^{\frac{1}{2}|m+\frac{1}{2}|}(1+\tau)^{\frac{1}{2}|m-\frac{1}{2}|}J_n^{|m+\frac{1}{2}||m-\frac{1}{2}|}(\tau)\end{pmatrix}, \tag{4.124}$$

and their respective **surface state energies** are given by

$$E_{s,n,m} = \frac{sA}{R}\left(n + |m| + \frac{1}{2}\right). \tag{4.125}$$

4.4.2 The nanodisk

Moving on to the limit $\zeta_0 \ll 1$, we find a **nanodisk** of radius $R \approx a$ and depth $h \approx 2a\zeta_0$. To ensure confinement in the radial direction, we must physically restrict ourselves to $R \lessapprox 100$ nm,[13] and to ensure a true bulk we limit $h \gtrapprox 10$ nm. This realistically sets the lower limit of $\zeta_0 \approx 0.05$. However, the mathematical limit of $\zeta_0 \ll 1$ can be taken to find the energy levels for the **ideal nanodisk** and I include this result for completion. To retrieve the ideal nanodisk limit, it is useful to note the reduced **scale factors**,

$$h_\zeta^0 \approx a|\tau|, \quad h_\tau^0 \approx a\frac{|\tau|}{\sqrt{1-\tau^2}} \quad \text{and} \quad h_\varphi^0 \approx a\sqrt{1-\tau^2}. \tag{4.126}$$

We then find that the four component surface state,

$$|\Phi_m\rangle = e^{im\varphi}\left(\alpha_{m+}(\tau,\zeta_0)|+\rangle + \alpha_{m-}(\tau,\zeta_0)|-\rangle\right), \tag{4.127}$$

is a linear combination of the $\mathbf{H}_\perp$ eigenstates,

$$|+\rangle = \frac{\sqrt{1-\tau}}{2}\left((1,i)\,e^{i\varphi/2}\frac{2R}{h}\frac{(|\tau|+\tau)}{\sqrt{1-\tau^2}},\ (1,i)\,e^{-i\varphi/2}\right)^\dagger, \tag{4.128}$$

$$|-\rangle = \frac{\sqrt{1+\tau}}{2}\left((1,-i)\,e^{i\varphi/2}\frac{2R}{h}\frac{(|\tau|-\tau)}{\sqrt{1-\tau^2}},\ (-1,i)\,e^{-i\varphi/2}\right)^\dagger. \tag{4.129}$$

The 2×2 effective Hamiltonian,

[13] For radii greater than approximately 100 nm, there is no longer quantum confinement in the radial direction and m is not considered a good quantum number.

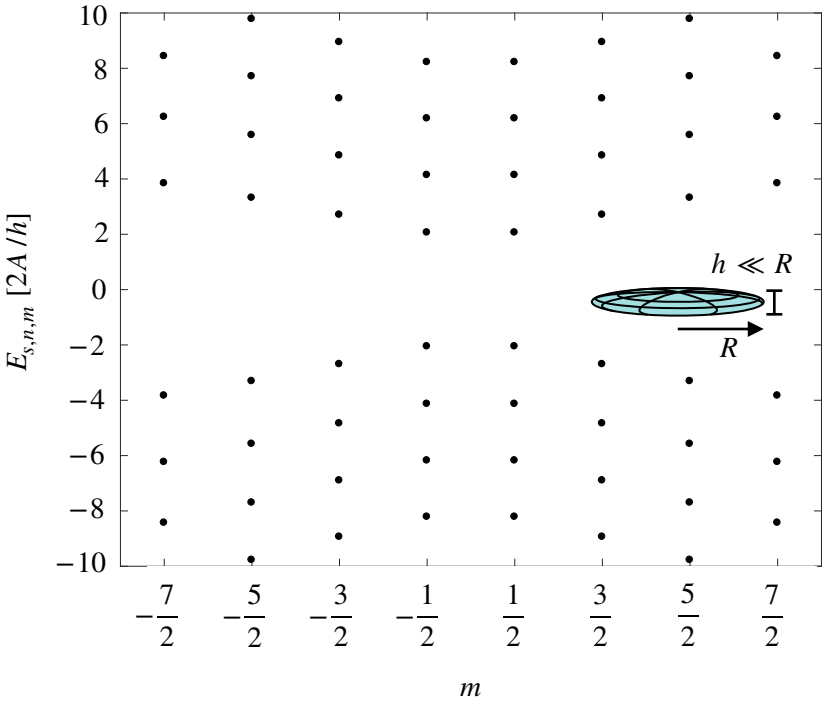

Figure 4.9: **The ideal TI nanodisk:** The energy levels of an ideal TI nanodisk of radius R and depth h, with aspect ratio $\ll 1$. This limit breaks the physically required conditions of confinement in the radial direction and a finite bulk, but is given here for completion. These energy levels are doubly degenerate, corresponding to $\text{sign}(\tau) = \pm 1$, which relate to the decoupled upper and lower surfaces of the disk.

$$\mathbf{H}_{\text{surf}} \begin{pmatrix} \alpha_{m,+} \\ \alpha_{m,-} \end{pmatrix} = \begin{pmatrix} \mathbf{H}^{++}_{\text{surf}} & \mathbf{H}^{+-}_{\text{surf}} \\ \mathbf{H}^{-+}_{\text{surf}} & \mathbf{H}^{--}_{\text{surf}} \end{pmatrix} \begin{pmatrix} \alpha_{m,+} \\ \alpha_{m,-} \end{pmatrix} = E_m \begin{pmatrix} \alpha_{m,+} \\ \alpha_{m,-} \end{pmatrix}, \tag{4.130}$$

reduces to the coupled first-order equations

$$\frac{2A}{h\sqrt{1-\tau^2}}\left[-(1-\tau^2)\partial_\tau - m|\tau| - \frac{1}{2|\tau|} + \frac{(1+\tau)}{2} - \frac{(1-\tau^2)}{2\tau}\right]\alpha_{m,+} = E_m \alpha_{m,-}, \tag{4.131}$$

$$\frac{2A}{h\sqrt{1-\tau^2}}\left[(1-\tau^2)\partial_\tau - m|\tau| - \frac{1}{2|\tau|} + \frac{(1-\tau)}{2} + \frac{(1-\tau^2)}{2\tau}\right]\alpha_{m,-} = E_m \alpha_{m,+}. \tag{4.132}$$

We can combine these into a single, second order equation for $\alpha_{m,x}$, where the subscript x denotes the spin index and we rewrite the eigenvalues as $E_m = 2A\lambda_m/h$.

$$\left[F(\tau)\partial_\tau^2 + G(\tau)\partial_\tau + H_x(\tau) - E_m^2\right]\alpha_{m,x} = 0, \tag{4.133}$$

where

$$F(\tau) = -(1-\tau^2), \tag{4.134}$$

$$G(\tau) = 3\tau - \frac{1}{\tau}, \tag{4.135}$$

$$\begin{aligned} H_x(\tau) = \frac{1}{4\tau^2(1-\tau^2)}\Big[&2 + \tau^2\left(4(m^2-1)\tau^2 - 2x\tau + 5 + 4m\right) \\ &- 2\left(\tau - x\right)\left(2\tau(m\tau - x) - 1\right)\operatorname{sign}(\tau)\Big]. \end{aligned} \tag{4.136}$$

by substituting $t = |\tau|$ and $b = \operatorname{sign}(\tau)$ such that $\tau = bt$, we can rewrite the equation such that

$$\left[F(t)\partial_t^2 + G(t)\partial_t + H_x(t) - E_m^2\right]\alpha_{m,x} = 0, \tag{4.137}$$

where

$$F(t) = -(1-t^2), \tag{4.138}$$

$$G(t) = 3t - \frac{1}{t}, \tag{4.139}$$

$$\begin{aligned} H_x(t) = \frac{1}{4t^2(1-t^2)}\Big[&2 - 2t + 4(m^2-1)t^4 - 2bx \\ &- 2t^3(2m + bx) + t^2(5 + 4bx + 4m(1+bx))\Big]. \end{aligned} \tag{4.140}$$

In this form, we can notice that b and x always occur as a product, so we rewrite $z = bx$,

where $z = \pm 1$. We can then rewrite the $H(t)$ term as

$$H_z(t) = \frac{1}{4t^2(1-t^2)}\Big[2 - 2t + 4(m^2-1)t^4 - 2z \\ - 2t^3(2m+z) + t^2(5+4z+4m(1+z))\Big]. \tag{4.141}$$

Using a **finite difference method** (given in more detail in Appendix C.1), we plot the resulting energy levels of the ideal TI nanodisk in Figure 4.9.

The fact that the degenerate eigenvalues correspond to $z = x\text{sign}(\tau) = \pm 1$ (where $x = \pm 1$ and $\text{sign}(\tau) = \pm 1$) presents a departure from the solutions for the sphere and the nanowire, which rely only on the spin-index, x. Recalling that $\tau \in [-1, 1]$ relates to the polar angle $\tau = \cos(\nu)$, this distinction pertains to the top and bottom surfaces of the disk. These two surfaces have separate sets of energy levels, which intuitively makes sense as this system should tend towards the expected behaviour of a thin film, in which surface states on the top and bottom surfaces can be treated separately. It is interesting to note that the energy eigenvalues of the ideal TI nanodisk appear to scale inversely with disk height, h, rather than radius, R. This conclusion is a little misleading, as the two parameters are of course related by the aspect ratio of the disk, $h = 2\zeta_0 R$, where $\zeta_0 \ll 1$. The energy levels thus also scale inversely with R. So, the continuous Dirac cone is recovered in the limit that h and R become large with fixed ζ_0. The limit of a 2D thin film is expected if h remains small but R is large. In this limit, a gap at $\mathbf{k} = 0$ is expected, $\Delta \sim 1/h^2$ [194].

4.4.3 General oblate spheroid

We now have successfully recovered the analytical limit of the nanosphere for $\zeta_0 \gg 1$ and discussed the previously unknown limit of the ideal nanodisk for $\zeta_0 \ll 1$. We now undertake a numerical study for oblate spheroids of arbitrary ζ_0 using the same **finite-difference** method used already (and again, given in more detail in Appendix C.1).

We recall that the two coupled first order differential equations to be solved are

$$\frac{A}{a\zeta_0\sqrt{1-\tau^2}}\left[(1-\tau^2)\partial_\tau - \frac{mh_\zeta^0}{a} - \frac{a}{2h_\zeta^0} + \frac{(1-\tau)}{2} + \frac{a^2\tau}{2\left(h_\tau^0\right)^2}\right]\alpha_{m-} = E_m\alpha_{m+}, \tag{4.142}$$

$$\frac{A}{a\zeta_0\sqrt{1-\tau^2}}\left[-(1-\tau^2)\partial_\tau - \frac{mh_\zeta^0}{a} - \frac{a}{2h_\zeta^0} + \frac{(1+\tau)}{2} - \frac{a^2\tau}{2\left(h_\tau^0\right)^2}\right]\alpha_{m+} = E_m\alpha_{m-}. \tag{4.143}$$

In order to solve this set of coupled equations, we must again combine them into a single, second-order differential equation. In doing so, we find the equation

$$\left[F(\tau)\partial_\tau^2 + G(\tau)\partial_\tau + H_x(\tau) - E_m^2\right]\alpha_{mx} = 0, \tag{4.144}$$

where

$$F(\tau) = -\frac{A^2}{a^2\zeta_0^2}(1-\tau^2), \tag{4.145}$$

$$G(\tau) = \frac{A^2}{a^2\zeta_0^2}\tau\left[3 - \frac{a^2}{\left(h_\zeta^0\right)^2}\right], \tag{4.146}$$

$$\begin{aligned} H(\tau) = \frac{A^2}{2a^2\zeta_0^2}\Bigg[&\frac{a\tau x\left(a^2 - 2\left(h_\zeta^0\right)^2 m\right)}{\left(\zeta_0^2+1\right)\left(h_\zeta^0\right)^3} + \frac{\tau^2\left(a^2 - \left(h_\tau^0\right)^2\right)^2}{2\left(h_\tau^0\right)^4(\tau^2-1)} + \frac{2\left(\frac{h_\zeta^0 m}{a} + \frac{a}{2h_\zeta^0} - \frac{1}{2}\right)^2}{1-\tau^2} \\ &- \frac{2h_\zeta^0 m\tau x}{a(1-\tau^2)} + \frac{a\tau x}{h_\zeta^0(\tau^2-1)} + \frac{\tau^2}{\zeta_0^2+\tau^2} - \frac{a^2}{\left(h_\tau^0\right)^2} \\ &- \frac{2\tau^2\left(\tau^2-1\right)}{\left(\zeta_0^2+\tau^2\right)^2} - \frac{\tau(\tau+x)}{\tau^2-1} + 1\Bigg]. \end{aligned} \tag{4.147}$$

We then solve this second-order equation numerically for E_m, and I present the results for varying ratio R_1/R_2 in Figure 4.10. I plot the first four positive energy levels (such that $s = +1$) for values of the quantum number $|m| \in [7/2, 9/2, 11/2, 13/2]$, normalised by $A/R_1 = 2A/h$, where $h = 2R_1$ is the height of the spheroid. For $R_1 \approx R_2$ (such that $\zeta_0 \gg 1$), we see that the eigenvalues of the nanosphere are recovered, such that $E_{+,\mathrm{n},\mathrm{m}} = 2A(n + |m| + 1/2)/h$, where $h = 2R$. For $R_1 \ll R_2$ ($\zeta_0 \ll 1$), such that the ratio between the height and radius of the disk becomes vanishingly small, the limit of the ideal nanodisk is recovered. The physical cutoff $R_1 \approx 0.05R_2$ is highlighted (corresponding to $\zeta_0 = 0.05$).

In Figure 4.11 I plot the eigenvalues of the finite disk at the physical cutoff $\zeta_0 = 0.05$, where I use the values $h = 10$ nm and $R = 100$ nm. This is the largest ratio between R and h before either confinement is lost in the radial direction, or the depth of the disk becomes too thin for the bulk Hamiltonian to be valid. As this disk thickness the degeneracy of the states corresponding to the upper and lower surface states has begun to lift, but the limit of the ideal, flat disk gives a satisfactory approximation. This may allow for simplified results in later calculations. As the thickness of the disk is increased, this approximation should instead be replaced by the values obtained for a disk of the correct thickness.

In Figure 4.12 I summarise the results of this chapter by plotting the first three energy levels for $|m| \in [7/2, 9/2, 11/2, 13/2]$ for all geometries from the nanodisk to the nanowire as a function of the spheroid aspect ratio, R_1/R_2. The energies in this plot are normalised with

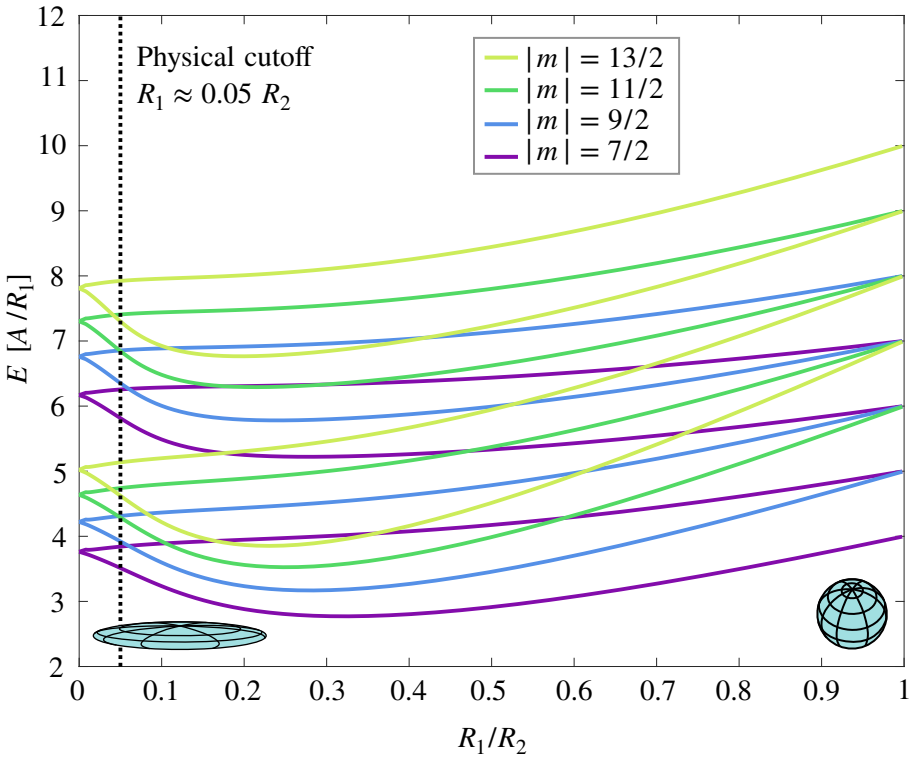

Figure 4.10: **Eigenvalues of the general oblate nanospheroid:** First four energy levels of the nanospheroid for varying R_1/R_2, for the $|m|$ values $[7/2, 9/2, 11/2, 13/2]$ and normalised by $A/R_1 = 2A/h$, where R_1 is the minor-axis of the spheroid or equivalently $h = 2R_1$, where h is the height of the spheroid. In the limit $R_1 \approx R_2$ ($\zeta_0 \gg 1$) we recover the limit of the sphere such that $E = s\frac{A}{R}(n + |m| + \frac{1}{2})$ and in the limit of the ideal, flat nanodisk $R_1 \ll R_2$ ($\zeta_0 \ll 1$), we observe the onset of degeneracy relating to the two sets of degenerate energy levels corresponding to the decoupled upper and lower surfaces off the disk. The physical limit of a nanodisk with complete quantum confinement ($R \leq 100$ nm)and a true bulk ($h = 2R_1 \geq 10$ nm) is denoted with the dotted line at $R_1 = 0.05R_2$ (which corresponds to $\zeta_0 = 0.05$).

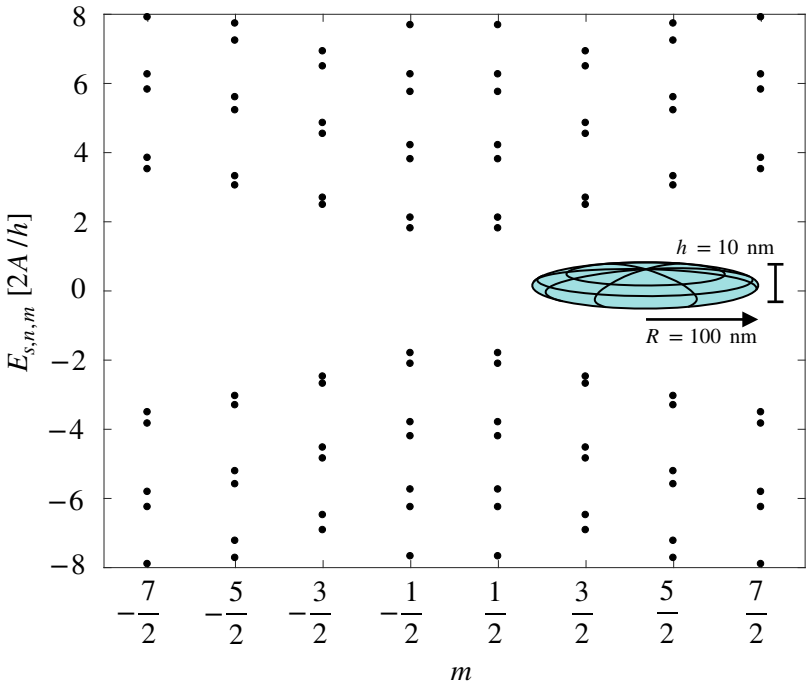

Figure 4.11: **Finite nanodisk:** Energy levels for the finite nanodisk, in which the disk is assumed to be as flat as possible without losing the 3D bulk of the material ($h = 10$ nm) and the disk is as wide as possible before axial quantum confinement is relinquished ($R = 100$ nm). These combined conditions give a minimum value of $\zeta_0 = 0.05$.

respect to A/R_2, where for the oblate spheroid R_2 is the semi-major axis (in comparison to Figure 4.10 in which values are normalised with respect to A/R_1), which accounts for the large energy values when tending towards the limit of the ideal nanodisk. Now that we have the full spectrum of possible energy levels for the nanospheroid, the next chapters will be devoted to the study of the optical properties of nanostructures and their applications. For mathematical simplicity we use a spherical TINP for all applications in Chapters 5 and 6, but with these new electronic structure calculations all results in the following chapters could be extended to systems of any spheroidal geometry.

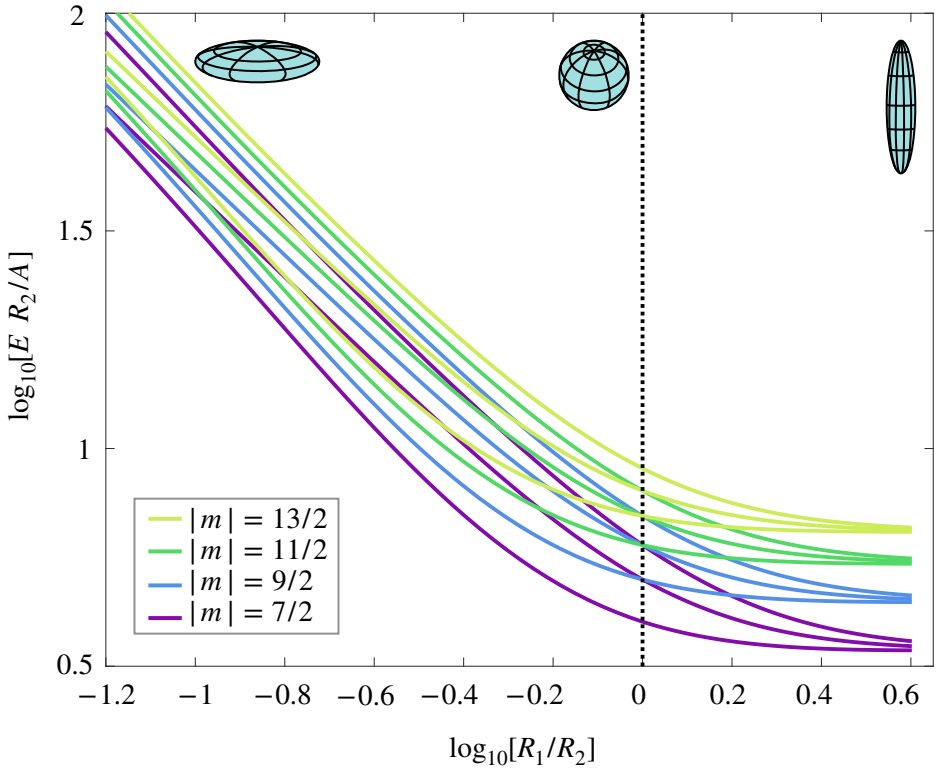

Figure 4.12: **TI spheroidal nanoparticles:** Energy levels, normalised by A/R_2, for all cases from the nanodisk to the nanowire as a function of their aspect ratio, R_1/R_2, where $R_1/R_2 \leq 1$ for the oblate spheroid, and $R_1/R_2 \geq 1$ for the prolate spheroid. The prolate and oblate spheroids meet at the shared limit of the nanosphere, $R_1 = R_2$. At the limit $R_1 = R_2$ we recover the nanosphere energy levels $E_{+,n,m} = A(n + |m| + 1/2)/R_2$. For the limit $R_1 \gg R_2$ we recover the analytical nanowire energy levels for small $|\mathbf{k}|$, $E_{+,m} \approx A|m|/R_2$, and for $R_1 \ll R_2$ we recover the limit of the ideal nanodisk

.

I finish this chapter with a quote from *Absorption and Scattering of Light by Small Particles*, the seminal textbook by Bohren and Huffman [195].

> *" ...the reader who has painstakingly followed the derivation, and thereby acquired virtue through suffering, may derive some comfort from the knowledge that it is relatively clear sailing from here on."*
>
> - Craig Bohren

Strictly speaking Bohren was commenting on the cumbersome process of expanding the electromagnetic field in spherical harmonics, but I think the sentiment is equally valid for writing the Hamiltonian of a rhombohedral crystal lattice in ellipsoidal coordinates. Mirroring Bohren's optimism, now that we have the energy levels and wave functions of the general nanospheroid, I feel that calculating their optical properties is mathematically less taxing than the derivation of their electronic structure.

5. TQDs as a THz Lasing Source

"When God said, 'Let there be light', he surely must have meant perfectly coherent light."
- Charles Townes[1]

This chapter is the first time in this thesis that we bring together the two main threads of this work - topological electronic nanostructures and light. For mathematical simplicity we work with the **spherical topological quantum dot (TQD)**[2] (whose energy levels and wave functions were described in Section 4.3), and study how the surface states of the TQD can be coupled with THz light. These results could also naturally be extended to non-spherical nanostructures, using the results from Chapter 4. This will be discussed in the outlook of this thesis in Chapter 7.

Much like other types of quantum dots and atomic systems, the discrete energy levels of the TQD make it a natural system for controlled interactions with light. TQDs have energy levels separated by THz frequencies, making them a potential route to **THz lasing**. Success has been found in other THz systems, such as molecular gases [196] and topological insulator quantum dots (TIQDs) [118] pumped with an infrared (IR) source, although as I will demonstrate, TQDs can be pumped with THz frequency light. This feature, alongside the robustness of the TQD states and their unusual spin-momentum locking make for a novel implementation. As well as adding another tool to the tool-box of THz lasing, they could also find use in other technological applications [120, 197].

I derive the results needed to demonstrate that a spherical TQD can lase in an open cavity at $T = 0$ K. In order to demonstrate this we need to know the transition rates in a **1D Fabry-Pérot cavity**[3], and also in **3D free space** (to taken into account interactions out of the cavity axis). A schematic is given in Figure 5.1a. While these results are certainly not new, there are multiple routes to arrive at these results, and I have chosen to utilise the concept of **spectral densities** (which I introduced in Section 3.4.3), giving a powerful method of calculating **transition rates** in any geometry by simply knowing the form of the time-dependent electric field in the system. The applications of this chapter rely heavily on these results and in particular intermediate results which are not usually quoted in

[1] Charles Townes was one of the inventors of the **maser**, standing for **m**icrowave **a**mplification by **s**timulated **e**mission of **r**adiation, and was also the chairman of the NASA Science Advisory committee for the Apollo lunar landing programme.

[2] Recall from Chapter 4 that **topological quantum dot** is an alternative name for topological insulator nanoparticles, due to their analogy with semiconductor quantum dots and 2D topological insulator quantum dots.

[3] This is an open cavity in 3D space, comprised of two parallel mirrors. By assuming photons emitted out of the cavity axis are lost directly to free space, this geometry simplifies to a 1D cavity embedded in 3D free space.

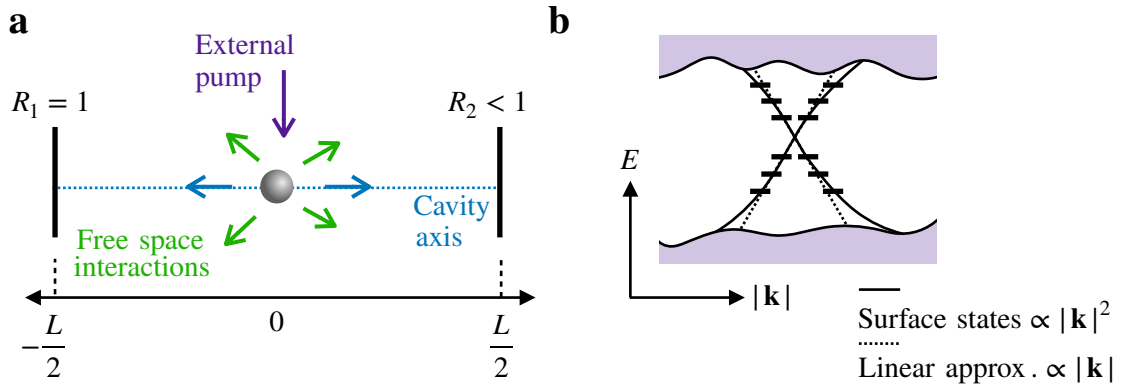

Figure 5.1: **TQD in a cavity: (a)** TQD in an open, 1D Fabry-Pérot cavity, in which photons interact with the cavity along the cavity axis, or with free space in all other directions. An external pump can be implemented from outside the cavity. **(b)** The dispersion relation of the topological surface states is usually well approximated as a linear Dirac cone, however in a high Q cavity tuned to one of the TQD transitions near the Dirac cone, small quadratic deviations will result in the suppression of transitions away from the Dirac cone.

textbooks, hence why I felt these derivations deserved to be in this chapter rather than introduced as background theory in Chapter 3. Excellent general references on quantum electrodynamics (QED) and cQED are [149, 153].

I calculate the **selection rules** of the system, which describe the allowed transitions (both interband and intraband) within the TQD surface states, in agreement with the existing literature [120, 183]. I demonstrate that the allowed transitions have an angular dependence, such that the orientation of incoming light affects which transitions are allowed, which is important when modelling the system and provides an additional tool in the control of topological states using light.

I demonstrate that when a TQD is placed in a cavity, **higher order corrections** to the surface state energy levels become very important when considering intraband transitions (see Figure 5.1b). The energy levels away from the Dirac-point become increasingly non-equidistant in spacing, and so for a high quality cavity tuned to a specific frequency close to the Dirac-point, transitions away from the Dirac-point become quickly suppressed. This results in a **closed scheme** of energy levels, in which a conserved number of electrons can be controlled and pumped within a small subset of energy levels.

I employ this set of closed energy levels to make a **lasing scheme**. The dynamics of multiple electrons in the closed scheme must be considered, and so standard rate equations will not capture the dynamics of the system as Pauli blocking[4] is not taken into account. I use **Monte Carlo simulations** to model the multi-fermionic dynamics of the system when driven by an external, low power THz source. I demonstrate that a single TINP

[4]The phenomenon by which fermion particles such as electrons cannot transition to a state which is already occupied.

in an open 1D cavity will lase in the THz, by calculating the evolution of surface state occupation, coherent photon number and gain.

One of the major technological distinctions between the TQD laser and other THz lasers is that we do not pump between bulk bands (as done in molecular THz lasers and TIQD lasers), but instead we employ transitions within the Dirac cone to both pump and lase. This is only possible due to the unusual energy level configuration and selection rules of the TQD. An important consequence of THz pumping is that the density of thermal, room temperature photons at this frequency (as opposed to those present at optical and IR frequencies) is high enough that, in principle, there would be enough to pump the system without a need for an additional external pumping source. In order to achieve this, a 3D closed cavity will be needed and so I derive these results in full. I discuss how harnessing thermal photons in a 3D cavity would present a path towards **finite-temperature THz lasing using thermal photons as a pump**. This results of this chapter form the manuscript:

- **Proposal for THz lasing from a 3D topological quantum dot**, Marie Rider, Vincenzo Giannini, **arXiv:2105.04316** (2021) [4].

5.1 TQDs interacting with light

Using the concept of **spectral densities** first introduced in Section 3.4.3, we will now derive the **transition rates** between TQD surface states in free space and in an open 1D cavity, where

$$\frac{d}{d\omega}\Gamma_{\mathrm{i}\to\mathrm{f},\beta,\mathbf{k}} = \frac{2\pi}{\hbar^2} S_{\mathrm{i,f},\beta,\mathbf{k}}(\omega)\delta(\omega-\omega_{\mathrm{i,f}}), \tag{5.1}$$

taken from Equation 3.61 and repeated here for clarity. The transition rate $\Gamma_{\mathrm{i}\to\mathrm{f},\beta,\mathbf{k}}$ is calculated via the spectral density $S_{\mathrm{i,f},\beta,\mathbf{k}}$, which describes the coupling of electronic states $|\Psi_{\mathrm{i}}\rangle$ and $|\Psi_{\mathrm{f}}\rangle$, facilitated by photons in mode $(\beta,\mathbf{k})$. While I apply the results of this section to TQD states, these are general results and could be applied to any electronic system.

5.1.1 Photon-mediated transitions in free space

In free space (i.e. with no interesting boundary conditions or restrictions on the EM field), the electric field is described by plane waves as in Equation 3.45. As the electric field is **steady-state** (i.e. its Fourier decomposition has a finite number of terms), we are interested in the **power spectral density**[5], such that

$$S_{\mathrm{i,f},\beta,\mathbf{k}}(\omega) = \lim_{T\to\infty}\frac{1}{T}\left|\langle\Psi_{\mathrm{f}}|\otimes\langle n'_{\beta,\mathbf{k}}|\tilde{\mathbf{H}}^{\mathrm{int}}_{\beta,\mathbf{k}}(\mathbf{r},\omega)|\Psi_{\mathrm{i}}\rangle\otimes|n_{\beta,\mathbf{k}}\rangle\right|^2, \tag{5.2}$$

[5] As opposed to the situation we will come across later in which the electric field is transient and the energy spectral density must be employed instead.

where

$$\tilde{\mathbf{H}}^{\text{int}}_{\beta,\mathbf{k}}(\mathbf{r},\omega) = \frac{1}{\sqrt{2\pi}} \int_{-\frac{T}{2}}^{\frac{T}{2}} \mathbf{H}^{\text{int}}_{\beta,\mathbf{k}}(\mathbf{r},t) e^{i\omega t} dt, \tag{5.3}$$

and $\mathbf{H}^{\text{int}}_{\beta,\mathbf{k}}$ is the paramagnetic Hamiltonian describing the strength and nature of photon-mediated electronic transitions. There are initially $n_{\beta,\mathbf{k}}$ photons in mode $(\beta,\mathbf{k})$, and $n'_{\beta,\mathbf{k}}$ after the transition. $|\Psi_\text{i}\rangle$ is the initial state of the TQD, and $|\Psi_\text{f}\rangle$ is the TQD state after the transition. Using the explicit form of the Hamiltonian in the **electric dipole approximation** (from Equation 3.59),

$$\mathbf{H}^{\text{int}}_{\beta,\mathbf{k}}(\mathbf{r},t) = -e\frac{\omega_{\text{i,f}}}{\omega_\mathbf{k}} \mathbf{E}_{\beta,\mathbf{k}}(\mathbf{r}_0,t)\cdot\mathbf{r}, \tag{5.4}$$

we can write the spectral density as

$$S_{\text{i,f},\beta,\mathbf{k}}(\omega) = e^2\frac{\omega_{\text{i,f}}}{\omega_\mathbf{k}} \lim_{T\to\infty}\frac{1}{T}\left|\langle\Psi_\text{f}|\otimes\langle n'_{\beta,\mathbf{k}}|\tilde{\mathbf{E}}_{\beta,\mathbf{k}}(\mathbf{r}_0,\omega)\cdot\mathbf{r}|\Psi_\text{i}\rangle\otimes|n_{\beta,\mathbf{k}}\rangle\right|^2. \tag{5.5}$$

Specifically for processes in which the electronic transition is facilitated by the the **absorption** of a photon, such that $|n_{\beta,\mathbf{k}}\rangle \to |n_{\beta,\mathbf{k}}-1\rangle$, the spectral density is given by

$$\begin{aligned} S^{\text{abs}}_{\text{i,f},\beta,\mathbf{k}}(\omega) &= e^2\frac{\omega_{\text{i,f}}}{\omega_\mathbf{k}} \lim_{T\to\infty}\frac{1}{T}|\langle\Psi_\text{f}|\otimes\langle n_{\beta,\mathbf{k}}-1|\tilde{\mathbf{E}}_{\beta,\mathbf{k}}(\mathbf{r}_0,\omega)\cdot\mathbf{r}|\Psi_\text{i}\rangle\otimes|n_{\beta,\mathbf{k}}\rangle|^2 \\ &= \frac{\hbar\omega_{\text{i,j}}e^2}{4\pi V\epsilon_0} n_{\beta,\mathbf{k}}|\langle\Psi_\text{f}|\mathbf{r}\cdot\mathbf{e}_\beta|\Psi_\text{i}\rangle|^2 \lim_{T\to\infty}\frac{1}{T}\left|\int_{-\frac{T}{2}}^{\frac{T}{2}} dt e^{i(\omega-\omega_\mathbf{k})t}\right|^2, \end{aligned} \tag{5.6}$$

and thus the transition rate (from Equation 5.1) is given by

$$\frac{d}{d\omega}\Gamma^{\text{abs}}_{\text{i}\to\text{j},\beta,\mathbf{k}} = \frac{\omega_{\text{i,j}}e^2}{2V\epsilon_0\hbar} n_{\beta,\mathbf{k}}|\langle\Psi_\text{f}|\mathbf{r}\cdot\mathbf{e}_\beta|\Psi_\text{i}\rangle|^2 \lim_{T\to\infty}\frac{1}{T}\left|\int_{-\frac{T}{2}}^{\frac{T}{2}} dt e^{i(\omega-\omega_\mathbf{k})t}\right|^2 \delta(\omega-\omega_{\text{i,f}}). \tag{5.7}$$

Integrating both sides,

$$\Gamma^{\text{abs}}_{\text{i}\to\text{j},\beta,\mathbf{k}} = \frac{\omega_{\text{i,j}}e^2}{2V\epsilon_0\hbar} n_{\beta,\mathbf{k}}|\langle\Psi_\text{f}|\mathbf{r}\cdot\mathbf{e}_\beta|\Psi_\text{i}\rangle|^2 \lim_{T\to\infty}\frac{1}{T}\left|\int_{-\frac{T}{2}}^{\frac{T}{2}} dt e^{i(\omega_{\text{i,f}}-\omega_\mathbf{k})t}\right|^2, \tag{5.8}$$

and then calculating the first time integral (integral given in Appendix A.7),

$$\Gamma^{\text{abs}}_{\text{i}\to\text{j},\beta,\mathbf{k}} = \frac{\omega_{\text{i,j}}\pi e^2}{V\epsilon_0\hbar} n_{\beta,\mathbf{k}}|\langle\Psi_\text{f}|\mathbf{r}\cdot\mathbf{e}_\beta|\Psi_\text{i}\rangle|^2 \delta(\omega_{\text{i,f}}-\omega_\mathbf{k}) \lim_{T\to\infty}\frac{1}{T}\int_{-\frac{T}{2}}^{\frac{T}{2}} dt e^{i(\omega_{\text{i,f}}-\omega_\mathbf{k})t}. \tag{5.9}$$

Note that total energy is conserved here. As the electronic structure absorbs a photon, energy is taken from the EM field and the change in energy of the electronic system is positive, such that $E_\text{f} - E_\text{i} = \hbar\omega_\mathbf{k}$. If we wish to find the transition rate for $|\Psi_\text{i}\rangle \to |\Psi_\text{f}\rangle$ via all possible absorption events (i.e. via incoming light from any direction) with a given

polarisation β, we have that

$$\Gamma^{\text{abs}}_{\text{i}\to\text{j},\beta} = \frac{\omega_{\text{i,j}}\pi e^2}{\hbar V \epsilon_0} \sum_{\mathbf{k}} n_{\beta,\mathbf{k}} |\langle \Psi_\text{f}|\mathbf{r}\cdot\mathbf{e}_\beta|\Psi_\text{i}\rangle|^2 \delta(\omega_{\text{i,f}} - \omega_{\mathbf{k}}) \lim_{T\to\infty} \frac{1}{T} \int_{-\frac{T}{2}}^{\frac{T}{2}} dt e^{i(\omega_{\text{i,f}}-\omega_{\mathbf{k}})t}. \tag{5.10}$$

We use the trick that summing over $\mathbf{k}$ can be turned into an integral, (which is justified when the sample space V is very large, such that the space occupied by one state in $\mathbf{k}$-space, $(2\pi)^3/V$ can be seen as an infinitesimal volume $\Delta k_x \Delta k_y \Delta k_z \to d^3\mathbf{k}$). Summing over all available states can be done with knowledge of the photonic density of states (DOS) (see Section 3.7), or by simply calculating the integral explicitly, such that in 3D free space (where space is isotropic),

$$\sum_{\mathbf{k}} \to \frac{V}{(2\pi)^3}\int_V d^3\mathbf{k} = \frac{V}{2\pi^2}\int_V d\mathbf{k}\ \mathbf{k} = \frac{V}{2\pi^2 c^3}\int_V d\omega_{\mathbf{k}}\ \omega_{\mathbf{k}}^2. \tag{5.11}$$

Here we will use the explicit form of the integral, and so

$$\begin{aligned}
\Gamma^{\text{abs}}_{\text{i}\to\text{j},\beta} &= \frac{e^2\omega_{\text{i,j}}}{2\pi\hbar\epsilon_0 c^3}\int_V d\omega_{\mathbf{k}}\ \omega_{\mathbf{k}}^2 n_{\beta,\mathbf{k}} |\langle \Psi_\text{f}|\mathbf{r}\cdot\mathbf{e}_\beta|\Psi_\text{i}\rangle|^2 \delta(\omega_{\text{i,f}} - \omega_{\mathbf{k}}) \lim_{T\to\infty}\frac{1}{T}\int_{-\frac{T}{2}}^{\frac{T}{2}} dt e^{i(\omega_{\text{i,f}}-\omega_{\mathbf{k}})t} \\
&= \frac{e^2}{2\pi\hbar\epsilon_0 c^3}\omega_{\text{i,f}}^3 n_{\beta,\text{i,f}} |\langle \Psi_\text{f}|\mathbf{r}\cdot\mathbf{e}_\beta|\Psi_\text{i}\rangle|^2 \lim_{T\to\infty}\frac{1}{T}\int_{-\frac{T}{2}}^{\frac{T}{2}} dt \\
&= \frac{e^2}{2\pi\hbar\epsilon_0 c^3}\omega_{\text{i,f}}^3 n_{\beta,\text{i,f}} |\langle \Psi_\text{f}|\mathbf{r}\cdot\mathbf{e}_\beta|\Psi_\text{i}\rangle|^2,
\end{aligned} \tag{5.12}$$

where we have also assumed that the radiation is isotropic such that $n_{\beta,\text{i,f}} = n_\beta(\omega_{\text{i,f}})$. Using that $\alpha = \frac{1}{4\pi\varepsilon_0}\frac{e^2}{\hbar c}$ and summing over both polarisations,

$$\Gamma^{\text{abs}}_{\text{i}\to\text{j}} = \frac{2\alpha\omega_{\text{i,f}}^3}{c^2}\sum_{\beta=1,2} n_\beta(\omega_{\text{i,f}}) |\langle \Psi_\text{f}|\mathbf{r}\cdot\mathbf{e}_\beta|\Psi_\text{i}\rangle|^2. \tag{5.13}$$

Similarly for photon **emission**, such that $|n_{\beta,\mathbf{k}}\rangle \to |n_{\beta,\mathbf{k}}+1\rangle$, the transition rate will be given by

$$\frac{d}{d\omega}\Gamma^{\text{emis}}_{\text{i}\to\text{f},\beta,\mathbf{k}} = \lim_{T\to\infty}\frac{4\pi^2}{T\hbar^2}|\langle\Psi_\text{f}|\otimes\langle n_{\beta,\mathbf{k}}+1|\mathbf{H}^{\text{int}}(\mathbf{r},\omega_{\beta,\mathbf{k}})|\Psi_\text{i}\rangle\otimes|n_{\beta,\mathbf{k}}\rangle|^2\delta(\omega_{\text{i,f}}+\omega), \tag{5.14}$$

which results in

$$\Gamma^{\text{emis}}_{\text{i}\to\text{j}} = \frac{2\alpha\omega_{\text{f,i}}^3}{c^2}\sum_{\beta=1,2}\left(n_\beta(\omega_{\text{f,i}})+1\right)|\langle\Psi_\text{f}|\mathbf{r}\cdot\mathbf{e}_\beta|\Psi_\text{i}\rangle|^2. \tag{5.15}$$

We can separate this into two contributions,

$$\Gamma^{\text{emis}}_{\text{i}\to\text{j}} = \Gamma^{\text{stim}}_{\text{i}\to\text{j}} + \Gamma^{\text{spon}}_{\text{i}\to\text{j}}, \tag{5.16}$$

where

$$\Gamma^{\text{stim}}_{\text{i}\to\text{j}} = \frac{2\alpha\omega^3_{\text{f,i}}}{c^2} \sum_{\beta=1,2} n_\beta(\omega_{\text{f,i}}) |\langle\Psi_\text{f}|\mathbf{r}\cdot\mathbf{e}_\beta|\Psi_\text{i}\rangle|^2, \tag{5.17}$$

$$\Gamma^{\text{spon}}_{\text{i}\to\text{j}} = \frac{2\alpha\omega^3_{\text{f,i}}}{c^2} \sum_{\beta=1,2} |\langle\Psi_\text{f}|\mathbf{r}\cdot\mathbf{e}_\beta|\Psi_\text{i}\rangle|^2. \tag{5.18}$$

For the **spontaneous emission rate**, we average over all possible polarisations (i.e. all possible orientations of $\mathbf{e}_\beta$)[6], such that

$$\begin{aligned}\Gamma^{\text{spon}}_{\text{i}\to\text{j}} &= \frac{2\alpha\omega^3_{\text{f,i}}}{c^2} \sum_{\beta=1,2} |\overline{\langle\Psi_\text{f}|\mathbf{r}\cdot\mathbf{e}_\beta|\Psi_\text{i}\rangle}|^2 \\ &= \frac{4\alpha\omega^3_{\text{f,i}}}{3c^2} |\langle\Psi_\text{f}|\mathbf{r}|\Psi_\text{i}\rangle|^2.\end{aligned} \tag{5.19}$$

Note that none of these transition rates have a spatial dependence. This is a direct consequence of the photonic density of states in free space being spatially invariant. If we also assume that there is no underlying structure to the number of modes per polarisation (i.e. there are equal numbers of photons with either polarisation), we can assume that $n_1(\omega) = n_2(\omega) = n(\omega)/2$, and we arrive at the final expressions for the transition rates. It is worth noting that the form of the transition rates here are the same as when calculated using **Fermi's golden rule**, in which the transition rate is found to be proportional to the photonic local density of states (LDOS) in the system. I cover this insight in more detail in Appendix B.5.

Result: Transition rates in free space

$$\textbf{Spontaneous emission} \quad \Gamma^{\text{spon}}_{\text{i}\to\text{f}} = \frac{4\alpha\omega^3_{\text{f,i}}}{3c^2} |\langle\Psi_\text{f}|\mathbf{r}|\Psi_\text{i}\rangle|^2 \tag{5.20}$$

$$\textbf{Stimulated emission} \quad \Gamma^{\text{stim}}_{\text{i}\to\text{f}} = \frac{\alpha\omega^3_{\text{f,i}}}{c^2} n(\omega_{\text{f,i}}) \sum_{\beta=1,2} |\langle\Psi_\text{f}|\mathbf{r}\cdot\mathbf{e}_\beta|\Psi_\text{i}\rangle|^2 \tag{5.21}$$

$$\textbf{Stimulated absorption} \quad \Gamma^{\text{abs}}_{\text{i}\to\text{f}} = \frac{\alpha\omega^3_{\text{i,f}}}{c^2} n(\omega_{\text{i,f}}) \sum_{\beta=1,2} |\langle\Psi_\text{f}|\mathbf{r}\cdot\mathbf{e}_\beta|\Psi_\text{i}\rangle|^2 \tag{5.22}$$

For a 50 nm radius nanoparticle of Bi_2Te_3, the smallest frequency is $A/hR = \nu = 0.97$ THz (where $\omega = 2\pi\nu$) and the spontaneous emission rate for the intraband transition between e.g. levels $|+,1,1/2\rangle$ and $|+,0,-1/2\rangle$ is $6.7\cdot10^3$ s^{-1}. Interband transitions are typically much

[6]Note that we only need to do this for spontaneous emission, in which a photon can be emitted with any polarisation - for stimulated emission, the photon will have the same polarisation as the initial photon.

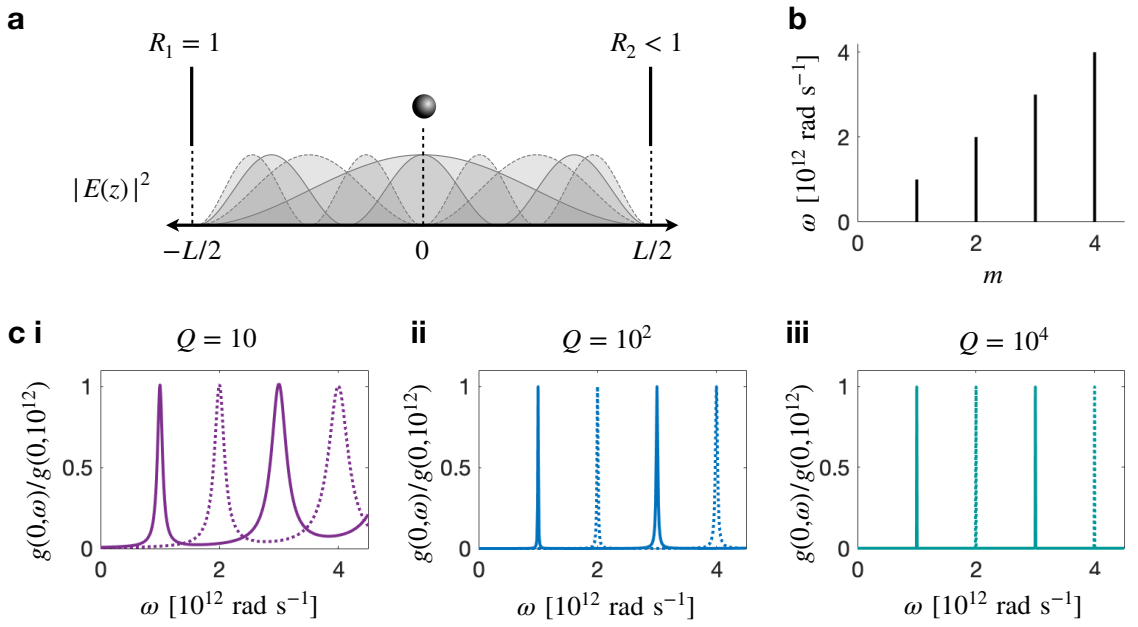

Figure 5.2: **Light in a cavity: (a)** Schematic for 1D Fabry-Pérot cavity in free space. The mirrors of the cavity have reflectivities R_1 and R_2 respectively. The spatial electric field pattern is given for the first four modes of the cavity. At the centre of the cavity, only odd modes are non-zero. **(b)** Discrete dispersion relation $\omega = m\pi c/L$, for light in a cavity of length $L = 0.94$ mm. **(c)** LDOS at position $z = 0$, normalised by the LDOS at frequency $\omega = \omega_{\text{cav}} = 1$ THz, for cavities with Q factor given by **(i)** 10, **(ii)** 10^2 and **(iii)** 10^4. Only modes with odd m (solid line) contribute to the LDOS at $z = 0$, due to the structure of the electric field. Contributions from even modes (dotted line) do not contribute to the LDOS at $z = 0$, and thus transitions at these frequencies will be suppressed in the cavity axis. However, shifting by a fraction of a wavelength along the cavity axis will give a different set of transition rates.

faster, with the spontaneous transition from $|+, 1, -1/2\rangle$ to $|-, 1, 1/2\rangle$ given by $1.4 \cdot 10^5$ s^{-1}. This is much slower than comparable processes in semiconductor dots, whose spontaneous emission rates are typically in the range 10^6–10^9 s^{-1} depending on their structure [198, 199].

5.1.2 Cavity QED: Transitions in a 1D Fabry-Pérot cavity

A **1D Fabry-Pérot cavity** in its simplest form can be taken to be a pair of parallel, imperfect cavity walls (mirrors) separated by a distance L along the z-axis (illustrated in Figure 5.2a). The electric field $\mathbf{E}(z, t)$ inside the cavity will obey boundary conditions at the mirrors, and is best described by a standing wave solution. The dispersion relation of light inside this cavity thus takes quantised values, such that

$$\omega_m = \frac{m\pi c}{L}, \tag{5.23}$$

where $m = 1, 2, ...$ Note that this is because $k_z = \frac{m\pi}{L}$. The fundamental mode of the cavity $\omega_{\text{cav}} = 2\pi c/\lambda_{\text{cav}}$ for $L = \lambda_{\text{cav}}/2$, so we can rewrite the dispersion relation as $\omega_m = m\omega_{\text{cav}}$, plotted in Figure 5.2b. Any mode not propagating directly in the cavity axis is considered a free space mode[7] and will interact via the free space transitions covered in Section 5.1.1.

The imperfect mirrors allow a **time-dependent decay of the electric field** out of the cavity, quantified by the ***Q* factor** (Appendix B.8 goes into more detail on the Q factor and its connection to the energy stored in the cavity), given by

$$Q_m = \tau_m \omega_m, \tag{5.24}$$

where τ_m is the **photon-decay time** (and conversely $1/\tau_m$ is the **cavity decay-rate constant**) of mode ω_m. Note that we are defining a frequency-dependent Q factor. Often for a particular cavity, Q is treated as a single constant as the cavity is either considered single-mode, or the multiple modes of the cavity are close enough in frequency that the Q factor will be practically the same over the entire operating range. However, by adding in this mathematical formality we open ourselves to the potential of more flexible cavity engineering. In practice, this can be achieved by constructing the cavity out of a material whose reflectivity varies over the operating frequency of the material.[8] By applying the boundary conditions $\mathbf{E}(0,t) = \mathbf{E}(L,t) = 0$, the electric field inside the cavity can be found to be

$$\mathbf{E}(z,t) = \sum_{\beta=1,2} \sum_{m} \sqrt{\frac{\hbar\omega_m}{2L\epsilon_0}} \sin\left(\frac{m\pi z}{L}\right) \left[\mathbf{e}_\beta a_{\beta,m} e^{-i\omega_m t} - \mathbf{e}^*_\beta a^\dagger_{\beta,m} e^{i\omega_m t}\right] e^{-\frac{\omega_m t}{2Q_m}}, \tag{5.25}$$

where it is important to note the exponential time-decay. There is now also a spatial-dependence, which was not the case in free space. The spatial variance of the electric field is illustrated in Figure 5.2. Due to the **transient** nature of the electric-field in this setup, we work with the **energy spectral density** of the field, given by

$$S_{\text{i,f},\beta,m}(\omega) = \frac{1}{\tau_m} \left| \langle \Psi_{\text{f}}| \otimes \langle n'_{\beta,m}| \tilde{\mathbf{H}}^{\text{int}}_{\beta,m}(\mathbf{r},\omega) |\Psi_{\text{i}}\rangle \otimes |n_{\beta,m}\rangle \right|^2. \tag{5.26}$$

The **characteristic timescale** of the system is τ_m (the photon-decay time), rather than T (in the limit that $T \to \infty$) as in free-space. Substituting the electric dipole approximation

[7] This is of course a simplification. In reality, this system should be considered similar to a 2D waveguide in which $\omega^2_{m,\beta} = \left(\frac{m\pi c}{L}\right)^2 + c^2\beta^2$, where $\beta^2 = k_x^2 + k_y^2$.

[8] While this may seem like a theorist wilfully ignoring physical practicalities, recent advancements in metamaterials make this type of cavity engineering possible - albeit technically challenging - for the THz frequency range I focus on in this thesis.

and looking specifically at the absorption process,

$$\begin{aligned} S^{\text{abs}}_{\text{i}\to\text{f},\beta,m}(\omega) &= \frac{e^2}{\tau_m}\frac{\omega_{\text{i,f}}}{\omega_m}|\langle\Psi_\text{f}|\otimes\langle n_{\beta,m}-1|\mathbf{r}\cdot\mathbf{E}(z_0,\omega)|\Psi_\text{i}\rangle\otimes|n_{\beta,m}\rangle|^2 \\ &= \frac{\hbar\omega_{\text{i,f}}e^2}{4\pi\epsilon_0\tau_m L}n_{\beta,m}\sin^2\left(\frac{m\pi z_0}{L}\right)|\langle\Psi_\text{f}|\mathbf{r}\cdot\mathbf{e}_\beta|\Psi_\text{i}\rangle|^2\left|\int_{-\infty}^{\infty}dt e^{i(\omega-\omega_m)t-\frac{\omega_m t}{2Q_m}}\right|^2. \end{aligned} \tag{5.27}$$

Evaluating the time component (making use of the integral given in Appendix A.7) and using that $\alpha = \frac{1}{4\pi\epsilon_0}\frac{e^2}{\hbar c}$,

$$S^{\text{abs}}_{\text{i}\to\text{f},\beta,m}(\omega) = \frac{4\alpha\hbar^2 c\omega_{\text{i,f}}}{L}n_{\beta,m}\sin^2\left(\frac{m\pi z_0}{L}\right)|\langle\Psi_\text{f}|\mathbf{r}\cdot\mathbf{e}_\beta|\Psi_\text{i}\rangle|^2\frac{Q_m\omega_m}{\omega_m^2+4Q_m^2(\omega-\omega_m)^2}. \tag{5.28}$$

The transition rate is then recovered as usual from

$$\frac{d}{d\omega}\Gamma_{\text{i}\to\text{f},\beta,m}(\omega) = \frac{2\pi}{\hbar^2}S_{\text{i,f},\beta,m}(\omega)\delta(\omega-\omega_{\text{i,f}}). \tag{5.29}$$

Integrating over ω, and summing over all modes and polarisations, we find for absorption processes that

$$\Gamma^{\text{abs}}_{\text{i}\to\text{f}} = \frac{8\pi\alpha c}{L}\sum_{\beta,m}n_{\beta,m}\sin^2\left(\frac{m\pi z_0}{L}\right)|\langle\Psi_\text{f}|\mathbf{r}\cdot\mathbf{e}_\beta|\Psi_\text{i}\rangle|^2\frac{Q_m\omega_m\omega_{\text{i,f}}}{\omega_m^2+4Q_m^2(\omega_{\text{i,f}}-\omega_m)^2}. \tag{5.30}$$

Similarly for emission processes, we find that

$$\Gamma^{\text{emis}}_{\text{i}\to\text{f}} = \frac{8\pi\alpha c}{L}\sum_{\beta,m}(n_{\beta,m}+1)\sin^2\left(\frac{m\pi z_0}{L}\right)|\langle\Psi_\text{f}|\mathbf{r}\cdot\mathbf{e}_\beta|\Psi_\text{i}\rangle|^2\frac{Q_m\omega_m\omega_{\text{i,f}}}{\omega_m^2+4Q_m^2(\omega_{\text{f,i}}-\omega_m)^2}, \tag{5.31}$$

which can be separated into stimulated and spontaneous emissions, such that

$$\Gamma^{\text{stim}}_{\text{i}\to\text{f}} = \frac{8\pi\alpha c}{L}\sum_{\beta,m}n_{\beta,m}\sin^2\left(\frac{m\pi z_0}{L}\right)|\langle\Psi_\text{f}|\mathbf{r}\cdot\mathbf{e}_\beta|\Psi_\text{i}\rangle|^2\frac{Q_m\omega_m\omega_{\text{i,f}}}{\omega_m^2+4Q_m^2(\omega_{\text{f,i}}-\omega_m)^2}, \tag{5.32}$$

$$\Gamma^{\text{spon}}_{\text{i}\to\text{f}} = \frac{8\pi\alpha c}{L}\sum_{\beta,m}\sin^2\left(\frac{m\pi z_0}{L}\right)|\langle\Psi_\text{f}|\mathbf{r}\cdot\mathbf{e}_\beta|\Psi_\text{i}\rangle|^2\frac{Q_m\omega_m\omega_{\text{i,f}}}{\omega_m^2+4Q_m^2(\omega_{\text{f,i}}-\omega_m)^2}. \tag{5.33}$$

Note that these processes only occur in the cavity axis, such that $\mathbf{k} = (0,0,k_z)$, and so the polarisation basis vectors will only exist in the x-y plane. So, in order to find the spontaneous emission rate we average over all polarisation vector orientations and sum the two basis vectors,

$$\Gamma^{\text{spon}}_{\text{i}\to\text{f}} = \frac{8\pi\alpha c}{L}\sum_{m}\sin^2\left(\frac{m\pi z_0}{L}\right)|\langle\Psi_\text{f}|\mathbf{r}|\Psi_\text{i}\rangle|^2\frac{Q_m\omega_m\omega_{\text{i,f}}}{\omega_m^2+4Q_m^2(\omega_{\text{f,i}}-\omega_m)^2} \tag{5.34}$$

When the radiation is exactly resonant with a particular cavity mode, $\omega_{\text{i,f}} = \omega_m = m\omega_\text{c}$,

this expression reduces to

$$\Gamma_{\mathrm{i}\to\mathrm{f}}^{\mathrm{spon}} = 8\pi\alpha c|\langle\Psi_{\mathrm{f}}|\mathbf{r}|\Psi_{\mathrm{i}}\rangle|^2 \sum_m \sin^2\left(\frac{m\pi z_0}{L}\right)\frac{Q_m}{L}. \tag{5.35}$$

This can be compared to the spontaneous emission rate in 1D free space (derived in Appendix B.9), and shows a maximum enhancement of

$$F_{\mathrm{1D}} = \frac{2Q_m\lambda_{\mathrm{free}}}{\pi L}, \tag{5.36}$$

which is the **1D Purcell factor**. The enhancement is maximised for small cavity sizes (i.e. small L) and high quality cavities (such that Q is large). Processes involving frequencies which are off-resonant with the cavity modes will be greatly suppressed and the transition rates will be much less than those in free space.

Result: Transition rates in an open 1D Fabry-Pérot cavity

Spontaneous emission in cavity axis

$$\Gamma_{\mathrm{i}\to\mathrm{f}}^{\mathrm{spon}} = \frac{8\pi\alpha c}{L}\sum_m \sin^2\left(\frac{m\pi z_0}{L}\right)|\langle\Psi_{\mathrm{f}}|\mathbf{r}|\Psi_{\mathrm{i}}\rangle|^2 \frac{Q_m\omega_m\omega_{\mathrm{i,f}}}{\omega_m^2 + 4Q_m^2(\omega_{\mathrm{f,i}}-\omega_m)^2} \tag{5.37}$$

Stimulated emission in cavity axis

$$\Gamma_{\mathrm{i}\to\mathrm{f}}^{\mathrm{stim}} = \frac{8\pi\alpha c}{L}\sum_{\beta,m} n_{\beta,m}\sin^2\left(\frac{m\pi z_0}{L}\right)|\langle\Psi_{\mathrm{f}}|\mathbf{r}\cdot\mathbf{e}_\beta|\Psi_{\mathrm{i}}\rangle|^2 \frac{Q_m\omega_m\omega_{\mathrm{i,f}}}{\omega_m^2 + 4Q_m^2(\omega_{\mathrm{f,i}}-\omega_m)^2} \tag{5.38}$$

Stimulated absorption in cavity axis

$$\Gamma_{\mathrm{i}\to\mathrm{f}}^{\mathrm{abs}} = \frac{8\pi\alpha c}{L}\sum_{\beta,m} n_{\beta,m}\sin^2\left(\frac{m\pi z_0}{L}\right)|\langle\Psi_{\mathrm{f}}|\mathbf{r}\cdot\mathbf{e}_\beta|\Psi_{\mathrm{i}}\rangle|^2 \frac{Q_m\omega_m\omega_{\mathrm{i,f}}}{\omega_m^2 + 4Q_m^2(\omega_{\mathrm{i,f}}-\omega_m)^2} \tag{5.39}$$

Maximum Purcell factor in 1D

$$F_{\mathrm{1D}} = \frac{2Q_m\lambda_{\mathrm{free}}}{\pi L}, \tag{5.40}$$

The transition rates parallel to the cavity axis increase with small cavity length, L, and large Q factor. The maximal transition rate will occur at a peak of the electric field density, and when the electronic structure is exactly on resonance with a cavity mode such that $\omega_{\mathrm{f,i}} = m\omega_m$. Transitions will be suppressed for frequencies which are far-off resonance with the cavity, or at positions in the cavity where the spatial variance of the electric field is minimised. A lower transition frequency $\omega_{\mathrm{f,i}}$ and increased matrix element can increase the rate of transition. As with the free transition rates of Section 5.1.1, these transition rates are in the same form as those found using Fermi's golden rule as covered in Appendix B.5. If the spatial dependence of the matrix element can be taken outside of the element, Fermi's

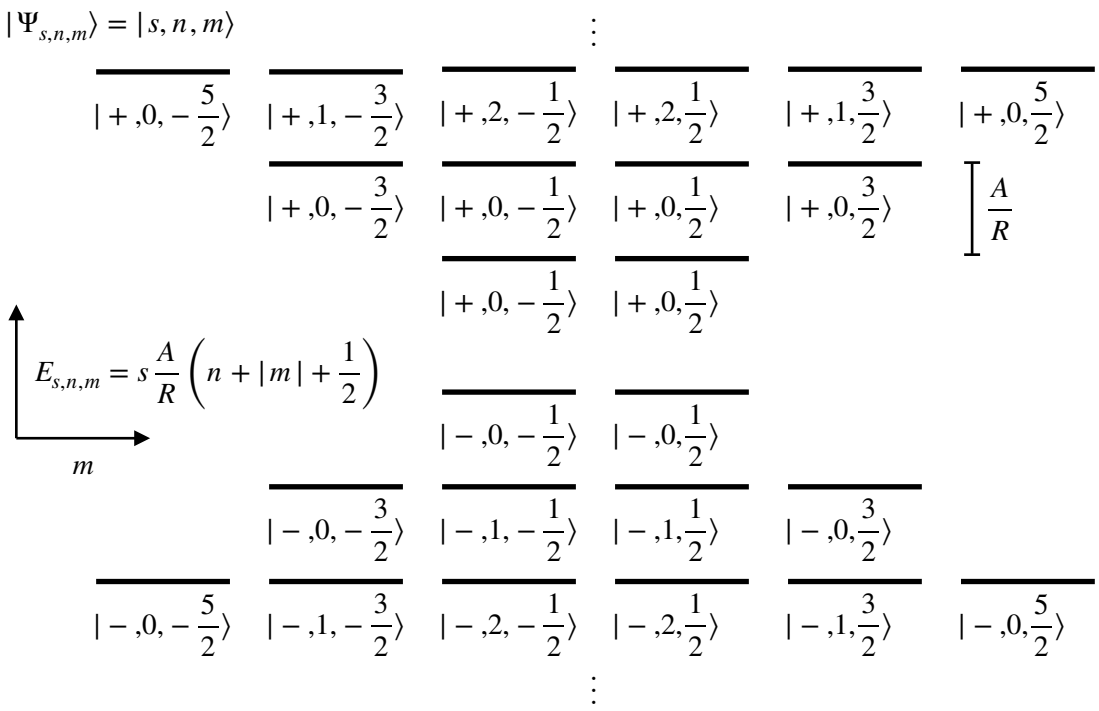

Figure 5.3: **TQD state labels and energies:** The states, $|\Psi_{s,n,m}\rangle = |s,n,m\rangle$ and corresponding energy levels are labelled for the first three energies above and below the Dirac point.

golden rule tells us that the transition rate can be written in terms of the local density of states (LDOS) of the system. In Figure 5.2c, for a cavity with fundamental frequency ω_{cav}, I give three examples of the LDOS at the centre of the cavity, normalised to the value of the LDOS at $\omega = \omega_{\text{cav}} = 1$ THz, while varying Q. We can see that for increasing Q, the sharpness of the peaks in the LDOS increases until the Lorentzian shape of the peaks becomes a delta distribution. Peaks only appear for odd multiples of ω_{cav} (bold line), as resonances at even multiples of ω_{cav} give minima of the electric field density due to the spatial variance. However, if we were to traverse the cavity axis we would see contributions from both odd and even modes.

5.1.3 Selection rules

By inspecting the form of the transition rates both in free space and in a cavity, we can see that for a particular polarisation of light described by $\mathbf{e}_\beta$, the transition rate will only be non-zero if the **E1 matrix element**, $V_{\beta,\text{i,f}}$, is non-zero, where

$$V_{\beta,\text{i,f}} = \langle \Psi_\text{f} | \mathbf{r} \cdot \mathbf{e}_\beta | \Psi_\text{i} \rangle. \tag{5.41}$$

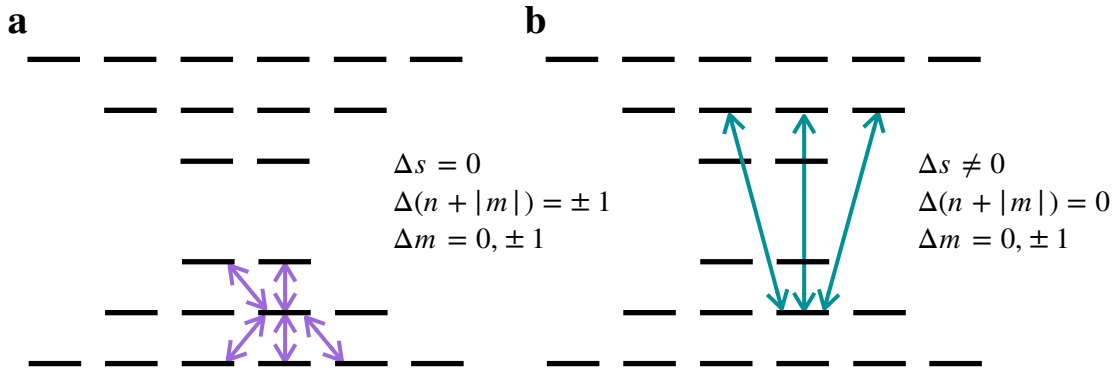

Figure 5.4: **TQD E1 selection rules:** Allowed transitions from the state $|-,1,1/2\rangle$. For light propagating from all directions, **(a)** intraband (purple) transitions couple energy levels within the same section of the Dirac cone and **(b)** interband (green) transitions couple levels above and below the Dirac point.

Calculating $V_{\beta,\mathrm{i,f}}$ thus gives us the **electric dipole (E1) selection rules**.[9] For the c-axis of the material oriented along the z-axis, the explicit form of the TQD wave function (Equation 4.61 given in Chapter 4 but repeated here for convenience) is given by

$$\Psi_{s,n,m}(\vartheta,\varphi) = \langle \vartheta,\varphi|\Psi_{s,n,m}\rangle = \frac{e^{im\varphi}}{2\sqrt{\pi}R} N_{n,m}\chi_{s,n,m}(\vartheta), \tag{5.42}$$

where

$$\chi_{s,n,m}(\vartheta) = \begin{pmatrix} (1-\cos\vartheta)^{\frac{1}{2}|m-\frac{1}{2}|}(1+\cos\vartheta)^{\frac{1}{2}|m+\frac{1}{2}|} J_n^{|m-\frac{1}{2}||m+\frac{1}{2}|}(\cos\vartheta) \\ -\frac{sm}{|m|}(1-\cos\vartheta)^{\frac{1}{2}|m+\frac{1}{2}|}(1+\cos\vartheta)^{\frac{1}{2}|m-\frac{1}{2}|} J_n^{|m+\frac{1}{2}||m-\frac{1}{2}|}(\cos\vartheta) \end{pmatrix}, \tag{5.43}$$

$s = \pm 1$, $n = 0,1,2,...$ and $m = \pm 1/2, 3/2, 5/2, ...$ In Figure 5.3 I give explicit examples of the state labels and their corresponding energies, demonstrating the increasing degeneracy of energy levels away from the Dirac point.

We recall from Section 3.2.3 that for light propagating in the direction

$$\hat{\mathbf{k}} = (\sin\vartheta_0\cos\varphi_0, \sin\vartheta_0\sin\varphi_0, \cos\vartheta_0), \tag{5.44}$$

where ϑ_0 is the angle the light makes with the z-axis, the general polarisation vectors are given by

$$\mathbf{e} = ae^{i\alpha_1}(\cos\vartheta_0\cos\varphi_0, \cos\vartheta_0\sin\varphi_0, -\sin\vartheta_0) + \sqrt{1-a^2}e^{i\alpha_2}(-\sin\varphi_0, \cos\varphi_0, 0). \tag{5.45}$$

We can now calculate the selection rules for a transition $\mathrm{i} = (s,n,m) \rightarrow \mathrm{f} = (s',n',m')$

[9] This matrix element applies to free space and the 1D cavity. For the 3D cavity (covered in Section 5.3), the matrix element depends on the spatial position of the TQD within the cavity. To include the 3D cavity in these general results we can assume the TQD to be at the maximal field amplitude. This does not affect the selection rules, but does affect the magnitude of the matrix-element and thus the final transition rate.

mediated by light of any polarisation. A non-zero matrix element means that the transition rate will be non-zero and thus that particular transition is **allowed**. A matrix-element of value zero means that the transition is **forbidden** (at least for the perturbation order of E1. The transition may be allowed at higher order, for example M1 or E2, but the transition rate will be much slower. See Appendix B.4). In terms of (s, n, m), the selection rules are given below.

Result: E1 selection rules

The general selection rules for the system are given by

$$\Delta s = 0, \quad \Delta(n + |m|) = \pm 1, \quad \Delta m = 0, \pm 1. \tag{5.46}$$

$$\Delta s \neq 0, \quad \Delta(n + |m|) = 0, \quad \Delta m = 0, \pm 1. \tag{5.47}$$

Both intra- ($\Delta s = 0$) and interband ($\Delta s \neq 0$) transitions are allowed. As an example, the allowed transitions from state $|-, 1, 1/2\rangle$ are given in Figure 5.4. Figure 5.4a shows the **intraband transitions** (purple arrows), where states within the same section of the Dirac cone are coupled. Figure 5.4b illustrates the **interband transitions** (green arrows), in which energy levels above and below the Dirac point are coupled.

The angular dependence of the matrix element and thus the selection rules is illustrated in Figure 5.5. This angular dependence gives us another tool for controlling the interaction between light and TQDs. For light approaching with an incidence angle ϑ_0, (illustrated in Figure 5.5a), transitions may be facilitated by left-handed light, right-handed light, or both. For the special case of light propagating parallel to the c-axis of the material (which we take to be the z-axis), the general selection results are reduced and only left-handed **or** right-handed light will facilitate a transition (as depicted in Figure 5.5c, where the polarisation vectors $\mathbf{e}_1$ and $\mathbf{e}_2$ are given by $\mathbf{e}_{\mathrm{LH}}$ and $\mathbf{e}_{\mathrm{RH}}$ when $\vartheta_0 = 0$, and become mixed as ϑ_0 increases). Defining the polarisation basis vectors such that $\varphi_0 = 0$, we can write down the reduced selection rules for incident light parallel to the z-axis.

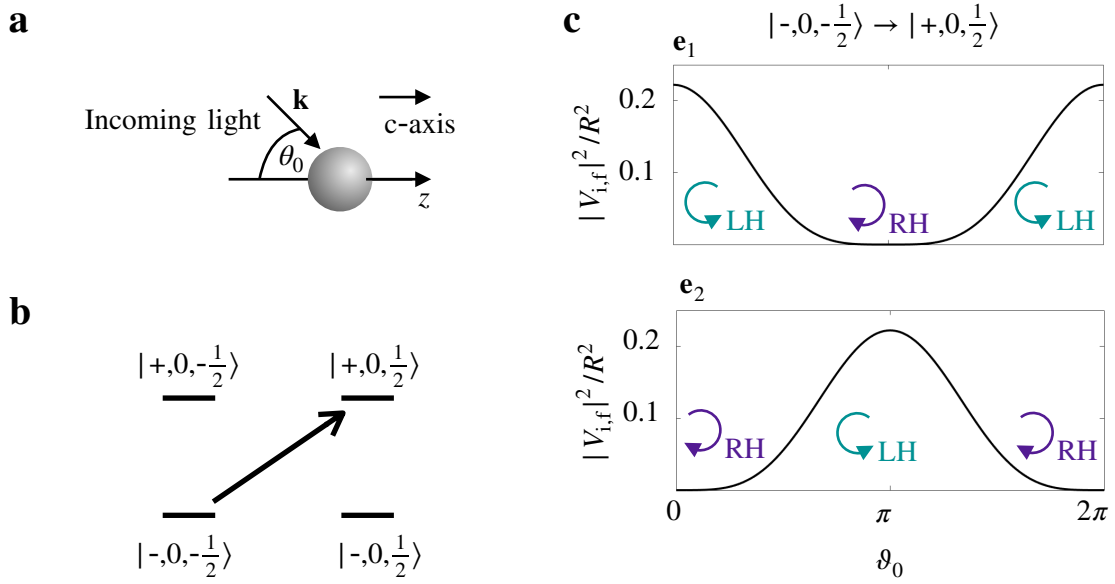

Figure 5.5: **Angular dependence of E1 matrix element: (a)** Schematic of incoming light with momentum $\mathbf{k}$, polar angle ϑ_0, with the c-axis of the material aligned with the z-axis. **(b)** Example of an interband transition $|\text{-},0,-\frac{1}{2}\rangle \rightarrow |+,0,\frac{1}{2}\rangle$. **(c)** The matrix element $V_{\text{i,f}}$ for the transition in **(b)** varies as the polar angle ϑ_0 of incoming light varies. For light travelling parallel to the z-axis, only ϵ_{LH} **or** ϵ_{RH} light will mediate a transition. At intermediate angles, **both** polarisations may facilitate a transition.

Result: E1 selection rules for incoming light parallel to *c*-axis

Selection rules for light propagating along the z-axis such that $\hat{\mathbf{k}} = (0,0,1)$:
For left-hand (LH) polarised light such that $\mathbf{e}_{\text{LH}} = \frac{1}{\sqrt{2}}(1,i,0)$,

$$\Delta s = 0, \quad \Delta(n+|m|) = \pm 1, \quad \Delta m = -1. \tag{5.48}$$

$$\Delta s \neq 0, \quad \Delta(n+|m|) = 0, \quad \Delta m = -1. \tag{5.49}$$

For right-hand (RH) polarised light such that $\mathbf{e}_{\text{RH}} = \frac{1}{\sqrt{2}}(1,-i,0)$,

$$\Delta s = 0, \quad \Delta(n+|m|) = \pm 1, \quad \Delta m = 1. \tag{5.50}$$

$$\Delta s \neq 0, \quad \Delta(n+|m|) = 0, \quad \Delta m = 1. \tag{5.51}$$

As an example, the reduced selection rules for transitions from state $|-,1,1/2\rangle$ are given in Figure 5.6. For the incident angle $\vartheta_0 = 0, \pm\pi, \pm 2\pi, ...$, transitions will only be mediated by left-hand or right-hand polarised light, while at intermediate angles both polarisations may facilitate a transition.

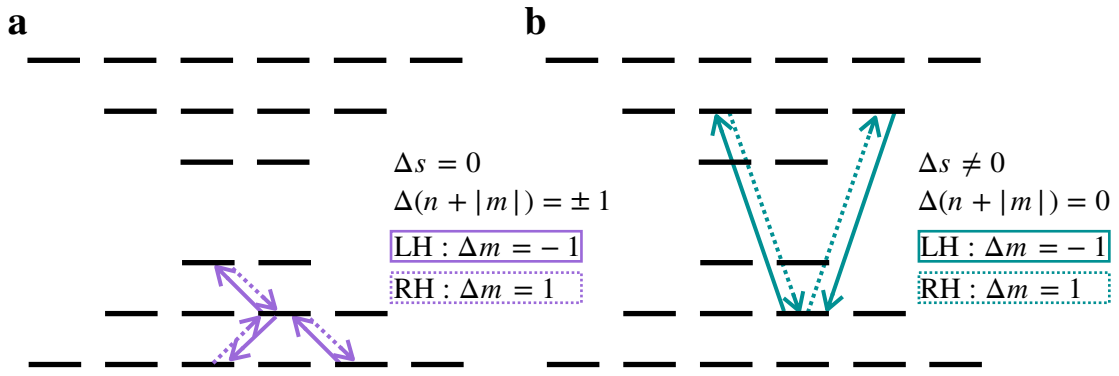

Figure 5.6: **TQD E1 selection rules:** Allowed transitions from the state $|-, 1, 1/2\rangle$. For light propagating parallel to the c-axis of the material, **(a)** intraband and **(b)** interband transitions.

5.1.4 Higher order corrections

Close to the Γ-point the surface state dispersion relation is described well by **k · p theory** and taken to be linear, and so the energy levels of the TQD surface states can be considered equidistant in this region. This is the assumption we have used in Chapter 4, and which is generally assumed in literature [35, 120, 183]. However, as states are considered increasingly further from the Γ-point, this assumption breaks down. This is particularly important when considering a TQD in a high quality cavity, as off-resonant transitions will be rapidly suppressed, so it becomes imperative to take into account minor variations in transition frequencies.

In order to take high-order corrections of the surface state dispersion relation into account, we return to the continuum model (covered in Subsection 2.3.3) and include the next term in the $\mathbf{k} \cdot \mathbf{p}$ expansion. The surface state dispersion relation becomes

$$E_{\mathrm{c,v}}(|\mathbf{k}|) = \pm A|\mathbf{k}| + A_1|\mathbf{k}|^2, \tag{5.52}$$

where A is 2.0 eVÅ for Bi_2Te_3 and 3.0 eVÅ for Bi_2Se_3 (as covered in Chapter 2), and for Bi_2Te_3, $A_1 = 41.4$ eVÅ^2 and for Bi_2Se_3, $A_1 = 23.7$ eVÅ^2 [49]. The continuum surface-state dispersion relation is plotted in Figure 5.7a for Bi_2Te_3, without correction ($E^{(0)}_{\mathrm{c,v}}(|\mathbf{k}|)$) and with correction ($E_{\mathrm{c,v}}(|\mathbf{k}|)$). The linear nature of the Dirac cone clearly breaks down away from the Γ-point.

On confinement of the surface states, $|\mathbf{k}| \sim 1/R$ and so the correction is proportional to $1/R^2$. For a Bi_2Te_3 TQD of $R = 30$ nm, without the correction all nearest-level transitions occur with frequency $\nu^{(0)} = 1.61$ THz (asides from the transition coupling levels directly above and below the Γ-point, which couples at frequency $2\nu^{(0)}$). When taking the correction into account, transition frequencies in both the valence and conduction band rapidly become off-resonant with the first transition in each band. The first and second transition energies in

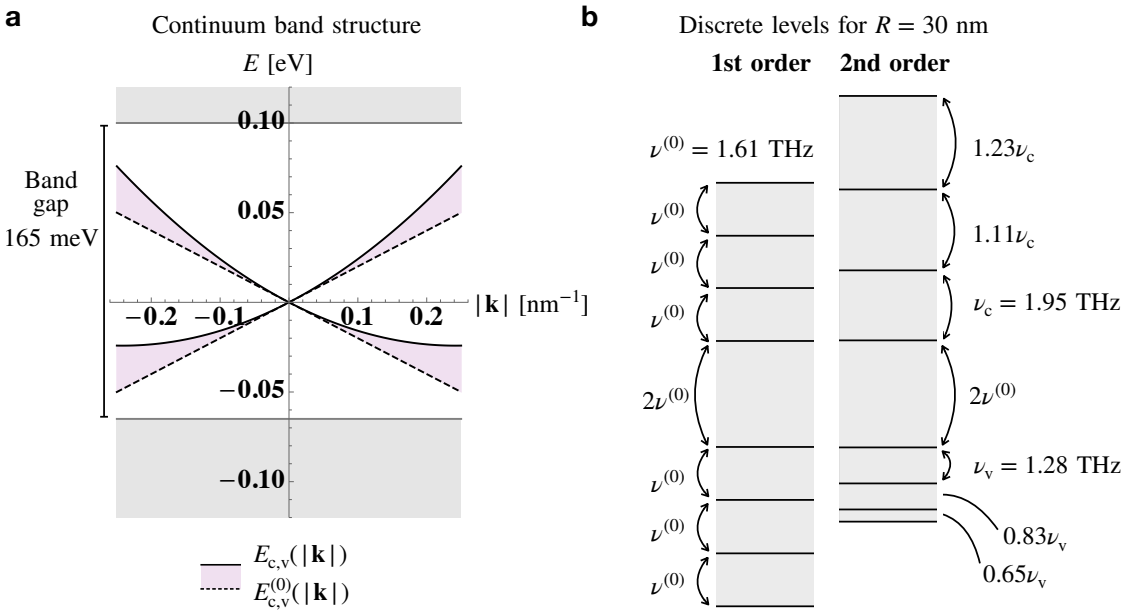

Figure 5.7: **k.p breakdown**: **(a)** Continuum band structure for Bi_2Te_3 with Dirac cone seen in the band gap (=165 meV [45]). Band structure up to and including $|\mathbf{k}|^2$ terms (solid black line) deviates from the linear $\mathbf{k}\cdot\mathbf{p}$ approximation (dotted black line) substantially away from the Γ-point. **(b)** For a $R = 30$ nm nanoparticle, discretised energy levels are expected. To first order (i.e. in the linear approximation), the transition frequency $\nu^{(0)} = 1.61$ THz. To second order (i.e. taking into account the $|\mathbf{k}|^2$ term) sequential transitions in the conduction band rapidly supersede the first transition, which when including the $|\mathbf{k}|^2$ correction has a frequency of $\nu_c = 1.95$ THz. The first valence band transition is $\nu_v = 1.28$ THz. Transitions in the valence band rapidly decrease in frequency away from the Γ-point. Interband transitions are unaffected by the second order correction due to cancellation of the $|\mathbf{k}|^2$ terms.

the upper Dirac cone show a disparity of 11%. The first and third transition energies differ by 23%, as shown in Figure 5.7b. Variation in frequency is more rapid in smaller particles, and in materials for which A_1 is large. This disparity can thus be reduced by considering a TQD of larger radius, or by using a different material such as Bi_2Se_3. Examples of transition frequencies with and without the second-order correction for varying particle sizes and material are given in Table 5.1. It should be noted that **interband transitions are unaffected** due to the cancellation of the second-order correction, so occur at even multiples of $\nu^{(0)}$.

TQDs have multiple important energy scales. In comparison to the band gap (~ 0.1 eV, as in Figure 5.7a), the intraband transitions of the surface states are roughly the same. However, when placed in a high Q cavity (such as the 1D open cavity described in Section 5.1.2), the variation of the transition frequencies becomes of major importance. If the cavity is tuned to a single intraband frequency, for example $\nu_{cav} = \nu_v$, transitions between other energy levels could be greatly suppressed. For a cavity with a lifetime on a similar timescale to spontaneous emission of the TQD, $Q = \tau\omega_{cav}$, where $\tau \approx 10^{-3}s$ for a $R = 30$ nm particle,

Bi_2Te_3

R [nm]	$\nu^{(0)}$ [THz]	ν_c [THz]	ν_v [THz]	No. transitions in E_c within 10% of ν_c
10	4.83	7.86	1.84	1: ν_c
20	2.41	3.18	1.67	1: ν_c
30	1.61	1.95	1.28	1: ν_c
50	0.97	1.09	0.85	2: $(1,\ 1.07)\nu_c$
100	0.48	0.52	0.45	3: $(1,\ 1.04,\ 1.08)\nu_c$

Bi_2Se_3

R [nm]	$\nu^{(0)}$ [THz]	ν_c [THz]	ν_v [THz]	No. transitions in E_c within 10% of ν_c
10	7.24	9.00	5.55	1: ν_c
20	3.62	4.07	3.21	2: $(1,\ 1.07)\nu_c$
30	2.41	2.62	2.23	3: $(1,\ 1.05,\ 1.09)\nu_c$
50	1.48	1.52	1.39	4: $(1,\ 1.03,\ 1.06,\ 1.09)\nu_c$
100	0.72	0.74	0.71	7: $(1,\ 1.02,\ 1.03,\ 1.05,\ 1.06,\ 1.08,\ 1.09)\nu_c$

Table 5.1: **Transition frequencies for TQDs:** To first order, $\nu^{(0)} = A/hR$ Hz, where R nm is the nanoparticle radius and A is 2.0 eVÅ for Bi_2Te_3 and 3.0 eVÅ for Bi_2Se_3. Including the second order term, the first transition frequency in each band is $\nu_{c,v} = A/hR \pm A_1/hR^2$ Hz, where A_1 is 41.4 eVÅ^2 for Bi_2Te_3 and 23.7 eVÅ^2 for Bi_2Se_3.

so $Q \approx 10^9$, which corresponds to an incredibly high quality cavity[10]. Recalling from Section 5.1.2 that transition rates in a cavity scale as

$$\Gamma_{i\to f} \sim \frac{Q\omega_{cav}\omega_{i,f}}{\omega_{cav}^2 + 4Q^2(\omega_{i,f} - \omega_{cav})^2}, \tag{5.53}$$

for a frequency directly on resonance such that $\omega_{i,f} = \omega_v = \omega_{cav}$, we have that $\Gamma_{i\to f} \sim Q$. For the next level in the valence band (for $R = 30$ nm, $\omega = 0.83\ \omega_v = 0.83\ \omega_{cav}$), the transition rate is drastically reduced, such that $\Gamma_{i\to f} \sim 1/Q$. Interband transitions, such as $\omega = 2\omega^{(0)}$ will be similarly suppressed. It is clear that for a cavity of high Q factor, the only modes coupled to the cavity will be those which are almost perfectly resonant. All other transitions will be drastically suppressed in the cavity axis and considered negligible. However, in an open cavity such as the one described in Subsection 5.1.2 these transitions can still occur in all directions not directly parallel to the cavity axis via the free-space transition rate[11].

It is important to note that corrections to the surface state energy levels must be considered when calculating transition frequencies in a high quality cavity, due to the high frequency-sensitivity of the density of states and transition rates. However, we use the unperturbed

[10] This is an exceedingly large Q factor, owing to the unusual combination of a high transition frequency and long timescale.

[11] In a closed 3D cavity such as the one described in Section 5.3.2, only transitions that are nearly-resonant with a cavity mode will avoid suppression.

surface states when calculating the matrix elements, as this correction to the transition rates is very small [200].

5.2 Lasing TQD at zero temperature

"All models are wrong, but some are useful."
- George Box[12]

I now put together the information gathered in the previous sections to demonstrate **lasing**. This model is not particularly physical, requiring zero temperature and simplistically assuming that photonic interactions only occur either (i) in the 1D cavity axis or (ii) in free space. However, it provides us with a good toy model with which to study the idea of lasing with TQDs. A more realistic, finite temperature model will be discussed afterwards.

5.2.1 Setup

We place a single Bi_2Te_3 TQD in the centre of an open, 1D Fabry-Pérot cavity of length L (illustrated in Figure 5.8a) with the material c-axis aligned with the cavity-axis and Fermi level at $E_F = 0$. We work at zero temperature, such that there are negligible ambient photons. Thus, the only photons entering the model are those coming from the pump, and those which are produced by the TQD.

The TQD is pumped using an interband transition, $\nu_{\text{pump}} = (E_+^2 - E_-^2)/h = 4\nu^{(0)}$, and the cavity is tuned to the first valence band transition, $\nu_{\text{las}} = (E_-^1 - E_-^2)/h$, as illustrated in Figure 5.8b. This is the lowest transition in the scheme. The arguments in Section 5.1.4 show that all other transitions will be suppressed in the cavity axis, however free-space transitions can occur at any frequency away from the cavity axis. The cavity is tuned to the desired lasing frequency by choosing $L = a\lambda_{\text{las}}/2$ with a an integer and $\lambda_{\text{las}} = c/\nu_{\text{las}}$. This scheme can be made more general, by choosing to pump via any interband transition and tuning the cavity to the lowest transition in the scheme, resulting in lasing in this transition frequency. It is important to note here that **multiple schemes give successful lasing**, and I present one option.

The relevant rates (assuming transitions in the cavity are on resonance such that $\omega_{\text{f,i}} = b\omega_{\text{las}}$

[12]George Box was a British statistician known for his work on time-series analysis and response surface methodologies. The underlying concept of this aphorism predates Box, but it is generally attributed to him.

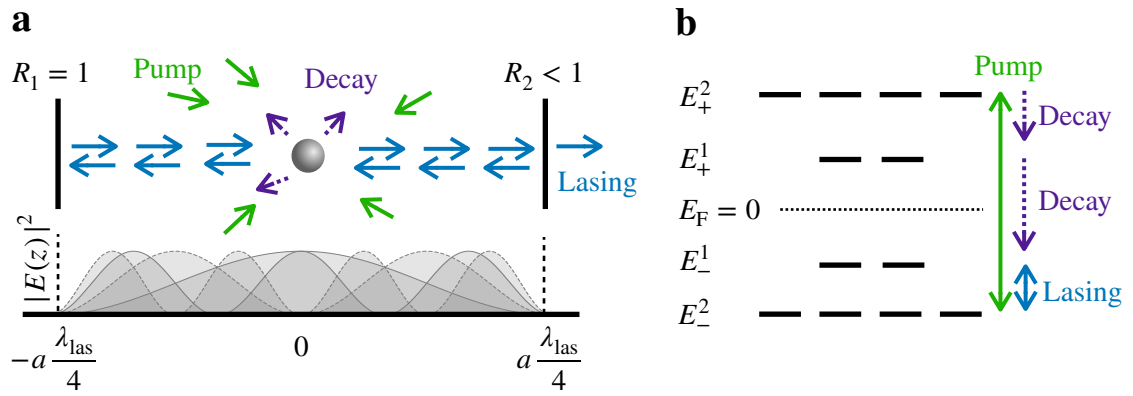

Figure 5.8: **Toy model lasing**: **(a)** Schematic of a TQD in a 1D open Fabry-Pérot cavity and allowed transitions. **(b)** Transitions involved in the lasing scheme.

for integer b) are given as follows:

$$\textbf{Pump} \qquad \Gamma^{\text{stim}}_{\text{i}\to\text{f}} = \frac{2\alpha\omega^3_{\text{f,i}}}{3c^2}\bar{n}(\omega_{\text{f,i}})|\langle\Psi_\text{f}|\mathbf{r}|\Psi_\text{i}\rangle|^2 \tag{5.54}$$

$$\textbf{Lasing} \qquad \Gamma^{\text{stim}}_{\text{i}\to\text{f}} = 4\pi\alpha c\frac{Q}{L}\bar{n}(\omega_{\text{f,i}})\sum_\beta|\langle\Psi_\text{f}|\mathbf{r}\cdot\mathbf{e}_\beta|\Psi_\text{i}\rangle|^2 \tag{5.55}$$

$$\textbf{Spon. emission in axis} \qquad \Gamma^{\text{spon}}_{\text{i}\to\text{f}} = 8\pi\alpha c\frac{Q}{L}|\langle\Psi_\text{f}|\mathbf{r}|\Psi_\text{i}\rangle|^2 \tag{5.56}$$

$$\textbf{Spon. emission out of axis} \qquad \Gamma^{\text{spon}}_{\text{i}\to\text{f}} = \frac{4\alpha\omega^3_{\text{f,i}}}{3c^2}|\langle\Psi_\text{f}|\mathbf{r}|\Psi_\text{i}\rangle|^2 \tag{5.57}$$

where we have also assumed symmetry in photon polarisation, such that $n_1 = n_2 = \bar{n}/2$. Assuming a particle of fixed material, Bi_2Te_3, the physical variables we can manipulate are: Q, R, L, and the number of photons per mode at the pump frequency.

For a particle with $R = 30$ nm, the lasing frequency will be $\nu_{\text{las}} = 1.28$ THz, and the pump will be at $\nu_{\text{pump}} = 6.44$ THz. We may choose Q and L. While we have a seemingly large parameter space to play with, we have an important physical restriction. As covered in Chapter 3, in order to achieve lasing we rely on a hierarchy in rates, in which a non-radiative transition which is much faster than other transitions in the system is used to close the lasing scheme. In our system, we use free-space spontaneous decay instead. This rate is fundamentally capped, relying only on the frequency of the light emitted. So, all other transitions must be tuned to be slower than this rate. This fixes the timescale of our system and corresponding lasing rates. Q and L must be chosen accordingly.

We must also remember that the cavity itself is of paramount importance. In order for sufficient feedback such that coherent photons can build up in the cavity and reach steady state (rather than simply leaking out or leaving the cavity via free space spontaneous emission), we must ensure that the Q factor of our cavity is high enough such that we have sufficient feedback. This means that the cavity time-scale must be roughly commensurate with the spontaneous decay rate out of the cavity by any mode. As discussed in Section 5.1.4,

for a particle of $R = 30$ nm, spontaneous rates go roughly as $10^3\ s^{-1}$, and so a commensurate cavity time scale results in $Q \sim 10^9$. We choose a cavity length $L = 50\lambda_{\text{las}}$. For these fixed values, the dynamics of the system are tuned only with the number of photons with pumping frequency present, $\bar{n}_{\text{pump}} = \bar{n}\,(\omega_{\text{pump}})$.

5.2.2 System dynamics

In Section 3.5, we covered the general theory of lasing in an ensemble of single-electron, three-level systems. We wrote down the rate equations and found the condition of relative rates such that **population inversion** is achieved. We also included the feedback-effect of the cavity which allows for a buildup of photons and consequently **lasing**, which can be quantified by calculating **gain** in the cavity. While the principle of lasing using a topological quantum dot is largely the same, there is a subtlety which must be considered. We must take into account that multiple electrons will be active in the scheme, and **fermionic occupation rules** (and thus **Pauli-blocking**) must be included in the dynamics. This drastically changes the methods available to us when studying this system.

In this chapter I present the results of **Monte Carlo simulations**, which capture the fermionic nature of this system using a **probabilistic hopping method** (with more details of the Monte Carlo method given in Appendix C.2.). Electrons traverse the system of energy levels according to the transition rates calculated in Section 5.1 but forbidding double occupation of levels (thus fulfilling the necessary fermionic occupation rules), and then averaging over many runs to obtain a statistical mean of surface state occupation densities. We convert the transition rate between two surface states to a probability of hopping within a discretised time interval

$$p_{\text{i}\to\text{j}} = \Gamma_{\text{i}\to\text{j}} dt, \tag{5.58}$$

with suitably small time step, dt. This versatile method allows us to model the time evolution of the surface states when interacting with a cavity and pumped with an external source, while easily enforcing Pauli blocking. This method also allows for the straightforward calculation of time-dependent quantities such as gain and coherent photon number.

To perform a **Monte Carlo simulation** describing the evolution of this system (with the parameters given in Section 5.2.1), we begin with a single Bi_2Te_3 TQD of $R = 30$ nm and $E_{\text{F}} = 0$, in the centre of a cavity ($z = 0$), with $L = 50\lambda_{\text{las}}$. The TQD is irradiated with light of frequency $\nu_{\text{pump}} = 6.44$ THz and $\bar{n}_{\text{pump}} = 1$, with transition rate given by Equation 5.55. A schematic of the allowed transitions in the scheme is given in Figure 5.9a. The electronic state population evolves via the absorption and emissions of photons, and the evolution of the normalised occupation of energy levels, $\bar{N}/N_{\text{max}}$, is given in Figure 5.9b. Steady state is quickly achieved, with clear population inversion between levels E^1_- and E^2_-. Recalling the concept of **gain** from Chapter 3, the gain for this multi-level lasing transition is given

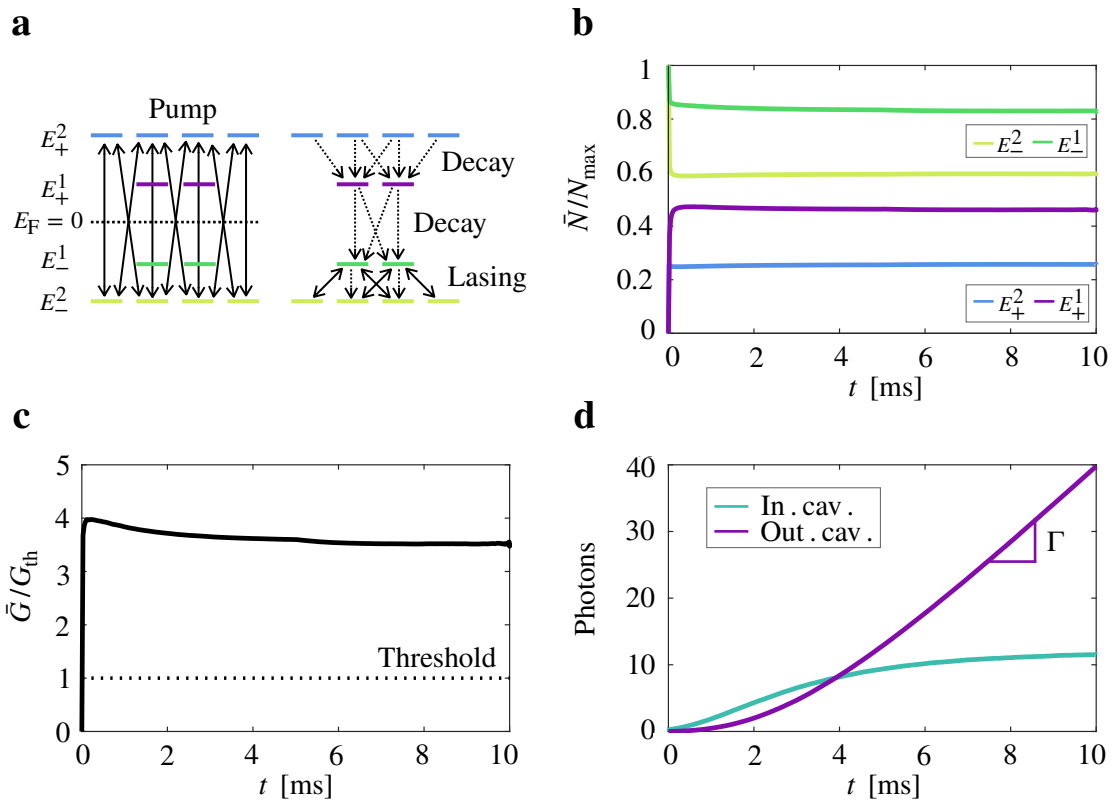

Figure 5.9: **Evolution of toy model lasing system**: For a TQD of $R = 30$ nm in a cavity of length $50\lambda_v$ and $\tau = 10^{-3}s$, pumped with incident photons $\bar{n}_{pump} = 1$. **(a)** Schematic of transitions involved in the lasing scheme. **(b)** Average state occupation of energy levels in lasing scheme. Population inversion can be seen for lasing transition $E_-^1 \rightarrow E_-^2$. **(c)** Average gain, normalised to the threshold value. The threshold value is exceeded nearly immediately. **(d)** Photon dynamics, with number of coherent photons in the cavity building up to a constant density and steady emission of coherent photons out of the cavity. Lasing rate, Γ, given by the gradient of photon number leaving the cavity.

by

$$\bar{G} = \sum_{i<j} \sigma_{j\rightarrow i} \left(\bar{N}_j - \bar{N}_i\right) \delta(\omega_{ij} - 2\pi\nu_c), \tag{5.59}$$

where $\Gamma_{j\rightarrow i} = c\bar{n}_{i,j}\sigma_{j\rightarrow i}$ and $\bar{N}_i$ is the average occupation of surface state i. $\bar{G}$ for $\bar{n}_{pump} = 1$ is plotted in Figure 5.9c. It is immediately positive, and nearly instantaneously above threshold. Threshold gain is given by $G_{th} = 1/\tau_{cav}c$, as internal losses are taken to be negligible in this simulation.

It is assumed that the first spontaneous emission of frequency $\nu_{las} = 1.28$ THz occurs in the cavity axis[13]. This photon is retained in the cavity long enough that it may trigger stimulated emission in the cavity axis and coherent photons will begin to build up in the

[13]This is a reasonable assumption due to the large enhancement of photonic DOS in the cavity axis, such that the spontaneous emission rate in the cavity is much more likely than spontaneous emission out of the cavity, but this assumption is not strictly necessary.

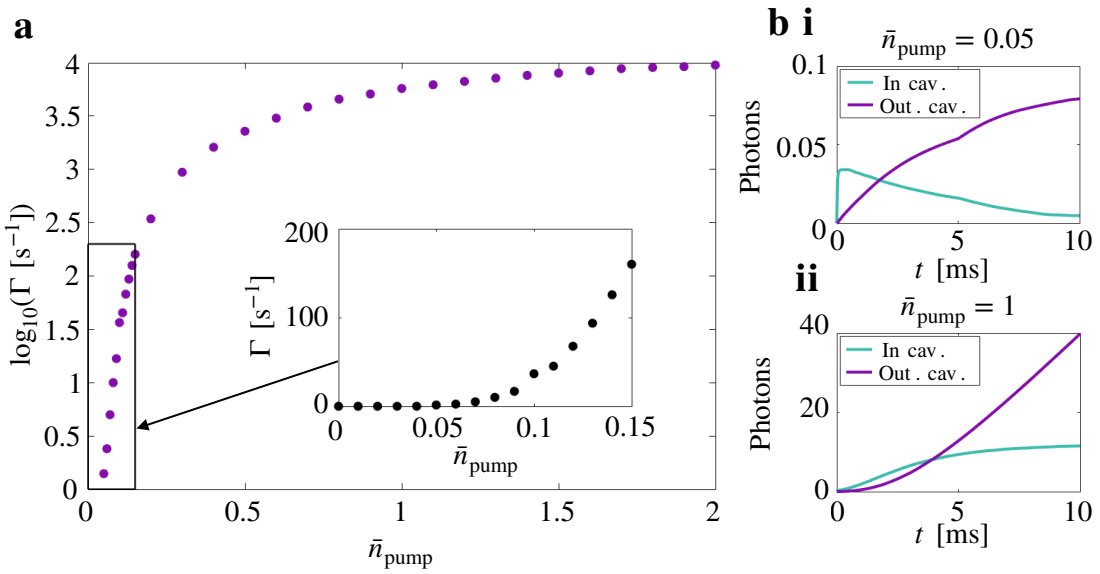

Figure 5.10: **Threshold for toy model lasing**: **(a)** Steady-state lasing rate (coherent photons emitted from cavity per second) for a TQD with $E_F = 0$ and $R = 30$ nm, and a cavity of length $50\lambda_v$ and $\tau = 10^{-3}$ s., and varying $\bar{n}_{pump}$. Inset showing ultra-low pumping regime $0 \leq \bar{n}_{pump} \leq 0.15$, with a lasing threshold of ∼0.08. **(b)** Coherent photon number inside (green) and outside (purple) the cavity plotted for **(i)** $\bar{n}_{pump} = 0.05$ which is below the lasing threshold and **(ii)**, $\bar{n}_{pump} = 1$ which is above lasing threshold.

cavity. The coherent photon dynamics for this system are given in Figure 5.9d. The number of coherent photons in the cavity (teal line) slowly increases from 0 until a steady state is achieved. Coherent photons are emitted from the cavity (purple line), at a constant rate. The slope of this line gives the photon emission rate, $\Gamma \sim 5.7 \cdot 10^3$ s^{-1}. The power of this lasing can be calculated by assuming photons are emitted over an area commensurate with the cross-section of the nanoparticle, such that $P = \Gamma h\nu_{las}/A_{TINP} \sim 1.7 \cdot 10^{-3}$ W/m^2. The incoming power is approximately 1.2 W/m^2. The **power conversion** (power in vs power out) is roughly 0.14% efficiency. This may seem very low, but it should be remembered that we are considering a single TQD. As will be discussed later, the power output and thus efficiency increases dramatically with increased number of TQDs.

Displayed in Figure 5.10a is the dependence of lasing rate with varying $\bar{n}_{pump}$. Lasing is found to occur for $\bar{n}_{pump} \geq 0.08$ (see inset of Figure 5.10a). Below threshold, such as $\bar{n}_{pump} = 0.05$ as demonstrated in Figure 5.10b i, coherent photons in the cavity do not build up rapidly enough to compensate for photons being absorbed by the TQD or emitted from the cavity and so the number of cavity photons decays to 0. Lasing does not occur. Above threshold, such as for $\bar{n}_{pump} = 1$ (already discussed extensively, but included in Figure 5.10b ii for completion), a critical number of coherent photons build up in the cavity such that lasing can occur. At steady state, there is a constant number of coherent photons in the cavity and coherent photons are emitted from the cavity at a constant rate. Above the threshold value of $\bar{n}_{pump}$ is a small range in which the lasing rate exponentially

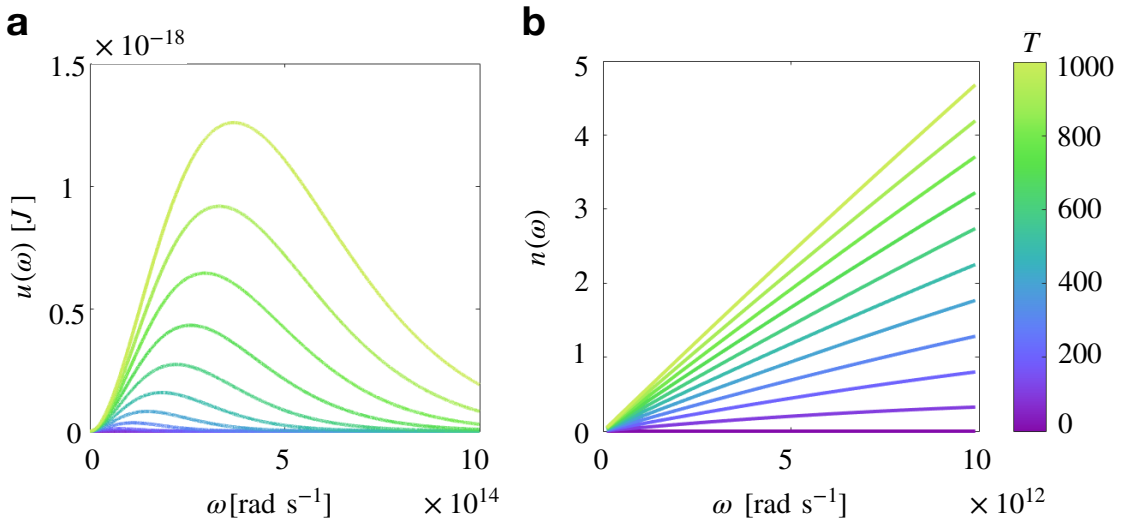

Figure 5.11: **Thermal radiation: (a)** Energy spectrum of photons at finite temperature **(b)** Average mode occupation of photonic states at finite temperature.

increases, and then the lasing rate increases approximately linearly with increased $\bar{n}_{\text{pump}}$. Competition between processes of different time-scales in the system (cavity emission rate, spontaneous emission rate and stimulated emission rate at the cavity frequency) eventually results in a slowing of the increase in lasing rate, and a maximum lasing rate of 10^4 s^{-1}.

All results presented so far have been for a single TQD. For multiple TQDs interacting via a single cavity mode (i.e. multiple TQDs aligned along the cavity axis), coherent photons emitted from one TQD will be available to trigger stimulated emission events in other TQDs. It is expected that the lasing rate will be amplified exponentially with increasing number of TQDs. This will in turn exponentially increase the lasing power, and the overall efficiency of the laser.

5.3 Finite temperature lasing

The toy model we have so far discussed gives **proof of principle of lasing**, using a 1D open cavity at $T = 0$. While experimental setups can reach temperatures close to absolute zero (or more simply can achieve temperatures at which ambient THz frequency photons can be considered negligible), it would be a great triumph to find a system which can successfully operate at **room temperature**. As will be discussed in this section, I find that the number of **thermal photons** present at room temperature is commensurate with the number of photons needed to pump the system, and so it may be possible to pump the system with **no additional, external pump**.

I present a road map to modelling more realistic, finite temperature conditions. As the lasing scheme discussed in the previous section operates at THz frequencies (both pump and emission), I first give a brief overview of thermal photons, and discuss THz frequency

photon density at room temperature. In order to control thermal photons, a fully quantised, 3D cavity would be needed and so I present the derivation of the transition rates in this system in full. I then present a tentative setup and outline the steps that will be necessary to realise this system.

5.3.1 Thermal photons

At finite temperature, a space in thermal equilibrium with its environment is filled with **black-body** electromagnetic radiation [201], with energy spectrum given by

$$u(\omega) = \hbar\omega g(\omega) f(\omega), \tag{5.60}$$

where $\hbar\omega$ is the energy of a single photon of angular frequency ω, $g(\omega) = \omega^2/c^3\pi^2$ is the photonic density of states in free space derived in Section 3.7, and $f_{\mathrm{BE}}(\omega) = 1/(e^{\frac{\hbar\omega}{k_B T}} - 1)$ is the Bose-Einstein distribution, discussed more in Appendix B.10. We can thus write the energy spectrum as

$$u(\omega) = \frac{\hbar}{\pi^2 c^3} \frac{\omega^3}{e^{\frac{\hbar\omega}{k_B T}} - 1}, \tag{5.61}$$

where $k_B = 1.38 \times 10^{-23}$ m^2 kg s^{-2} K^{-1} is the Boltzmann constant. The energy spectrum is both angular frequency ω and temperature T dependent, as plotted in Figure 5.11a. The average number of photons of a particular ω can be found by $u(\omega)/\hbar\omega$, which includes all polarisations. At ambient temperature (which we take to be ~ 293 K) the number of photons at THz frequencies is of order 1 as can be seen in Figure 5.11b.

5.3.2 Cavity QED: Transitions in a 3D Fabry-Pérot cavity

Unlike the open 1D cavity embedded in 3D space described previously in Section 5.1.2, we now consider a fully closed, **3D cuboidal Fabry-Pérot cavity**, with the electromagnetic field discretised in all three axes (see Figure 5.12a). The dispersion relation inside this cavity is given by

$$\omega_{l,m,n} = c\sqrt{\left(\frac{l\pi}{L_x}\right)^2 + \left(\frac{m\pi}{L_y}\right)^2 + \left(\frac{n\pi}{L_z}\right)^2}, \tag{5.62}$$

where (l, m, n) can all take values $0, 1, 2, 3, ...$ but only one index can be 0 per mode for a non-trivial electric field. Without loss of generality we take $L_x \leq L_y \leq L_z$, and $V = L_x L_y L_z$ is the volume of the cavity. The allowed cavity frequencies for $l + m + n = 2, 3$ are given in Figure 5.12b. The 3D cavity (in particular the cuboidal cavity in which all three sides are of different length) has a rich mode structure, making for a highly tunable platform. The

electromagnetic field is given by

$$\mathbf{E}(\mathbf{r},t)=\sum_{\beta}\sum_{l,m,n}\sqrt{\frac{\hbar\omega_{l,m,n}}{2V\epsilon_0}}\mathcal{E}_{l,m,n}(\mathbf{r})\circ\mathbf{R}_{\beta,l,m,n}(t), \tag{5.63}$$

where the symbol $\circ$ represents Hadamard multiplication[14]. The spatial variation of the electric field, $\mathcal{E}_{l,m,n}(\mathbf{r})$ is found from the boundary conditions at the cavity walls, such that

$$\mathcal{E}_{l,m,n}(\mathbf{r})=\begin{pmatrix}\cos\left(\frac{l\pi x}{L_x}\right)\sin\left(\frac{m\pi y}{L_y}\right)\sin\left(\frac{n\pi z}{L_z}\right)\\ \sin\left(\frac{l\pi x}{L_x}\right)\cos\left(\frac{m\pi y}{L_y}\right)\sin\left(\frac{n\pi z}{L_z}\right)\\ \sin\left(\frac{l\pi x}{L_x}\right)\sin\left(\frac{m\pi y}{L_y}\right)\cos\left(\frac{n\pi z}{L_z}\right)\end{pmatrix}, \tag{5.64}$$

and the part of the electric-field containing the temporal component is given by

$$\mathbf{R}_{\beta,l,m,n}(t)=\left(\mathbf{e}_\beta a_{\beta,l,m,n}e^{-i\omega_{l,m,n}t}-\mathbf{e}^*_\beta a^\dagger_{\beta,l,m,n}e^{i\omega_{l,m,n}t}\right)e^{-\frac{\omega_{l,m,n}t}{2Q_{l,m,n}}}. \tag{5.65}$$

Examples of the electric-field spatial patterns are given in Figures 5.12c and d. Like the 1D cavity, the 3D cavity supports a **transient** EM field and so to calculate transition rates within the cavity we employ the **energy spectral density**,

$$S^{\text{abs}}_{\text{i}\to\text{f},\beta,l,m,n}(\omega)=\frac{e^2}{\tau_{l,m,n}}\frac{\omega_{\text{i,f}}}{\omega_{l,m,n}}|\langle\Psi_\text{f}|\otimes\langle n_{\beta,l,m,n}-1|\mathbf{r}\cdot\mathbf{E}_{\beta,l,m,n}(\mathbf{r}_0,\omega)|\Psi_\text{i}\rangle\otimes|n_{\beta,l,m,n}\rangle|^2. \tag{5.66}$$

We thus have that

$$\begin{aligned}S^{\text{abs}}_{\text{i}\to\text{f},\beta,l,m,n}(\omega)&=\frac{e^2\hbar\omega_{\text{i,f}}n_{\beta,l,m,n}}{4\pi V\epsilon_0\tau_{l,m,n}}|\langle\Psi_\text{f}|\mathbf{r}\cdot\left(\mathcal{E}_{l,m,n}(\mathbf{r}_0)\circ\mathbf{e}_\beta\right)|\Psi_\text{i}\rangle|^2\left|\int_{-\infty}^{\infty}dte^{i(\omega_{l,m,n}-\omega)t-\frac{t}{2\tau(\omega_{l,m,n})}}\right|^2\\&=\frac{e^2\hbar}{\pi V\epsilon_0}n_{\beta,l,m,n}|\langle\Psi_\text{f}|\mathbf{r}\cdot\left(\mathcal{E}_{l,m,n}(\mathbf{r}_0)\circ\mathbf{e}_\beta\right)|\Psi_\text{i}\rangle|^2\frac{Q_{l,m,n}\omega_{l,m,n}\omega_{\text{i,f}}}{\omega^2_{l,m,n}+4Q^3_{l,m,n}(\omega-\omega_{l,m,n})^2}.\end{aligned} \tag{5.67}$$

As usual we then find the transition rate from

$$\frac{d}{d\omega}\Gamma^{\text{abs}}_{i\to f}(\omega)=\frac{2\pi}{\hbar^2}\sum_{\beta,l,m,n}S_{\text{i}\to\text{f},\beta,l,m,n}(\omega)\delta(\omega-\omega_{\text{f,i}}), \tag{5.68}$$

and specifically for absorption processes, upon integration we find that

$$\Gamma^{\text{abs}}_{i\to f}=\frac{8\pi c\alpha}{V}\sum_{\beta,l,m,n}n_{\beta,l,m,n}|\langle\Psi_\text{f}|\mathbf{r}\cdot\left(\mathcal{E}_{l,m,n}(\mathbf{r}_0)\circ\mathbf{e}_\beta\right)|\Psi_\text{i}\rangle|^2\frac{Q_{l,m,n}\omega_{l,m,n}\omega_{\text{i,f}}}{\omega^2_{l,m,n}+4Q^3_{l,m,n}(\omega_{\text{i,f}}-\omega_{l,m,n})^2}. \tag{5.69}$$

[14]Hadamard multiplication is element-wise matrix multiplication such that $(a_1,a_2,a_3)\circ(b_1,b_2,b_3)=(a_1b_1,a_2b_2,a_3b_3)$.

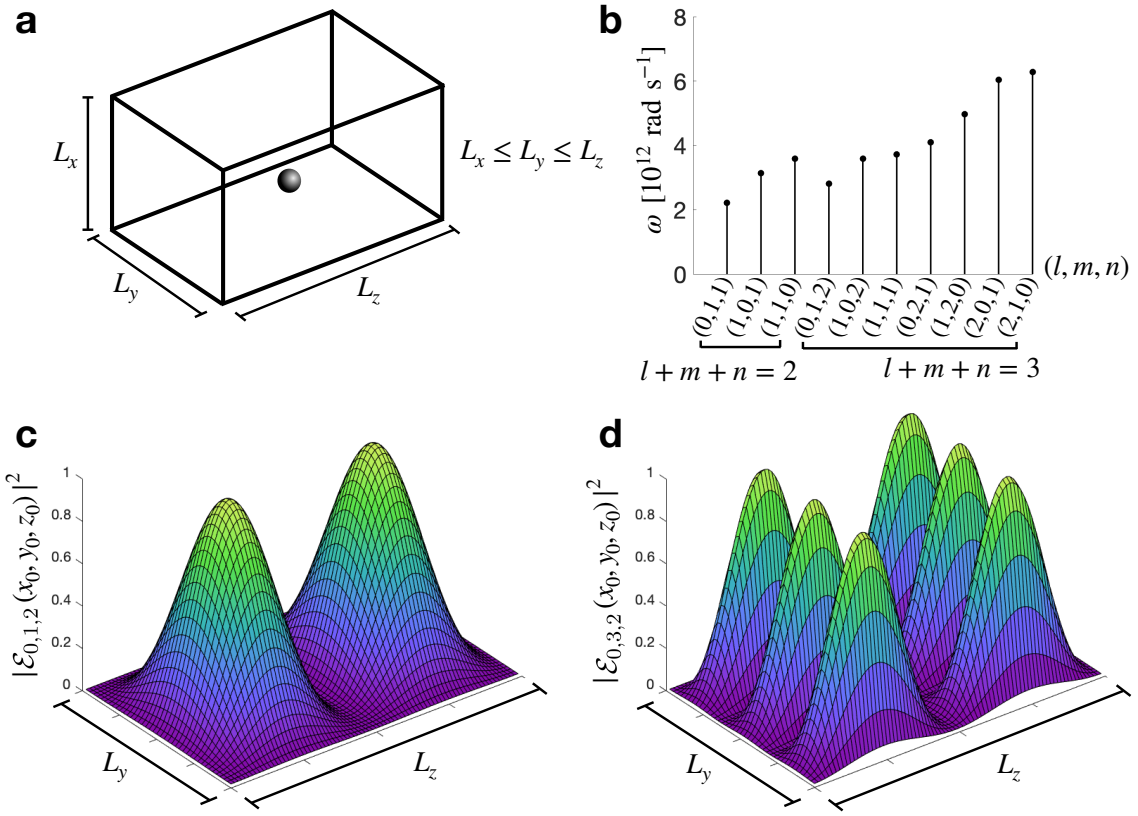

Figure 5.12: **Light in a 3D cavity: (a)** Schematic for 3D Fabry-Pérot cavity with sides of length L_x, L_y, L_z, where $L_x < L_y < L_z$. **(b)** Allowed cavity frequencies for $l+m+n = 2, 3$. **(c)** Normalised electric field spatial patterns for the mode (0,1,2) and **(d)** the mode (0,3,2) showing periodic minima and maxima.

Similarly for emission processes, we find that

$$\Gamma^{\text{stim}}_{i\to f} = \frac{8\pi c\alpha}{V} \sum_{\beta,l,m,n} n_{\beta,l,m,n} |\langle \Psi_{\text{f}}| \mathbf{r} \cdot (\mathcal{E}_{l,m,n}(\mathbf{r}_0) \circ \mathbf{e}_\beta) |\Psi_{\text{i}}\rangle|^2 \frac{Q_{l,m,n}\omega_{l,m,n}\omega_{\text{i,f}}}{\omega^2_{l,m,n} + 4Q^3_{l,m,n}(\omega_{\text{f,i}} - \omega_{l,m,n})^2} \tag{5.70}$$

$$\Gamma^{\text{spon}}_{i\to f} = \frac{8\pi c\alpha}{V} \sum_{\beta,l,m,n} |\langle \Psi_{\text{f}}| \mathbf{r} \cdot (\mathcal{E}_{l,m,n}(\mathbf{r}_0) \circ \mathbf{e}_\beta) |\Psi_{\text{i}}\rangle|^2 \frac{Q_{l,m,n}\omega_{l,m,n}\omega_{\text{i,f}}}{\omega^2_{l,m,n} + 4Q^3_{l,m,n}(\omega_{\text{f,i}} - \omega_{l,m,n})^2}. \tag{5.71}$$

The **3D Purcell factor** is found by dividing the spontaneous emission rate in the cavity by the spontaneous emission rate in 3D free space, such that

$$\begin{aligned} F &= \frac{\Gamma^{\text{spon}}_{\text{i}\to\text{f,cavity}}}{\Gamma^{\text{spon}}_{\text{i}\to\text{f,free}}} \\ &= \frac{6\pi c^3}{\omega^3_{\text{f,i}} V} \sum_{\beta,l,m,n} \frac{|\langle \Psi_{\text{f}}| \mathbf{r} \cdot (\mathcal{E}_{l,m,n}(\mathbf{r}_0) \circ \mathbf{e}_\beta) |\Psi_{\text{i}}\rangle|^2}{|\langle \Psi_{\text{f}}| \mathbf{r} |\Psi_{\text{i}}\rangle|^2} \frac{Q_{l,m,n}\omega_{l,m,n}\omega_{\text{i,f}}}{\omega^2_{l,m,n} + 4Q^3_{l,m,n}(\omega_{\text{f,i}} - \omega_{l,m,n})^2}, \end{aligned} \tag{5.72}$$

where we have used the spontaneous emission rate in free space calculated in Section 5.1.1.

While this result is incredibly useful, it does not look much like the famous, maximum enhancement Purcell factor yet [172]. We make some simplifying assumptions - maximum enhancement will come at the centre of the cavity, such that $\mathcal{E}_{l,m,n}(0) = 1$. We also assume that we are at perfect resonance with a cavity mode, such that $\omega_{\mathrm{f,i}} = \omega_{l,m,n}$. Any deviation from this resonance will decrease the transition rate and a large deviation will eventually lead to suppression of the process entirely. We also assume that the electric dipole moment is perfectly aligned with the electric field in the cavity. All these assumptions give that

$$F = \frac{6\pi c^3}{\omega_{\mathrm{f,i}}^3} \sum_{l,m,n} \frac{Q_{l,m,n}}{V}. \tag{5.73}$$

For a single mode cavity (such that we only consider one term in the sum and rewrite $Q = Q_{l,n,m}$, and rewriting $\omega_{f,i}$ in terms of $\lambda_{\mathrm{i,f}}$, we recover the expected Purcell factor,

$$F = \frac{3\lambda_{\mathrm{i,f}}^3 Q}{4\pi^2 V}. \tag{5.74}$$

As with the 1D cavity, we can see that transition rates rely on a great many factors. Transition rates increase with small cavity size, V and large Q factor. The maximal transition rate will occur at a peak of the electric field density, and when the TQD is exactly on resonance with a cavity mode such that $\omega_{\mathrm{f,i}} = \omega_{l,m,n}$. A lower transition frequency $\omega_{\mathrm{f,i}}$ and increased matrix element will also increase the rate of transition.

Note that for this system the spatial dependence of the electric field is inside the matrix element. For most purposes it is preferable to assume that the electronic system is at a field-maximum inside the cavity, to simplify calculations. This simplified form is what is normally found in textbooks. However, this reduces the parameters which can be tuned when engineering a system, so I keep it in my expression for the transition rates, and we will see later that it can be an important and useful tool.

The expressions for transition rates in the 3D cavity cannot be written in the form of Fermi's golden rule, as the spatial dependence of the electric field cannot be taken outside of the matrix element unless simplifications are made. The spatial dependence of the transition rates will be a crucial tool in the success of finite T lasing in this system, making the method of spectral densities necessary.

Result: Transition rates in a closed 3D Fabry-Pérot cavity

Spontaneous emission

$$\Gamma^{\text{spon}}_{i\to f} = \frac{8\pi c\alpha}{V}\sum_{\beta,l,m,n} |\langle\Psi_{\text{f}}|\mathbf{r}\cdot(\mathcal{E}_{l,m,n}(\mathbf{r}_0)\circ\mathbf{e}_\beta)\,|\Psi_{\text{i}}\rangle|^2 \ldots \times \frac{Q_{l,m,n}\omega_{l,m,n}\omega_{\text{i,f}}}{\omega^2_{l,m,n}+4Q^3_{l,m,n}(\omega_{\text{f,i}}-\omega_{l,m,n})^2} \tag{5.75}$$

Stimulated emission

$$\Gamma^{\text{stim}}_{i\to f} = \frac{8\pi c\alpha}{V}\sum_{\beta,l,m,n} n_{\beta,l,m,n}|\langle\Psi_{\text{f}}|\mathbf{r}\cdot(\mathcal{E}_{l,m,n}(\mathbf{r}_0)\circ\mathbf{e}_\beta)\,|\Psi_{\text{i}}\rangle|^2 \ldots \times \frac{Q_{l,m,n}\omega_{l,m,n}\omega_{\text{i,f}}}{\omega^2_{l,m,n}+4Q^3_{l,m,n}(\omega_{\text{f,i}}-\omega_{l,m,n})^2} \tag{5.76}$$

Stimulated absorption

$$\Gamma^{\text{abs}}_{i\to f} = \frac{8\pi c\alpha}{V}\sum_{\beta,l,m,n} n_{\beta,l,m,n}|\langle\Psi_{\text{f}}|\mathbf{r}\cdot(\mathcal{E}_{l,m,n}(\mathbf{r}_0)\circ\mathbf{e}_\beta)\,|\Psi_{\text{i}}\rangle|^2 \ldots \times \frac{Q_{l,m,n}\omega_{l,m,n}\omega_{\text{i,f}}}{\omega^2_{l,m,n}+4Q^3_{l,m,n}(\omega_{\text{i,f}}-\omega_{l,m,n})^2} \tag{5.77}$$

General Purcell factor

$$F = \frac{6\pi c^3}{\omega^3_{\text{f,i}}V}\sum_{\beta,l,m,n}\frac{|\langle\Psi_{\text{f}}|\mathbf{r}\cdot(\mathcal{E}_{l,m,n}(\mathbf{r}_0)\circ\mathbf{e}_\beta)\,|\Psi_{\text{i}}\rangle|^2}{|\langle\Psi_{\text{f}}|\mathbf{r}|\Psi_{\text{i}}\rangle|^2}\ldots \times \frac{Q_{l,m,n}\omega_{l,m,n}\omega_{\text{i,f}}}{\omega^2_{l,m,n}+4Q^3_{l,m,n}(\omega_{\text{f,i}}-\omega_{l,m,n})^2} \tag{5.78}$$

Maximal enhancement Purcell factor

$$F = \frac{3\lambda^3_{\text{i,f}}Q}{4\pi^2 V} \tag{5.79}$$

5.3.3 Setup and outlook

Now that I have covered the concepts of thermal THz frequency photons and 3D cavities, I now present a road map to **room-temperature THz lasing**. The frequencies of interest in the four level scheme already proposed in Section 5.2 are $4\omega^{(0)}$, $2\omega^{(0)}$ $\omega_{\text{c}} = \omega^{(0)} + \delta\omega^{(0)}$ and $\omega_{\text{v}} = \omega^{(0)} - \delta\omega^{(0)}$, where $\delta\omega^{(0)}$ is due to higher order corrections of the Dirac cone, as described in Section 5.1.4.

We can design a 3D cavity with sides of length

$$L_x = \sqrt{2}\frac{\pi c}{\omega^{(0)} + 2\delta\omega^{(0)}}, \quad L_y = \sqrt{2}\frac{\pi c}{\omega^{(0)}}, \quad L_z = \sqrt{2}\frac{\pi c}{\omega^{(0)} - 2\delta\omega^{(0)}}, \tag{5.80}$$

which (from Equation 5.62) will support modes with frequencies

$$\omega_{l,m,n} = \frac{\omega^{(0)}}{\sqrt{2}}\sqrt{l^2\left(1+2\delta\right)^2 + m^2 + n^2\left(1-2\delta\right)^2}. \tag{5.81}$$

For $\delta \ll 1$,

$$\omega_{l,m,n} = \frac{\omega^{(0)}}{\sqrt{2}}\sqrt{l^2 + m^2 + n^2 + 4\delta(l^2 - n^2)}. \tag{5.82}$$

The cavity thus supports the modes needed for the lasing scheme, where $\omega_{4,0,4} = 4\omega^{(0)}$, $\omega_{2,0,2} = 2\omega^{(0)}$, $\omega_{1,1,0} = \omega^{(0)} + \delta\omega^{(0)} = \omega_{\mathrm{c}}$ and $\omega_{0,1,1} = \omega^{(0)} - \delta\omega^{(0)} = \omega_{\mathrm{v}}$. Modes with frequencies $\omega^{(0)} \pm 2\delta\omega^{(0)}$ are suppressed (as they are not resonant modes of the cavity), and the modes with frequency $3\omega^{(0)}$ will not result in any E1 transition within TQD states. The four energy levels thus form a closed scheme, decoupled from the rest of the Dirac cone. The only photons in the system will be at these four frequencies.

The transition rates, as found in Section 5.3.2, can be tuned with mode-dependent Q factor, $Q_{l,m,n}$, and spatial position, $\mathbf{r}$, such that the electric field density is modified as $\mathcal{E}_{l,m,n}(\mathbf{r})$. In tuning these parameters, it should be possible to find a set of parameters which give the correct conditions population inversion and resulting lasing can be achieved.

As we are now working at finite temperature, we can calculate the density of thermal photons at each frequency of the scheme. We pay particular attention to the number of available photons at the pumping frequency. The simulations at $T = 0$ described in this chapter were conducted for a $R = 30$ nm Bi_2Te_3 TQD. For particles $15 \leq R/\mathrm{nm} \leq 50$, the pump frequency will be $3.8 - 12.9$ THz. At room temperature, $0.14 \leq \bar{n}_{\mathrm{pump}} \leq 1.17$, which is above the lasing threshold found for the proof-of-principle case. For the same lasing scheme but using Bi_2Se_3 $15 \leq R/\mathrm{nm} \leq 50$, the number of photons per mode at room temperature at the pumping frequency is in the range $0.044 - 0.63$, which again is well above lasing threshold.

Of course, **population inversion cannot be achieved for a system in thermal equilibrium**. Cavities with time-varying Q factors can be made with moving mirrors [202], or time-varying metamaterials [203]. Time-varying Q factors (and thus time-varying photonic LDOS) could avoid the system thermalising, making it possible to demonstrate population inversion and consequent lasing with no pumping source other than thermal photons. This is an exciting avenue of research, and I will revisit it in the outlook of Chapter 7.

6. Modifying Light with Topology

"In thinking about nanotechnology today, what's most important is understanding where it leads..."
- Eric Drexler[1]

In this chapter I discuss how the quantised topological surface states of topological insulator nanostructures modify the **bulk optical properties** of the nanostructure, and how the resulting effects can be used to manipulate the properties of light in the surrounding environment. As with the work in Chapter 5, I focus on spherical TI nanoparticles for mathematical simplicity, which also allows me to compare theoretical results with available experimental data for **equiaxial[2] Bi_2Te_3 nanoparticles**. All results given could naturally be extended to non-spherical TI nanostructures, as discussed in Chapter 7. Understanding and experimentally demonstrating how topological insulator nanostructures interact with THz frequency light will be of paramount importance when it comes to considering how these systems can be used in new nanoscale and THz technologies.

In Section 6.1 I introduce the **S**urface **To**pological **P**article (**SToP**) mode, a new hybrid light-matter mode[3] which was predicted in 2016 [5] for a single, spherical Bi_2Se_3 nanoparticle. I present an extended study describing a physically realisable system of multiple Bi_2Te_3 nanoparticles in suspension, with irregular sizes and shape. The model is then validated with experimental data, presenting the first experimental observation of the SToP mode and evidence of the discrete nature of the Dirac cone. This section is based on the paper:

- **Experimental signature of a topological quantum dot**, Marie Rider, Maria Sokolikova, Stephen Hanham, Stefano Lupi, Peter Haynes, Derek Lee, Maddalena Daniele, Mariangela Cestelli Guidi, Cecilia Mattevi, Vincenzo Giannini, **Nanoscale** (2020) [6].

In Section 6.2 I discuss the effect of a spherical TINP on the **photonic LDOS of the surrounding environment**. I find that the photonic LDOS is amplified by a factor up to $\sim 10^9$ relative to that in homogeneous free space at a frequency tunable with the TINP material, size and Fermi level. This section is based on the unpublished manuscript:

- **Manipulating photonic local density of states with topological insulator nanostructures**, Marie Rider, Vincenzo Giannini, **In preparation** (2021) [7].

[1] Eric Drexler is an engineer known for his seminal work on molecular nanotechnology and is author of the book *Nanosystems: Molecular machinery, manufacturing and computation* [204].
[2] Equiaxial: Having axes of commensurate length.
[3] Technically a polariton mode, but this terminology is not necessary to understand the following work.

The purpose of the work in this chapter is two-fold:

(i) We can exploit the optical properties of these systems to indirectly probe the topological features of **TI band structures** and gain a better fundamental understanding of topological light-matter interactions at the nanoscale (both theoretically and experimentally).

(ii) The **bulk optical properties** of TI nanostructures and the **photonic LDOS** surrounding the nanostructure are both drastically modified by the presence of the topological surface states. Both of these phenomena present a novel path towards the much-desired control of light at the nanoscale and new applications therefrom.

6.1 The SToP mode

We have extensively covered the transitions between discrete energy levels in the Dirac cone of spherical TINPs in Chapter 5. For materials such as Bi_2Te_3 and Bi_2Se_3, these transitions occur at frequencies commensurate with a subset of the **bulk optical phonons** of the material first introduced in Section 2.3.4. The interference in scattering amplitudes of the two types of excitation (i.e. the coupling of the surface states and the optical phonons) leads to a **strong Fano resonance**[4], presenting as an asymmetric line shape in the scattering cross-section of the system. This new mode was first predicted in 2016 [5], and dubbed the **S**urface **To**pological **P**article (**SToP**) mode. This is a purely quantum mechanical feature of the system, and the asymmetric profile of this resonance creates a **point of zero-absorption** when the energy spacing of the surface states is matched exactly by the incident light, meaning that the excitation of a single electron occupying a topological surface state can shield the bulk from the absorption of incoming light.

Some nanostructures (such as **nanoribbons** and **thin films** [192, 205, 206]) can already be reliably produced, but TINPs (such as spherical TINPs, whose surface to volume ratio is maximal while maintaining a true 3D bulk) have so far proved more challenging and so their experimental study has been limited. The identification and classification of modes in the optical spectra of TI nanostructure samples has been a lively endeavour, oftentimes leading to contradictory conclusions [82, 207–212]. Unexpected peaks observed with Raman and IR spectroscopy[5] have been attributed to multiple different origins, such as surface oxidation, phonon confinement effects, unverified topological effects or simply left unclassified. This work presents evidence of a new, purely topological contribution to the spectra of TINPs.

To study the SToP mode theoretically, I review how the surface states of a TINP contribute to its **surface charge density**, and consequently how this charge density modifies the **absorption cross-section** of the nanoparticle, comparing to that of a trivially insulating particle. This theory was originally described for a single Bi_2Se_3 particle in vacuum [5],

[4] Fano resonances are ubiquitous within physics, and I give more details in Appendix B.11.
[5] A discussion of the differences between Raman and IR spectroscopy is given in Appendix B.2.

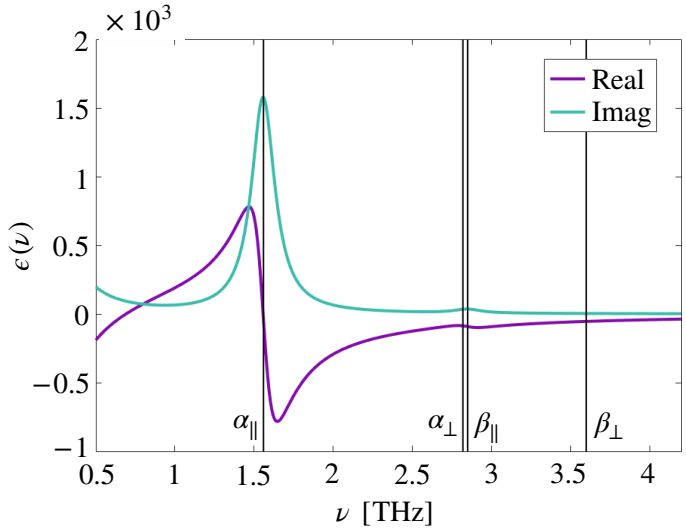

Figure 6.1: **Bi_2Te_3 bulk dielectric function:** The real (purple) and imaginary (green) components of Bi_2Te_3 bulk dielectric function $\epsilon_{\parallel}(\nu)$, for incident light parallel to the **c**-axis using parameters fitted to data in reference [213], presented in Table 6.1. The positions of the α and β phonon frequencies are annotated for both $\mathbf{k}\|\mathbf{c}$ and $\mathbf{k}\perp\mathbf{c}$ incoming light (denoted $\alpha_{\parallel}$, $\beta\|$, $\alpha_{\perp}$, and $\beta\perp$ respectively).

but I refer to Bi_2Te_3 throughout this section in order to compare to experimental results later on. I then extend the model to describe an array of nanoparticles of non-uniform size suspended in a medium (mineral oil), and compare to experimental results. I also discuss the effects of non-uniform geometry and particle orientation.

6.1.1 Dielectric function

In the theoretical treatment of a TINP irradiated with THz frequency light, we treat the bulk behaviour classically with a **bulk dielectric function** and the surface states are treated quantum mechanically. As briefly mentioned in Chapter 3, the bulk dielectric function here is both **dispersive** (i.e. ϵ is a function of frequency, ν, rather than constant) and **anisotropic** (such that the material responds differently to light travelling parallel and perpendicular to the c-axis of the material). The bulk dielectric function of Bi_2Te_3 is a dyadic[6] and to treat the system analytically we write $\epsilon(\nu)$ as a diagonal matrix with principal components $[\epsilon_{\perp}(\nu), \epsilon_{\perp}(\nu), \epsilon_{\parallel}(\nu)]$ and all other components equal to 0. $\epsilon_{\parallel}(\nu)$ gives the dielectric function along the c-axis of the material, while $\epsilon_{\perp}(\nu)$ is the dielectric function in both axes perpendicular to the c-axis. Each principal component is of the form

$$\epsilon(\nu) = \sum_{\mathrm{j}=\alpha,\beta,\mathrm{f}} \frac{\nu_{\mathrm{p,j}}^2}{\nu_{0,\mathrm{j}}^2 - \nu^2 - i\gamma_{\mathrm{j}}\nu}, \tag{6.1}$$

[6]See Appendix A.3 for a reminder on dyadics.

	$\nu_{\mathrm{p,j}}$ (THz)	$\nu_{0,\mathrm{j}}$ (THz)	γ_{j} (THz)
α	21	1.56	0.18
β	4	2.85	0.2
f	11	0	0.24

Table 6.1: **Parameters of $\epsilon_{\parallel}(\nu)$ for Bi_2Te_3:** Calculated from experimental data in [213]. $\nu_{\mathrm{p,j}}$, $\nu_{0,\mathrm{j}}$ and γ_{j} denote the amplitude, resonance frequency and harmonic broadening parameters for each mode.

which contains contributions from **optical phonons** labelled α and β, and **free charge carriers** (denoted by f) arising from bulk defects. The $\alpha_{\parallel}$ and $\beta_{\parallel}$ phonons correspond respectively to the A^1_{1u} and A^2_{1u} phonons described in Section 2.3.4 and depicted in Figure 2.7. The $\alpha_{\perp}$ phonon and $\beta_{\perp}$ phonons correspond to the E^1_u and E^2_u modes.

The parameters (given in Table 6.1) for $\epsilon_{\parallel}(\nu)$ have been determined by fitting to experimental data for samples irradiated with light propagating along the c-axis of the material [213], and measured at 300 K. The real and imaginary parts of $\epsilon_{\parallel}(\nu)$ are plotted in Figure 6.1a with purple and green lines respectively. To present a transparent analysis, the following theoretical study only considers the contribution to the TINP optical response from $\epsilon_{\parallel}(\nu)$. We also expect a contribution from $\epsilon_{\perp}(\nu)$ (and so should average over all three material axes), but due to limited reliable $\epsilon_{\perp}(\nu)$ data, we present theoretical results derived using only $\epsilon_{\parallel}(\nu)$. Considering the material **isotropic** in this manner does not affect the conclusions of this work. However for reference, the plot of $\epsilon_{\parallel}(\nu)$ in Figure 6.1 is annotated with vertical lines denoting the α and β phonon frequencies for both $\epsilon_{\parallel}(\nu)$ and $\epsilon_{\perp}(\nu)$ (values taken from [78]). For $\epsilon_{\parallel}(\nu)$, the resonance frequencies for the α and β phonons are 1.56 THz and 2.85 THz respectively (as given in Table 6.1), while for $\epsilon_{\perp}(\nu)$, the frequencies used are 2.82 THz and 3.60 THz respectively.

6.1.2 Absorption cross-section for a topological insulator nanoparticle

In this section I review the derivation of the **absorption cross-section** of a topological insulator nanoparticle, as given in Reference [5] but modified to include a background medium (such as mineral oil). I show how the surface charge density of the nanoparticle is modified due to the excitation of a surface state, and from there find the absorption cross-section of the nanoparticle. I work in the limit in which the particle radius R is much smaller than the wavelength of incoming light $R \ll \lambda$, and so the derivation begins by treating light in the **electric dipole approximation** as usual, such that system experiences a time-varying perturbation to an otherwise time-invariant potential, $\Phi_{\mathrm{in}}(\mathbf{r}) \to \Phi_{\mathrm{in}}(\mathbf{r}) + \delta\Phi(\mathbf{r}, t)$, where

$$\delta\Phi(\mathbf{r}, t) = \mathbf{E}(t) \cdot \mathbf{r} = \mathrm{Re}\left[Br\sin\vartheta\left(e^{i(\varphi - 2\pi\nu t)} + e^{i(\varphi + 2\pi\nu t)}\right)\right], \tag{6.2}$$

where B is the strength of the potential inside the bulk of the TINP. Considering a system initially in state $|\Psi_\mathrm{i}\rangle$ in the presence of a time-varying potential, the wave function of the surface state becomes

$$\Psi(\mathbf{r}) = \Psi_\mathrm{i}(\mathbf{r}) + \delta\Psi(\mathbf{r}, t). \tag{6.3}$$

The perturbed part, $\delta\Psi(\mathbf{r}, t)$, can be expanded in terms of unperturbed wavefunctions, such that

$$\delta\Psi(\mathbf{r}, t) = \sum_{\mathrm{n}\neq\mathrm{i}} c_\mathrm{n}(t)\Psi_\mathrm{n}(\mathbf{r})e^{-i2\pi\nu_{\mathrm{n,i}}t}, \tag{6.4}$$

where $h\nu_{\mathrm{n,i}} = E_\mathrm{n} - E_\mathrm{i}$. Due to the rapid decay of the surface state into the bulk, we can assume $r = R$, and as $\delta V(\mathbf{r}, t)$ is a harmonic perturbation with frequency $\omega = 2\pi\nu$, the coefficients of the expansion are to first order given by (see Appendix A.8 for more details)

$$c_\mathrm{n}^{(1)} = -\frac{i}{\hbar}\int_0^t dt' \ \langle\Psi_\mathrm{n}|e\delta\Phi|\Psi_\mathrm{i}\rangle e^{i2\pi\nu_{\mathrm{n,i}}t'} \tag{6.5}$$

$$\begin{aligned} &= -\langle\Psi_\mathrm{n}|e\mathrm{Re}\left[BR\sin\vartheta e^{i(\varphi-\omega t)}\right]|\Psi_\mathrm{i}\rangle\frac{e^{i2\pi\nu_{\mathrm{n,i}}t}}{h(\nu_{\mathrm{n,i}}-\nu)} \\ &\quad - \langle\Psi_\mathrm{n}|e\mathrm{Re}\left[BR\sin\vartheta e^{i(\varphi+2\pi\nu t)}\right]|\Psi_\mathrm{i}\rangle\frac{e^{i2\pi\nu_{\mathrm{n,i}}t}}{h(\nu_{\mathrm{n,i}}+\nu)}. \end{aligned} \tag{6.6}$$

$\delta\Phi(\mathbf{r}, t)$ causes a **time-dependent probability density** and thus a **time-varying charge density**. The resultant charge density is then given by

$$\rho(\mathbf{r}, t) = e|\Psi(\mathbf{r}, t)|^2 = e|\Psi_i(\mathbf{r})|^2 + e\Psi_i(\mathbf{r})^*\delta\Psi(\mathbf{r}, t) + e\Psi_i(\mathbf{r})(\delta\Psi(\mathbf{r}, t))^*. \tag{6.7}$$

We consider a transition from the initial state $|\Psi_\mathrm{i}\rangle = |s, n, m\rangle$ to a final state $|\Psi_\mathrm{f}\rangle = |s', n', m'\rangle$, induced by circularly polarised light travelling along the c-axis of the material. For a Fermi level at $E_\mathrm{F} = A/R$, the only allowed transitions are those described in Section 5.1.3, such that $\Delta s = 0$ and $\Delta m = \pm 1$, with the respective matrix elements given by

$$\langle +, 0, 3/2|\sin\vartheta e^{i\varphi}|+, 0, 1/2\rangle = \sqrt{\frac{2}{3}}, \tag{6.8}$$

$$\langle +, 1, -1/2|\sin\vartheta e^{i\varphi}|+, 0, 1/2\rangle = \frac{\sqrt{2}}{3}, \tag{6.9}$$

$$\langle +, 0, -3/2|\sin\vartheta e^{i\varphi}|+, 0, -1/2\rangle = \sqrt{\frac{2}{3}}, \tag{6.10}$$

$$\langle +, 1, 1/2|\sin\vartheta e^{i\varphi}|+, 0, -1/2\rangle = \frac{\sqrt{2}}{3}. \tag{6.11}$$

The time-varying charge density is then given by

$$\rho(\vartheta,\varphi,t) = -\frac{e^2}{3\pi\epsilon_0}\left(\frac{1}{A-h\nu R}+\frac{1}{A+h\nu R}\right)\mathrm{Re}\left[B\sin\vartheta\left(e^{i(\varphi-2\pi\nu t)}+e^{i(\varphi+2\pi\nu t)}\right)\right]. \quad (6.12)$$

We write this as

$$\rho(\mathbf{r},t) = -\delta_R(\nu)\epsilon_0\mathrm{Re}\left[B\sin\vartheta\left(e^{i(\varphi-2\pi\nu t)}+e^{i(\varphi+2\pi\nu t)}\right)\right] = -\frac{\delta_R(\nu)\epsilon_0}{R}\Phi_{\mathrm{in}}, \quad (6.13)$$

where

$$\delta_R(\nu) = \frac{e^2}{3\pi\epsilon_0}\left(\frac{1}{A-h\nu R}+\frac{1}{A+h\nu R}\right). \quad (6.14)$$

For a Fermi level within $\pm A/R$, $\delta_R(\nu)$ is modified owing to the absence of an energy level at $E=0$, meaning that the spacing between energy levels directly above and below the Dirac point is $2A/R$. For a Fermi energy at $E_{\mathrm{F}}=0$, we can repeat the process and find that

$$\delta_R(\nu) = \frac{e^2}{6\pi\epsilon_0}\left(\frac{1}{2A-h\nu R}+\frac{1}{2A+h\nu R}\right). \quad (6.15)$$

We thus far have an expression for the potential inside the TINP and the charge density on the surface. The potential outside of the TINP will be of the form

$$\Phi_{\mathrm{out}} = \mathrm{Re}\left[\frac{C}{r^2}\sin\vartheta e^{i\varphi}-\mathcal{E}r\sin\vartheta e^{i\varphi}\right], \quad (6.16)$$

where $\mathcal{E}$ is the incident field strength. The **interface conditions for Maxwell's equations** (following from the conditions given in Chapter 3, reformulated in terms of potentials in spherical coordinates) at the surface of the TINP are given by

$$\left.\frac{\partial\Phi_{\mathrm{in}}}{\partial\vartheta}\right|_R = \left.\frac{\partial\Phi_{\mathrm{out}}}{\partial\vartheta}\right|_R, \quad (6.17)$$

$$\epsilon(\nu)\left.\frac{\partial\Phi_{\mathrm{in}}}{\partial r}\right|_R = \epsilon_{\mathrm{oil}}\left.\frac{\partial\Phi_{\mathrm{out}}}{\partial r}\right|_R+\frac{\rho}{\epsilon_0}, \quad (6.18)$$

where ϵ_{oil} is the dielectric constant of the suspension material, in our case mineral in order to preserve the quality of the particles, for which $n_{\mathrm{oil}}=1.47$ and $\epsilon_{\mathrm{oil}}=2.16$). Solving these equations for B and C, we find

$$B = \frac{-3\epsilon_{\mathrm{oil}}}{\epsilon(\nu)+\delta_R(\nu)+2\epsilon_{\mathrm{oil}}}\mathcal{E}, \quad (6.19)$$

$$C = R^3\frac{\epsilon(\nu)+\delta_R(\nu)-\epsilon_{\mathrm{oil}}}{\epsilon(\nu)+\delta_R(\nu)+2\epsilon_{\mathrm{oil}}}\mathcal{E}. \quad (6.20)$$

The latter expression is the term giving the induced dipole moment in the external field, such that $\mathbf{E} = \mathcal{E}\alpha_0/r^3$, where the **polarizability** $\alpha_0(\nu)$ is given by

$$\alpha_0(\nu) = 4\pi\epsilon_0 R^3 \frac{\epsilon(\nu) + \delta_R(\nu) - \epsilon_{\text{oil}}}{\epsilon(\nu) + \delta_R(\nu) + 2\epsilon_{\text{oil}}}. \tag{6.21}$$

From the polarizability we can then find the absorption cross-section [172],

$$\sigma_{\text{abs}}(\nu) = \frac{|\mathbf{k}|}{\epsilon_0}\text{Im}\left[\alpha_0(\nu)\right] \tag{6.22}$$

$$= 4\pi R^3 n_{\text{oil}} \frac{2\pi}{\lambda}\text{Im}\left[\frac{\epsilon(\nu) + \delta_R(\nu) - \epsilon_{\text{oil}}}{\epsilon(\nu) + \delta_R(\nu) + 2\epsilon_{\text{oil}}}\right]. \tag{6.23}$$

Result: Absorption cross-section of a TINP

Polarizability of a TINP of radius R,

$$\alpha_0(\nu) = 4\pi\epsilon_0 R^3 \frac{\epsilon(\nu) + \delta_R(\nu) - \epsilon_{\text{oil}}}{\epsilon(\nu) + \delta_R(\nu) + 2\epsilon_{\text{oil}}}. \tag{6.24}$$

Absorption cross-section of a TINP of radius R,

$$\sigma_{\text{abs}}(\nu) = 4\pi R^3 n_{\text{oil}} \frac{2\pi}{\lambda}\text{Im}\left[\frac{\epsilon(\nu) + \delta_R(\nu) - \epsilon_{\text{oil}}}{\epsilon(\nu) + \delta_R(\nu) + 2\epsilon_{\text{oil}}}\right], \tag{6.25}$$

where $\delta_R(\nu)$ depends on the Fermi level, E_{F},

$$E_{\text{F}} = \frac{A}{R}: \qquad \delta_R(\nu) = \frac{e^2}{3\pi\epsilon_0}\left(\frac{1}{A - h\nu R} + \frac{1}{A + h\nu R}\right), \tag{6.26}$$

$$E_{\text{F}} = 0: \qquad \delta_R(\nu) = \frac{e^2}{6\pi\epsilon_0}\left(\frac{1}{2A - h\nu R} + \frac{1}{2A + h\nu R}\right), \tag{6.27}$$

and for a trivial insulator, $\delta_R(\nu) = 0$.

6.1.3 Understanding the absorption cross-section

For a given Fermi level, $\delta_R(\nu)$ varies only with R and ν. In Figure 6.2a, I plot the theoretically expected absorption cross-sections of TINPs with $E_{\text{F}} = A/R$ and radii 15, 20 and 25 nm respectively, and the topologically trivial case where $\delta_R(\nu) = 0$. Each cross-section with a topological contribution has a characteristic shape of three peaks, corresponding to the **β phonon mode**, a **localised surface plasmon-polariton (LSPP) mode**[7], and the **SToP mode**. A **point of zero absorption** can be seen for each SToP mode, at which

[7] The LSPP is not of major importance in this work, we just need to know of its existence. The experimental data analysed in this chapter is not at frequencies low enough to capture the LSPP.

a single electron in a topological surface state shields the bulk from absorbing incoming light. The LSPP and β modes are bulk contributions and as such, their positions do not change with particle size. The SToP peak position and point of zero-absorption do vary with R. As the particle size varies, the spacing between discretized surface state energies varies as $\sim 1/R$. This in turn changes the frequency at which the particle polarizability is modified when a surface state is excited, as described by $\delta_R(\nu)$. This in turn leads to a R-dependence of the absorption cross-section of the nanoparticle. As particle size is reduced, the frequency of surface state excitations increases, and thus the SToP mode peak and point of zero-absorption both shift to higher frequencies. For particles of approximately $R = 15$ nm, the SToP mode appears on top of the β phonon mode, resulting in a double peak structure of broader linewidth. The behaviour of the SToP mode and zero absorption trough can also be seen in Figure 6.2c, which shows the behaviour of the absorption cross-section for varying R and ν for $E_{\mathrm{F}} = A/R$.

Figure 6.2b shows $\sigma_{\mathrm{abs}}(\nu)/\pi R^2$ for a particle $R = 40$ nm, at the two Fermi levels $E_{\mathrm{F}} = A/R$ and $E_{\mathrm{F}} = 0$. While the bulk modes remain in the same positions, we see a shift in the SToP mode peaks. Although we do not know the precise Fermi level of each TINP in the sample, for particles whose Fermi level resides in the band gap (and thus contribute to the SToP mode peak in the absorption cross-section) it is most likely that transitions are occurring between energy levels separated by A/R rather than $2A/R$.

The R and ν dependence of the absorption cross-section is illustrated in Figure 6.2c. In order to demonstrate how the various contributions to the dielectric function manifest in the absorption cross-section, I perform a further study in which we artificially remove first the α phonon and then the β phonon contribution from the theoretical calculation. Figure 6.3a gives the absorption cross-section with no modifications. Figure 6.3b gives the absorption cross-section as a function of ν and R with the LSPP contribution artificially removed (such that $\nu_{\mathrm{p,f}} = 0$). The position of the removed mode is given in white, while the β phonon peak, SToP mode and trough of zero absorption can be clearly seen. In Figure 6.3c, the α phonon contribution is also removed, (such that $\nu_{\mathrm{p,f}} = \nu_{\mathrm{p},\alpha} = 0$). The trough of zero absorption can still be seen, but the SToP mode peak is no longer present. This confirms that the SToP mode is mediated by the α phonon. This is further confirmed in Figure 6.3d, in which both the LSPP and β phonon contributions are removed ($\nu_{\mathrm{p,f}} = \nu_{\mathrm{p},\beta} = 0$) and the SToP mode is still present.

6.1.4 Modifying theory parameters

Throughout the work of this thesis, the crystal structure has been taken to be isotropic, such that $A = \frac{1}{3}(A_0 + 2B_0)$. Figure. 6.4a shows how the theoretically calculated absorption cross-section varies with uncertainty in A. Shifting $A \to A'$ by 10% shifts the position of the SToP peak by $< 10\%$. Figure 6.4b illustrates that modifying the magnitude of the topological contribution to the particle polarizability $\delta_R(\nu)$ (by multiplying by a constant

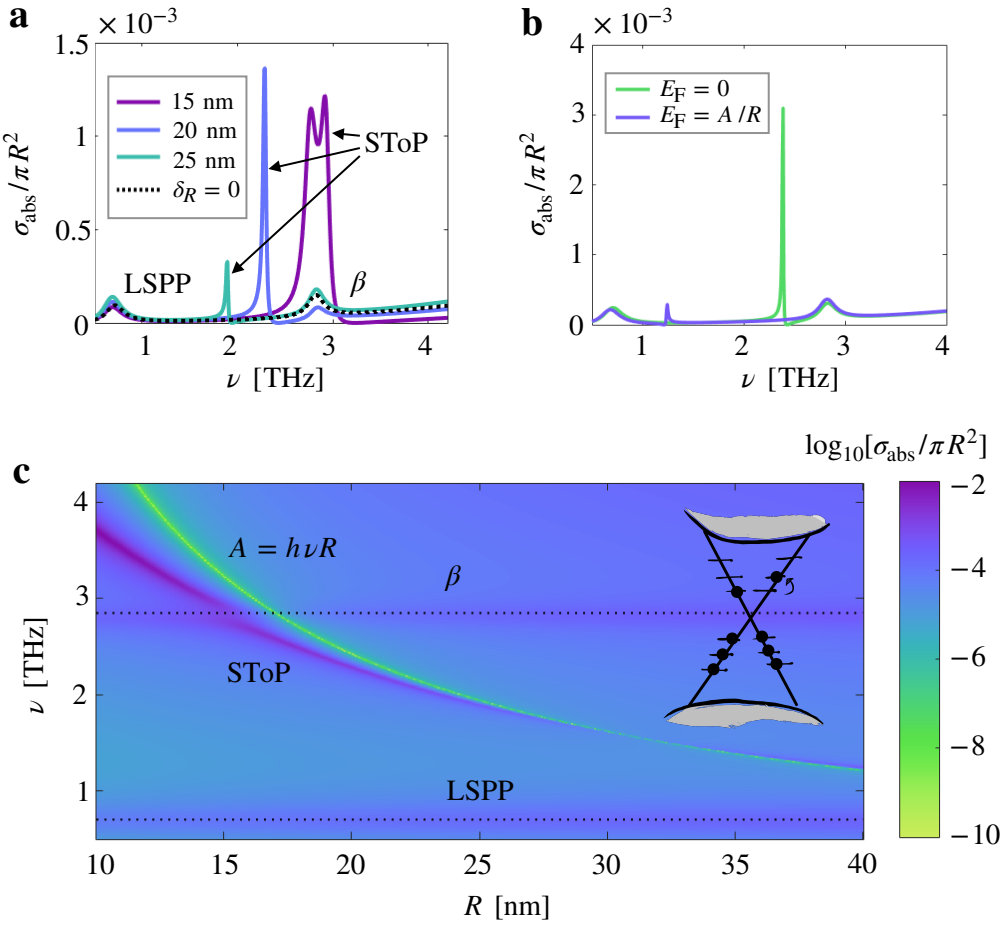

Figure 6.2: **TINP absorption cross-section:(a)** Absorption cross-section of a TINP with $E_F = A/R$, R=(15, 20, 25) nm and a TINP of radius 15 nm for which $\delta_R = 0$. The LSPP and β mode are visible and labelled, whilst the α mode is over-damped and thus not seen in the theoretically calculated absorption cross-section. Increased TINP radius results in a lower frequency SToP mode peak (also labelled). For $R = 15$ nm, the SToP mode and β modes overlap and a split peak is seen. For each SToP mode there is a point of zero absorption which occurs to the right of the peak. **(b)** Changing the Fermi level from $E_F = A/R$ to $E_F = 0$ (for $R = 40$ nm) results in the SToP mode occurring in the absorption cross-section at twice the frequency of incoming light, shown for $R = 40$ nm. **(c)** Absorption cross-section varying with R and ν. The bulk LSPP and β phonon positions remain constant for varying radius size, and the line of zero-absorption is annotated ($A = h\nu R$). Figures modified from [6], published by The Royal Society of Chemistry.

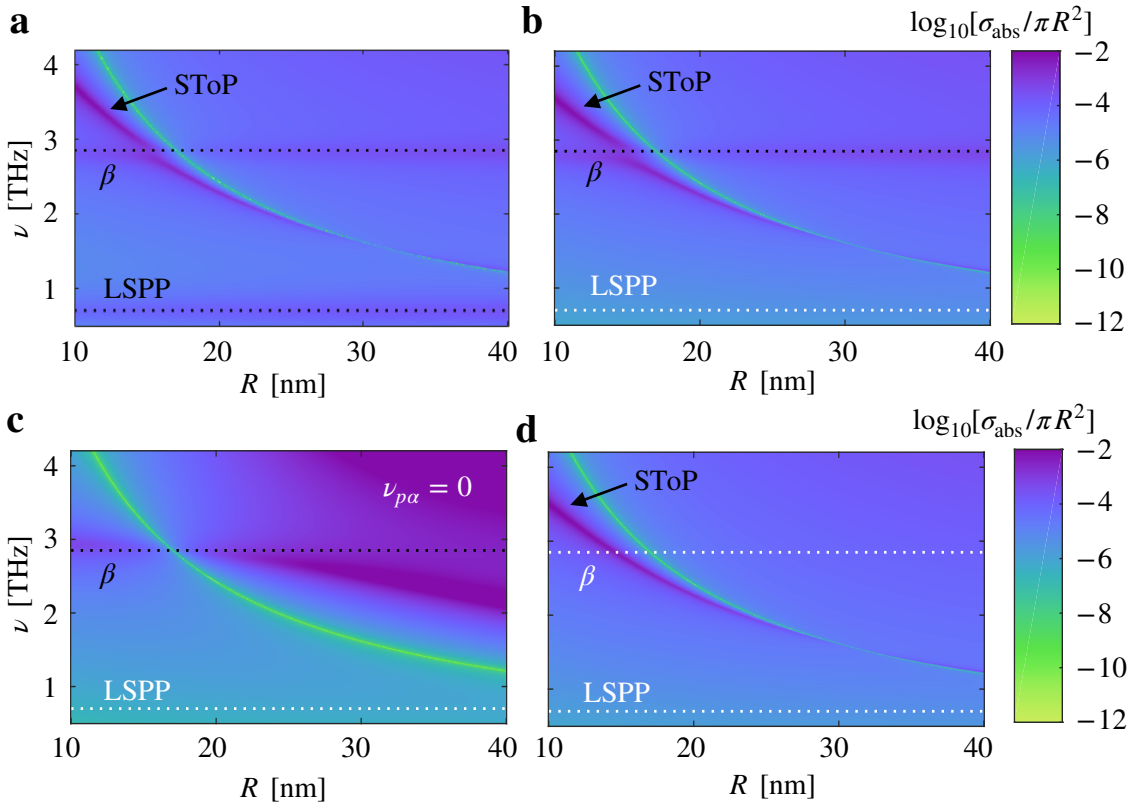

Figure 6.3: **Modifying the dielectric function: (a)** Absorption cross-section with no modifications. **(b)** Absorption cross-section with LSPP mode (highlighted with white dotted line)) removed from the dielectric function ($\nu_{\mathrm{p,f}} = 0$). **(c)** Absorption cross-section with both LSPP and α phonon contributions removed ($\nu_{\mathrm{p,f}} = \nu_{\mathrm{p},\alpha} = 0$). The trough of zero-absorption is still seen, but the SToP mode is no longer present. **(d)** Absorption cross-section with both LSPP and β phonon contributions (highlighted with a white dotted line) removed ($\nu_{\mathrm{p,f}} = \nu_{\mathrm{p},\beta} = 0$). Figures modified from [6], published by The Royal Society of Chemistry.

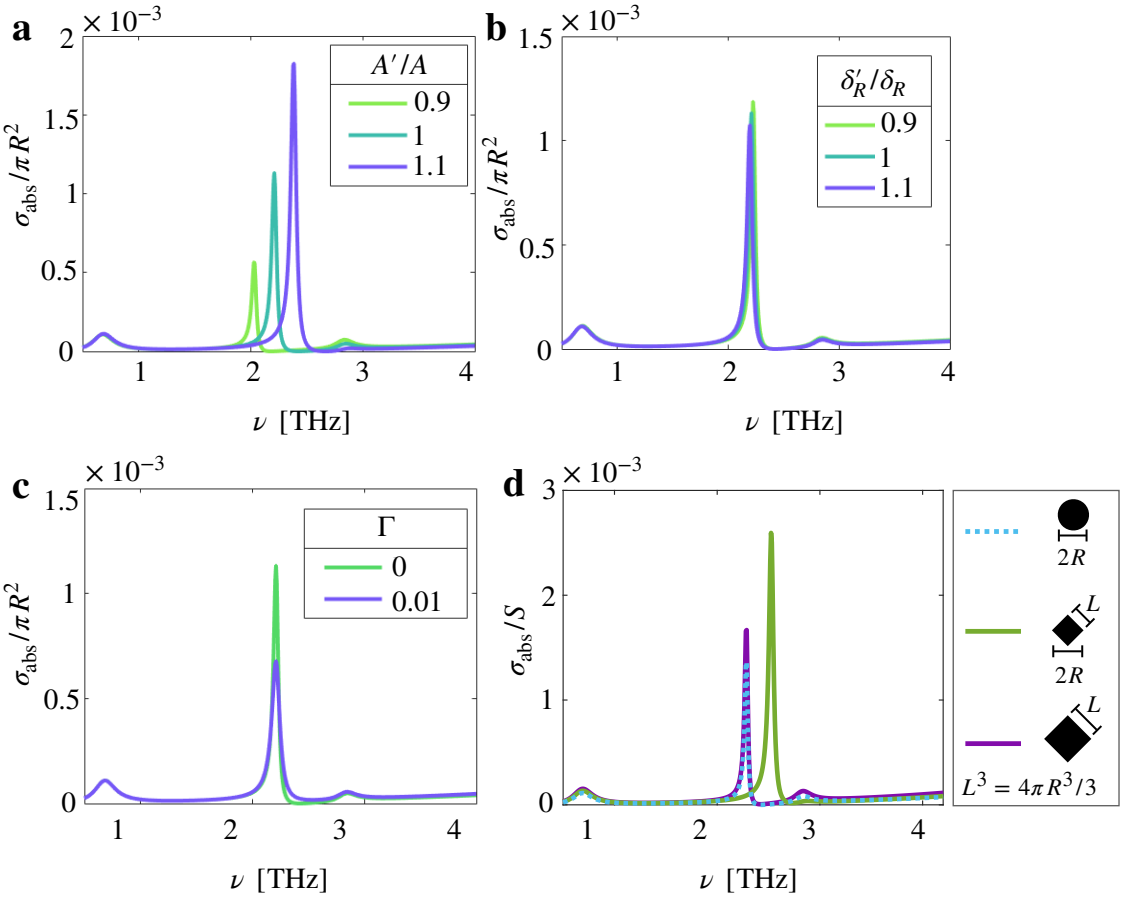

Figure 6.4: **Modifying theory parameters: (a)** For $R = 20$ nm, varying A by 10%, which shifts the position of the SToP mode peak and modifies the height of the peak. **(b)** Varying the magnitude of $\delta_R(\nu)$ by 10 %, which has no effect on the position of the SToP mode peak and very little effect on the height of the peak. **(c)** Introducing a small complex component to the denominator of $\delta_R(\nu)$, $i\Gamma A$, equivalent to introducing a finite life time to the excited surface states. Introduction of this finite lifetime reduces the height of the SToP mode peak. **(d)** Comparison of absorption cross-section for nanoparticles of varying geometry and size. Absorption cross-section of sphere (dotted blue) with $R = 20$ nm, projection $S = \pi R^2$. Absorption cross-section for a cube with diagonal length $2R = 40$ nm (green), such that $L = 28.2$ nm, and projection $S = L^2$. Absorption cross-section of cube of length $L = 32.2$ nm (purple) and $S = L^2$, with volume $V = L^3 = 4\pi R_{\text{eff}}^3/3$ such that effective radius $R_{\text{eff}} = 20$ nm. Figures modified from [6], published by The Royal Society of Chemistry.

coefficient δ_{coeff}), has little effect on the position of the SToP peak. Figure 6.4c shows that when a **finite lifetime** of excited surface states is considered (by subtracting a small, complex component $i\Gamma A$ from the denominator of all $\delta_R(\nu)$ terms), the height of the SToP mode peak becomes smaller (for a particle of $R = 20$ nm and $\Gamma = 0.01$, the height of the SToP mode peak reduces by $\sim 45\%$) and the position remains the same.

$\delta_R(\nu)$ has no dependence on the dielectric function of either the topological material or the mineral oil, but is affected by the A value. The peak in absorption due to the topological term will experience a shift dependent on which material is being used. For example, the SToP peak for a R=20 nm TINP made of Bi_2Te_3 and Fermi level $E_F = A/R$ will occur at 2.21 THz, whereas for a Bi_2Se_3 TINP of the same radius (with A=3.0 eVÅ [49], as studied in the original work by Siroki *et al.* [5]) the peak will occur at 3.1 THz.

As can be seen in the **tunneling electron microscope (TEM)** images of Figure 6.6a, the synthesised Bi_2Te_3 nanoparticles[8] discussed in this work are **rhombohedral**, however their topological properties are well-approximated by those of spherical particles, due to the robustness of topological states against surface deformation. This is demonstrated in References [5, 35] in which it is shown that the discrete energy levels of TI nanospheres and nanocubes of equal volume converge for particles of radius $R > 10$ nm. This idea is also demonstrated in Figure 4.7a of Chapter 4, in which a TI nanosphere is deformed to a prolate nanospheroid at constant volume. The energy levels are fairly robust against this deformation, and the degeneracy of the energy levels is not lifted until the particle axes differ by $\sim 10\%$. This means that the topological contribution to the absorption cross-section is also approximately the same for equiaxial particles of equal volume.

If a cube of volume V were to be deformed to a sphere, it would have an effective radius R_{eff}, such that $V = 4\pi R_{\text{eff}}^3/3$. This value of R_{eff} can then be used in Equation 6.26 to calculate the topological contribution to the absorption cross-section, $\delta_R(\nu)$. The absorption cross-section of a cube can also be calculated analytically [214], with the topological contribution described as above. In Figure 6.4d we plot the absorption cross-sections of a sphere with $R = 20$ nm (dotted blue), a cube with diagonal length $2R$ (green), such that $L = 28.3$ nm and a cube with $R_{\text{eff}} = 20$ nm (purple), such that it has the same volume as the sphere. The cross-sections are normalised by the projection of each nanostructure, i.e. $S = \pi R^2$ for the sphere and $S = L^2$ for the cubes. The qualitative results for each nanostructure are very similar, with the sphere and cube of equal volume demonstrating a SToP peak and point of zero-absorption at the same positions. The cube with diagonal length equal to the diameter of the sphere has a slightly smaller effective radius, and thus presents a SToP mode and point of zero-absorption shifted to a slightly higher frequency. As the rhombohedral nanoparticles in our experiment fall between the two limits of a sphere and a

[8] I include some details on how the nanoparticles are synthesised in Appendix B.12 for interested experimentalists, but do not include it in the main text as this was not my work, and an in-depth understanding of the experimental method is not needed to understand the results of this section.

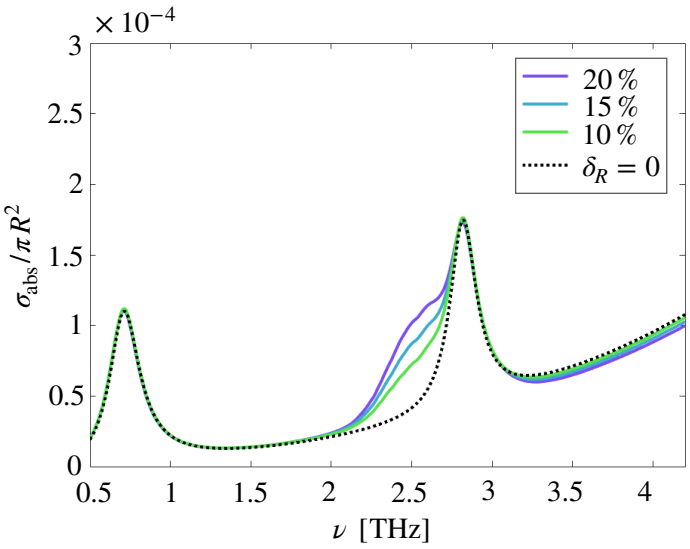

Figure 6.5: **Ensembles of TINPs:** For an ensemble of particles with a Gaussian distribution of radii ($\bar{R} = 17.5$ nm and standard deviation 1.8 nm) and in which only (10,15,20) % of TINPs show a SToP mode, the peak height is greatly reduced and no longer displays a point of zero absorption. Figure modified from [6], published by The Royal Society of Chemistry.

cube, we conclude that approximating the rhombohedral nanoparticles as spherical should give a qualitatively good result.

6.1.5 Ensembles of TINPs

So far we have discussed the optical properties of a single TINP, which is representative of an ensemble of non-interacting particles of equal radius, normalised to the number of TINPs. However in our experimental sample, we have a partial **agglomerate**[9] of nanoparticles, and the nanoparticles have a range of radii. Before measurements were taken, the sample was agitated to separate the nanoparticles. It is, however, inevitable that some particles will remain as an agglomerate. We would expect this agglomerate to contribute to the bulk properties of the absorption-cross section, but lose the quantum confinement effects expected from small, separate nanoparticles. Any topological peak from such a large mass of material would occur at such a low frequency as to not be measured in our experiment. For example, a particle of $R = 100$ nm would be expected to exhibit a SToP mode peak at approximately 0.45 THz with a greatly suppressed amplitude. This is outside of the frequency range of our measured data. So, we do not expect partial agglomerates to contribute topological features to the absorption cross-section.

Due to uncertainty in the Fermi level and orientation of each TINP in relation to the incoming light, it can be assumed that while all TINPs contribute to the bulk properties of

[9] Agglomerate: Some of the particles have grouped into a single mass.

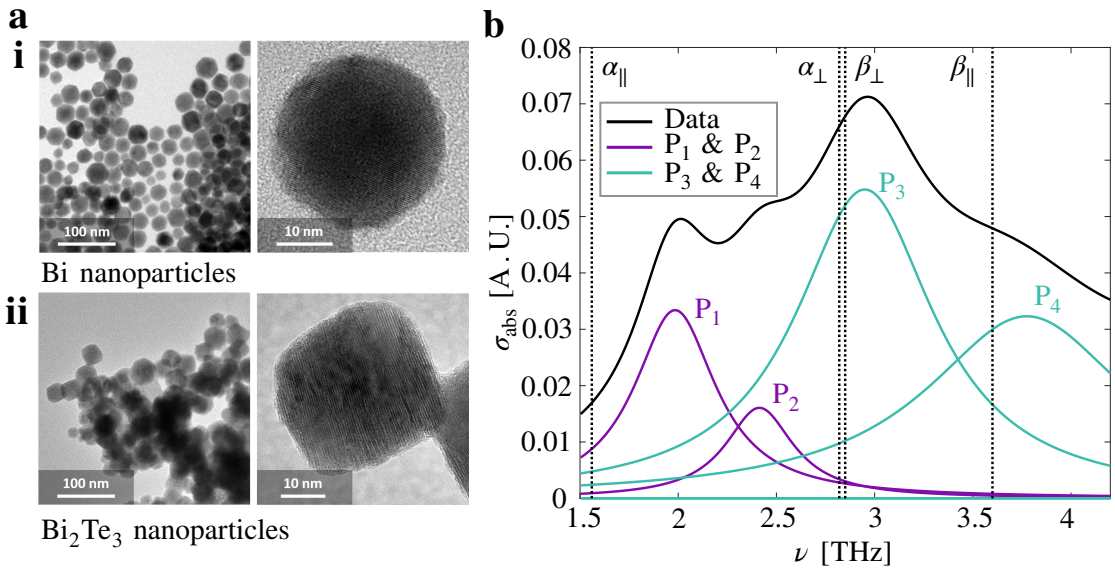

Figure 6.6: **Experimental results:** **(a)** TEM images of **(i)** Bi nanoparticles, which are nearly spherical and of average radius 14.4 nm. **(ii)** Successfully synthesized Bi_2Te_3 nanoparticles with a slightly rhombohedral shape and average radius of 17.5 nm. **(b)** Experimental absorption cross-section data with impurity absorption band subtracted, superimposed with a Lorentzian decomposition of the same data, fitted with four peaks, P_1-P_4. Figure modified from [6], published by The Royal Society of Chemistry.

the absorption cross-section, only a small percentage will give a topological contribution. Figure 6.5 illustrates the theoretically calculated absorption cross-section of an ensemble of TINPs of mean radius 17.5 nm and standard deviation 1.8 nm (values taken from analysis of TEM images of the experimental sample), with a varying percentage contributing to the topological property. The peak height is greatly suppressed and a point of zero-absorption is no longer observed.

6.1.6 Comparison to experimental results

In Figure 6.6b, we show the experimental absorption cross-section (solid black line) of Bi_2Te_3 TINPs suspended in mineral oil, measured at 300 K. The vertical dotted lines denote the four phonon frequencies ($\alpha_\parallel$, $\beta_\parallel$, $\alpha_\perp$, $\beta\perp$) corresponding to the two bulk dielectric functions $\epsilon_\parallel$ and $\epsilon_\perp$ respectively.[10] We have performed a **Lorentzian decomposition** using four Lorentz peaks, with fit values given in Table 6.2. Using four peaks (which we label P_1-P_4) yields a fitting error of 0.23%, whereas using three or five peaks results in an error of 2.3% or 3.4% respectively. This method is described in more detail in Appendix C.3. We assign P_3 and P_4 to the $\beta_\parallel$ and $\beta_\perp$ phonons respectively. α phonons are typically under-damped in bulk samples and so not observed in the theoretical calculations of the absorption cross-section using the bulk dielectric function (as demonstrated in Figures 6.2a-

[10] Recalling that $\alpha_\parallel$ and $\beta_\parallel$ are the A^1_{1u} and A^2_{1u} modes from Chapter 2, and $\alpha_\parallel$ and $\beta_\parallel$ are the E^1_u and E^2_u modes respectively.

	P_1	P_2	P_3	P_4
Peak position (THz)	1.98	2.41	2.95	3.77
Peak width (THz)	0.51	0.42	0.86	1.26

Table 6.2: **Parameters of Lorentzian fit**: Parameters of the four peak Lorentzian fit with a fit error of 0.24%.

c). This can be understood by studying the bulk dielectric function for Bi_2Te_3 depicted in Figure 6.1, where the very large value of $\mathrm{Im}[\epsilon(\nu)]$ at the α phonon frequency will result in a very small contribution to $\sigma_{\mathrm{abs}}(\nu)$ (given in equation 6.25) at this frequency. However, finite size effects may reduce damping of transverse modes, resulting in an increased amplitude which may be visible in the absorption cross-section. So, it is possible that the $\alpha_\perp$ phonon also slightly contributes to the amplitude of P_3.

P_1 and P_2 do not appear to relate to any expected bulk modes. We rule out oxidation effects as the sample was kept in chloroform, and exchanged for mineral oil for THz measurements. Samples typically show oxidation effects on the time-scale of days [209], which is not the case for our sample. We note that P_2 appears at a frequency commensurate with the SToP mode peak predicted for an ensemble of varying radius as demonstrated in Figure 6.5. While the short height of the SToP mode peak is partially explained by the assumption that very few particles contribute to the topological properties of the sample, we also note that our theory is modelled at zero temperature, whereas the experiment operates at room temperature (~ 6 THz), where the probability of finding a level empty in our system is low. Temperature smearing will result in the modes seen experimentally being less visible than those seen in theory. This could be remedied by studying a TI with a bigger band gap and/or smaller particles. It is possible that the presence of two new non-bulk modes (P_1 and P_2) is due to SToP modes resulting from both the $\alpha_\parallel$ and $\alpha_\perp$ phonons.

The observation of two unexpected peaks at frequencies which do not relate to expected bulk modes allows us to conclude that **at least one of the peaks is likely topological in origin**. We conclude from this experimental comparison with the theory model that we have observed the SToP mode in Bi_2Te_3 nanoparticles, which was theoretically predicted in [5].

6.2 TINP modifying the photonic local density of states (LDOS)

In the previous section we demonstrated that excitations of the topological surface states of a TI nanostructure can modify the **absorption cross-section** of the structure - a bulk optical property. We now look at how these excitations can alter the environment surrounding the TI nanostructure via the **photonic local density of states**.

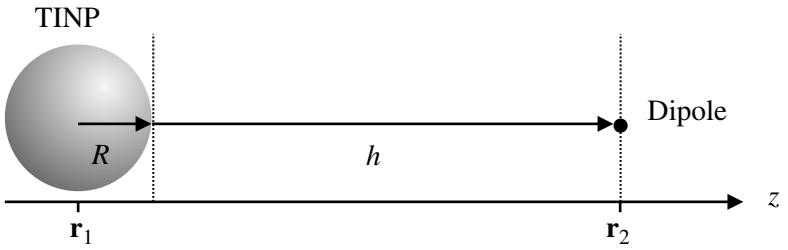

Figure 6.7: **Probing the photonic LDOS near a TINP:** Dipole at a distance h from the surface of a of a spherical TINP of radius R.

It is already well known that **dielectric nanostructures**[11] will modify the **photonic LDOS** in their immediate surroundings by producing an effective dipole in response to a probe dipole [172]. The strength of the effective dipole will depend on the polarizability of the material, $\alpha_0(\nu)$, and this effective dipole will contribute to the electric field outside of the material and ultimately modify the photonic LDOS. The nanostructure will also absorb some of the power radiated by the probe dipole, and the energy will be redistributed as heat. This absorption of power will also affect the photonic LDOS.

We already demonstrated in Section 6.1.2 that excitations between topological surface states result in modifications to both the polarizability of TINP and the boundary conditions of the electric field at the TINP surface, and so we can also expect a **topological modification to the photonic LDOS**.

6.2.1 Setup

We consider a spherical TINP at position $\mathbf{r}_1 = 0$, and place a probe dipole, $\boldsymbol{\mu}_2$, at position $\mathbf{r}_2 = (R+h)\hat{\mathbf{z}}$ as displayed in Figure 6.7. R is the radius of the TINP and h is the distance of the probe dipole from the surface. We take the c-axis of the material to be parallel to the z-axis, and we also assume that $\boldsymbol{\mu}_2$ is aligned with the z-axis such that $\boldsymbol{\mu}_2 = \mu_z\hat{\mathbf{z}}$. This greatly simplifies the calculation, but means that in what follows we are technically calculating the **partial LDOS**, $g_z(\mathbf{r},\omega)$. To calculate the full LDOS we would need to consider a general dipole with components both parallel and perpendicular to the z axis, such that $\boldsymbol{\mu}_2 = \mu_x\hat{\mathbf{x}} + \mu_z\hat{\mathbf{z}}$. This calculation is much more cumbersome, and so it is omitted from the current work. The presence of dipole $\boldsymbol{\mu}_2$ will induce a dipole in the TINP, which we denote $\boldsymbol{\mu}_1$.

We will be employing **Green's functions** (see Section 3.6), which are normally expressed using angular frequency, $\omega = 2\pi\nu$ and so all calculations in this section will be undertaken using ω. The **polarizability** of the TINP was derived in Section 6.1.2 and in terms of ω,

[11] Dielectric materials are electrical insulators that can be polarized by an incoming electric field.

is given by

$$\alpha(\omega) = 4\pi\epsilon_0 R^3 \left[\frac{\epsilon(\omega) + \delta_R(\omega) - 1}{\epsilon(\omega) + \delta_R(\omega) + 2}\right], \tag{6.28}$$

where R is the radius of the particle, and $\epsilon(\omega)$ is the dielectric function of the particle given in Equation 6.1. $\delta_R(\omega)$ is the contribution to the polarizability due to changes in the surface charge density when transitions occur between topological surface states and depends on the Fermi level of the system, given in Equation 6.26 for $E_F = A/R$ and Equation 6.27 for $E_F = 0$.

The electric fields acting on the dipoles at $\mathbf{r}_1$ and $\mathbf{r}_2$ respectively are given by

$$\mathbf{E}_1(\omega) = \frac{1}{\epsilon_0}\frac{\omega^2}{c^2}\underline{\mathbf{G}}(0, (R+h)\hat{\mathbf{z}}, \omega)\boldsymbol{\mu}_2, \tag{6.29}$$

$$\mathbf{E}_2(\omega) = \frac{1}{\epsilon_0}\frac{\omega^2}{c^2}\underline{\mathbf{G}}((R+h)\hat{\mathbf{z}}, 0, \omega)\boldsymbol{\mu}_1, \tag{6.30}$$

where $\underline{\mathbf{G}}(0, R+h, \omega)$ is the **dyadic Green's function**. Introducing polarizability of the nanoparticle, we can write $\boldsymbol{\mu}_1$ in the form

$$\boldsymbol{\mu}_1 = \alpha_0(\omega)\mathbf{E}_1 = \alpha_0(\omega)\frac{1}{\epsilon_0}\frac{\omega^2}{c^2}\underline{\mathbf{G}}(0, (R+h)\hat{\mathbf{z}}, \omega)\boldsymbol{\mu}_2. \tag{6.31}$$

We recall from Section 3.6 that the dyadic Green's function $\underline{\mathbf{G}}(\mathbf{r}_1, \mathbf{r}_2, \omega)$ is given by

$$\underline{\mathbf{G}}(\mathbf{r}_1, \mathbf{r}_2, \omega) = \left(\mathbb{I} + \frac{1}{k^2}\nabla^2\right)\frac{e^{ik|\mathbf{r}_2 - \mathbf{r}_1|}}{4\pi|\mathbf{r}_2 - \mathbf{r}_1|}. \tag{6.32}$$

By explicitly calculating this expression (or by recalling the form of $\underline{\mathbf{G}}(\mathbf{r}_1, \mathbf{r}_2, \omega)$ found in Section 3.6 for Cartesian coordinates and substituting), we find the dyadic Green's function to be

$$\underline{\mathbf{G}}(0, (R+h)\hat{\mathbf{z}}, \omega) \approx \frac{2}{k^2}\frac{1}{4\pi(R+h)^3}\mathbb{I}. \tag{6.33}$$

From Equation 6.31 we can find $\boldsymbol{\mu}_1$ to be

$$\boldsymbol{\mu}_1 = \alpha_0(\omega)\frac{1}{\epsilon_0}\frac{\omega^2}{c^2}\mathbf{G}(0, (R+h)\hat{\mathbf{z}}, \omega)\boldsymbol{\mu}_2 \tag{6.34}$$

$$= 2\tilde{\alpha}_0(\omega)\frac{R^3}{(R+h)^3}\boldsymbol{\mu}_2, \tag{6.35}$$

where we have re-scaled the polarizability such that $\alpha_0(\omega) = 4\pi\epsilon_0 R^3\tilde{\alpha}_0(\omega)$.

6.2.2 Calculating photonic LDOS

In order to calculate the **photonic LDOS** for the system, we recall from Section 3.7 the relationship between the photonic LDOS and **dissipated power**, P,

$$g(\mathbf{r}_2,\omega) = \frac{\omega^2}{\pi^2 c^3}\frac{P}{P^0} = \frac{\omega^2}{\pi^2 c^3}\frac{P_{rad}+P_{loss}}{P^0}, \tag{6.36}$$

where the total power dissipated by the system is given by $P = P_{\text{rad}} + P_{\text{loss}}$, taking into account the two dissipation channels of **radiation** and **intrinsic losses**. In order to calculate the LDOS, we need to calculate both P_{rad}/P^0 and P_{loss}/P^0, where we will assume that P^0 is given by $P^0 = P^0_{\text{rad}}$ such that the probe dipole is **lossless**. The dipole radiation in free space for the probe dipole (from Equation 3.127) is given by

$$P^0_{\text{rad}} = \frac{\omega^4}{12\pi\epsilon_0 c^3}|\boldsymbol{\mu}_2|^2. \tag{6.37}$$

6.2.2.1 Radiated power

As the nanoparticle radius is much smaller than the radiation wavelength, we take the **long wavelength limit** [173] in which the power radiated from the probe dipole in the presence of the nanoparticle is given by

$$P_{\text{rad}} = \frac{\omega^4}{12\pi\epsilon_0 c^3}|\boldsymbol{\mu}_2+\boldsymbol{\mu}_1|^2. \tag{6.38}$$

The **normalised radiated power**, (i.e. the ratio of power radiated by a dipole in the presence of a nanoparticle and power radiated in the absence of a nanoparticle) is thus given by

$$\frac{P_{\text{rad}}}{P^0_{\text{rad}}} = \frac{|\boldsymbol{\mu}_2+\boldsymbol{\mu}_1|^2}{|\boldsymbol{\mu}_2|^2} \tag{6.39}$$

$$= \left|1+2\tilde{\alpha}(\omega)\frac{R^3}{(R+h)^3}\right|^2. \tag{6.40}$$

6.2.2.2 Lost power

We now calculate the **normalised power loss**, P_{loss}/P^0. We assume the probe dipole is close enough to the surface that we can treat the surface of the TINP as flat[12] [173] - in order to calculate the power lost from being close to the surface, we recall from Section 3.6

[12] Corrections can be added to account for curvature [188, 215, 216] but do not affect the qualitative result at small values of h/R.

that the power dissipated by a probe dipole near a surface can be calculated from

$$P_{\text{loss}} = \frac{\omega}{2}\text{Im}\left[\boldsymbol{\mu}_2^* \mathbf{E}(\mathrm{r}_2)\right]. \tag{6.41}$$

To calculate P_{loss}, we thus need to calculate $\mathbf{E}(\mathrm{r}_2)$, taking into account the effect of the TINP and its surface states. In order to do so, we use the **method of images**[13].

We model the TINP as a half space with boundary at $z = R$. The probe dipole $\boldsymbol{\mu}_2 = \mu_2\hat{\mathbf{z}}$ is located at $z = R + h$, and the presence of the dipole induces a bound charge on the interface. This boundary condition can be mimicked by the introduction of an image dipole, $\boldsymbol{\mu}_3 = \mu_3\hat{\mathbf{z}}$, placed at $z = R - h$. The potential outside of the TINP will be given by

$$\Phi_{\text{out}} = \frac{1}{4\pi\epsilon_0}\frac{\mu_2}{|\mathbf{r} - (R+h)\hat{\mathbf{z}}|^2}\sin\vartheta + \frac{1}{4\pi\epsilon_0}\frac{\mu_3}{|\mathbf{r} - (R-h)\hat{\mathbf{z}}|^2}\sin\vartheta. \tag{6.42}$$

The potential inside the TINP will be a dipole field due to the probe dipole at $R + h$, with a modified dipole moment $\boldsymbol{\mu}_4 = \mu_4\hat{\mathbf{z}}$,

$$\Phi_{\text{in}} = \frac{1}{4\pi\epsilon_0}\frac{\mu_4}{|\mathbf{r} - (R+h)\hat{\mathbf{z}}|^2}\sin\vartheta. \tag{6.43}$$

Following the same derivation as in Section 6.1.2, the charge density on the surface $z = R$ is given by

$$\rho = -\frac{\delta_R(\omega)\epsilon_0}{R}\Phi_{\text{in}}, \tag{6.44}$$

and the interface conditions that must be satisfied are

$$\left.\frac{\partial\Phi_{\text{in}}}{\partial\vartheta}\right|_R = \left.\frac{\partial\Phi_{\text{out}}}{\partial\vartheta}\right|_R, \tag{6.45}$$

$$\epsilon(\omega)\left.\frac{\partial\Phi_{\text{in}}}{\partial r}\right|_R = \left.\frac{\partial\Phi_{\text{out}}}{\partial r}\right|_R + \frac{\rho}{\epsilon_0}. \tag{6.46}$$

Using the expressions for Φ_{in}, Φ_{out} and the surface charge density, these equations reduce to the conditions

$$\mu_2 + \mu_3 = -\left(\epsilon(\omega) + \frac{h}{2R}\delta_R(\omega)\right)\mu_4, \tag{6.47}$$

$$\mu_3 - \mu_2 = \mu_4. \tag{6.48}$$

Combined, we find that

$$\mu_3 = \left(\frac{\epsilon(\omega) + \frac{h}{2R}\delta_R(\omega) - 1}{\epsilon(\omega) + \frac{h}{2R}\delta_R(\omega) + 1}\right)\mu_2 \tag{6.49}$$

[13] The method of images to solve electromagnetic problems should be familiar from a standard undergraduate electromagnetism course. Jackson's textbook provides excellent coverage of this method [147].

The expression for Φ_{out} can then be written as

$$\Phi_{\text{out}} = \left(\frac{1}{4\pi\epsilon_0} \frac{1}{|\mathbf{r} - (R+h)\hat{\mathbf{z}}|^2} \sin\vartheta \right. \tag{6.50}$$

$$\left. + \frac{1}{4\pi\epsilon_0} \left(\frac{\epsilon(\omega) + \frac{h}{2R}\delta_R(\omega) - 1}{\epsilon(\omega) + \frac{h}{2R}\delta_R(\omega) + 1} \right) \frac{1}{|\mathbf{r} - (R-h)\hat{\mathbf{z}}|^2} \sin\vartheta \right) \mu_2. \tag{6.51}$$

The electric field acting at the position of the probe dipole, $\mathbf{E}_2 = -\nabla\Phi_{\text{out}}|_{z=R+h,\vartheta=0}$, is given by

$$\mathbf{E}_2(\omega) = \frac{1}{16\pi\epsilon_0 h^3} \left[\frac{\epsilon(\omega) + \frac{h}{2R}\delta_R(\omega) - 1}{\epsilon(\omega) + \frac{h}{2R}\delta_R(\omega) + 1} \right] \mu_2 \hat{\mathbf{z}} \tag{6.52}$$

$$= \frac{1}{16\pi\epsilon_0 h^3} \left[\frac{\epsilon(\omega) + \frac{h}{2R}\delta_R(\omega) - 1}{\epsilon(\omega) + \frac{h}{2R}\delta_R(\omega) + 1} \right] \boldsymbol{\mu}_2. \tag{6.53}$$

We can then calculate the power dissipated,

$$P_{\text{loss}} = \frac{\omega}{2} \text{Im}\left\{ \boldsymbol{\mu}_2^* \cdot \mathbf{E}_2(\omega) \right\} \tag{6.54}$$

$$= \frac{\omega}{32\pi\epsilon_0 z^3} |\boldsymbol{\mu}_2|^2 \text{Im}\left\{ \frac{\epsilon(\omega) + \frac{h}{2R}\delta_R(\omega) - 1}{\epsilon(\omega) + \frac{h}{2R}\delta_R(\omega) + 1} \right\}. \tag{6.55}$$

As we have treated the system as a half space, $P_0 = \omega^4 |\boldsymbol{\mu}_2^2| / 24\pi\epsilon_0 c^3$, we can then find P_{loss}/P_0 as

$$\frac{P_{\text{loss}}}{P^0} = \frac{3}{4k^3} \text{Im}\left[\frac{\epsilon(\omega) + \frac{h}{2R}\delta_R(\omega) - 1}{\epsilon(\omega) + \frac{h}{2R}\delta_R(\omega) + 1} \right] \frac{1}{h^3}. \tag{6.56}$$

With these results we can then write down the LDOS at $\mathbf{r}_2$ using Equation 6.36, such that

$$g_z(h,\omega) = \frac{\omega^2}{\pi^2 c^3} \left[\left| 1 + 2\tilde{\alpha}(\omega) \frac{R^3}{(R+h)^3} \right|^2 + \frac{3}{4k^3} \text{Im}\left[\frac{\epsilon(\omega) + \frac{h}{2R}\delta_R(\omega) - 1}{\epsilon(\omega) + \frac{h}{2R}\delta_R(\omega) + 1} \right] \frac{1}{h^3} \right]. \tag{6.57}$$

For $\delta_R(\omega) = 0$, this result simplifies to the expected result for the partial LDOS modified near a dielectric nanoparticle [173, 217].

Result: The photonic LDOS modified near a TINP

The **partial photonic LDOS** at distance h from a TINP of radius R,

$$g_z(h,\omega) = \frac{\omega^2}{\pi^2 c^3}\left[\left|1 + 2\tilde{\alpha}(\omega)\frac{R^3}{(R+h)^3}\right|^2 + \frac{3}{4k^3}\mathrm{Im}\left[\frac{\epsilon(\omega) + \frac{h}{2R}\delta_R(\omega) - 1}{\epsilon(\omega) + \frac{h}{2R}\delta_R(\omega) + 1}\right]\frac{1}{h^3}\right]. \tag{6.58}$$

where $\delta_R(\omega)$ depends on the Fermi level, E_F,

$$E_\mathrm{F} = A/R: \qquad \delta_R = \frac{e^2}{3\pi\epsilon_0}\left(\frac{1}{A - \hbar\omega R} + \frac{1}{A + \hbar\omega R}\right) \tag{6.59}$$

$$E_\mathrm{F} = 0: \qquad \delta_R = \frac{e^2}{6\pi\epsilon_0}\left(\frac{1}{2A - \hbar\omega R} + \frac{1}{2A + \hbar\omega R}\right) \tag{6.60}$$

and for a trivial insulator, $\delta_R(\omega) = 0$.

The results are presented in Figure 6.8. In Figure 6.8a the normalised partial LDOS, $g_z(h,\omega)/g_{3\mathrm{D}}(\omega)$, is plotted as a function of h and $\nu = \omega/2\pi$ for a TINP of $R = 30$ nm and $E_\mathrm{F} = 0$. A broad mode can be seen resulting from the β mode. A sharp peak due to the SToP mode is seen, followed by a minimum at $2A = \hbar\omega R$. This sharp peak followed by a minimum is typical of Fano resonances (as already seen in Section 6.1 and discussed in Appendix B.11). In Figure 6.8b, $g_z(h,\omega)/g_{3\mathrm{D}}(\omega)$ is plotted for $R = (30, 40, 50)$ nm at a distance of 5 nm away from the TINP surface. The topological peak moves to lower frequencies as R is increased, as the energy spacing between topological surface states decreases. The height of the peak also decreases as R increases. I plot the result for a TINP of $R = 30$ nm with the same bulk dielectric function $\epsilon(\omega)$, but no topological surface states. The broad mode due to the β mode is retained, but the SToP mode is absent. Results for $E_\mathrm{F} = A/R$ (depicted in Figures 6.8c and d) are qualitatively the same, with results plotted for $R = (15, 20, 25)$ nm. In Figure 6.8e I plot the maximal enhancement of the partial LDOS near a TINP with $R = 30$ nm $E_\mathrm{F} = 0$ (purple line) and a non-topological NP of the same radius (black dotted line), for varying distance from the TINP surface, h. The enhancement due to the NP reduces monotonically with increasing h, while the enhancement due to the TINP also reduces with increasing h, but exhibits oscillatory behaviour. Finally in Figure 6.8f, I plot the normalised partial LDOS at a distance 5 nm from a TINP with $R = 30$ nm, for differing Fermi levels $E_\mathrm{F} = 0$ (purple) and $E_\mathrm{F} = A/R$ (green). The SToP peak is greatly suppressed for the $E_\mathrm{F} = A/R$ case.

We can see that the presence of the topological surface states and the subsequent SToP mode presents a radical enhancement of the photonic LDOS near the TINP. Very close to the TINP, this enhancement can be on the order of $\sim 10^9$, much greater than the effect of an equivalent non-topological particle. This setup has the benefit of many parameters which can be tuned, giving another tool for controlling THz frequency light at the nanoscale.

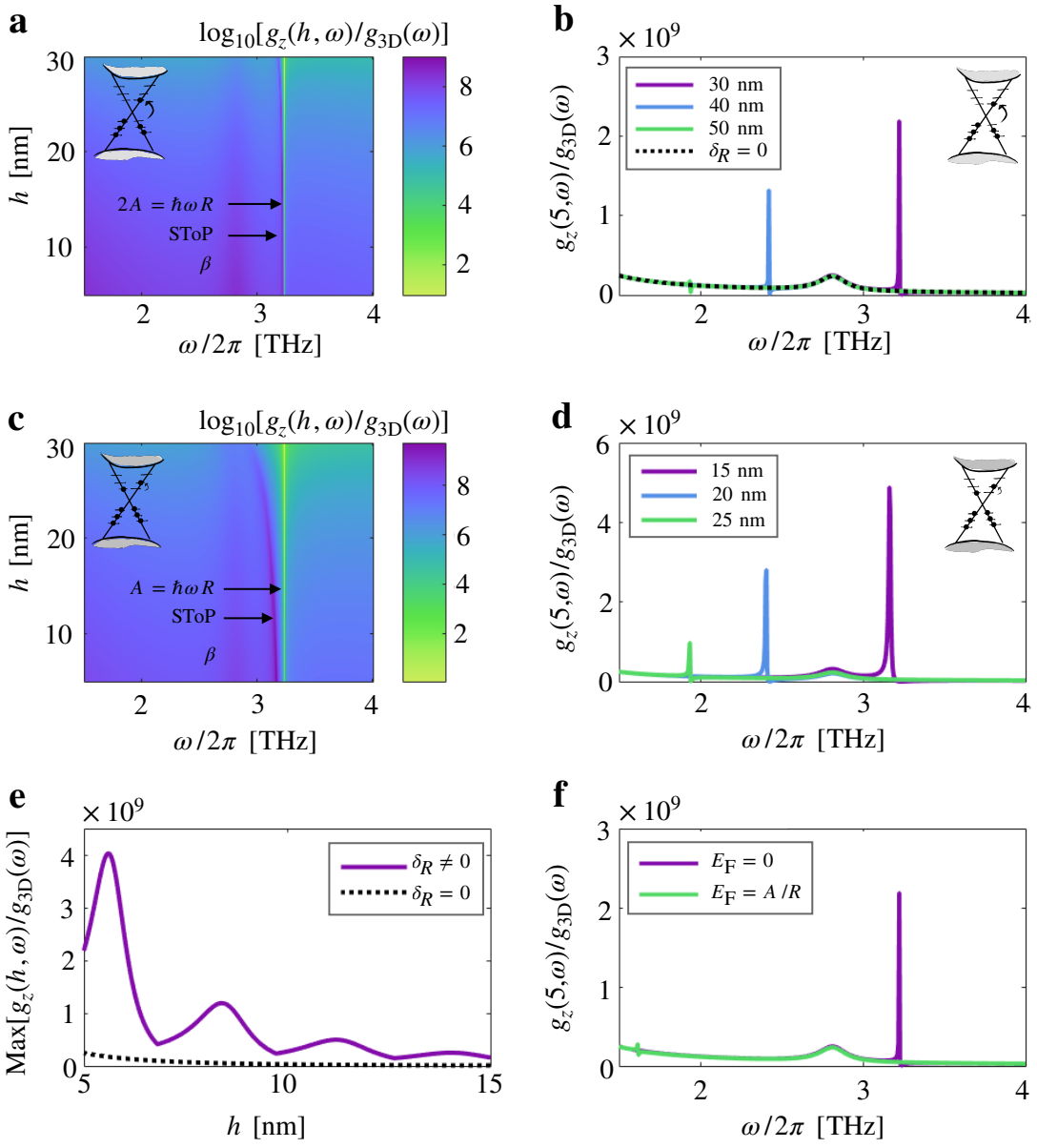

Figure 6.8: **Modifying the photonic LDOS near a TINP: (a)** Plot of the normalised partial LDOS, $g_z(h,\omega)/g_{3D}(\omega)$, near a $R = 30$ nm particle with $E_F = 0$ as a function of h and $\omega/2\pi$. **(b)** The normalised partial LDOS at a distance of 5 nm from the surface of a TINP with $E_F = 0$ and $R = (30, 40, 50)$nm. **(c)** The normalised partial LDOS near a 15 nm particle with $E_F = A/R$ as a function of h and $\omega/2\pi$. **(d)** The normalised partial LDOS at a distance of 5 nm from the surface of a TINP with $E_F = A/R$ and $R = (15, 20, 25)$nm. **(e)** Maximum enhancement for a TINP of $R = 30$ nm, $E_F = 0$ as a function of h, compared to a NP with the same $\epsilon(\nu)$ but no topological surface states. **(b)** A comparison of the normalised partial LDOS for varying E_F for TINPs of radius $R = 30$ nm.

7. Conclusions

7.1 Summary

In this thesis, I set out to expand the current knowledge of **topological nanophotonics** while providing an accessible resource allowing students to enter the field from a general physics background.

The research undertaken for this thesis has spanned three strands. **Topological (TI) nanostructures** have quantised, symmetry-protected surface states with discrete energies. I have extended the knowledge of the electronic structure of TI spheroidal nanostructure surface states and their respective energies. Their energy levels can be tuned with the nanostructure dimensions, and I have presented results spanning from the infinite nanowire to the ideal nanodisk. These TI nanostructure surface states can be coupled with **terahertz (THz) frequency light**, which is a much coveted operating frequency range and I refer to them as **topological quantum dots (TQDs)**.

I have demonstrated that a single TQD can successfully **lase in the THz** when placed in a 1D open cavity at zero temperature, with an ultra-low threshold. I have given a road map towards room temperature lasing using nothing but thermal photons as a pump.

I have presented the results of an experimental collaboration, in which we demonstrated that a **new polariton mode (the STOP mode)** has been observed in Bi_2Te_3 nanoparticles at room temperature, as a direct consequence of the quantised surface states. Transitions between surface states occur at frequencies commensurate with a bulk phonon, leading to a strong Fano resonance. Even in real-world samples of non-spherical, non-uniformly sized nanoparticles at room temperature we can observe a signature of the quantised topological surface states. I show that the presence of this mode also allows us to manipulate light in the environment of a TQD. I give a theoretical study of the photonic local density of states in the vicinity of a TQD, and demonstrate an **amplification of the photonic LDOS** of a factor of up to 10^9. This could have potential impact in THz technologies in which control of THz light is desired at the nanoscale.

7.2 Outlook and future work

Topological nanophotonics is a youthful and fast developing field, and there is much work yet to be done. Every topic I have encountered has sparked new questions and potential research directions. Direct extensions of the work in this thesis include but are not limited to the following.

Finite temperature lasing from a single TQD in a 3D cavity is a realistic goal, based on the results of Chapter 5. Following the road map detailed in that chapter, it should be possible to design a system in which this goal can be realised. A system employing multiple TQDs should provide an exponential enhancement of output power, so this is an avenue which should be explored.

The experimental results of Chapter 6 represent an important milestone in the detection of topological states at the nanoscale. However, on the path to complete control of THz light using TI nanostructures, it will be important to extend this work. By comparing the results of this work with similar experiments with Sb_2Se_3 (a material in the same family as Bi_2Te_3 but without topological properties) we can definitively show that the extra peaks seen in our work are due to topology. Additionally, it will be crucial to show control of the SToP mode by demonstrating its dependence on the shape and size of different TI nanostructures. This will require experimental efforts to reliably produce TI nanostructures of well-defined shape, size and doping.

All of the results of this thesis have been based on individual TQDs, or multiple non-interacting TQDs. Hybrid systems involving TQDs coupled to quantum emitters have been subject to their first study [197], and this opens up a large new area of using the unusual optical and electronic properties of TQDs as part of larger, hybrid systems. This could include studies of TQDs interacting with each other, and other quantum systems such as metallic and semiconductor nanoparticles, and 2D materials.

Due to the robustness of TQD surface states, this system lends itself naturally as a platform to host a qubit. The long lifetime of the states, and potentially high-level of tunability and control of the states means that this could be an exciting area of study. The M1 and E2 transitions in this system have even longer lifetimes than the E1 transitions of focus in this thesis, and so it would be important to understand how these transitions could be utilised. The long lifetimes of these states also suggest that TQDs could be used as a single THz photon source, an idea that can already be envisaged by studying the results of Chapter 5, in which a single TQD slowly produces coherent photons.

Any of these suggested research avenues, and in fact all of the results in Chapters 5 and 6 of this thesis could also be extended by considering TI nanostructure shapes other than the nanosphere. I used the nanosphere in this work due to the simplicity of the energy levels and known analytical form of the surface states. However, with the results of Chapter 4 we can now study any of the phenomena discussed in this thesis applied to non-spherical nanostructures. As discussed in Chapter 4, some geometries are easier to experimentally produce that others - notably, the growth of wires (which can then be truncated into nanopillars) and the growth of thin films (which can then be cut into nanodisks via lithography). By studying the phenomena discussed in this thesis in these geometries, they could be experimentally verified and developed, with the aim of using them in THz technologies. Calculations have already been done for spontaneous emission

of an atom near a spheroidal nanostructure [188]. These calculations could be extended with the addition of the SToP mode for complete control of photonic LDOS with potential for experimental validation and technological use.

Overall, I have demonstrated that topological nanophotonics using TI nanostructures is an exciting field with plenty of opportunities for understanding topological light-matter interactions at the nanoscale, and potential for controlling THz light which could be transformative in THz technologies.

A. Useful maths, formalisms and conventions

In this appendix I give the definitions and conventions used in this thesis. I also include some additional information on some of the formalisms used in my work.

A.1 Pauli matrices

The **Pauli matrices**[1] are a set of 2×2 complex matrices, which are both unitary and Hermitian.They are given by

$$\boldsymbol{\sigma_1} = \begin{pmatrix} 0 & 1 \\ 1 & 0 \end{pmatrix}, \quad \boldsymbol{\sigma_2} = \begin{pmatrix} 0 & -i \\ i & 0 \end{pmatrix} \quad \text{and} \quad \boldsymbol{\sigma_3} = \begin{pmatrix} 1 & 0 \\ 0 & -1 \end{pmatrix}. \tag{A.1}$$

Together with the 2×2 identity matrix, $\mathbb{1}_2$, they form a basis for all 2×2 Hermitian matrices, such that any 2×2 Hermitian matrix can be written as a linear sum of Pauli matrices with real coefficients.

A.2 Unusual algebraic operations

There are various times in this thesis where I make reference to less-common algebraic operations in order to exploit convenient notation. I give a quick overview of these operations here.

Tensor product

The **tensor product** of two matrices is given explicitly by

$$\mathbf{a} \otimes \mathbf{b} = \begin{pmatrix} a_{11} & a_{12} \\ a_{21} & a_{22} \end{pmatrix} \otimes \begin{pmatrix} b_{11} & b_{12} \\ b_{21} & b_{22} \end{pmatrix} = \begin{pmatrix} a_{11}b_{11} & a_{11}b_{12} & a_{12}b_{11} & a_{12}b_{12} \\ a_{11}b_{21} & a_{11}b_{22} & a_{12}b_{21} & a_{12}b_{22} \\ a_{21}b_{11} & a_{21}b_{12} & a_{22}b_{11} & a_{22}b_{12} \\ a_{21}b_{21} & a_{21}b_{22} & a_{22}b_{21} & a_{22}b_{22} \end{pmatrix}. \tag{A.2}$$

For our purposes (and with apologies to mathematicians everywhere), we use this interchangeably with the **outer product** $\mathbf{a} \otimes \mathbf{b}$ or **dyadic product**, $\mathbf{ab}$.

[1] Named for Wolfgang Pauli, one of the pioneers of quantum theory. Interestingly, Pauli seldom published papers but preferred to write to colleagues such as Bohr and Heisenberg, who would then circulate the ideas contained in the correspondence.

Hadamard product

The **Hadamard product** is element-wise multiplication, given by

$$\mathbf{a} \circ \mathbf{b} = \begin{pmatrix} a_{11} & a_{12} \\ a_{21} & a_{22} \end{pmatrix} \circ \begin{pmatrix} b_{11} & b_{12} \\ b_{21} & b_{22} \end{pmatrix} = \begin{pmatrix} a_{11}b_{11} & a_{12}b_{12} \\ a_{21}b_{21} & a_{22}b_{22} \end{pmatrix}. \tag{A.3}$$

Hadamard multiplication requires $\mathbf{a}$ and $\mathbf{b}$ to be of the same dimensions.

A.3 Scalars, vectors and dyads

Dyads may not be discussed in a standard undergraduate physics course, and so I briefly give their definition here, with other algebraic objects for context.

Scalar: Rank 0 tensor. A quantity with no associated direction.

Vector: Rank one tensor. A quantity with a magnitude and one associated direction.

Dyad: Rank one, order two tensor. A quantity that has a magnitude and two associated directions.

Dyadic: Tensor of order two (may be full rank or not). A sum of dyads.

Dyadics and **matrices** have similarities, and in Euclidean space can be considered the same, although a dyadic is more strictly defined as the sum of dyads, which are a result of dyadic products (see Appendix A.2) of two vectors.

A.4 Coordinate systems

Multiple coordinate systems are used in this thesis, which are summarised below. Oblate and prolate spheroidal coordinates are less-widely used and yet are crucial for the work in Chapter 4, so I discuss them in more detail.

Cartesian coordinates: (x, y, z)

Spherical coordinates: (r, ϑ, φ)
Conversion to Cartesian coordinates given by $(x, y, z) = (r\sin\vartheta\cos\varphi, r\sin\vartheta\sin\varphi, r\cos\vartheta)$

Oblate spheroidal coordinates: (ζ, ξ, φ)
The variable can be written as $\zeta = \sinh\mu$ and $\xi = \sin\nu$. A non-conventional form can also be written, (ζ, τ, φ), where $\tau = \cos\nu$. Conversion to Cartesian coordinates is given by $(x, y, z) = \left(a\sqrt{(1+\zeta^2)(1-\tau^2)}\cos\varphi, a\sqrt{(1+\zeta^2)(1-\tau^2)}\sin\varphi, a\zeta\tau\right)$

Constant $\mu = \mu_0$ gives a spheroid surface,

$$\frac{x^2+y^2}{a^2\cosh^2\mu_0} + \frac{z^2}{a^2\sinh^2\mu_0} = \frac{x^2+y^2}{a^2(1+\zeta_0^2)} + \frac{z^2}{a^2\zeta_0^2} = 1, \tag{A.4}$$

For a particle with semi-major and semi-minor axes of R_1 and R_2 respectively,

$$R_1 = a\cosh\mu_0 = a\sqrt{1+\zeta_0^2} \tag{A.5}$$

$$R_2 = a\sinh\mu_0 = a\zeta_0, \tag{A.6}$$

$$\tanh\mu_0 = \frac{R_2}{R_1}, \tag{A.7}$$

$$R_1^2 - R_2^2 = a^2. \tag{A.8}$$

The scale factors are given by

$$h_\zeta = a\sqrt{\frac{\zeta^2+\xi^2}{1+\zeta^2}}, \quad h_\xi = a\sqrt{\frac{\zeta^2+\xi^2}{1-\xi^2}}, \quad h_\varphi = a\sqrt{(1+\zeta^2)(1-\xi^2)}. \tag{A.9}$$

For a sphere, $\tanh^2\mu_0 = 1$ ($\zeta_0 \gg 1$) and for a disk, $\tanh^2\mu_0 \ll 1$ ($\zeta_0 \ll 1$).

When transforming the Cartesian form of the 4-band Hamiltonian for TIs into spheroidal coordinates, in Chapter 4, it is necessary to know how the derivatives transform.

$$\frac{\partial\zeta}{\partial x} = \frac{a\zeta}{h_\zeta h_\xi}\cos\varphi, \quad \frac{\partial\zeta}{\partial y} = \frac{a\zeta}{h_\zeta h_\xi}\sin\varphi, \quad \frac{\partial\zeta}{\partial z} = \frac{a\xi}{h_\zeta^2}, \tag{A.10}$$

$$\frac{\partial\xi}{\partial x} = -\frac{a\xi}{h_\zeta h_\xi}\cos\varphi, \quad \frac{\partial\xi}{\partial y} = -\frac{a\xi}{h_\zeta h_\xi}\sin\varphi, \quad \frac{\partial\xi}{\partial z} = \frac{a\zeta}{h_\xi^2}, \tag{A.11}$$

$$\frac{\partial\varphi}{\partial x} = -\frac{\sin\varphi}{h_\varphi}, \quad \frac{\partial\varphi}{\partial y} = \frac{\cos\varphi}{h_\varphi}, \quad \frac{\partial\varphi}{\partial z} = 0. \tag{A.12}$$

We can then write

$$\partial_x = \frac{a\zeta}{h_\zeta h_\xi}\cos\varphi\partial_\zeta - \frac{a\xi}{h_\zeta h_\xi}\cos\varphi\partial_\xi - \frac{\sin\varphi}{h_\varphi}\partial_\varphi, \tag{A.13}$$

$$\partial_y = \frac{a\zeta}{h_\zeta h_\xi}\sin\varphi\partial_\zeta - \frac{a\xi}{h_\zeta h_\xi}\sin\varphi\partial_\xi + \frac{\cos\varphi}{h_\varphi}\partial_\varphi, \tag{A.14}$$

$$\partial_z = \frac{a\xi}{h_\zeta^2}\partial_\zeta + \frac{a\zeta}{h_\xi^2}\partial_\xi. \tag{A.15}$$

This allows us to write down expressions for $k_\pm$,

$$k_+ = k_x + ik_y = -i\partial_x + \partial_y = -ie^{i\varphi}\frac{a\zeta}{h_\zeta h_\xi}\partial_\zeta + ie^{i\varphi}\frac{a\xi}{h_\zeta h_\xi}\partial_\xi + e^{i\varphi}\frac{1}{h_\varphi}\partial_\varphi \tag{A.16}$$

$$k_- = k_x - ik_y = -i\partial_x - \partial_y = -ie^{-i\varphi}\frac{a\zeta}{h_\zeta h_\xi}\partial_\zeta + ie^{i\varphi}\frac{a\xi}{h_\zeta h_\xi}\partial_\xi - e^{-i\varphi}\frac{1}{h_\varphi}\partial_\varphi \tag{A.17}$$

The expression for ∇^2 can then be found through some algebra to be

$$\begin{aligned}\nabla^2 &= \frac{\partial^2}{\partial x^2} + \frac{\partial^2}{\partial y^2} + \frac{\partial^2}{\partial z^2} \\ &= \frac{1}{h_\zeta^2}\frac{\partial^2}{\partial \zeta^2} + \frac{2\zeta}{a^2(\zeta^2+\xi^2)}\frac{\partial}{\partial \zeta} - \frac{2\xi}{a^2(\zeta^2+\xi^2)}\frac{\partial}{\partial \xi} + \frac{1}{h_\xi^2}\frac{\partial^2}{\partial \xi^2} + \frac{1}{h_\varphi^2}\frac{\partial^2}{\partial \varphi^2} \\ &= \frac{1}{a^2(\zeta^2+\xi^2)}\left(\frac{\partial}{\partial \zeta}\left[(1+\zeta^2)\frac{\partial}{\partial \zeta}\right] + \frac{\partial}{\partial \xi}\left[(1-\xi^2)\frac{\partial}{\partial \xi}\right]\right) \\ &\quad + \frac{1}{a^2(1+\zeta^2)(1-\xi^2)}\frac{\partial^2}{\partial \varphi^2}.\end{aligned} \tag{A.18}$$

Prolate spheroidal coordinates: (σ, τ, φ)
Prolate spheroidal coordinates can be defined in a similar way to oblate spheroidal coordinates. Their conversion to Cartesian coordinates is given by $(x, y, z) = \left(a\sqrt{(\sigma^2-1)(1-\tau^2)}\cos\varphi, a\sqrt{(\sigma^2-1)(1-\tau^2)}\sin\varphi, a\sigma\tau\right)$, where $\sigma = \cosh(\mu)$ is real-valued ≥ 1, $\tau = \cos(\nu) \in [-1, 1]$, $\varphi \in [-\pi, \pi]$, and a is a constant of dimension L. A spheroidal surface can be found from constant $\sigma = \sigma_0$, such that

$$\frac{x^2+y^2}{a^2(\sigma_0^2-1)} + \frac{z^2}{a^2\sigma_0^2} = 1, \tag{A.19}$$

The scale factors are given by

$$h_\sigma = a\sqrt{\frac{\sigma^2-\tau^2}{\sigma^2-1}}, \quad h_\tau = a\sqrt{\frac{\sigma^2-\tau^2}{1-\tau^2}}, \quad \text{and} \quad h_\varphi = a\sqrt{(\sigma^2-1)(1-\tau^2)}, \tag{A.20}$$

where the momentum operators are given by

$$k_\sigma = -\frac{i}{h_\sigma}\partial_\sigma, \quad k_\tau = -\frac{i}{h_\tau}\partial_\tau \quad \text{and} \quad k_\varphi = -\frac{i}{h_\varphi}\partial_\varphi, \tag{A.21}$$

A.5 Jacobi polynomials

The **Jacobi polynomials**[2], $J_n^{\alpha,\beta}(x)$ satisfy the differential equation

$$\left[(1-x^2)\frac{d^2}{dx^2} + (\beta - \alpha - (\alpha+\beta+2)x)\frac{d}{dx} + n(n+\alpha+\beta+1)\right] J_n^{\alpha,\beta}(x) = 0, \tag{A.22}$$

where the polynomials are orthogonal with respect to the weight $(1-x)^\alpha (1+x)^\beta$ on the interval $x \in [-1, 1]$, where $\alpha, \beta > -1$, such that

$$\int_{-1}^{1} (1-x)^\alpha (1+x)^\beta J_n^{\alpha\beta}(x) J_{n'}^{\alpha\beta}(x) dx = \frac{\delta_{nn'}}{N_{n\alpha\beta}^2}. \tag{A.23}$$

[2]Named after their creator, Carl Gustav Jacob Jacobi. Jacobi was the first Jewish mathematician to be appointed as a professor at a German university, and made many contributions to mathematics on the topics differential equations, determinants and elliptic functions.

The normalisation of the polynomials is made such that $J_0^{\alpha,\beta}(x) = 1$, enforced by

$$N^2_{n\alpha\beta} = \frac{(2n+\alpha+\beta+1)!(n+\alpha+\beta)!n!}{2^{\alpha+\beta+1}\Gamma(n+\alpha)!(n+\beta)!}. \tag{A.24}$$

A.6 2nd order ODEs from coupled 1st order ODES

A pair of coupled first order differential equations can be combined into a single, **second order differential equation**. To solve the equations in Chapter 4, we are interested in first order differential equations of the form

$$f(x)y'(x) + g(x)y(x) = \lambda z(x) \tag{A.25}$$
$$p(x)z'(x) + q(x)z(x) = \lambda y(x). \tag{A.26}$$

We can combine these into a second order equation in either $y(x)$ or $z(x)$, such that

$$F(x)z''(x) + G(x)z'(x) + H(x)z(x) = \lambda^2 z(x) \tag{A.27}$$

where

$$F(x) = f(x)p(x) \tag{A.28}$$
$$G(x) = f(x)p'(x) + f(x)q(x) + g(x)p(x) \tag{A.29}$$
$$H(x) = f(x)q'(x) + g(x)q(x), \tag{A.30}$$

or alternatively for $y(x)$,

$$F(x)y''(x) + Q(x)y'(x) + R(x)y(x) = \lambda^2 y(x), \tag{A.31}$$

where

$$F(x) = p(x)f(x) \tag{A.32}$$
$$Q(x) = p(x)f'(x) + p(x)g(x) + q(x)f(x) \tag{A.33}$$
$$R(x) = p(x)g'(x) + q(x)g(x). \tag{A.34}$$

A.7 Useful integrals

Some useful integrals and definitions used in this thesis:

$$\int_{-\infty}^{\infty} dt\ e^{i(\omega'-\omega)t} = 2\pi\delta(\omega'-\omega) \tag{A.35}$$

$$\left| \int_{-\infty}^{\infty} dt \; e^{i(\omega'-\omega)t-\gamma t} \right|^2 = \frac{1}{(\omega'-\omega)^2+\gamma^2} \tag{A.36}$$

We define the **Fourier transform** (and its inverse) using angular frequency, such that

$$\tilde{f}(\omega) = \frac{1}{\sqrt{2\pi}} \int_{-\infty}^{\infty} dt \; f(t) e^{i\omega t} \quad \text{and} \quad f(t) = \frac{1}{\sqrt{2\pi}} \int_{-\infty}^{\infty} d\omega \; \tilde{f}(\omega) e^{-i\omega t}. \tag{A.37}$$

A.8 Time-dependent perturbation theory

Time-dependent perturbation theory [200, 218] allows us to study the effect of a time-dependent perturbation, $V(t)$, on a time-dependent Hamiltonian, $\mathbf{H}_0$, such that $\mathbf{H} + \mathbf{H}_0 + V(t)$.

A quantum state of the perturbed system, $|\psi(t)\rangle$ obeys the time-dependent Schrödinger equation,

$$\mathbf{H}(t)|\psi(t)\rangle = (H_0 + V(t))\,|\psi(t)\rangle = i\hbar \frac{\partial}{\partial t}|\psi(t)\rangle. \tag{A.38}$$

The state at each instant of time can be written in terms of the eigenstates of $|n\rangle$ of the unperturbed Hamiltonian, such that

$$|\psi(t)\rangle = \sum_n c_n(t) e^{-iE_n t}|n\rangle. \tag{A.39}$$

By substituting this expression into Equation A.38, and iteratively solving the resulting differential equations, an iterative solution can be found

$$c_n(t) = c_n^{(0)}(t) + c_n^{(1)}(t) + c_n^{(2)}(t) + ... \tag{A.40}$$

The first order term is given by

$$c_n^{(1)}(t) = -\frac{i}{\hbar} \sum_k \int_0^t dt' \langle n|V(t')|k\rangle c_k^{(0)} e^{-i(E_k-E_n)t'/\hbar} \tag{A.41}$$

B. Supplementary derivations and information

In this appendix I give extra background theory and derivations that are useful in arriving at results in the main text, but which did not make it into the body of the thesis.

B.1 Berry phase

Evolve a quantum state on a cyclic path of adiabatic evolution. Hamiltonian $\mathbf{H}(\mathbf{r})$, where $\mathbf{r}$ varies with time t. n-th eigenvalue E_n should remain non-degenerate on the whole path, and variation with time t should be very slow. Then, $|n(\mathbf{r}(0))\rangle$ will remain an instantaneous eigenstate, $|n(\mathbf{r}(t))\rangle$, of the Hamiltonian, $\mathbf{H}(\mathbf{r})$ through the evolution, up to a phase. The state at time t can be written as

$$|\Psi_n(t)\rangle = e^{i\gamma_n(t)} e^{-\frac{i}{\hbar}\int_0^t dt' E_n(\mathbf{r}(t))} |n(\mathbf{r}(t))\rangle. \tag{B.1}$$

The first exponent gives the geometric phase, γ_n, and the second exponent gives the dynamical phase. By plugging the state into the time-dependent Sch odinger equation, it can be shown that

$$\gamma_n = i\int_0^t dt' \langle n(\mathbf{r}(t'))\frac{d}{dt'}|n(\mathbf{r}(t'))\rangle = i\int_{\mathbf{r}(0)}^{\mathbf{r}(t)} d\mathbf{r}\langle n(\mathbf{r})|\nabla|n(\mathbf{r})\rangle \tag{B.2}$$

In the case of a cyclic evolution around a path $\mathcal{C}$, such that $\mathbf{r}(t) = \mathbf{r}(0)$, the Berry phase becomes

$$\gamma_n = i\int_{\mathcal{C}} d\mathbf{r}\langle n(\mathbf{r})|\nabla|n(\mathbf{r})\rangle. \tag{B.3}$$

This can be expressed in terms of the **Berry connection**, $\mathcal{A}_n(\mathbf{r})$,

$$\gamma_n = \int_{\mathcal{C}} d\mathbf{r}\mathcal{A}_n(\mathbf{r}), \tag{B.4}$$

where $\mathcal{A}_n(\mathbf{r}) = i\langle n(\mathbf{r})|\nabla|n(\mathbf{r})\rangle$. In a 3D parameter space the Berry curvature can then be written as

$$\Omega_n(\mathbf{r}) = \nabla \times \mathcal{A}_n(\mathbf{r}). \tag{B.5}$$

Calculating the Berry curvature for a particular closed surface, for example a torus, it can be found that its magnitude is identical to that of the Gaussian curvature covered in the

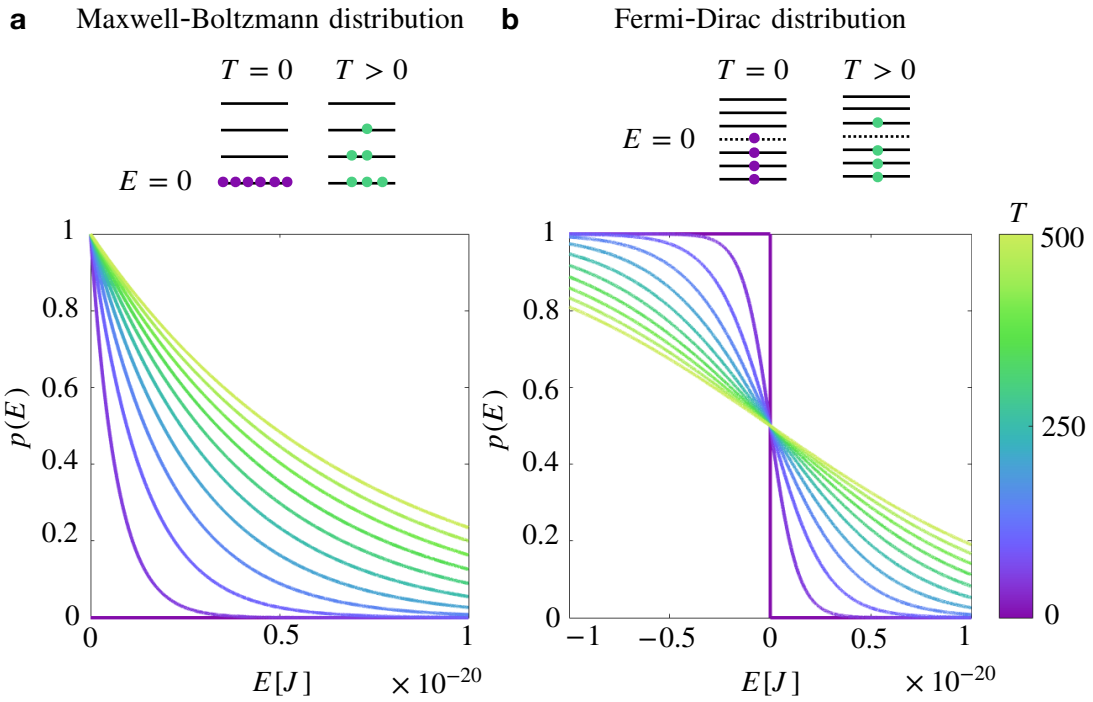

Figure B.1: **Thermal occupation: (a)** Probability of finding a boson in an excited state above the ground state ($E = 0$) as a function of temperature. At $T = 0$ all bosonic particles reside in the ground state. **(b)** For fermionic particles, at $T = 0$ electronic states are occupied to the Fermi-level $E_F = 0$. As the system increases in temperature particles have a non-zero probability of being found in an excited state. Occupancy of energy levels above the Fermi-level $\sim k_B T$.

main text of Section 2.1.2 [66], where the Berry phase is equivalent to the anholonomy angle [69][1].

B.2 Spectroscopy

The experimental data analysed in Chapter 6 is from **Infrared (IR) spectroscopy**, where the IR range is normally understood to range from the red edge of the visible spectrum (700 nm, ∼430 THz) to the edge of the microwave range (1 mm, ∼ 300 GHz), where the longer IR wavelengths are designated as THz radiation. Both IR spectroscopy and **Raman spectroscopy** are vital tools in probing the dynamics of materials and are often used to complement each other. As described in Chapter 2, some phonons are either IR active or Raman active, while others can be activated in both methods. I briefly summarise the two methods here, as extra information for the reader.

Raman spectroscopy involves the inelastic scattering of photons (known as Raman scattering). A system is irradiated with light, and this light interacts with phonons, molecular

[1]The anholonomy angle (or defect angle) is the angular difference between the starting and final vectors in the cyclic evolution.

vibrations or other excitations in the system. This interaction results in a change in energy of the incoming photons, and this energy shift gives information about the excitation modes of the material.

While Raman spectra result from the scattering of light by excitations, IR spectra result from the absorption, emission or reflection of light. In the case of the experimental data in Chapter 6, absorption data is found.

While Raman spectra result from changes in polarizability of the system, IR spectra result from changing dipole moments. Raman measurements can usually be conducted across the UV, visible and IR regions, whereas IR spectroscopy is limited to infrared frequencies.

B.3 Choosing Gauges in electromagnetism

I use a couple of different gauges when discussing electromagnetism in this thesis - I summarise them and their properties here.

Coloumb gauge

The **Coloumb gauge** (also known as the transverse gauge) is given by

$$\nabla \cdot \mathbf{A}(\mathbf{r}, t) = 0. \tag{B.6}$$

This gauge is often used if one wants to quantise the vector potential, but not the Coloumb interaction. It also means that the potentials can be expressed in terms of instantaneous values of the fields and densities, such that

$$\phi(\mathbf{r}, t) = \frac{1}{4\pi\epsilon_0} \int d^3\mathbf{r}' \frac{\rho(\mathbf{r}', t)}{R}, \tag{B.7}$$

$$\mathbf{A}(\mathbf{r}, t) = \nabla \times \int d^3\mathbf{r}' \frac{\mathbf{B}(\mathbf{r}', t)}{4\pi R} \tag{B.8}$$

Lorenz gauge

The **Lorenz gauge** is given by

$$\nabla \cdot \mathbf{A}(\mathbf{r}, t) + \frac{1}{c^2} \frac{\partial \phi(\mathbf{r}, t)}{\partial t} = 0. \tag{B.9}$$

This gauge is unique in preserving Lorentz invariance (but note that the gauge is Ludvig Lorenz, not Hendrik Lorentz). The Lorenz gauge leads to inhomogeneous wave equations

for the potentials, such that

$$\frac{1}{c^2}\frac{\partial^2\phi(\mathbf{r},t)}{\partial t^2} - \nabla^2\phi(\mathbf{r},t) = \frac{\rho(\mathbf{r},t)}{\epsilon_0} \tag{B.10}$$

$$\frac{1}{c^2}\frac{\partial^2\mathbf{A}(\mathbf{r},t)}{\partial t} - \nabla^2\mathbf{A}(\mathbf{r},t) = \mu_0\mathbf{J}(\mathbf{r},t). \tag{B.11}$$

For time-harmonic potentials, Equation B.9 can also be reduced to

$$\nabla\cdot\mathbf{A}(\mathbf{r}) = i\frac{\omega_\mathbf{k}}{c^2}\phi(\mathbf{r}). \tag{B.12}$$

B.4 Beyond the electric dipole approximation

Throughout the work of this thesis I have worked in the **electric dipole (E1) approximation**. We recall from Section 3.4.1 that the interaction Hamiltonian has the form

$$\mathbf{H}^{\text{int}}_{\beta,\mathbf{k}}(\mathbf{r},t) = \frac{e}{m_\text{e}}\sqrt{\frac{\hbar}{2\omega_\mathbf{k}V\epsilon_0}}\left[\mathbf{e}_\beta\cdot\mathbf{p}\ a_{\beta,\mathbf{k}}e^{i(\mathbf{k}\cdot\mathbf{r}-\omega_\mathbf{k}t)} + \mathbf{e}^*_\beta\cdot\mathbf{p}\ a^\dagger_{\beta,\mathbf{k}}e^{-i(\mathbf{k}\cdot\mathbf{r}-\omega_\mathbf{k}t)}\right], \tag{B.13}$$

For an electronic structure with centre of mass at $\mathbf{r}_0$ we can rewrite the exponential as

$$e^{i\mathbf{k}\cdot\mathbf{r}} = e^{i\mathbf{k}\cdot\mathbf{r}_0}e^{i\mathbf{k}\cdot(\mathbf{r}-\mathbf{r}_0)}, \tag{B.14}$$

and selection rules can be found by studying the **matrix element**

$$V_{\beta,\text{i,j}} = \langle\Psi_\text{f}|\mathbf{e}_\beta\cdot\mathbf{p}e^{i\mathbf{k}\cdot(\mathbf{r}-\mathbf{r}_0)}|\Psi_\text{i}\rangle. \tag{B.15}$$

For electronic structures whose spatial expanse is much smaller than the wavelength of irradiating light, we made the approximation that $e^{i\mathbf{k}\cdot(\mathbf{r}-\mathbf{r}_0)} = 1 + i\mathbf{k}\cdot(\mathbf{r}-\mathbf{r}_0) + ... \approx 1$. The matrix element can then be written as

$$V_{\beta,\text{i,j}} = \langle\Psi_\text{f}|\mathbf{e}_\beta\cdot\mathbf{p}|\Psi_\text{i}\rangle \approx im_\text{e}\omega_{\text{i,f}}\langle\Psi_\text{f}|\mathbf{e}_\beta\cdot\mathbf{r}|\Psi_\text{i}\rangle. \tag{B.16}$$

However, we can go beyond the electric dipole approximation by including **higher order terms**. Including the next term of the exponential expansion, we have that $e^{i\mathbf{k}\cdot(\mathbf{r}-\mathbf{r}_0)} \approx 1 + i\mathbf{k}\cdot(\mathbf{r}-\mathbf{r}_0)$. The matrix element is then

$$V_{\beta,\text{i,j}} \approx im_\text{e}\omega_{\text{i,f}}\langle\Psi_\text{f}|\mathbf{e}_\beta\cdot\mathbf{r}|\Psi_\text{i}\rangle + i\omega_{\text{i,f}}\langle\Psi_\text{f}|\left[\mathbf{k}\cdot(\mathbf{r}-\mathbf{r}_0)\right]\left[\mathbf{e}_\beta\cdot\mathbf{p}\right]|\Psi_\text{i}\rangle. \tag{B.17}$$

For ease of notation we rewrite $\mathbf{x} = \mathbf{r}-\mathbf{r}_0$. If a transition $|\Psi_\text{i}\rangle \to |\Psi_\text{f}\rangle$ were to be **forbidden**, such that the E1 contribution to the matrix element would be zero, the matrix element then becomes

$$V_{\beta,\text{i,j}} \approx i\omega_{\text{i,f}}\langle\Psi_\text{f}|\left(\mathbf{k}\cdot\mathbf{x}\right)\left(\mathbf{e}_\beta\cdot\mathbf{p}\right)|\Psi_\text{i}\rangle. \tag{B.18}$$

From this we find that a forbidden transition is not really forbidden, but it would just take place at a much slower rate than an E1 transition.

According to classical electromagnetism, $\hat{\mathbf{k}} = \mathbf{b}_\beta \times \mathbf{e}_\beta$, where $\mathbf{b}_\beta$ is the polarisation direction of the magnetic component of the wave. We also note that $\mathbf{L} = \mathbf{x} \times \mathbf{p}$ is angular momentum. It can be calculated through some algebraic gymnastics that

$$\mathbf{b}_\beta \cdot \mathbf{L} = (\hat{\mathbf{k}} \times \mathbf{e}_\beta)(\mathbf{x} \times \mathbf{p}) = (\hat{\mathbf{k}} \cdot \mathbf{x})(\mathbf{e}_\beta \cdot \mathbf{p}) - (\mathbf{e}_\beta \cdot \mathbf{x})(\hat{\mathbf{k}} \cdot \mathbf{p}). \tag{B.19}$$

It can also be calculated that

$$\frac{im_\mathrm{e}}{\hbar}\left[\mathbf{H}^\mathrm{elec}, (\mathbf{e}_\beta \cdot \mathbf{x})(\mathbf{n} \cdot \mathbf{x})\right] = (\mathbf{e}_\beta \cdot \mathbf{x})(\mathbf{e}_\beta \cdot \mathbf{p}) + (\mathbf{n} \cdot \mathbf{x})((\mathbf{e}_\beta \cdot \mathbf{p})), \tag{B.20}$$

where $\mathbf{H}^\mathrm{elec}$ is the unperturbed electron Hamiltonian first encountered in Section 3.4. Using the previous three equations, we then arrive at the result that

$$V_{\beta,\mathrm{i,j}} = \frac{i\omega_\mathrm{i,f}}{2c}\mathbf{b}_\beta \langle \Psi_\mathrm{f}|\mathbf{L}|\Psi_\mathrm{i}\rangle - \frac{m_\mathrm{e}\omega_\mathrm{i,f}}{2}\mathbf{e}_\beta \cdot \mathbf{Q}_\mathrm{i,f} \cdot \mathbf{k}, \tag{B.21}$$

where

$$(\mathbf{Q}_\mathrm{i,f})_\mathrm{j,k} = \langle \Psi_\mathrm{f}|x_\mathrm{j}x_\mathrm{k} - r^2\delta_\mathrm{j,k}/3|\Psi_\mathrm{i}\rangle, \tag{B.22}$$

where $r^2 = x_\mathrm{j}x_\mathrm{j}$. The two terms on the right-hand-side are usually treated separately, as they can give rise to different selection rules. The first term governs **magnetic dipole (M1) transitions**, while the second term governs **electric quadrupole (E2) transitions**. However, in this system the selection rules for each term coincide, although they will result in different transition rates.

For the spherical TINP, the M1 and E2 selection rules are as follows:

Result: M1 and E2 selection rules

The **M1 and E2 selection rules** for light propagating along the z-axis such that $\hat{\mathbf{k}} = (0, 0, 1)$: For left-hand (LH) polarised light such that $\mathbf{e} = \frac{1}{\sqrt{2}}(1, i, 0)$,

$$\Delta s = 0, \quad \Delta(n + |m|) = \pm 2, \quad \Delta m = -1 \tag{B.23}$$

$$\Delta s \neq 0, \quad \Delta(n + |m|) = \pm 1, \quad \Delta m = -1 \tag{B.24}$$

For right-hand polarised light such that $\mathbf{e} = \frac{1}{\sqrt{2}}(1, -i, 0)$,

$$\Delta s = 0, \quad \Delta(n + |m|) = \pm 2, \quad \Delta m = 1 \tag{B.25}$$

$$\Delta s \neq 0, \quad \Delta(n + |m|) = \pm 1, \quad \Delta m = 1 \tag{B.26}$$

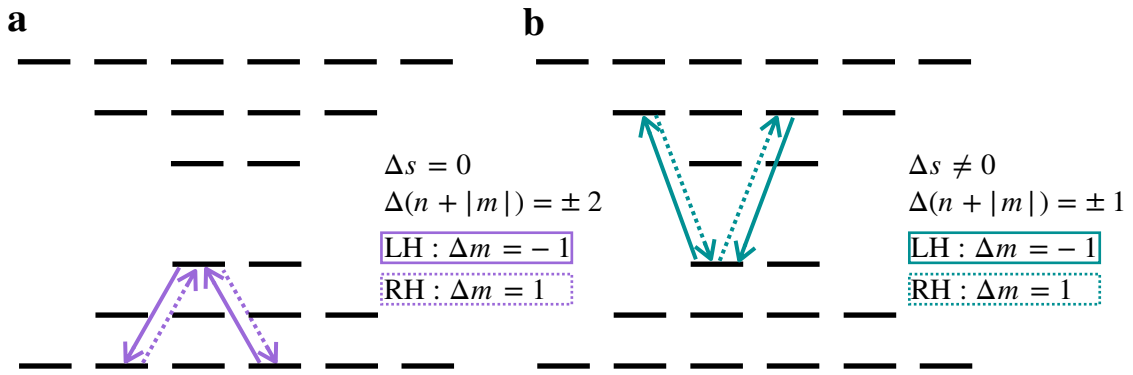

Figure B.2: **Selection rules beyond E1:** Selection rules for left- and right-hand polarised light for M1 and E2 transitions, which coincide.

B.5 Fermi's golden rule

For many situations, the transition rates can be written in terms of photonic density of states, although this is not always the case as will be discussed in Chapter 5. It should also be noted that when explicitly calculated, it can be seen that stimulated transition rates rely on the number of photons in the system, systems spontaneous transition rates are independent on photon number. For many transitions, **Fermi's golden rule** can be employed,

$$\Gamma_{\mathrm{i}\to\mathrm{f},\beta}(\mathbf{r}) = \frac{2\pi}{\hbar}|V_{\mathrm{i,f},\beta}|^2 g(\mathbf{r},\omega_{\mathrm{i,f}}), \tag{B.27}$$

where $g(\mathbf{r},\omega_{\mathrm{i,f}})$ is the photonic LDOS described in Section 3.7, and $V_{\mathrm{i,f},\beta}$ is the matrix element given in Equation 3.57. Writing the transition rate in this form relies on being able to factorise the expectation value into separate contributions from the matrix element, electric field spatial distribution and DOS. This is possible in free space and the 1D cavity, as will be seen in Chapter 5, but in higher dimensions (such as the 3D cavity discussed in Chapter 5, the transition rate cannot generally be factorised into this form. This was the driving factor in using the method of spectral densities in this thesis. However, in many situations, it is generally assumed that the maximal DOS modification is wanted, and so results will often reduce to Fermi's golden rule.

B.6 Cross-section, spectral density and transition rates

The transition rate between two states, $\Gamma_{\mathrm{i}\to\mathrm{f}}$ can be written in terms of the transition cross-section, $\sigma_{\mathrm{i}\to\mathrm{f}}$, such that

$$\Gamma_{\mathrm{i}\to\mathrm{f}} = c\int_{-\infty}^{\infty} d\omega n(\omega)\sigma_{\mathrm{i}\to\mathrm{f}}(\omega). \tag{B.28}$$

For the situation where $n(\omega) = n\delta(\omega - \omega_{\mathrm{i,f}})$, this simplifies to

$$\Gamma_{\mathrm{i}\to\mathrm{f}} = cn\omega_{\mathrm{i,f}}\sigma_{\mathrm{i}\to\mathrm{f}}(\omega). \tag{B.29}$$

These quantities can also be linked to spectral density, where

$$\Gamma_{\mathrm{i}\to\mathrm{f}} = \frac{2\pi}{\hbar^2}\sum_{\beta,\mathbf{k}}\int d\omega S_{\mathrm{i}\to\mathrm{f},\beta,\mathbf{k}}(\omega)\delta(\omega - \omega_{\mathrm{i,f}}), \tag{B.30}$$

and so we can relate spectral density and transition cross-section by

$$\sigma_{\mathrm{i}\to\mathrm{f}}(\omega) = \frac{2\pi}{c\hbar^2}\frac{S_{\mathrm{i}\to\mathrm{f}}(\omega)}{n(\omega)}\delta(\omega - \omega_{\mathrm{i,f}}). \tag{B.31}$$

B.7 Deriving the effective surface Hamiltonian

In Chapter 4 I find the effective surface Hamiltonian, $\mathbf{H}_{\mathrm{surf}}$, via the projection of $\mathbf{H}_{\parallel}$ onto the surface state $|\Phi\rangle = \alpha_+|+\rangle + \alpha_-|-\rangle$. $\mathbf{H}_{\mathrm{surf}}$, acts on $(\alpha_+, \alpha_-)^T$, i.e.

$$\mathbf{H}_{\mathrm{surf}}\begin{pmatrix}\alpha_+\\ \alpha_-\end{pmatrix} = \begin{pmatrix}\langle +|\mathbf{H}_{\parallel}|\Phi\rangle\\ \langle -|\mathbf{H}_{\parallel}|\Phi\rangle\end{pmatrix}. \tag{B.32}$$

I do this for both prolate and oblate spheroidal nanoparticles. The symmetries of $\mathbf{H}_{\parallel}$ can be used to simplify this task. We note that

$$\mathbf{H}_{\parallel}^{11} = \mathbf{H}_{\parallel}^{33} = -\mathbf{H}_{\parallel}^{22} = -\mathbf{H}_{\parallel}^{44} \tag{B.33}$$
$$\mathbf{H}_{\parallel}^{12} = \mathbf{H}_{\parallel}^{21} = -\mathbf{H}_{\parallel}^{34} = -\mathbf{H}_{\parallel}^{43} \tag{B.34}$$
$$\mathbf{H}_{\parallel}^{13} = \mathbf{H}_{\parallel}^{31} = \mathbf{H}_{\parallel}^{24} = \mathbf{H}_{\parallel}^{42} = 0 \tag{B.35}$$
$$\mathbf{H}_{\parallel}^{14} = \mathbf{H}_{\parallel}^{23} = -(\mathbf{H}_{\parallel}^{32})^* = -(\mathbf{H}_{\parallel}^{41})^* \tag{B.36}$$

By writing $\langle +| = (a_1^*, a_2^*, a_3^*, a_4^*)$ and $\langle -| = (b_1^*, b_2^*, b_3^*, b_4^*)$, we note the simplification that

$$\begin{aligned} &a_2 = -ia_1, \quad a_4 = -ia_3, \quad a_2^* = ia_1^*, \quad a_4^* = ia_3^*,\\ &b_2 = ib_1, \quad b_4 = ib_3, \quad b_2^* = -ib_1^*, \quad b_4^* = -ib_3^*. \end{aligned} \tag{B.37}$$

We also set all m_1 terms to 0. We can then write that

$$\mathbf{H}_{\mathrm{surf}}^{++} = \mathbf{H}_{\mathrm{surf}}^{--} = 0 \tag{B.38}$$

$$\mathbf{H}_{\mathrm{surf}}^{-+} = 2i\left(b_3^*a_3 - b_1^*a_1\right)H_{12} - 2ib_1^*a_3H_{14} - 2ib_3^*a_1H_{41} \tag{B.39}$$
$$+ 2ib_3^*H_{12}a_3 - 2ib_1^*H_{12}a_1 - 2ib_1^*H_{14}a_3 - 2ib_3^*H_{41}a_1 \tag{B.40}$$

and

$$\mathbf{H}^{+-}_{\text{surf}} = 2i\left(a_1^* b_1 - a_3^* b_3\right) H_{12} + 2ia_1^* H_{12} b_1 + 2ia_1^* b_3 H_{14} + 2ia_3^* b_1 H_{41} \tag{B.41}$$

$$- 2ia_3^* H_{12} b_3 + 2ia_1^* H_{14} b_3 + 2ia_3^* H_{41} b_1. \tag{B.42}$$

From calculating these results explicitly, the results of Chapter 4 follow.

B.8 The Q factor

The Q factor (or Quality factor) of a resonant cavity can be described in terms of the **stored energy**, such that

$$Q = 2\pi \frac{\text{Energy stored in cavity}}{\text{Energy lost per cycle via cavity walls}} \tag{B.43}$$

By conservation of energy, the rate of change of **stored energy**, U, is equal to the power dissipated via **Ohmic losses**[2], such that

$$\frac{dU}{dt} = -\frac{\omega_0}{Q} U, \tag{B.44}$$

where ω_0 is a normal mode. The solution to this equation is given by

$$U = U_0 e^{-\omega_0 t/Q} = U_0 e^{-t/\tau}, \tag{B.45}$$

where we define $1/tau$ as the cavity decay constant such that $Q = \omega_0 \tau$. The time-dependence of the stored energy suggested that the electric field in the cavity will undergo damped oscillations, such that

$$\mathbf{E}(t) = \mathbf{E}_0 e^{-\omega_0 t/2} e^{-i\omega_0 t}. \tag{B.46}$$

A damped oscillation such as this does not consist of a pure frequency, but instead will be composed of a superposition of frequencies centred around $\omega = \omega_0$. Performing a Fourier transform,

$$\mathbf{E}(\omega) = \frac{1}{\sqrt{2\pi}} \int_0^\infty d\omega \mathbf{E}_0 e^{-\omega_0 t/2Q} e^{i(\omega - \omega_0)t}, \tag{B.47}$$

and so (as per the integral in Equation A.36),

$$|\mathbf{E}(\omega)|^2 \propto \frac{1}{(\omega - \omega_0)^2 + (\omega_0/2Q)^2}. \tag{B.48}$$

[2] Ohmic losses result in energy dissipation in the form of heat.

This curve has a full-width at half-maximum equal to ω_0/Q. I think it is useful to note here that it is because Q is defined via energy that the electric field decays with a decay constant of $\omega_0/2Q$, rather than ω_0/Q (as $U \propto |\mathbf{E}|^2$).

B.9 Spontaneous emission and Purcell effect in 1D free space

This topic is relegated to the appendix in order to keep Chapter 5 a bit more concise. It is not strictly needed for the calculations in Chapter 5, but is useful if we want to calculate the 1D Purcell factor. As for the 3D free space case given in 5.1.1, we begin with the power spectral density

$$S_{\mathrm{i,f},\beta,\mathbf{k}}(\omega) = e^2 \lim_{T\to\infty} \frac{1}{T} \left| \langle \Psi_\mathrm{f}| \otimes \langle 1|\tilde{\mathbf{E}}_{\beta,\mathbf{k}}(\mathbf{r}_0,\omega)\cdot\mathbf{r}|\Psi_\mathrm{i}\rangle \otimes |0\rangle \right|^2. \tag{B.49}$$

Everything is the same as the 3D case (apart from normalisation of the electric field) until we need to sum over $\mathbf{k}$ states.

$$\Gamma^{\mathrm{spon}}_{\mathrm{i}\to\mathrm{j},\beta} = \frac{\pi e^2}{\hbar L \epsilon_0} \sum_{\mathbf{k}} \omega_{\mathbf{k}} |\langle \Psi_\mathrm{f}|\mathbf{r}\cdot\mathbf{e}_\beta|\Psi_\mathrm{i}\rangle|^2 \delta(\omega_{\mathrm{i,f}} - \omega_{\mathbf{k}}). \tag{B.50}$$

Then, instead of integrating over a volume, we're integrating over a length, such that the space occupied by one state in $\mathbf{k}$-space $2\pi/L$ is an infinitesimal length, $\Delta k_z \to dk_z$, such that

$$\sum_k \delta(\omega_{\mathrm{i,f}} - \omega_k) \to \frac{L}{2\pi}\int_L dk \delta(\omega_{\mathrm{i,f}} - \omega_k) =\to \frac{L}{2\pi c}\int_L d\omega \delta(\omega_{\mathrm{i,f}} - \omega_k), \tag{B.51}$$

and so

$$\Gamma^{\mathrm{spon}}_{\mathrm{i}\to\mathrm{f}} = \frac{2\pi\alpha c}{L} \sum_{\beta,m} \sin^2\left(\frac{m\pi z}{L}\right) |\langle \Psi_\mathrm{f}|\mathbf{r}\cdot\mathbf{e}_\beta|\Psi_\mathrm{i}\rangle|^2 \frac{4Qm\omega_\mathrm{c}^2}{\omega_\mathrm{c}^2 + 4Q^2(\omega_{\mathrm{i,f}} - m\omega_\mathrm{c})^2} \tag{B.52}$$

$$\Gamma^{\mathrm{spon}}_{\mathrm{i}\to\mathrm{j},\beta} = \frac{\pi e^2}{\hbar L\epsilon_0}\frac{L}{2\pi c}\omega_{\mathrm{i,f}} |\langle \Psi_\mathrm{f}|\mathbf{r}\cdot\mathbf{e}_\beta|\Psi_\mathrm{i}\rangle|^2 \tag{B.53}$$

$$= \frac{e^2}{2\hbar c\epsilon_0}\omega_{\mathrm{i,f}} |\langle \Psi_\mathrm{f}|\mathbf{r}\cdot\mathbf{e}_\beta|\Psi_\mathrm{i}\rangle|^2 \tag{B.54}$$

A slightly strange interpretation of 1D space has to be taken here, where k is uni-directional, but the electric and magnetic fields of the EM field are still perpendicular to it. This means that the polarisation vectors are restricted to a single plane. Averaging in all directions for

polarisation thus results in the overall transition rate

$$\Gamma_{\mathrm{i}\to\mathrm{j}}^{\mathrm{spon}} = \frac{e^2}{2\hbar c\epsilon_0}\omega_{\mathrm{i,f}} \sum_{\beta} |\langle\Psi_{\mathrm{f}}|\mathbf{r}\cdot\mathbf{e}_\beta|\Psi_{\mathrm{i}}\rangle|^2 \tag{B.55}$$

$$= \frac{e^2}{2\hbar c\epsilon_0\omega_{\mathrm{i,f}}} |\langle\Psi_{\mathrm{f}}|\mathbf{r}|\Psi_{\mathrm{i}}\rangle|^2 \tag{B.56}$$

Written in terms of $\alpha = \frac{1}{4\pi\epsilon_0}\frac{e^2}{\hbar c}$,

$$\Gamma_{\mathrm{i}\to\mathrm{j}}^{\mathrm{spon}} = \frac{e^2}{2\hbar c\epsilon_0}\omega_{\mathrm{i,f}} \sum_{\beta} |\langle\Psi_{\mathrm{f}}|\mathbf{r}\cdot\mathbf{e}_\beta|\Psi_{\mathrm{i}}\rangle|^2 \tag{B.57}$$

$$= 2\pi\alpha\omega_{\mathrm{i,f}} |\langle\Psi_{\mathrm{f}}|\mathbf{r}|\Psi_{\mathrm{i}}\rangle|^2. \tag{B.58}$$

Recalling the spontaneous transition rate in a 1D cavity,

$$\Gamma_{\mathrm{i}\to\mathrm{f}}^{\mathrm{spon}} = \frac{2\pi\alpha c}{L} \sum_m \sin^2\left(\frac{m\pi z}{L}\right) |\langle\Psi_{\mathrm{f}}||\Psi_{\mathrm{i}}\rangle|^2 \frac{4Qm\omega_{\mathrm{c}}^2}{\omega_{\mathrm{c}}^2 + 4Q^2(\omega_{\mathrm{i,f}} - m\omega_{\mathrm{c}})^2}. \tag{B.59}$$

we can calculate the **1D Purcell factor** (in the middle of the cavity, for the fundamental cavity mode) of

$$F_{\mathrm{1D}} = \frac{\Gamma_{\mathrm{i}\to\mathrm{j,cavity}}^{\mathrm{spon}}}{\Gamma_{\mathrm{i}\to\mathrm{j,free}}^{\mathrm{spon}}} = \frac{8\pi\alpha c Q\omega_{\mathrm{c}}^2 |\langle\Psi_{\mathrm{f}}|\mathbf{r}|\Psi_{\mathrm{i}}\rangle|^2}{2\pi\alpha\omega_{\mathrm{i,f}} |\langle\Psi_{\mathrm{f}}|\mathbf{r}|\Psi_{\mathrm{i}}\rangle|^2 L\left(\omega_{\mathrm{c}}^2 + 4Q^2\left(\omega_{\mathrm{i,f}} - \omega_{\mathrm{c}}\right)^2\right)} \tag{B.60}$$

$$= \frac{4cQ\omega_{\mathrm{c}}^2}{\omega_{\mathrm{i,f}}\left(\omega_{\mathrm{c}}^2 + 4Q^2\left(\omega_{\mathrm{i,f}} - \omega_{\mathrm{c}}\right)^2\right) L} \tag{B.61}$$

For resonant frequencies, such that $\omega_{\mathrm{i,j}} = \omega_{\mathrm{c}}$,

$$F_{\mathrm{1D}} = \frac{2Q\lambda_{\mathrm{free}}}{\pi L} \tag{B.62}$$

where λ_{free} is the wavelength of light in free space.

Result: Spontaneous emission and Purcell effect in 1D

Spontaneous emission rate

$$\Gamma_{\mathrm{i}\to\mathrm{j}}^{\mathrm{spon}} = 2\pi\alpha\omega_{\mathrm{i,f}} |\langle\Psi_{\mathrm{f}}|\mathbf{r}|\Psi_{\mathrm{i}}\rangle|^2 \tag{B.63}$$

Purcell factor

$$F_{\mathrm{1D}} = \frac{4cQ\omega_{\mathrm{c}}^2}{\omega_{\mathrm{i,f}}\left(\omega_{\mathrm{c}}^2 + 4Q^2\left(\omega_{\mathrm{i,f}} - \omega_{\mathrm{c}}\right)^2\right) L} \tag{B.64}$$

Resonant Purcell factor

$$F_{\mathrm{1D}} = \frac{2\lambda_{\mathrm{free}}Q}{\pi L} \tag{B.65}$$

B.10 Particle statistics

Bosonic systems (such as phonons, magnons, molecules etc) obey the **Maxwell-Boltzmann distribution** (illustrated in Figure B.1a), while fermionic particles (such as electrons) obey the **Fermi-Dirac distribution**. The energy to which particles can be excited is $\sim k_{\mathrm{B}}T$.

B.11 Fano resonances

Fano resonances[3] are the result of an interference between two scattering amplitudes, one due the excitation of a **discrete state** (the resonant process) and one due to scattering within a **continuum of states** (the background process). The processes should occur at commensurate frequencies. Normally, a phonon would constitute the discrete mode and the environment would constitute the broad, continuous mode. However, in the case of the SToP mode, the surface state excitation is discrete, and the phonon mode is broad in comparison.

Near the resonant energy, the background scattering amplitude usually varies slowly with energy while the resonant scattering amplitude changes both in magnitude and phase quickly. It is this variation that creates the typical, **asymmetric line-shape** of the Fano resonance.

B.12 Experimental method for producing bismuth telluride nanoparticles

This experimental method is taken from the manuscript [6], and was contributed by M. Sokolikova. I include it here as additional content for interested experimentalists.

In a standard synthesis, 114 mg of bismuth acetate ($Bi(CH_3COO)_3$, 99% Aldrich) and 3.5 mL of 1-dodecanethiol (DDT, 98% Aldrich) were mixed in a three-neck flask and heated to 45°C under vacuum and kept at this temperature until a transparent pale-yellow solution is formed. Then the flask was flashed with nitrogen and heated to 60°C and 6.5 mL of oleylamine (OlAm, 70%, Aldrich) was quickly added. After 24 hours the as-prepared bismuth nanoparticles were used without any further purification. For tellurisation 0.45 mL of 1M trioctylphosphine telluride (TOP:Te) was injected at 60°C into the solution containing bismuth nanoparticles. The reaction mixture was kept at this temperature for 48 hours until complete tellurisation and then annealed at 110°C for 8 hours in order to restore crystallinity. Thus produced Bi_2Te_3 nanoparticles were washed three times with ethanol and then redispersed in chloroform. For THz measurements solvent was exchanged to mineral oil.

[3] Named for Ugo Fano. His paper on the topic [219], is one of the highest cited papers in *Physical Review*, owing to the ubiquity of Fano resonances in across scientific topics.

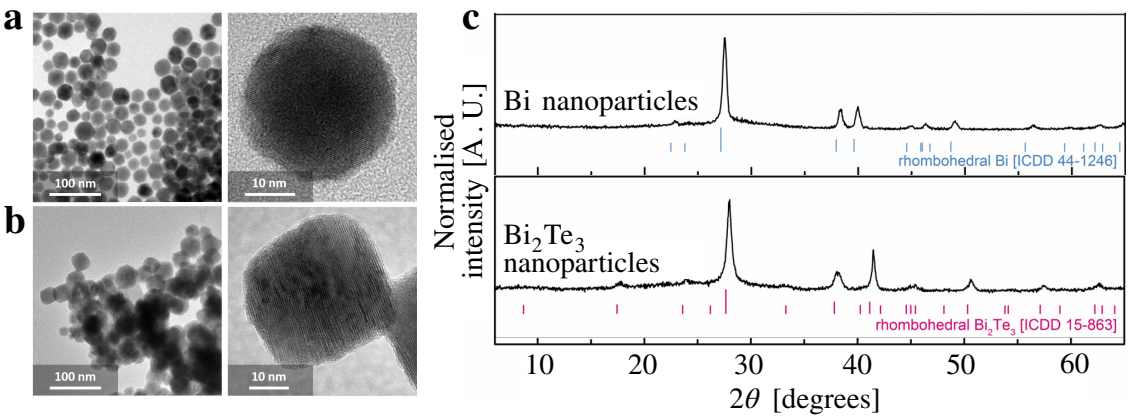

Figure B.3: **Bi_2Te_3 nanoparticle synthesis: (a)** TEM images of Bi nanoparticles, which are nearly spherical and of average radius 14.4 nm. **(b)** Successfully synthesized Bi_2Te_3 nanoparticles with a slightly rhombohedral shape and average radius of 17.5 nm. **(c)** X-ray diffraction patterns illustrating the successful tellurisation of the Bi nanoparticles to form Bi_2Te_3 nanoparticles. Figure modified from [6], published by The Royal Society of Chemistry.

C. Numerical methods

In this appendix I give a brief overview of the numerical methods used in this thesis.

C.1 Finite difference method for solving ODEs

We are interested in solving ordinary differential equations of the form found in Chapter 4, such as

$$F(x)z''(x) + G(x)z'(x) + H(x)z(x) = \lambda^2 z(x). \tag{C.1}$$

In order to solve this equation numerically, we discretise x to create a series of equations at points x_i., and we can write $z(x)$ as a vector, such that

$$z(x) = \begin{pmatrix} z(x_0) \\ z(x_1) \\ z(x_2) \\ ... \\ z(x_{N-1}) \\ z(x_N) \end{pmatrix}. \tag{C.2}$$

The equations can be reformulated as an eigenvalue problem of a single operator, such that

$$\mathbf{M}(x)z(x) = Ez(x), \tag{C.3}$$

where $\mathbf{M}(x)$ is an operator given by

$$\mathbf{M}(x) = F(x)\frac{d^2}{dx^2} + G(x)\frac{d}{dx} + H(x). \tag{C.4}$$

We can discretise $\mathbf{M}(x)$ by considering that

$$\frac{d}{dx}z(x_i) = \frac{z(x_{i+1}) - z(x_{i-1})}{2\Delta x} \tag{C.5}$$

$$\frac{d^2}{dx^2}z(x_i) = \frac{z(x_{i+1}) - 2z(x_i) + z(x_{i-1})}{\Delta x^2}, \tag{C.6}$$

where $\delta x = x_{i+1} - x_i$ is a small, constant interval. We can thus write terms as matrices acting in the vector $z(x)$, such that

$$H(x) = \begin{pmatrix} H(x_1) & 0 & 0 & ... & 0 \\ 0 & H(x_2) & 0 & ... & 0 \\ 0 & 0 & H(x_3) & ... & 0 \\ ... & ... & ... & ... & ... \\ 0 & 0 & 0 & H(x_{N-1}) & 0 \\ 0 & 0 & 0 & 0 & H(x_N) \end{pmatrix} \tag{C.7}$$

$$G(x)\frac{d}{dx} = \frac{1}{2\Delta x}\begin{pmatrix} 0 & G(x_1) & 0 & ... & 0 \\ -G(x_2) & 0 & G(x_2) & ... & 0 \\ 0 & -G(x_3) & 0 & ... & 0 \\ ... & ... & ... & ... & ... \\ 0 & 0 & -G(x_{N-1}) & 0 & G(x_{N-1}) \\ 0 & 0 & 0 & -G(x_N) & 0 \end{pmatrix} \tag{C.8}$$

and

$$F(x)\frac{d^2}{dx^2} = \frac{1}{\Delta x^2}\begin{pmatrix} -2F(x_1) & F(x_1) & 0 & ... & 0 \\ F(x_2) & -2F(x_2) & F(x_2) & ... & 0 \\ 0 & F(x_3) & -2F(x_3) & ... & 0 \\ ... & ... & ... & ... & ... \\ 0 & 0 & F(x_{N-1}) & -2F(x_{N-1}) & F(x_{N-1}) \\ 0 & 0 & 0 & F(x_N) & -2F(x_N) \end{pmatrix} \tag{C.9}$$

Combining all of these terms, we can then use standard linear algebra to find the eigenvalues of the equation, E.

C.2 Fermionic rate equations from Monte Carlo simulations

In a typical atomic lasing system, the system of rate equations can be simply modelled with a statistical model. In these systems, the initial condition of a single atom is given by a single electron in its ground state, and the combined system of many atoms can be treated as a non interacting system as the electrons in separate atoms do not interact. However in the system of a TINP, an interacting system must be considered, as multiple electrons in a single Dirac cone will participate in the system evolution. In order to correctly capture the fermionic nature of this system, we use a probabilistic 'hopping' method which allows electrons to traverse the system of energy levels according to the transition rates but forbidding double occupation of levels, and then averaging over many runs to obtain a statistical mean of energy-level occupation densities.

We move to a Fock basis, in which the total wave function of the system can be described by

$$|\Psi\rangle = \prod_{i=1}^{M} \otimes |n_i\rangle, \tag{C.10}$$

where M is the number of states involved in the lasing scheme. Each state obeys fermionic occupation rules such that $n_i = 0$ or 1. For a given time step dt, transition rates are converted to probabilities $p_{\mathrm{i}\to\mathrm{j}} = \Gamma_{\mathrm{i}\to\mathrm{j}} dt \ll 1$, where for transitions at the cavity frequency, $\Gamma_{\mathrm{i}\to\mathrm{j}} \propto \bar{n}_{\mathrm{i,j}}$ and the rate will dynamically change as $\bar{n}_{ij}$ as evolves via the dynamics.

The model is described below in pseudo-code.

```
Initialise state (particle basis)
Initialise state (photon basis)
Convert all transition rates to probabilities
for 1:number_repeats
% Repeat and average to give accurate mean observables
        for t=1:number_time_steps
                for 1:number_particles
                % Electronic statistics
                        For particle i, identify which
                        transitions i-> j are non-zero

                        Convert total transition rate to probability
                        Generate random number a to see
                        whether transition occurs

                        If transition occurs, weight allowed transitions

                        Generate random number b to pick which
                        transition occurs

                        Particle i transitions to new state

                % Photonic statistics
                        if cavity mode
                            if absorption, remove photon from mode
                            elseif emission, generate random number
                            to decide spontaneous or stimulated
                            end
                    end
```

```
                Repeat for all particles.
                Check for multiple occupancy.
                If no multiple occupancy, state at next
                time state = new state.

                leak cavity mode photons according to Q factor

                elseif multiple occupancy has occurred, state
                at next time state = old state.
                end
        end
end
```

The initial conditions are set by occupying states up to the desired Fermi level E_F. For a given time step, all electrons may transition between states with the probabilities calculated from the relations given in Chapter 5. The number of photons in each mode is updated accordingly, as photons are emitted and absorbed. At the end of the time step, it is checked of the transitions have obeyed fermionic occupation rules (such that there is maximum one electron in any given state). If the transitions have resulted in multiple occupancy of any state, the time step is reset and the system required to undertake the step again. When a physically allowed time step has been undertaken, the entire system updates and progresses to the next time step. In this way, the system evolves whilst observing fermionic occupation rules.

The coherent photons in the cavity will leak from the cavity at each time step, according to the cavity time scale. The number of photons leaving the cavity is tracked, as if steady state is achieved this will be used to calculate lasing rate.

A single evolution of the system gives a so-called **quantum leap** simulation, while averaging the simulation over many iterations gives the average expected results of a single TQD, or if multiplied by N, gives the result of N uncorrelated TQDs.

C.3 Lorentzian decomposition

In order to decompose the experimental **absorption cross-section data** in Chapter 6 using **Lorentzian** peaks, the Matlab peak-fitting programme **Peakfit.m** was used.

```
peakfit(signal,center,window,NumPeaks,peakshape)
```

Center: 2.39 THz. Window: 2.66 THz. Number of peaks: four. Peak shape: Lorentzian. Error: 2.3% with three peaks, 0.241% with with four peaks, 3.4% with five peaks.

Bibliography

1. Rider, M. S., Palmer, S. J., Pocock, S. R., Xiao, X., Arroyo Huidobro, P. & Giannini, V. **A perspective on topological nanophotonics: Current status and future challenges. Journal of Applied Physics 125,** 120901 (2019).
2. Hasan, M. Z. & Moore, J. E. **Three-Dimensional Topological Insulators. Annual Review of Condensed Matter Physics 2,** 55–78 (2011).
3. Rider, M. S. & Giannini, V. **Spheroidal topological insulator nanoparticles. In preparation** (2021).
4. Rider, M. S. & Giannini, V. **Proposal for THz lasing from a 3D topological quantum dot. arXiv:2105.04316** (2021).
5. Siroki, G., Lee, D., Haynes, P. & Giannini, V. **Single-electron induced surface plasmons on a topological nanoparticle. Nature communications 7,** 1–6 (2016).
6. Rider, M. S., Sokolikova, M., Hanham, S. M., Navarro-Cia, M., Haynes, P. D., Lee, D. K., Daniele, M., Guidi, M. C., Mattevi, C., Lupi, S. & Giannini, V. **Experimental signature of a topological quantum dot. Nanoscale 12,** 22817–22825 (2020).
7. Rider, M. S. & Giannini, V. **Manipulating photonic local density of state with topological insulator nanostructures. In preparation** (2021).
8. Mancini, M., Pagano, G., Cappellini, G., Livi, L., Rider, M. S., Catani, J., Sias, C., Zoller, P., Inguscio, M., Dalmonte, M. & Fallani, L. **Observation of chiral edge states with neutral fermions in synthetic Hall ribbons. Science 349,** 1510–1513 (2015).
9. Pais, A. **Niels Bohr's times: In physics, philosophy, and polity. Oxford University Press** (1991).
10. Mortensen, N. A., Bozhevolnyi, S. I. & Alù, A. **Topological nanophotonics. Nanophotonics 8,** 1315–1317 (2019).
11. Khanikaev, A. B. & Shvets, G. **Two-dimensional topological photonics. Nature photonics 11,** 763–773 (2017).
12. Lu, L., Joannopoulos, J. D. & Soljačić, M. **Topological photonics. Nature photonics 8,** 821–829 (2014).

13. Ozawa, T., Price, H. M., Amo, A., Goldman, N., Hafezi, M., Lu, L., Rechtsman, M. C., Schuster, D., Simon, J., Zilberberg, O., *et al.* **Topological photonics. Reviews of Modern Physics 91,** 015006 (2019).

14. Kim, M., Jacob, Z. & Rho, J. **Recent advances in 2D, 3D and higher-order topological photonics. Light: Science & Applications 9,** 1–30 (2020).

15. Chang, M.-C. & Yang, M.-F. **Optical signature of topological insulators. Physical Review B 80,** 113304 (2009).

16. Tse, W.-K. & MacDonald, A. **Giant magneto-optical Kerr effect and universal Faraday effect in thin-film topological insulators. Physical Review Letters 105,** 057401 (2010).

17. Tse, W.-K. & MacDonald, A. **Magneto-optical Faraday and Kerr effects in topological insulator films and in other layered quantized Hall systems. Physical Review B 84,** 205327 (2011).

18. Qi, X.-L. & Zhang, S.-C. **Topological insulators and superconductors. Reviews of Modern Physics 83,** 1057 (2011).

19. Wu, L., Salehi, M., Koirala, N., Moon, J., Oh, S. & Armitage, N. **Quantized Faraday and Kerr rotation and axion electrodynamics of a 3D topological insulator. Science 354,** 1124–1127 (2016).

20. Siroki, G., Huidobro, P. A. & Giannini, V. **Topological photonics: From crystals to particles. Physical Review B 96,** 041408 (2017).

21. Mathanker, S. K., Weckler, P. R. & Wang, N. **Terahertz (THz) applications in food and agriculture: A review. Transactions of the ASABE 56,** 1213–1226 (2013).

22. Qin, J., Ying, Y. & Xie, L. **The detection of agricultural products and food using terahertz spectroscopy: A review. Applied Spectroscopy Reviews 48,** 439–457 (2013).

23. Amenabar, I., Lopez, F. & Mendikute, A. **In introductory review to THz non-destructive testing of composite matter. Journal of Infrared, Millimeter, and Terahertz Waves 34,** 152–169 (2013).

24. Humphreys, K., Loughran, J., Gradziel, M., Lanigan, W., Ward, T., Murphy, J. A. & O'Sullivan, C. **Medical applications of terahertz imaging. IEEE Engineering in Medicine and Biology Society 1,** 1302–1305 (2004).

25. Yu, C., Fan, S., Sun, Y. & Pickwell-MacPherson, E. **The potential of terahertz imaging for cancer diagnosis: A review of investigations to date. Quantitative imaging in medicine and surgery 2,** 33 (2012).

26. Federici, J. & Moeller, L. **Review of terahertz and subterahertz wireless communications. Journal of Applied Physics**, 6 (2010).

27. Kleine-Ostmann, T. & Nagatsuma, T. **A review on terahertz communications research. Journal of Infrared, Millimeter, and Terahertz Waves 32,** 143–171 (2011).

28. Federici, J. F., Schulkin, B., Huang, F., Gary, D., Barat, R., Oliveira, F. & Zimdars, D. **THz imaging and sensing for security applications. Semiconductor Science and Technology 20,** S266 (2005).

29. Wietzke, S., Jansen, C., Reuter, M., Jung, T., Kraft, D., Chatterjee, S., Fischer, B. & Koch, M. **Terahertz spectroscopy on polymers: A review of morphological studies. Journal of Molecular Structure 1006,** 41–51 (2011).

30. Zeitler, J. A., Taday, P. F., Newnham, D. A., Pepper, M., Gordon, K. C. & Rades, T. **Terahertz pulsed spectroscopy and imaging in the pharmaceutical setting: A review. Journal of Pharmacy and Pharmacology 59,** 209–223 (2007).

31. Xie, L., Yao, Y. & Ying, Y. **The application of terahertz spectroscopy to protein detection: A review. Applied Spectroscopy Reviews 49,** 448–461 (2014).

32. Siegel, P. H. **THz instruments for space. IEEE Transactions on Antennas and Propagation 55,** 2957–2965 (2007).

33. Pilbratt, G., Riedinger, J., Passvogel, T., Crone, G., Doyle, D., Gageur, U., Heras, A., Jewell, C., Metcalfe, L., Ott, S., *et al.* **Herschel Space Observatory - An ESA facility for far-infrared and submillimetre astronomy. Astronomy & Astrophysics 518,** L1 (2010).

34. Imura, K.-I., Takane, Y. & Tanaka, A. **Spin Berry phase in anisotropic topological insulators. Physical Review B 84,** 195406 (2011).

35. Imura, K.-I., Yoshimura, Y., Takane, Y. & Fukui, T. **Spherical topological insulator. Physical Review B 86,** 235119 (2012).

36. Byers, N. & Williams, G. **Out of the shadows: Contributions of twentieth-century women to physics. Cambridge University Press** (2006).

37. Einstein, A. **The late Emmy Noether. New York Times** (1935).

38. Landau, L. & Lifshitz, E. **Statistical physics, Part 1: Volume 5. Butterworth-Heinemann** (1980).

39. Cardy, J. **Scaling and renormalization in statistical physics. 5** (1996).

40. Thouless, D. J., Haldane, F. D. M. & Kosterlitz, J. M. **The Nobel prize in physics 2016. Current Science** (2016).

41. **Breakthrough Prize – Winners of the 2019 Breakthrough Prize in Life Sciences, Fundamental Physics and Mathematics Announced.** `https://breakthroughprize.org` (2018).

42. Hsieh, D., Qian, D., Wray, L., Xia, Y. Q., Hor, Y. S., Cava, R. J. & Hasan, M. Z. **A topological Dirac insulator in a quantum spin Hall phase. Nature 452,** 970–974 (2008).

43. Kane, C. L. & Mele, E. J. **Z_2 topological order and the quantum spin Hall effect. Physical Review Letters 95,** 146802 (2005).

44. Moore, J. E. & Balents, L. **Topological invariants of time-reversal-invariant band structures. Physical Review B 75,** 121306 (2007).

45. Chen, Y., Analytis, J. G., Chu, J.-H., Liu, Z., Mo, S.-K., Qi, X.-L., Zhang, H., Lu, D., Dai, X., Fang, Z., *et al.* **Experimental realization of a three-dimensional topological insulator, Bi_2Te_3. Science 325,** 178–181 (2009).

46. Moore, J. E. **The birth of topological insulators. Nature 464,** 194–198 (2010).

47. Fu, L., Kane, C. L. & Mele, E. J. **Topological insulators in three dimensions. Physical Review Letters 98,** 106803 (2007).

48. Zhang, H., Liu, C.-X., Qi, X.-L., Dai, X., Fang, Z. & Zhang, S.-C. **Topological insulators in Bi_2Se_3, Bi_2Te_3 and Sb_2Te_3 with a single Dirac cone on the surface. Nature Physics 5,** 438–442 (2009).

49. Liu, C.-X., Qi, X.-L., Zhang, H., Dai, X., Fang, Z. & Zhang, S.-C. **Model Hamiltonian for topological insulators. Physical Review B 82,** 045122 (2010).

50. Bernevig, B. A., Hughes, T. L. & Zhang, S.-C. **Quantum spin Hall effect and topological phase transition in HgTe quantum wells. Science 314,** 1757–1761 (2006).

51. König, M., Wiedmann, S., Brüne, C., Roth, A., Buhmann, H., Molenkamp, L. W., Qi, X.-L. & Zhang, S.-C. **Quantum spin Hall insulator state in HgTe quantum wells. Science 318,** 766–770 (2007).

52. Hasan, M. Z. & Kane, C. L. **Colloquium: Topological insulators. Reviews of Modern Physics 82,** 3045 (2010).

53. Shen, S.-Q. **Topological insulators. Springer 174** (2012).

54. Bernevig, B. A. & Hughes, T. L. **Topological insulators and topological superconductors. Princeton University Press** (2013).

55. Fradkin, E. **Field theories of condensed matter physics. Cambridge University Press** (2013).

56. Anderson, P. W. **More is different. Science 177,** 393–396 (1972).

57. Elliott, J. & Dawber, P. **Symmetry in Physics, Volume 1 and 2. Macmillan** (1979).

58. Zee, A. **Fearful symmetry: The search for beauty in modern physics. Princeton University Press** (2015).

59. Kosmann-Schwarzbach, Y. **The Noether Theorems. Springer** (2011).

60. Kühnel, W. **Differential geometry. American Mathematical Soc.** (2015).

61. Klitzing, K. v., Dorda, G. & Pepper, M. **New method for high-accuracy determination of the fine-structure constant based on quantized Hall resistance. Physical Review Letters 45,** 494 (1980).

62. Thouless, D. J., Kohmoto, M., Nightingale, M. P. & den Nijs, M. **Quantized Hall conductance in a two-dimensional periodic potential. Physical Review Letters 49,** 405 (1982).

63. Bernevig, B. A. & Zhang, S.-C. **Quantum spin Hall effect. Physical Review Letters 96,** 106802 (2006).

64. Kittel, C. & McEuen, P. **Introduction to solid state physics. Wiley New York** (1976).

65. Jones, W. & March, N. H. **Theoretical solid state physics. Courier Corporation** (1985).

66. Yang, D.-B., Meng, K., Wu, Y.-Z. & Meng, Y.-G. **The geometric and topological interpretation of Berry phase on a torus. arXiv:1904.07671** (2019).

67. Berry, M. V. **Quantal phase factors accompanying adiabatic changes. Proceedings of the Royal Society of London 392,** 45–57 (1984).

68. Bohm, A., Mostafazadeh, A., Koizumi, H., Niu, Q. & Zwanziger, J. **The geometric phase in quantum systems: Foundations, mathematical concepts, and applications in molecular and condensed matter physics. Springer Science** (2013).

69. Berry, M. *et al.* **Anticipations of the geometric phase. Physics Today 43,** 34–40 (1990).

70. Rhim, J.-W., Bardarson, J. H. & Slager, R.-J. **Unified bulk-boundary correspondence for band insulators. 97,** 115143 (2018).

71. Mong, R. S. & Shivamoggi, V. **Edge states and the bulk-boundary correspondence in Dirac Hamiltonians. Physical Review B 83,** 125109 (2011).

72. Isaev, L., Moon, Y. & Ortiz, G. **Bulk-boundary correspondence in three-dimensional topological insulators. Physical Review B 84,** 075444 (2011).

73. Heremans, J. P., Cava, R. J. & Samarth, N. **Tetradymites as thermoelectrics and topological insulators. Nature Reviews Materials 2,** 1–21 (2017).

74. Zhang, W., Yu, R., Zhang, H.-J., Dai, X. & Fang, Z. **First-principles studies of the three-dimensional strong topological insulators Bi_2Te_3, Bi_2Se_3 and Sb_2Te_3. New Journal of Physics 12,** 065013 (2010).

75. Allen, M. J., Tung, V. C. & Kaner, R. B. **Honeycomb carbon: A review of graphene. Chemical Reviews 110,** 132–145 (2010).

76. Alegria, L., Schroer, M., Chatterjee, A., Poirier, G., Pretko, M., Patel, S. & Petta, J. R. **Structural and electrical characterization of Bi_2Se_3 nanostructures grown by metal-organic chemical vapor deposition. Nano Letters 12,** 4711–4714 (2012).

77. Zhu, X.-G., Zhang, Y., Feng, W., Yuan, B.-K., Liu, Q., Qiu, R.-Z., Xie, D.-H., Tan, S.-Y., Duan, Y., Fang, Y., *et al.* **Electronic structures of topological insulator Bi_2Te_3 surfaces with non-conventional terminations. New Journal of Physics 18,** 093015 (2016).

78. Richter, W. & Becker, C. **A Raman and far-infrared investigation of phonons in the rhombohedral V2-VI3 compounds Bi_2Te_3, Bi_2Se_3, Sb_2Te_3 and $Bi_2(Te_{1-x}Se_x)_3$ ($0<x<1$), $(Bi_{1-y}Sb_y)_2Te_3$ ($0<y<1$). Physica Status Solidi (b) 84,** 619–628 (1977).

79. Vallone, M. **Higgs and Goldstone modes in crystalline solids. Physica Status Solidi (b) 257,** 1900443 (2020).

80. Wagner, V., Dolling, G., Powell, B. & Landweher, G. **Lattice vibrations of Bi_2Te_3. Physica Status Solidi (b) 85,** 311–317 (1978).

81. Cheng, W. & Ren, S.-F. **Phonons of single quintuple Bi_2Te_3 and Bi_2Se_3 films and bulk materials. Physical Review B 83,** 094301 (2011).

82. Shahil, K., Hossain, M., Goyal, V. & Balandin, A. **Micro-Raman spectroscopy of mechanically exfoliated few-quintuple layers of Bi_2Te_3, Bi_2Se_3, and Sb_2Te_3 materials. Journal of Applied Physics 111,** 054305 (2012).

83. Wen, X.-G., Wilczek, F. & Zee, A. **Chiral spin states and superconductivity. Physical Review B 39,** 11413 (1989).

84. Wen, X.-G. **Vacuum degeneracy of chiral spin states in compactified space. Physical Review B 40,** 7387 (1989).

85. Laughlin, R. & Zou, Z. **Properties of the chiral-spin-liquid state. Physical Review B 41,** 664 (1990).

86. Wen, X.-G. **Topological orders in rigid states. International Journal of Modern Physics B 4,** 239–271 (1990).

87. Witten, E. **Quantum field theory and the Jones polynomial. Communications in Mathematical Physics 121,** 351–399 (1989).

88. Keski-Vakkuri, E. & Wen, X.-G. **The Ground state structure and modular transformations of fractional quantum Hall states on a torus. International Journal of Modern Physics B** (1993).

89. Kalmeyer, V. & Laughlin, R. **Equivalence of the resonating-valence-bond and fractional quantum Hall states. Physical Review Letters 59,** 2095 (1987).

90. Tsui, D. C., Stormer, H. L. & Gossard, A. C. **Two-dimensional magnetotransport in the extreme quantum limit. Physical Review Letters 48,** 1559 (1982).

91. Laughlin, R. B. **Anomalous quantum Hall effect: An incompressible quantum fluid with fractionally charged excitations. Physical Review Letters 50,** 1395 (1983).

92. Wen, X.-G. & Niu, Q. **Ground-state degeneracy of the fractional quantum Hall states in the presence of a random potential and on high-genus Riemann surfaces. Physical Review B 41,** 9377 (1990).

93. Hansson, T., Oganesyan, V. & Sondhi, S. L. **Superconductors are topologically ordered. Annals of Physics 313,** 497–538 (2004).

94. Atiyah, M. F. **Topological quantum field theory. Publications Mathématiques de l'IHÉS 68,** 175–186 (1988).

95. Witten, E. **Topological quantum field theory. Communications in Mathematical Physics 117,** 353–386 (1988).

96. Wen, X.-G. **Quantum field theory of many-body systems: from the origin of sound to an origin of light and electrons. Oxford University Press** (2004).

97. Halperin, B. I. **Statistics of quasiparticles and the hierarchy of fractional quantized Hall states. Physical Review Letters 52,** 1583 (1984).

98. Arovas, D., Schrieffer, J. R. & Wilczek, F. **Fractional statistics and the quantum Hall effect. Physical Review Letters 53,** 722 (1984).

99. Moore, G. & Read, N. **Nonabelions in the fractional quantum Hall effect. Nuclear Physics B 360,** 362–396 (1991).

100. Kitaev, A. Y. **Fault-tolerant quantum computation by anyons. Annals of Physics 303,** 2–30 (2003).

101. Dennis, E., Kitaev, A., Landahl, A. & Preskill, J. **Topological quantum memory. Journal of Mathematical Physics 43,** 4452–4505 (2002).

102. Halperin, B. I. **Quantized Hall conductance, current-carrying edge states, and the existence of extended states in a two-dimensional disordered potential. Physical Review B 25,** 2185 (1982).

103. MacDonald, A. **Edge states in the fractional-quantum-Hall-effect regime. Physical Review Letters 64,** 220 (1990).

104. Xu, C. & Sachdev, S. **Global phase diagrams of frustrated quantum antiferromagnets in two dimensions: Doubled Chern-Simons theory. Physical Review B 79,** 064405 (2009).

105. Chen, X., Gu, Z.-C. & Wen, X.-G. **Local unitary transformation, long-range quantum entanglement, wave function renormalization, and topological order. Physical review b 82,** 155138 (2010).

106. Kitaev, A. **Toward topological classification of phases with short-range entanglement.** in (2011).

107. Senthil, T. **Symmetry-protected topological phases of quantum matter. Annual Review of Condensed Matter Physics 6,** 299–324 (2015).

108. Chen, X., Gu, Z.-C., Liu, Z.-X. & Wen, X.-G. **Symmetry protected topological orders and the group cohomology of their symmetry group. Physical Review B 87,** 155114 (2013).

109. Kitaev, A. **Periodic table for topological insulators and superconductors.** in. **1134** (2009), 22–30.

110. Asbóth, J. K., Oroszlány, L. & Pályi, A. **A short course on topological insulators. Lecture notes in physics 919,** 997–1000 (2016).

111. Su, W., Schrieffer, J. & Heeger, A. **Solitons in polyacetylene. Physical Review Letters 42,** 1698 (1979).

112. Su, W., Schrieffer, J. & Heeger, A. **Soliton excitations in polyacetylene. Physical Review B 22,** 2099 (1980).

113. Fu, L. **Topological crystalline insulators. Physical Review Letters 106,** 106802 (2011).

114. Ando, Y. & Fu, L. **Topological crystalline insulators and topological superconductors: From concepts to materials. Annual Review of Condensed Matter Physics 6,** 361–381 (2015).

115. Burkov, A. **Topological semimetals. Nature materials 15,** 1145–1148 (2016).

116. Yan, B. & Felser, C. **Topological materials: Weyl semimetals. Annual Review of Condensed Matter Physics 8,** 337–354 (2017).

117. Sato, M. & Ando, Y. **Topological superconductors: A review. Reports on Progress in Physics 80,** 076501 (2017).

118. Huang, Y., Lou, W., Cheng, F., Yang, W. & Chang, K. **THz Emission by Frequency Down-conversion in Topological Insulator Quantum Dots. Physical Review Applied 12,** 034003 (2019).

119. Pesin, D. & MacDonald, A. H. **Spintronics and pseudospintronics in graphene and topological insulators. Nature Materials 11,** 409–416 (2012).

120. Paudel, H. P. & Leuenberger, M. N. **Three-dimensional topological insulator quantum dot for optically controlled quantum memory and quantum computing. Physical Review B 88,** 085316 (2013).

121. He, M., Sun, H. & He, Q. L. **Topological insulator: Spintronics and quantum computations. Frontiers of Physics 14,** 1–16 (2019).

122. Yokoyama, T. & Murakami, S. **Spintronics and spincaloritronics in topological insulators. Physica E: Low-dimensional Systems and Nanostructures 55,** 1–8 (2014).

123. Fan, Y. & Wang, K. L. **Spintronics based on topological insulators.** in. **6** (2016), 1640001.

124. Fujita, T., Jalil, M. B. A. & Tan, S. G. **Topological insulator cell for memory and magnetic sensor applications. Applied Physics Express 4,** 094201 (2011).

125. Fu, L. & Kane, C. L. **Superconducting proximity effect and Majorana fermions at the surface of a topological insulator. Physical Review Letters 100,** 096407 (2008).

126. Fu, L. & Kane, C. L. **Josephson current and noise at a superconductor/quantum-spin-Hall-insulator/superconductor junction. Physical Review B 79,** 161408 (2009).

127. Williams, J., Bestwick, A., Gallagher, P., Hong, S. S., Cui, Y., Bleich, A. S., Analytis, J., Fisher, I. & Goldhaber-Gordon, D. **Unconventional Josephson effect in hybrid superconductor-topological insulator devices. Physical Review Letters 109,** 056803 (2012).

128. Chang, C.-Z., Zhang, J., Feng, X., Shen, J., Zhang, Z., Guo, M., Li, K., Ou, Y., Wei, P., Wang, L.-L., *et al.* **Experimental observation of the quantum anomalous Hall effect in a magnetic topological insulator. Science 340,** 167–170 (2013).

129. Tokura, Y., Yasuda, K. & Tsukazaki, A. **Magnetic topological insulators. Nature Reviews Physics 1,** 126–143 (2019).

130. Zhang, L., Ren, J., Wang, J.-S. & Li, B. **Topological magnon insulator in insulating ferromagnet. Physical Review B 87,** 144101 (2013).

131. Owerre, S. **A first theoretical realization of honeycomb topological magnon insulator. Journal of Physics: Condensed Matter 28,** 386001 (2016).

132. Khanikaev, A. B., Mousavi, S. H., Tse, W.-K., Kargarian, M., MacDonald, A. H. & Shvets, G. **Photonic topological insulators. Nature materials 12,** 233–239 (2013).

133. Goldman, N., Budich, J. C. & Zoller, P. **Topological quantum matter with ultracold gases in optical lattices. Nature Physics 12,** 639–645 (2016).

134. Volovik, G. E. **The universe in a helium droplet. Oxford University Press** (2003).

135. Karzig, T., Bardyn, C.-E., Lindner, N. H. & Refael, G. **Topological polaritons. Physical Review X 5,** 031001 (2015).

136. Fleury, R., Sounas, D., Haberman, M. R. & Alu, A. **Nonreciprocal acoustics. Acoustics Today 11,** 14–21 (2015).

137. Huber, S. D. **Topological mechanics. Nature Physics 12,** 621–623 (2016).

138. Vilenkin, A. & Shellard, E. P. S. **Cosmic strings and other topological defects. Cambridge University Press** (2000).

139. Durrer, R. **Topological defects in cosmology. New Astronomy Reviews 43,** 111–156 (1999).

140. Zurek, W. H. **Cosmological experiments in condensed matter systems. Physics Reports 276,** 177–221 (1996).

141. Teo, J. C. & Hughes, T. L. **Topological defects in symmetry-protected topological phases. Annual Review of Condensed Matter Physics 8,** 211–237 (2017).

142. Teo, J. C. & Kane, C. L. **Topological defects and gapless modes in insulators and superconductors. Physical Review B 82,** 115120 (2010).

143. Zurek, W. H. **Cosmological experiments in superfluid helium? Nature 317,** 505–508 (1985).

144. Vollhardt, D. & Wolfle, P. **The superfluid phases of Helium 3. Courier Corporation** (2013).

145. Bunkov, Y. M. & Godfrin, H. **Topological defects and the non-equilibrium dynamics of symmetry breaking phase transitions. Springer Science** (2012).

146. Ohanian, H. C. **Classical electrodynamics. Allyn and Bacon** (1988).

147. Jackson, J. D. **Classical electrodynamics. John Wiley & Sons** (2007).

148. Greiner, W. **Classical electrodynamics. Springer Science** (2012).

149. Cohen-Tannoudji, C., Dupont-Roc, J. & Grynberg, G. **Atom-photon interactions: Basic processes and applications. John Wiley & Sons** (1998).

150. Loudon, R. **The quantum theory of light. OUP Oxford** (2000).

151. Stoica, P., Moses, R. L., *et al.* **Spectral analysis of signals. Pearson** (2005).

152. Clerk, A. A., Devoret, M. H., Girvin, S. M., Marquardt, F. & Schoelkopf, R. J. **Introduction to quantum noise, measurement, and amplification. Reviews of Modern Physics 82,** 1155 (2010).

153. Milonni, P. W. **The quantum vacuum: An introduction to quantum electrodynamics** (2013).

154. Schawlow, A. L. & Townes, C. H. **Infrared and optical masers. Physical Review 112,** 1940 (1958).

155. Maiman, T. H. **Stimulated optical radiation in ruby. Nature 187,** 493–494 (1960).

156. Powell, J. **CO_2 laser cutting. Springer** (1993).

157. Ehrlich, D. & Tsao, J. **A review of laser–microchemical processing. Journal of Vacuum Science & Technology B: Microelectronics Processing and Phenomena 1,** 969–984 (1983).

158. Collis, R. **Lidar. Applied Optics 9,** 1782–1788 (1970).

159. Slusher, R. **Laser technology. Reviews of Modern Physics 71,** S471 (1999).

160. Gillner, A., Holtkamp, J., Hartmann, C., Olowinsky, A., Gedicke, J., Klages, K., Bosse, L. & Bayer, A. **Laser applications in microtechnology. Journal of Materials Processing Technology 167,** 494–498 (2005).

161. Bian, J., Zhou, L., Wan, X., Zhu, C., Yang, B. & Huang, Y. **Laser transfer, printing, and assembly techniques for flexible electronics. Advanced Electronic Materials 5,** 1800900 (2019).

162. Toyoshima, M., Takayama, Y., Takahashi, T., Suzuki, K., Kimura, S., Takizawa, K., Kuri, T., Klaus, W., Toyoda, M., Kunimori, H., *et al.* **Ground-to-satellite laser communication experiments. IEEE Aerospace and Electronic Systems Magazine 23,** 10–18 (2008).

163. Wolbarsht, M. L. *et al.* **Laser applications in medicine and biology. 1** (1971).

164. Tata, D. B. & Waynant, R. W. **Laser therapy: A review of its mechanism of action and potential medical applications. Laser & Photonics Reviews 5,** 1–12 (2011).

165. David, C. M., Gupta, P., *et al.* **Lasers in dentistry: A review. International Journal of Advances in Health Sciences 2,** 7–13 (2015).

166. Lee, H., Lim, C. H. J., Low, M. J., Tham, N., Murukeshan, V. M. & Kim, Y.-J. **Lasers in additive manufacturing: A review. International Journal of Precision Engineering and Manufacturing-Green Technology 4,** 307–322 (2017).

167. Lei, S., Zhao, X., Yu, X., Hu, A., Vukelic, S., Jun, M. B., Joe, H.-E., Yao, Y. L. & Shin, Y. C. **Ultrafast laser applications in manufacturing processes: A state-of-the-art review. Journal of Manufacturing Science and Engineering 142** (2020).

168. Titterton, D. H. **Military laser technology and systems. Artech House** (2015).

169. Menzel, E. R. **Fingerprint detection with lasers. M. Dekker New York** (1999).

170. Menzel, E. **Laser Applications in Criminalistics. Journal of Laser Applications 3,** 39–44 (1991).

171. Felguera-Martín, D., González-Partida, J.-T., Almorox-González, P. & Burgos-García, M. **Vehicular traffic surveillance and road lane detection using radar interferometry. IEEE transactions on vehicular technology 61,** 959–970 (2012).

172. Novotny, L. & Hecht, B. **Principles of nano-optics. Cambridge university press** (2012).

173. Bharadwaj, P., Deutsch, B. & Novotny, L. **Optical antennas. Advances in Optics and Photonics 1,** 438–483 (2009).

174. Novotny, L. **Physical Optics II - Electrodynamic Field Theory.** `https://www.photonics.ethz.ch/en/our-range/education/courses/physical-optics-ii`.

175. Ohtsu, M. & Kobayashi, K. **Optical near fields: Introduction to classical and quantum theories of electromagnetic phenomena at the nanoscale. Springer Science** (2013).

176. Jones, D. S. **Acoustic and electromagnetic waves. Clarendon Press** (1986).

177. Economou, E. N. **Green's functions in quantum physics. Springer Science 7** (2006).

178. Rickayzen, G. **Green's functions and condensed matter. Courier Corporation** (2013).

179. Chew, W. C., Sha, W. E. & Dai, Q. I. **Green's dyadic, spectral function, local density of states, and fluctuation dissipation theorem. Progress In Electromagnetics Research** (2019).

180. Narayanaswamy, A. & Chen, G. **Dyadic Green's functions and electromagnetic local density of states. Journal of Quantitative Spectroscopy and Radiative Transfer 111,** 1877–1884 (2010).

181. Feynman, R. P. **There's plenty of room at the bottom. California Institute of Technology, Engineering and Science magazine** (1960).

182. Kundu, A., Zazunov, A., Yeyati, A. L., Martin, T. & Egger, R. **Energy spectrum and broken spin-surface locking in topological insulator quantum dots. Physical Review B 83,** 125429 (2011).

183. Gioia, L., Christie, M., Zülicke, U., Governale, M. & Sneyd, A. **Spherical topological insulator nanoparticles: Quantum size effects and optical transitions. Physical Review B 100,** 205417 (2019).

184. Kong, D., Randel, J. C., Peng, H., Cha, J. J., Meister, S., Lai, K., Chen, Y., Shen, Z.-X., Manoharan, H. C. & Cui, Y. **Topological insulator nanowires and nanoribbons. Nano letters 10,** 329–333 (2010).

185. Tian, M., Ning, W., Qu, Z., Du, H., Wang, J. & Zhang, Y. **Dual evidence of surface Dirac states in thin cylindrical topological insulator Bi_2Te_3 nanowires. Scientific reports 3,** 1–7 (2013).

186. Chen, F. W., Jauregui, L. A., Tan, Y., Manfra, M., Klimeck, G., Chen, Y. P. & Kubis, T. **In-surface confinement of topological insulator nanowire surface states. Applied Physics Letters 107,** 121605 (2015).

187. Zhang, S.-f. & Gong, W.-j. **Interference effect in the electronic transport of a topological insulator quantum dot. Journal of Physics: Condensed Matter**.

188. Klimov, V. V., Ducloy, M. & Letokhov, V. S. **Spontaneous emission of an atom in the presence of nanobodies. Quantum electronics 31,** 569 (2001).

189. Min, Y., Moon, G. D., Kim, B. S., Lim, B., Kim, J.-S., Kang, C. Y. & Jeong, U. **Quick, controlled synthesis of ultrathin Bi_2Se_3 nanodiscs and nanosheets. Journal of the American Chemical Society 134,** 2872–2875 (2012).

190. Li, H., Cao, J., Zheng, W., Chen, Y., Wu, D., Dang, W., Wang, K., Peng, H. & Liu, Z. **Controlled synthesis of topological insulator nanoplate arrays on mica. Journal of the American Chemical Society 134,** 6132–6135 (2012).

191. Dubrovkin, A. M., Adamo, G., Yin, J., Wang, L., Soci, C., Wang, Q. J. & Zheludev, N. I. **Visible range plasmonic modes on topological insulator nanostructures. Advanced Optical Materials 5** (2017).

192. Cho, S., Kim, D., Syers, P., Butch, N. P., Paglione, J. & Fuhrer, M. S. **Topological insulator quantum dot with tunable barriers. Nano letters 12,** 469–472 (2012).

193. Zhang, Y., He, K., Chang, C.-Z., Song, C.-L., Wang, L.-L., Chen, X., Jia, J.-F., Fang, Z., Dai, X., Shan, W.-Y., *et al.* **Crossover of the three-dimensional topological insulator Bi_2Se_3 to the two-dimensional limit. Nature Physics 6,** 584–588 (2010).

194. Shan, W.-Y., Lu, H.-Z. & Shen, S.-Q. **Effective continuous model for surface states and thin films of three-dimensional topological insulators. New Journal of Physics 12,** 043048 (2010).

195. Bohren, C. F. & Huffman, D. R. **Absorption and scattering of light by small particles. John Wiley & Sons** (2008).

196. Chevalier, P., Armizhan, A., Wang, F., Piccardo, M., Johnson, S. G., Capasso, F. & Everitt, H. O. **Widely tunable compact terahertz gas lasers. Science 366,** 856–860 (2019).

197. Castro-Enriquez, L. A., Quezada, L. F. & Martín-Ruiz, A. **Optical response of a topological-insulator–quantum-dot hybrid interacting with a probe electric field. Physical Review A 102,** 013720 (2020).

198. Bera, D., Qian, L., Tseng, T.-K. & Holloway, P. H. **Quantum dots and their multimodal applications: A review. Materials 3,** 2260–2345 (2010).

199. Jacak, L., Hawrylak, P. & Wojs, A. **Quantum dots. Springer Science** (2013).

200. Griffiths, D. J. & Schroeter, D. F. **Introduction to quantum mechanics. Cambridge University Press** (2018).

201. Planck, M. **The theory of heat radiation. Courier Corporation** (2013).

202. Dodonov, V. & Dodonov, A. **The nonstationary Casimir effect in a cavity with periodical time-dependent conductivity of a semiconductor mirror. Journal of Physics A: Mathematical and General** (2006).

203. Shaltout, A., Kildishev, A. & Shalaev, V. **Time-varying metasurfaces and Lorentz non-reciprocity. Optical Materials Express 39,** 6271 (2006).

204. Eric, D. K., Erdman, M. F. & Berge, R. **Nanosystems: Molecular machinery, manufacturing, and computation. John Wiley & Sons** (1992).

205. Sokolikova, M., Sherrell, P., Palczynski, P., Bemmer, V. & Mattevi, C. **Room-temperature growth of colloidal Bi_2Te_3 nanosheets. Chemical Communications 53,** 8026–8029 (2017).

206. Cha, J. J., Koski, K. J. & Cui, Y. **Topological insulator nanostructures. Physica Status Solidi (RRL)–Rapid Research Letters 7,** 15–25 (2013).

207. Caha, O., Dubroka, A., Humlicek, J., Holy, V., Steiner, H., Ul-Hassan, M., Sánchez-Barriga, J., Rader, O., Stanislavchuk, T., Sirenko, A., *et al.* **Growth, structure, and electronic properties of epitaxial bismuth telluride topological insulator films on BaF_2 (111) substrates. Crystal Growth & Design 13,** 3365–3373 (2013).

208. Wang, C., Zhu, X., Nilsson, L., Wen, J., Wang, G., Shan, X., Zhang, Q., Zhang, S., Jia, J. & Xue, Q. **In situ Raman spectroscopy of topological insulator Bi_2Te_3 films with varying thickness. Nano Research 6,** 688–692 (2013).

209. Jian-Hua, G., Feng, Q., Yun, Z., Hui-Yong, D., Gu-Jin, H., Xiao-Nan, L., Guo-Lin, Y. & Ning, D. **Surface oxidation properties in a topological insulator Bi_2Te_3 film. Chinese Physics Letters 30,** 106801 (2013).

210. Xu, H., Song, Y., Gong, Q., Pan, W., Wu, X. & Wang, S. **Raman spectroscopy of epitaxial topological insulator Bi_2Te_3 thin films on GaN substrates. Modern Physics Letters B 29,** 1550075 (2015).

211. Qi, X., Ma, W., Zhang, X. & Zhang, C. **Raman characterization and transport properties of morphology-dependent two-dimensional Bi_2Te_3 nanofilms. Applied Surface Science 457,** 41–48 (2018).

212. Boulares, I., Shi, G., Kioupakis, E., Lošt'ák, P., Uher, C. & Merlin, R. **Surface phonons in the topological insulators Bi_2Se_3 and Bi_2Te_3. Solid State Communications 271,** 1–5 (2018).

213. Dubroka, A., Caha, O., Hronček, M., Friš, P., Orlita, M., Holý, V., Steiner, H., Bauer, G., Springholz, G. & Humlíček, J. **Interband absorption edge in the topological insulators $Bi_2(Te_{1-x}Se_x)_3$. Physical Review B 96,** 235202 (2017).

214. Massa, E., Maier, S. A. & Giannini, V. **An analytical approach to light scattering from small cubic and rectangular cuboidal nanoantennas. New Journal of Physics 15,** 063013 (2013).

215. Moskovits, M. **Surface-enhanced spectroscopy. Reviews of modern physics 57,** 783 (1985).

216. Klimov, V. & Letokhov, V. **Electric and magnetic dipole transitions of an atom in the presence of spherical dielectric interface. Laser physics 15,** 61–73 (2005).

217. Bharadwaj, P. & Novotny, L. **Spectral dependence of single molecule fluorescence enhancement. Optics Express 15,** 14266–14274 (2007).

218. Cohen-Tannoudji, C., Diu, B. & Laloë, F. **Quantum Mechanics, Volume 2: Angular Momentum, Spin, and Approximation Methods. John Wiley & Sons** (2020).

219. Fano, U. **Effects of Configuration Interaction on Intensities and Phase Shifts. Physical Review 124,** 1866 (1961).